Draft-2018/07/19

IHEP-CEPC-DR-2018-XX

IHEP-EP-2018-XX

IHEP-TH-2018-XX

Draft v0.2

CEPC

Conceptual Design Report

Volume II - Physics & Detector

The CEPC Study Group

Fall 2018

Draft-v0.2

ACKNOWLEDGMENTS

The CEPC Physics and Detector Conceptual Design Report (CDR) was prepared and written by the CEPC Study Group. The study was organised and led by scientists from the Institute of High Energy Physics (IHEP) of the Chinese Academy of Sciences (CAS), and from many universities and other institutes in China and abroad. The study was partially supported ...

...

Draft-v0.2

Draft-v0.2

CONTENTS

Acknowledgments iii

1 Executive Summary 1

1.1 The CEPC-SPPC Study Group and the CDR 1
1.2 The Case for the CEPC-SppC in China 1
1.3 The Science in the CDR 1
1.4 The Accelerator and the Experiment 1
1.5 Detector Research and Development 1

2 Overview of the Physics Case for CEPC 3

2.1 First theory subsection 3

3 Experimental conditions and detector concepts 5

3.1 Experimental conditions 5
3.1.1 Higgs Operation 5
3.1.2 Z pole Operation 8
3.1.3 W threshold scan 9
3.2 Physics Requirements 9
3.2.1 Multiplicity 9
3.2.2 Tracking 9
3.2.3 Lepton 11
3.2.4 Particle identification 12
3.2.5 Photons 12
3.2.6 Jets and Missing energy 14
3.2.7 Flavor Tagging 15
3.3 Detector concepts 15
3.3.1 The baseline detector concept 15

Draft-v0.2

3.3.2 Full silicon detector concept 19
3.3.3 An alternative low magnetic field detector concept 19

4 Tracking system 23

4.1 Vertex tracker detector 23
4.1.1 Performance Requirements and Detector Challenges 23
4.1.2 Baseline design 24
4.1.3 Detector performance studies 24
4.1.4 Beam-induced Background in the Vertex Detector 27
4.1.5 Sensor Technology Options 27
4.1.6 Mechanics and Integration 29
4.1.7 Critical R&D 31
4.1.8 Future R&D 31
4.1.9 Summary 32
4.2 Silicon tracker detector 32
4.2.1 Baseline design 33
4.2.2 Sensor technologies 35
4.2.3 Front-End electronics 35
4.2.4 Powering and cooling 36
4.2.5 Mechanics and integration 36
4.2.6 Tracking performance 36
4.2.7 Critical R&D 39
4.3 TPC tracker detector 39
4.3.1 Principle of Time Projection Chamber 40
4.3.2 Baseline design and technology challenges 42
4.3.3 Simulation and estimation for the key issues 49
4.3.4 Feasibility study of TPC detector module and future work 51
4.3.5 Conclusion 54
4.4 Full-silicon tracker detector 54
4.4.1 Full silicon tracker layout 55
4.4.2 Toy simulation 55
4.4.3 Detector simulation and reconstruction 57
4.4.4 Tracking performance 60
4.4.5 Conclusion 61
4.5 Drift chamber tracker detector 62
4.5.1 Introduction 62
4.5.2 Overview 65
4.5.3 Expected performance 65
4.5.4 Tracking system simulation results 66

5 Calorimetry 73

5.1 Introduction to calorimeters 73
5.2 Electromagnetic Calorimeter for Particle Flow Approach 75
5.2.1 Silicon-Tungsten Sandwich Electromagnetic Calorimeter 76
5.2.2 Scintillator-Tungsten Sandwich Electromagnetic Calorimeter 82
5.3 Hadronic Calorimeter for Particle Flow Approach 88
5.3.1 Introduction 88
5.3.2 Semi-Digital Hadronic Calorimeter (SDHCAL) 90

Draft-v0.2

5.3.3 Analog Hadronic Calorimeter based on Scintillator and SiPM 104
5.4 Dual-readout calorimetry 112
5.4.1 Introduction 112
5.4.2 Principle of dual-readout calorimetry 113
5.4.3 Layout and mechanics 114
5.4.4 Sensors and readout electronics 116
5.4.5 Performance studies with fibre-sampling prototypes 118
5.4.6 Montecarlo simulations 121
5.4.7 Final remarks 128

6 Detector magnet system 133

6.1 General Design Considerations 133
6.2 The Magnetic Field Requirements and Design 134
6.2.1 Main parameters 134
6.2.2 Magnetic field design 134
6.2.3 Coil mechanical analysis 136
6.2.4 Preliminary quench analysis 140
6.3 HTS/LTS Superconductor Options 141
6.3.1 HTS plan background 141
6.3.2 The latest development of high temperature superconducting cable 144
6.3.3 HTS magnetic design 148
6.3.4 Future work of HTS plan 150
6.4 Solenoid Coil Design 151
6.4.1 Solenoid Coil Structure 151
6.4.2 R&D of Superconducting Conductor 151
6.4.3 Coil fabrication and assembly 153
6.5 Magnet Cryogenics Design 153
6.5.1 Preliminary Simulation of the Thermosyphon Circuit 153
6.5.2 Preliminary results for 10:1 scale model 155
6.5.3 Experiment of a small-sized He thermosiphon 155
6.6 Quench Protection and Power supply 160
6.6.1 power supply 160
6.6.2 Quench Protection 160
6.7 Iron Yoke Design 161
6.7.1 The Barrel Yoke 162
6.7.2 The Endcap Yoke 162
6.7.3 Yoke assembly 162
6.8 Dual Solenoid Scenario 163
6.9 The low magnetic field detector magnet 164

7 Muon system 167

7.1 Baseline Design 167
7.2 The Resistive Plate Chamber technology 169
7.3 The μRWell technology 170
7.3.1 Large size μRWell detectors 171
7.3.2 Applications for a Muon detection system for a CepC experiment 173
7.4 Future R&D 174

Draft-v0.2

8 Readout electronics and data acquisition **177**

8.1 New Colliders for a New Frontier 178

9 CEPC interaction region and detector integration **179**

9.1 Interaction region 179
9.2 Final focusing magnets 180
9.3 Detector backgrounds 181
9.3.1 Synchrotron radiation 181
9.3.2 Beam-beam interactions 182
9.3.3 Off-energy beam particles 183
9.3.4 Predicted radiation background levels 184
9.4 Luminosity instrumentation 186
9.4.1 Technological and design options 187
9.4.2 Systematic effects 192
9.4.3 Summary on LumiCal 193
9.5 Detector integration 194

10 Physics performance **197**

10.1 Introduction 197
10.2 The CEPC Software and the Arbor 197
10.2.1 The cepcsoft 198
10.2.2 Arbor 200
10.3 Performance at the Physics Object level 204
10.3.1 Tracking performance 204
10.3.2 Leptons 205
10.3.3 Kaon Identification 208
10.3.4 Photons 210
10.3.5 Jet 212
10.3.6 Jet flavor tagging 219
10.4 conclusion 221

11 Benchmark Physics **223**

11.1 Higgs Boson Physics 225
11.1.1 Higgs boson production and decay 225
11.1.2 Higgs boson tagging 227
11.1.3 Measurements of $\sigma(ZH)$ and m_H 229
11.1.4 Analyses of individual Higgs boson decay modes 230
11.1.5 Combination of individual analyses 233
11.1.6 Higgs boson width 235
11.1.7 Higgs Boson Coupling Measurements 235
11.1.8 Searches for exotic decays 250
11.1.9 Tests of Higgs boson spin/CP 250
11.2 W, Z measurements at the CEPC 256
11.2.1 Z pole measurements 256
11.2.2 W mass measurement 261

12 Futrue plans and R&D prospects **265**

12.1 New Colliders for a New Frontier 266

Draft-v0.2

CHAPTER 1

EXECUTIVE SUMMARY

Draft-v0.2

This section is just a placeholder for now. It will be a short introducition 2-4 pages with a very short motivation for the CEPC project [1] and the workings of the CDR. We will define here the goals of the CDR and will already mention the connection between the different detector concepts. We will mention quickly some of the challenges and the future R&D program. We can also provide the short descriptions to the chapters in the CDR. There will be no subsections sections in this text.

1.1 The CEPC-SPPC Study Group and the CDR

1.2 The Case for the CEPC-SppC in China

1.3 The Science in the CDR

1.4 The Accelerator and the Experiment

1.5 Detector Research and Development

References

[1] CEPC project website. http://cepc.ihep.ac.cn.

By Copyright © 2018 HEP Community

Draft-v0.2

CHAPTER 2

OVERVIEW OF THE PHYSICS CASE FOR CEPC

Draft-v0.2

Lorem ipsum dolor sit amet, consectetuer adipiscing elit. Ut purus elit, vestibulum ut, placerat ac, adipiscing vitae, felis. Curabitur dictum gravida mauris. Nam arcu libero, nonummy eget, consectetuer id, vulputate a, magna. Donec vehicula augue eu neque. Pellentesque habitant morbi tristique senectus et netus et malesuada fames ac turpis egestas. Mauris ut leo. Cras viverra metus rhoncus sem. Nulla et lectus vestibulum urna fringilla ultrices. Phasellus eu tellus sit amet tortor gravida placerat. Integer sapien est, iaculis in, pretium quis, viverra ac, nunc. Praesent eget sem vel leo ultrices bibendum. Aenean faucibus. Morbi dolor nulla, malesuada eu, pulvinar at, mollis ac, nulla. Curabitur auctor semper nulla. Donec varius orci eget risus. Duis nibh mi, congue eu, accumsan eleifend, sagittis quis, diam. Duis eget orci sit amet orci dignissim rutrum.

Nam dui ligula, fringilla a, euismod sodales, sollicitudin vel, wisi. Morbi auctor lorem non justo. Nam lacus libero, pretium at, lobortis vitae, ultricies et, tellus. Donec aliquet, tortor sed accumsan bibendum, erat ligula aliquet magna, vitae ornare odio metus a mi. Morbi ac orci et nisl hendrerit mollis. Suspendisse ut massa. Cras nec ante. Pellentesque a nulla. Cum sociis natoque penatibus et magnis dis parturient montes, nascetur ridiculus mus. Aliquam tincidunt urna. Nulla ullamcorper vestibulum turpis. Pellentesque cursus luctus mauris.

This [1] is an example with plots, please edit ...

2.1 First theory subsection

Lorem ipsum dolor sit amet, consectetuer adipiscing elit. Ut purus elit, vestibulum ut, placerat ac, adipiscing vitae, felis. Curabitur dictum gravida mauris. Nam arcu libero, nonummy eget, consectetuer id, vulputate a, magna. Donec vehicula augue eu neque.

By Copyright © 2018 HEP Community

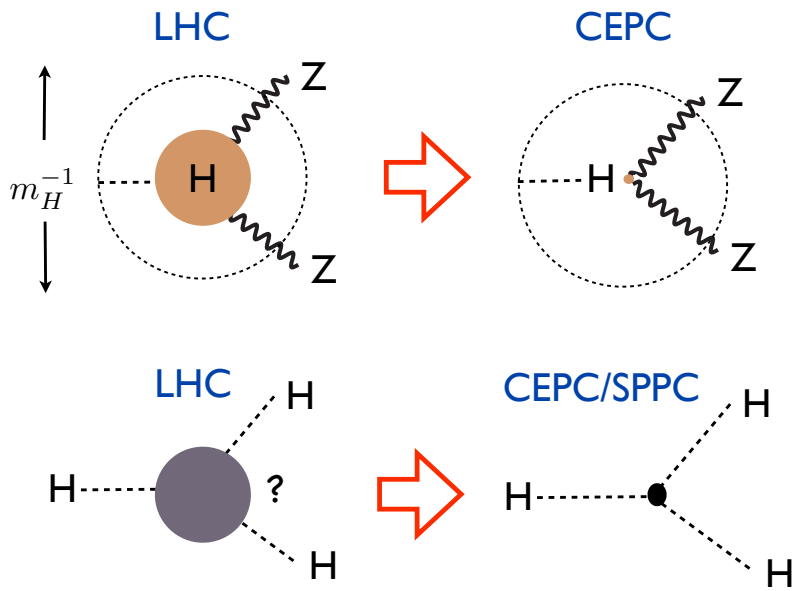

Figure 2.1: A sketch of two of the central goals of the CEPC and SPPC. The CEPC will probe whether the Higgs is truly "elementary", with a resolution up to a hundred times more powerful than the LHC. The SPPC will see, for the first time, a fundamentally new dynamical process — the self-interaction of an elementary particle — uniquely associated with the Higgs.

Pellentesque habitant morbi tristique senectus et netus et malesuada fames ac turpis egestas. Mauris ut leo. Cras viverra metus rhoncus sem. Nulla et lectus vestibulum urna fringilla ultrices. Phasellus eu tellus sit amet tortor gravida placerat. Integer sapien est, iaculis in, pretium quis, viverra ac, nunc. Praesent eget sem vel leo ultrices bibendum. Aenean faucibus. Morbi dolor nulla, malesuada eu, pulvinar at, mollis ac, nulla. Curabitur auctor semper nulla. Donec varius orci eget risus. Duis nibh mi, congue eu, accumsan eleifend, sagittis quis, diam. Duis eget orci sit amet orci dignissim rutrum.

Nam dui ligula, fringilla a, euismod sodales, sollicitudin vel, wisi. Morbi auctor lorem non justo. Nam lacus libero, pretium at, lobortis vitae, ultricies et, tellus. Donec aliquet, tortor sed accumsan bibendum, erat ligula aliquet magna, vitae ornare odio metus a mi. Morbi ac orci et nisl hendrerit mollis. Suspendisse ut massa. Cras nec ante. Pellentesque a nulla. Cum sociis natoque penatibus et magnis dis parturient montes, nascetur ridiculus mus. Aliquam tincidunt urna. Nulla ullamcorper vestibulum turpis. Pellentesque cursus luctus mauris.

References

[1] CEPC project website. http://cepc.ihep.ac.cn.

Draft-v0.2

CHAPTER 3

EXPERIMENTAL CONDITIONS AND DETECTOR CONCEPTS

Draft-v0.2

3.1 Experimental conditions

The CEPC can be operated as a Z factory ($\sqrt{s}$ = 91.2 GeV) and a Higgs factory ($\sqrt{s}$ = 240 GeV). It could also perform W threshold scan at $\sqrt{s}$ around 160 GeV and determines precisely the mass and width of the W boson. According to the CEPC Accelerator CDR [**?**], the luminosities at these center of mass energies are listed in Table 3.1.

As an electron positron collider, the CEPC is an extremely clean machine. Fig. 3.1 shows the cross section of leading SM processes at the electron positron collision. The ratio between the cross sections of the Higgs signal and the inclusive physics events is roughly $10^{-2} \sim 10^{-3}$ at CEPC [**?**], eight orders of magnitudes larger than that in the LHC [**?**]. At the CEPC, the entire physics event rate is so low that every physics event can be recorded, providing ideal samples for the precision measurements.

The beam parameters of different CEPC physics operations are summarized in Tab **??**. The main physics objective and leading physics requirements for the detector/collider system is discussed below.

3.1.1 Higgs Operation

The CEPC Higgs operation is expected to accumulate an integrated luminosity of $5\ ab^{-1}$ and produce 1 million Higgs boson. Its main physics objective is to determine precisely the Higgs boson properties. The Higgs signal event rate is roughly of the order of 0.01 Hz: roughly 1 Higgs boson every two minutes.

The typical measurements including the absolute measurement of $\sigma(ZH)$ via the recoil mass method, the Higgs event rates measurements, and the differential measurements on the Higgs events.

By Copyright © 2018 HEP Community

Draft 2018/07/10

Operation mode	Z factory	W threshold scan	Higgs factory
$\sqrt{s}$/GeV	91.2	158 - 172	240
L/$10^{34}\mathrm{cm}^{-2}\mathrm{s}^{-1}$	16-32	10	3
Running time/year	2	1	7
Integrated Luminosity/ab^{-1}	8 - 16	2.5	5
Higgs yield	-	-	10^6
W yield	-	10^7	10^8
Z yield	10^{11-12}	10^9	10^9

Table 3.1: Instance luminosity at different $\sqrt{s}$ and anticipated boson yields at the CEPC.

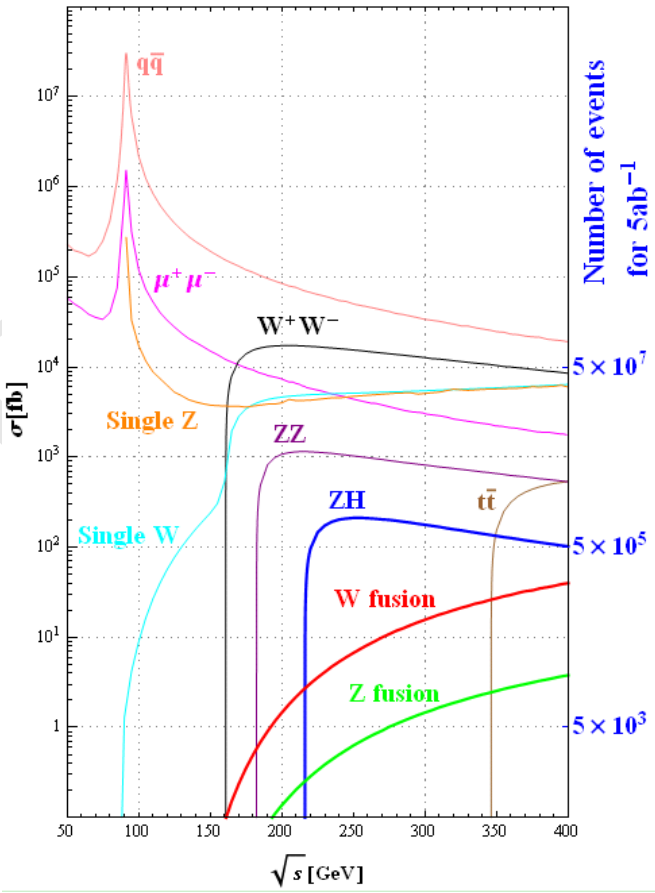

Figure 3.1: Cross sections of the leading Standard Model processes at non polarized electron positron collision (Left) and at proton collision (Right)

	Higgs	*W*	*Z (3T)*	*Z (2T)*
Number of IPs	2			
Beam energy (GeV)	120	80	45.5	
Circumference (km)	100			
Synchrotron radiation loss/turn (GeV)	1.73	0.34	0.036	
Crossing angle at IP (mrad)	16.5×2			
Piwinski angle	2.58	7.0	23.8	
Number of particles/bunch N_e (10^{10})	15.0	12.0	8.0	
Bunch number	242	1524	12000 (10% gap)	
Bunch spacing (ns)	680	210	25	
Beam current (mA)	17.4	87.9	461.0	
Synchrotron radiation power (MW)	30	30	16.5	
Bending radius (km)	10.7			
Momentum compaction (10^{-5})	1.11			
β function at IP β_x^* / β_y^* (m)	0.36/0.0015	0.36/0.0015	0.2/0.0015	0.2/0.001
Emittance x/y (nm)	1.21/0.0031	0.54/0.0016	0.18/0.004	0.18/0.0016
Beam size at IP σ_x /σ_y (μm)	20.9/0.068	13.9/0.049	6.0/0.078	6.0/0.04
Beam-beam parameters ξ_x /ξ_y	0.031/0.109	0.013/0.106	0.004/0.056	0.004/0.072
RF voltage V_{RF} (GV)	2.17	0.47	0.10	
RF frequency f_{RF} (MHz)	650			
Harmonic number	216816			
Natural bunch length σ_z (mm)	2.72	2.98	2.42	
Bunch length σ_z (mm)	3.26	5.9	8.5	
Damping time τ_x/ τ_y/ τ_E (ms)	46.5/46.5/23.5	156.4/156.4/ 74.5	849.5/849.5/425.0	
Natural Chromaticity	-493/-1544	-493/-1544	-520/-1544	-520/-3067
Betatron tune ν_x/ν_y	363.10 / 365.22			
Synchrotron tune ν_s	0.065	0.0395	0.028	
HOM power/cavity(2cell) (kw)	0.54	0.75	1.94	
Natural energy spread (%)	0.1	0.066	0.038	
Energy acceptance requirement (%)	1.35	0.40	0.23	
Energy acceptance by RF (%)	2.06	1.47	1.70	
Photon number due to beamstrahlung	0.29	0.35	0.55	
Lifetime _simulation (min)	100			
Lifetime (hour)	0.67	1.4	4.0	2.1
F (hour glass)	0.89	0.94	0.99	
Luminosity/IP *L* (10^{34}cm^{-2}s^{-1})	3	10	17	32

Figure 3.2: Main beam parameters for the CEPC operation

Combing these measurements leads to a model-independent determination of the Higgs boson decay branching ratio, the couplings between the Higgs boson and its decay final states, and the total Higgs width. These quantities could typically be determined to a relative precision of 0.1% - 1%, one order of magnitude better than the HL-LHC experiments. The differential measurements provides important input for the quantum number determination and the coefficient measurements within the Effective Lagrangian Theory framework. In addition, the recoil mass method and the clean collision environments make CEPC an extremely sensitive probe to the Higgs exotic decays. A general exploration shows that the 95% C.L. of the Higgs exotic decays could be limited to the range of per mille level to 10^{-6} [**?**]. On top of the Higgs events, roughly 100 million W bosons and 1 billion Z bosons will be generated. These events could be used for both EW precision measurements and in-situ calibration for the detector.

For the Higgs measurement, the integrated luminosity should be measured to an relative accuracy better than 0.1%. To limit the uncertainty on the Higgs mass measurement via the recoil mass spectrum, the beam energy need to be calibrated to an accuracy of 1 MeV.

3.1.2 Z pole Operation

The total statistic of the Z pole statistics would be 5 orders of magnitude higher than that of the LEP. In fact, the CEPC could produce the entire LEP I data sample in 5 minutes. From which, electroweak observables such as $A_{FB}^{0,b}$, R_b, and those measured with the Z line shape can be determined. In addition, the Z pole data also provide huge good access for the flavor physics.

At 91.2 GeV center of mass energy, the leading physics process is the $Z \to fermion$ events, plus a small fraction of the $\gamma\gamma$ background and the Bhabha events. These events have so clean signature that it's easy to distinguish them from each other. However, giving the extremely small statistic uncertainty, the understanding and calibration of the mis-identifications between different physics events are essential.

Being the weak interaction mediator, the Z boson decays into all kinds of the SM fermions except the top quark. In order to distinguish different Z boson decay modes, an high efficiency, high purity identification of leptons, taus, and jets, are highly appreciated. The precise energy-momentum reconstruction, especially the good angular resolution for these physics objects, are crucial for the Z pole physics measurements such as A_{FB}^{μ} and the weak mixing angle. To determine precisely the measurements associated with the b-jets, a precise reconstruction of jet flavor and jet charge is crucial.

In order to extract precisely the Z line shape information, the beam energy need to be calibrated to an accuracy better than MeV, and the luminosity is required to be controlled to a relative accuracy of 10^{-4}.

The CEPC Z pole operation provides a large statistic of $Z \to \tau^+\tau^-$ sample. Many photons are generated in the π^0s from the τ decay and it's crucial to identify these individual photons. In other word, the CEPC detector should provides good separation performance and count precisely how many photons (π^0s) are generated in the $Z \to \tau^+\tau^-$ events. As for the flavor physics measurement, the identification of the charged kaon is essential.

The Z line shape scan makes stringent requirement on the luminosity measurements. Typically, the luminosity need to be measured to a relative accuracy of 10^{-4}. The beam energy need to be calibrated to an accuracy of 100 keV.

In order to deliver ... The number of bunches in the Z pole

Draft v0.2

3.1.3 W threshold scan

At the W threshold scan, the CEPC could produce 10^7 W event in a year. The W threshold scan is mainly devoting to the W boson mass and W boson width measurements. In addition, it provides essential input for the TGC measurements.

A precise determination of the beam energy is indispensable for the W threshold scan. Typically, the beam energy need to be calibrated to sub-MeV level accuracy.

It need to be reminded that the EW and the Higgs measurements provide complementary information, and a combination significantly enhances the physics reach [**?**] [**?**]. The dedicated physics requirements for the CEPC physics program are summarized below.

3.2 Physics Requirements

As a tremendous Higgs, Z, and W boson factory, the CEPC should be equipped with detectors that can identify all the corresponding physics objects with high efficiency, high purity and to measure them with high precision. In addition, the CEPC physics program requires a precise determination of the instant luminosity, a precise control and monitoring of the beam energy. Generally, the CEPC detector is required to:

1, Be adequate to the CEPC collision environment: the detector should be fast enough to record all the physics events and robust enough against the irradiation.

2, Highly hermetic. The detector should provide a solid angle coverage of $|cos(\theta)| < 0.99$.

3, The luminosity should be measured to a relative accuracy of 0.1% for the Higgs operation, and 10^{-4} for the Z line shape scan.

4, The beam energy should be measured to an accuracy of the order of 1 MeV for the Higgs operation, and 100 keV for the Z pole and W mass threshold scan.

The detailed requirements on the physics objects are discussed below:

3.2.1 Multiplicity

The final state particles could be classified into charged particles, photons, and the neutral hadrons. Corresponding to the leading SM processes at the CEPC Higgs operation (the WW, ZZ, and ZH process), the multiplicities are shown in Fig. 3.3. The photons and the charged tracks follows a similar distribution, which is significantly higher than that for the neutral hadrons. In fact, the charged tracks and the photons carry most of the jet energy.

The multiplicity of photons and charged tracks could be as high as 100. Meanwhile, lots of final state particles have very small angles in between, as most of the tracks and photons are produced in jets. In other word, especially under the context of Particle Flow algorithm, it's essential to separate efficiently those final state particles.

3.2.2 Tracking

The CEPC detector should have excellent track finding efficiency and track momentum resolution. Corresponding to the leading SM processes at the CEPC Higgs operation

Draft-v0.2

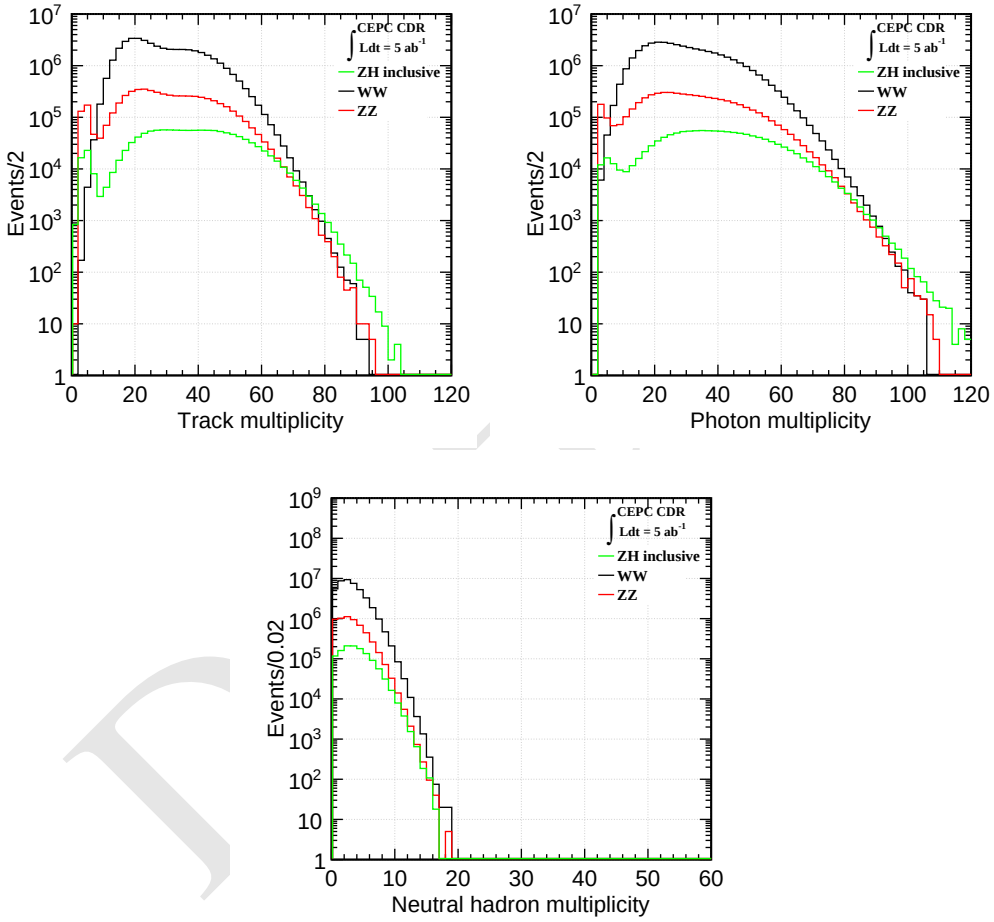

Figure 3.3: The multiplicity of charged particle, photons, and neutral hadrons at the leading physics processes at the CEPC Higgs operation.

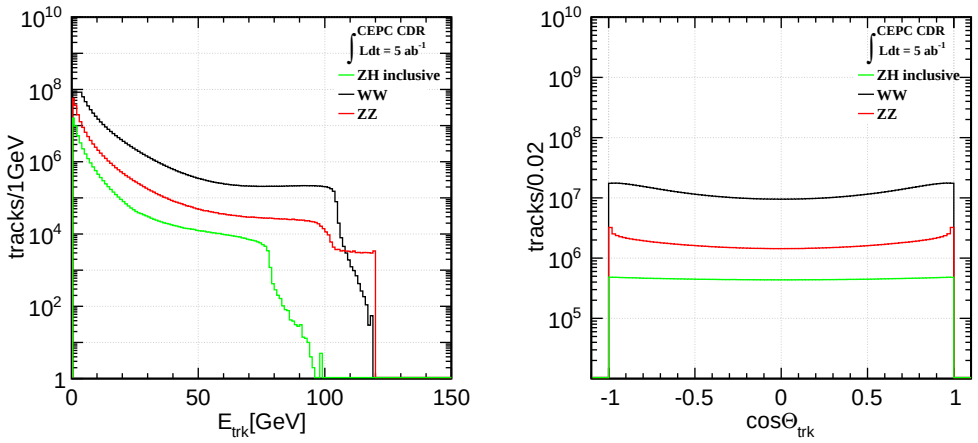

Figure 3.4: Energy and polar angle distribution of charged particles at the leading physics processes at the CEPC Higgs operation.

(the WW, ZZ, and ZH process), the energy and polar angle distributions of the charged particles are shown in Fig. 3.4. These distributions are normalized to $5\ ab^{-1}$, the nominal luminosity at the CEPC.

In terms of the polar angle distribution, the ZH process is almost flat in the polar angle direction, while the other two processes are more forward region oriented. In other word, the detector is required to have a full solid angle coverage.

In the energy distribution, these three processes shares the same pattern. For energy below 20 GeV, these distributions follow an exponential distribution, while in the high energy side there is a flat plateau with a steep cliff. Therefore, the CEPC detector is required to have a high efficiency track reconstruction, especially for these low energy tracks. Meanwhile, it should maintain an excellent momentum resolution and linearity for a wide energy range (0.1 GeV - 120). For any tracks within the detector acceptance and an transverse momentum larger than 1 GeV, we request an track finding efficiency better than 99%. The momentum resolution is required to achieve a relative accuracy at per mille level, in order to measure the $H \to \mu^+\mu^-$ signal and to reconstruct precisely the Higgs boson mass from the recoil mass distribution at l^+l^-H events.

3.2.3 Lepton

The classification of different physics event highly relies on the lepton information. It other word, the lepton is one of the most important physics signature.

At the CEPC Higgs opearation, roughly 7% of the Higgs bosons are generated with a pair of leptons. These l^+l^-H samples are the golden signal for the Higgs recoil mass analysis. Fig. 3.5 shows the energy and angular distribution of the leptons, where the prompt leptons and these generated in Higgs decay cascade are separated. The prompt muons at the $\mu^+\mu^-H$ events has a flat distribution within the kinematic allowance: from 20 - 100 GeV. The prompt muon energy distribution has a low energy tail, induced by the Final State Radiation effect (FSR). The prompt electron-positron at the e^+e^-H events follows a similar pattern, except the population increases at energy smaller than 10 GeV. These low-energy prompt electron-positrons are mainly induced by the Z fusion events.

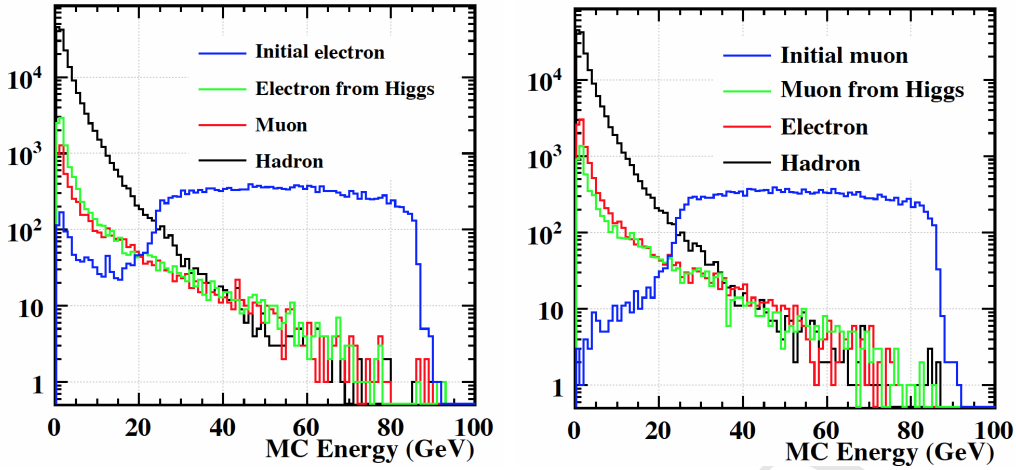

Figure 3.5: Energy spectrum of the leptons and the charged hardons in the e^+e^-H events (left) and the $\mu^+\mu^-H$ events (right).

The Higgs decay also generates leptons, which is mostly concentrated in the low energy side, but can have energies as high as 70 GeV. These high energy leptons are mainly generated from $H \to \tau^+ tau^-, ZZ^*, WW^*$ decay cascades.

In order to reconstruct all the prompt leptons, an excellent lepton identification performance for isolated leptons with energy higher than 5 GeV, is regarded as a must for the CEPC detector design. Meanwhile, the low energy leptons are numerous in the Higgs decay cascade, and a good lepton identification performance for these low energy leptons are highly appreciated.

3.2.4 Particle identification

The particle identification, especially the identification of charged kaons, is crucial for the flavor physics. In addition, the kaon identification is highly appreciated for the jet flavor tagging and jet charge reconstruction. Typically, we request the efficiency and purity of the kaon identification at the inclusive Z pole sample to be better than 90%.

3.2.5 Photons

The photons is crucial for the jet energy resolution, the $H \to \gamma\gamma$ branching ratio measurements, and the physics with τ final states. Fig. 3.7 shows the energy and polar angle distribution for the inclusive photons, and the ISR photons, from these benchmark physics processes at the CEPC Higgs operation.

As for the photon reconstruction, we request a photon identification efficiency higher than 99% and a misidentification rate smaller than 5%, for non-converted, isolated photons with energy higher than 1 GeV. In terms of the photon energy resolution, it should secures a relative mass resolution at $H \to \gamma\gamma$ final state better than 3%. In addition, the photons generated from π^0 decays, either from the τ decay cascade or from the jet fragmentations, should be clearly separated.

Draft-v0.2

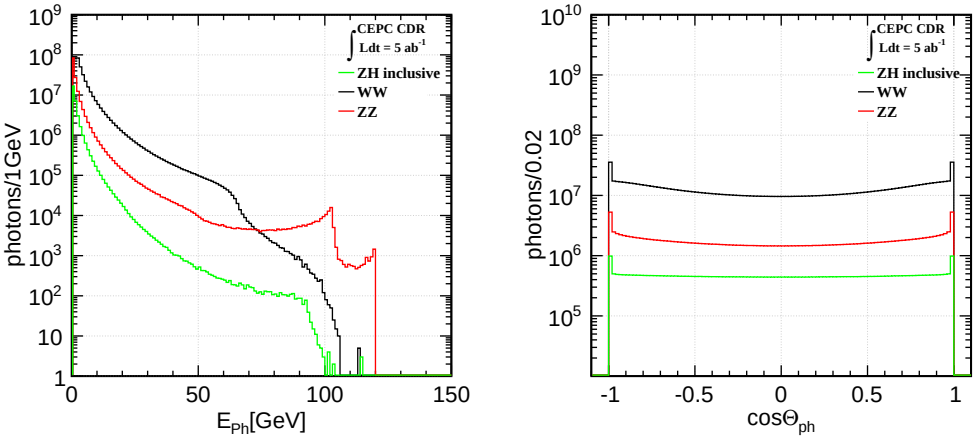

Figure 3.6: Energy and polar angle distribution of all photons at the leading physics processes at the CEPC Higgs operation.

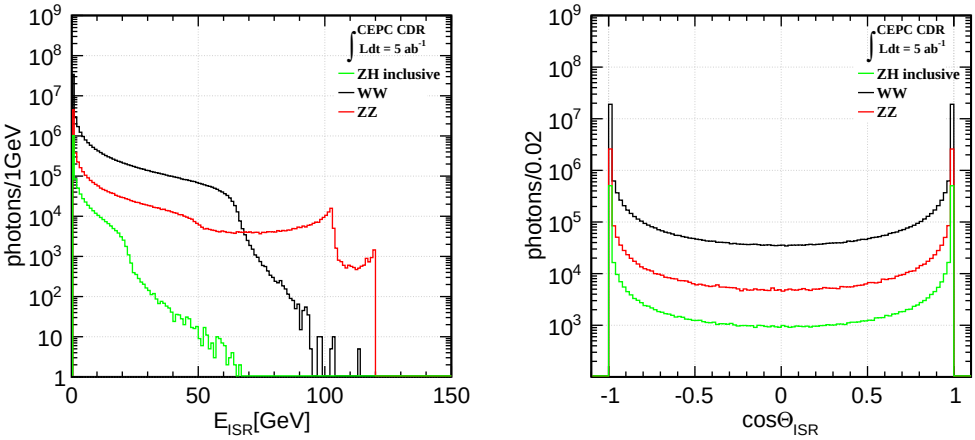

Figure 3.7: Energy and polar angle distribution of ISR photons from the leading physics processes at the CEPC Higgs operation.

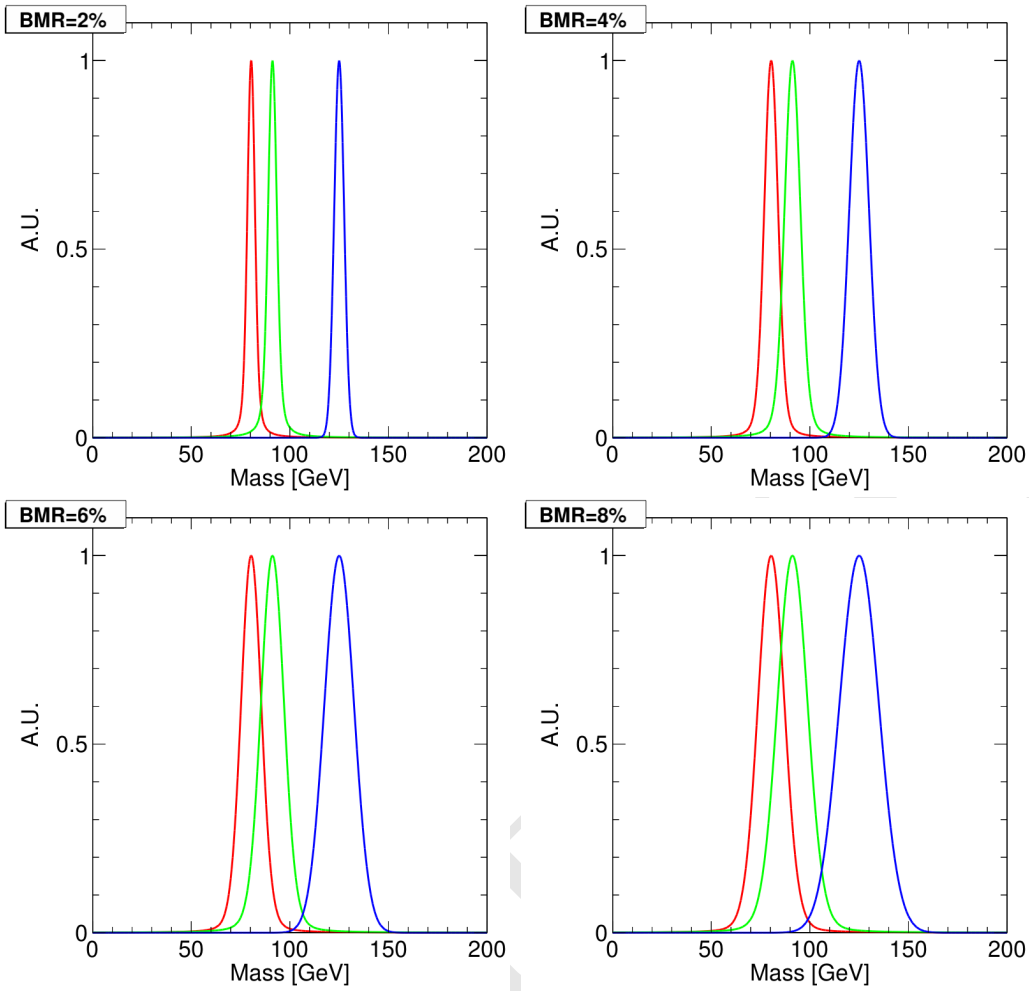

Figure 3.8: Invariant mass distribution of H, W, and Z bosons at different boson mass resolution.

3.2.6 Jets and Missing energy

The jet reconstruction is essential for the CEPC physics program, since the majority of W, Z, and Higgs bosons decays into hadronic final states. At the Particle Flow oriented design, the jet is constructed via clustering algorithms from the final state particles. Therefore, the jet reconstruction is determined by the reconstruction of final state particle, and the jet clustering algorithm. Consequently, the jet reconstruction performance should be evaluated at two stages.

The first is the boson mass resolution for massive SM bosons. The boson mass resolution represents the jet energy resolution with perfect jet clustering, or more accurately, a perfect identification of the color singlet. A good boson mass resolution is a pre-request for the distinguish of WW, ZZ, and ZH events decay into 4 jets final states, and to distinguish $H \to WW^*, ZZ^* \to 4jets$ from each other. In order to distinguish the W, Z, and the Higgs boson from their hadronic decay final state, a boson mass resolution better than 4% is required.

The missing energy measurement with jet final states is also determined by the boson mass resolution. The physics benchmark for the missing energy-momentum measurement

Figure 3.9: Recoil mass distribution of qqH, H->invisible events with $ZZ \rightarrow qqvv$ backgrounds at different boson mass resolution.

is the $Br(H \rightarrow invisible)$ measurement with qqH final states. For this benchmark, a boson mass resolution better than 4% is certainly appreciated.

The identification of individual jet, and its energy-momentum reconstruction is crucial for the CEPC physics measurements. The individual jet energy response is highly depending on the event topology and the jet clustering algorithms. A detailed analyses is required to disentangle the actual physics requirement, which need to be analyzed profoundly.

3.2.7 Flavor Tagging

One of the key physics objective of the CEPC Higgs program is the determination of $g(Hcc)$. The CEPC detector system is therefore required to efficiently distinguish the b-jets, the c-jets, and the light jets from each other. A decent flavor tagging performance is also highly appreciated in EW precision measurements.

The classification of different kinds of jets mainly relies on the reconstruction of secondary vertex, where the performance of the vertex system is crucial. The clean collision environment of the CEPC allows much aggressive vertex system design, a detailed vertex optimization study could be found in section **??**.

3.3 Detector concepts

3.3.1 The baseline detector concept

To address these physics requirements, a Particle Flow Oriented detector concept has been developed as the CEPC baseline detector, see Fig. 3.10. The Particle Flow principle, in short, interprets all the detector signal as the final state particles. For each physics event, all the physics objects are reconstructed from an unique list of final state particles. The single particle level physics objects, for example the leptons, the photons, and the kaons, are identified directly from the final state particle list. The composited physics objects, for example the converted photons, the K_s^0, the τ lepton and the jets, are identified using dedicated finding algorithm such as tau finder and jet clustering algorithms. Subtracting the total visible four-momentum of all the final state particle from the initial four momentum determines the missing four-momentum. This global interpretation of the final state particles leads to high efficiency, and high purity reconstruction of all the physics

Draft v0.2

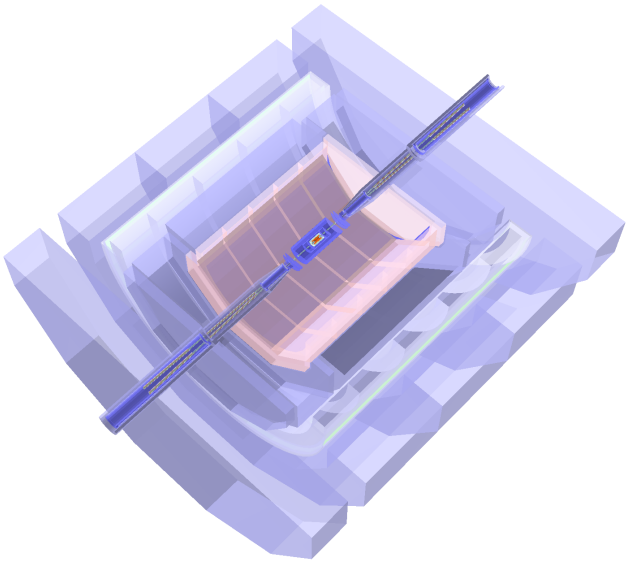

Figure 3.10: Sliced view of the APODIS detector concept, the baseline detector geometry for the CEPC CDR study. The APODIS uses double beam with 33 mrad cross angle, and have a short L* of 2.2 meter. In its Barrel, from inner to outer, the APODIS detector is composed of a Vertex system (Red), a Silicon Inner Tracker (Deep Blue), a TPC, a Silicon External Tracker, a ECAL (Pink), a HCAL (Violet), a Solenoid of 3 Tesla and a Return Yoke. In its forward region, 5 pairs of tracking disks is installed to enlarge the detector acceptance.

objects. In addition, the Particle Flow algorithm in principle associate the detector hits to each individual particle, therefore, the final state particle could be measured in the most-suited sub-detector system. For the charged particles, the relative accuracy of track momentum resolution at the tracking system is usually much better than the energy resolution at calorimeter system at the APODIS. Therefore, the Particle Flow algorithm also significantly improves the accuracies on the energy reconstruction of composed objects, especially for the τ lepton and the jets.

The baseline detector geometry is named APODIS, stands for A Particle Flow Oriented Detector for the HIggS factory. APODIS is optimized from the CEPC v_1 geometry, the reference detector geometry for the CEPC PreCDR studies. The CEPC v_1 is developed from the concept and International Large Detector (ILD), the baseline detector for the linear collider studies. Comparing to the CEPC v_1, the APODIS enhances the performance on the identification of charged Kaons; maintains the same performance on the Higgs measurements, meanwhile, it has significantly reduce the construction cost and the power consumption.

From inner to outer, the APODIS is composed of a silicon pixel vertex system, a silicon internal tracker, a TPC main tracker, a Silicon-tungsten sampling ECAL, a Iron-Glass Resistive Plate Chamber HCAL, a solenoid, and a return Yoke.

The APODIS has a dedicated design on the forward region and the MDI. The L* of APODIS has a length of 2.2 meters, and a compensation solenoid system is installed at z position of 1100 - 6000 mm. A LumiCal is installed at the end of this nose. A compact, forward tracking system composed of 5 pairs of tracking disks is installed in between z position of 200 - 1000 mm.

Draft-v.2

The solenoid B-Field of the APODIS is 3 Tesla. The CEPC uses double ring configuration, with a cross angle of 33 mrad at the interaction point. Each time the bunch passing through the detector, the beam emittance increases via the coupling to the detector solenoid B-Field (especially the vertical emittance). In order to achieve a high luminosity, this solenoid B-Field needs to be compensated locally. Therefore, a compensating solenoid is installed in the forward region of the CEPC detector. Considering the technology challenge of the compensating solenoid and the physics requirement at the CEPC, APODIS uses a solenoid of 3 Tesla for the CEPC Higgs operation, and the central solenoid might be further reduced to 2 Tesla for the CEPC Z pole operation.

The APODIS uses the Time Projection Chamber (TPC) as its main tracker. The TPC provides good energy resolution, excellent track reconstruction efficiency, low material budgets, and its $\mathrm{dE/dx}$ measurement is essential for the particle identification, see section **??**. On the other hand, compared to the silicon tracking, the TPC is a slow technology: the drift time of ions is of the order of one second at the APODIS TPC. At TPC, both primary ionization of charged tracks and ion backflow from the amplification procedure generates ions, which accumulate in the gas volume. These ions will distort the drift electric field and eventually limit the precision of track momentum measurement. The physics event rate at the CEPC Z pole operation is of the order of 10^{3-4} Hz, therefore, ions generated from thousands of events pile up in the gas volume. The control of backflow ion is then essential for the TPC operation.

Iterated with the hardware R&D, dedicated simulation studies are performed at the CEPC TPC study. Using double amplification layer, the ion backflow could be controlled to per mille level without gating [**?**]. On the other hand, the simulation analysis shows that at this level of ion backflow control, the degrading of spatial point resolution is smaller than the intrinsic TPC spatial resolution. The TPC occupancy is also analyzed at the TPC Z pole. Those studies lead to the conclusion that the TPC is a feasible technology option for the CEPC [**?**].

The TPC in the APODIS has an inner radius of 0.3 meters, an outer radius of 1.8 meters, and a length of 4.7 meters. It is divided into 220 radical layers, each has a thickness of 6 mm. Along the ϕ direction, each layer is segmented into 1 mm wide cells. In total, the TPC has 10 million readout channels in each endcap. Operating in 3 Tesla solenoid B-Field, the TPC provides a spatial resolution of 100 μm in the $R-\phi$ plane and 500 μm resolution in the Z direction for each tracker hit. The TPC reaches a standalone momentum resolution of $\delta(1/P_t) \sim 10^{-4}\mathrm{GeV}^{-1}$.

The APODIS is equipped with large-area silicon tracking devices, including the pixel vertex system, the forward tracking system, and the silicon inner/external tracking layers located at the boundary of the TPC. Combining the measurements from the silicon tracking system and the TPC, the track momentum resolution could be improved to $\delta(1/P_t) \sim 2 \times 10^{-5}\mathrm{GeV}^{-1}$. In fact, the TPC is mainly responsible for the pattern recognition and track finding, while the silicon tracking devices dominate the momentum measurement. The silicon pixel vertex system also provides precise impact parameter resolution ($\sim 5\mu\mathrm{m}$), which is highly appreciated for the τ lepton reconstruction and the jet flavor tagging.

The APODIS uses high granular sampling Electromagnetic Calorimeter (ECAL) and Hadronic Calorimeter (HCAL). The calorimeter is responsible for separating final state particle showers, measuring the neutral particle energy, and providing information for the lepton identification [**?**][**?**]. The entire ECAL and HCAL are installed inside the

Draft-v0.2

Concept	ILD	CEPC v_1	APODIS
Solenoid B-Field/Tesla	3.5	3.5	3
L*/m	3.5	1.5	2.2
Pairs of forward tracking disks	7	5	5
ECAL Cell Size/mm	5	5	10
ECAL Time resolution/ns	-	-	200 ps/hit
HCAL Layer Number	48	48	40
HCAL Absorber thickness/m	1.3	1.3	1.0
Total Weight/kton	15	10	8

Table 3.2: Comparison of detector parameters

Draft-v0.2

solenoid, providing 3-dimensional spatial position and the energy information. The ECAL geometry parameter is determined by a dedicated optimization study [**?**]. The ECAL is composed of 30 layers of alternating silicon sensor and tungsten absorber. It has a total absorber thickness of 84 mm. Transversely, each sensor layer is segmented into 10 mm by 10 mm cells. The HCAL uses Resistive Plate Chamber sensor and Iron absorber. It has 40 longitudinal layers, each consists of a 25 mm Iron absorber. Transversely, it is segmented into 10 mm by 10 mm cells.

This calorimeter system provides decent energy measurement for the neutral particles (i.e. roughly $16\%/\sqrt{E/\mathrm{GeV}}$ for the photons and $60\%/\sqrt{E/\mathrm{GeV}}$ for the neutral hadrons). More importantly, it records enormous information of the shower spatial development, ensuring efficient separation between nearby showers and providing essential information for the lepton identification, see section **??**. In addition, the silicon tungsten ECAL could provide precise time measurement. Requesting a cluster level time resolution of 50 ps, the ECAL Time of Flight (ToF) measurement plays a complementary role to the TPC $\mathrm{dE/dx}$ measurement, leading to a decent charged Kaon identification performance, see section **??**.

Table 3.2 listed the main parameters of ILD, CEPC v_1 and the APODIS. As will be introduced in the following chapter, the APODIS maintains the same performance for the CEPC Higgs measurements comparing to CEPC v_1. Meanwhile, the total cost, the total weight, and the calorimeter thickness have been significantly optimized (by 25%, 30% and 20% respectively). In addition, APODIS has a good performance in charged kaon identification, which is highly appreciated in the flavor physics and in the jet flavor/charge reconstruction.

3.3.2 Full silicon detector concept

3.3.3 An alternative low magnetic field detector concept

The baseline detector described in this CDR is a very straightforward evolution of the ILD detector originally conceived for the International Linear Collider (ILC) [1]. We propose here a new detector concept, IDEA (Innovative Detector for Electron-positron Accelerator), that is specifically designed for a circular electron-positron collider and also attempts to contain the overall cost of the detector.

While most detector requirements needed for detectors at ILC are very similar to those for CepC [2], there are however some notable differences. First of all the typical luminosity expected both at the Z pole ($\sqrt{s} = 90\,GeV$) and above the ZH threshold ($\sqrt{s} = 240\,GeV$) is expected to be one or two orders of magnitude larger, with a much shorter bunch spacing and no large time gaps in the beam structure. This places severe constraints on the tracking system. In particular one would prefer an intrinsically fast main tracker to fully exploit the cleanliness of the e^+e^- environment while integrating as little background as possible, and a very low power vertex detector, since power pulsing is not allowed by the bunch spacing. Additional issues of emittance preservation, typical of circular machines, set limits on the maximum magnetic field usable for the tracker solenoid, especially when running at the lower energy. This could be a problem for a large volume TPC, due to the resolution degradation, and also for a silicon tracker, since it would require more layers at a large radius, thus significantly increasing the cost.

Additional specific requirements on a detector for CepC come from precision physics at the Z pole, where the statistical accuracy on various electro-weak parameters is expected to be over an order of magnitude better than at the ILC. This calls for a very tight control of the systematic error on the acceptance, with a definition of the acceptance boundaries at the level of a few μm, and a very good $e - \gamma - \pi_0$ discrimination to identify τ leptons efficiently and measure their polarization. A layer of silicon microstrip detectors around the main tracker can provide the needed acceptance control for charged tracks, while also improving the tracking resolution. Similarly, the acceptance accuracy and improved identification efficiency of γ's can be obtained with a pre-shower based on MPGD detectors located just outside the detector magnet, which serves as a radiator.

The particle flow calorimeters, currently proposed for both ILC and CLIC, feature an extremely large number of readout channels and require significant data processing to obtain the optimal performance. A cheaper and more effective calorimeter can be made using the dual readout technique [3], which has been extensively studied and demonstrated in over ten years of R&D by the DREAM/RD52 collaboration [4, 5]. With this technology the electromagnetic and hadronic calorimeters come in a single package that plays both functions and allows an excellent discrimination between hadronic and electromagnetic showers [6]. Since all the readout electronics is located in the back of the calorimeter, its cooling is greatly simplified relative to the case of particle flow calorimeters.

Finally recent developments in multi-pattern gas detector technology, such as μRwell [7], can significantly reduce the cost of large area tracking chambers to be used for tracking muons outside the calorimeter volume.

The IDEA detector The structure of the IDEA detector is outlined in figure 3.11, which also shows its overall dimensions.

Draft-v0.2

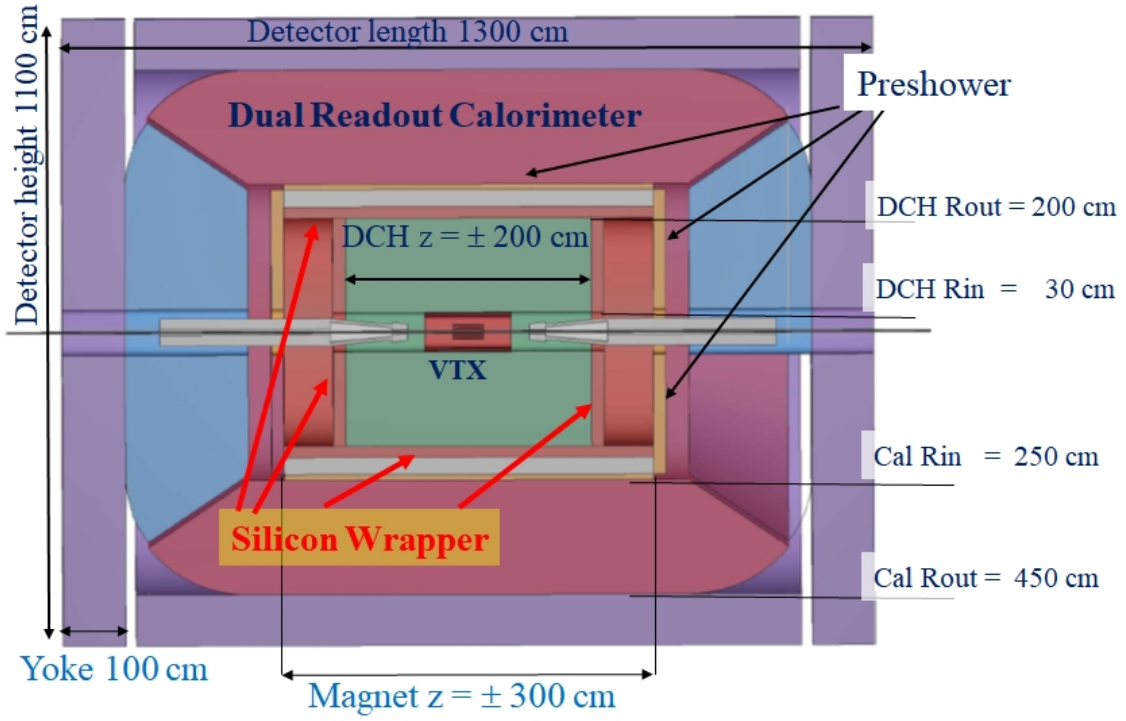

Figure 3.11: Schematic layout of the IDEA detector.

A key element of IDEA is a thin, ∼30 cm, and low mass, $\sim 0.8\,X_0$, solenoid with a magnetic field of 2 Tesla. This field is optimal, according to studies done for FCC-ee, as it minimizes the impact on emittance growth and allows for manageable fields in the compensating solenoids [8], but it is certainly not optimal for a large TPC or a silicon tracker of reasonable size. The low mass and thickness allows to locate the calorimeter outside the tracking volume without a significant performance loss.

The innermost detector, surrounding the 1.5 cm radius beam pipe, is a silicon pixel detector for the precise determination of the impact parameter of charged particle tracks. Recent test beam results on the detectors planned for the ALICE inner tracker upgrade (ITS), based on the ALPIDE readout chip [9], indicate an excellent resolution, ∼5 μm, and high efficiency at low power and dark noise rate [10]. This looks like a good starting point for the IDEA vertex detector and a similar approach is proposed for the CepC baseline detector (see section 4.5). The two detector concepts could then share the same pixel technology as well as profit from the electronic and mechanical work of the ALICE ITS.

Outside the vertex detector we find a 4 m long cylindrical drift chamber starting from a radius of ∼35 cm and extending until 2 m. The chamber can be made extremely light, with low mass wires and operation on 90% helium gas; less than 1% X_0 is considered feasible for 90° tracks. Additional features of this chamber, which is described in detail in section 6.3, are a good spatial resolution, <100 μm, dE/dx resolution at the 2% level and a maximum drift time of only 400 nsec. A layer of silicon microstrip detectors surrounds the drift chamber in both barrel and forward/backward regions. Track momentum resolution of less then 0.5% for 100 GeV tracks is expected when vertex detector and silicon wrapper information is included in the track fit. It is worth noting that the design of this chamber is the evolution of work done over many years on two existing chambers, that of the KLOE

detector [11] and that of the recent MEG experiment upgrade [12]; major R&D work was done also for the 4th concept at ILC [13] and then for the Mu2E tracker [14].

A pre-shower is located between the solenoid magnet and the calorimeter in the barrel region and between the drift chamber and the end-cap calorimeter in the forward region. This detector consists of two passive material radiators each followed by a layer of MPGD detectors. In the barrel region the solenoidal magnet plays the role of the first radiator, while in all other cases the radiators are made of lead. The actual thickness of the radiators are still being optimized based on test beams currently in progress. In the extreme case of using a total of two radiation lengths about 75% of the π^0's can be tagged by having both γ's from their decay identified by the pre-shower. Additional π^0 identification power comes from the high granularity of the calorimeter.

A solenoidal magnet surrounds the tracking system and the first pre-shower layer. Presently planned dimensions are 6 m of length and 4.2 m inner diameter. The relatively low two Tesla field and the small dimensions have important implications on the overall magnet package thickness, that can be kept at the 30-40 cm level, and on the size of the flux return yoke, which scales linearly with the field and the square of the coil diameter. With the given dimensions a yoke thickness of less than 100 cm of iron is sufficient to completely contain the magnetic flux and provide adequate shielding and support for the muon chambers.

A dual readout fiber calorimeter (see section 7) is located behind the second pre-shower layer. We assume a total calorimeter depth of 2 m, corresponding to approximately seven pion interaction lengths. The detector resolution is expected to be about $10.5\%/\sqrt{E}$ for electrons and $35\%/\sqrt{E}$ for isolated pions with negligible constant terms, as obtained from extrapolations from test beam data using GEANT4 without including the pre-shower. This detector has very good intrinsic discrimination between muons, electrons/photons and hadrons for isolated particles [6]. This discrimination power is further enhanced when the information of the pre-shower and the muon chambers is added, extending the separation power also into hadronic jets and making it suitable for the application of particle-flow-like algorithms. The intrinsic high transverse granularity provides a good matching of showers to tracks and pre-shower signals.

The muon system consists of layers of muon chambers embedded in the magnet yoke. The area to be covered is substantial, several hundreds of square meters, requiring an inexpensive chamber technology. Recent developments in the industrialization of μRwell based large area chambers, as planned for the CMS Phase II upgrade, are very promising (see section 9).

Conclusions A different concept for a detector at CepC has been proposed. This detector is designed specifically for CepC and its specific running conditions and physics goals. In particular it is safe with respect to interaction between the detector solenoid field and the beam. Although additional R&D to optimize performance, reduce costs and come to a detailed engineered design of the detector is still necessary, this detector is based on technologies which are established after many years of R&D and whose feasibility has by large been established. Furthermore several choices are made to simplify the detector structure and reduce the cost, which in the end should be smaller than for an ILD-like detector.

Draft V0.2

References

[1] H. Abramowicz et al., *The International Linear Collider Technical Design Report - Volume 4: Detectors*, arXiv:1306.6329 [physics.ins-det].

[2] C.-S. S. Group, *CEPC-SPPC Preliminary Conceptual Design Report. 1. Physics and Detector*, .

[3] DREAM Collaboration, R. Wigmans, *The DREAM project: Towards the ultimate in calorimetry*, Nucl. Instrum. Meth. **A617** (2010) 129–133.

[4] N. Akchurin et al., *The electromagnetic performance of the RD52 fiber calorimeter*, Nucl. Instrum. Meth. **A735** (2014) 130–144.

[5] RD52 (DREAM) Collaboration, R. Wigmans, *New results from the RD52 project*, Nucl. Instrum. Meth. **A824** (2016) 721–725.

[6] N. Akchurin et al., *Particle identification in the longitudinally unsegmented RD52 calorimeter*, Nucl. Instrum. Meth. **A735** (2014) 120–129.

[7] M. Poli Lener, G. Bencivenni, R. de Olivera, G. Felici, S. Franchino, M. Gatta, M. Maggi, G. Morello, and A. Sharma, *The μ-RWELL: A compact, spark protected, single amplification-stage MPGD*, Nucl. Instrum. Meth. **A824** (2016) 565–568.

[8] M. Koratzinos et al., *Progress in the FCC-ee Interaction Region Magnet Design*, http://inspirehep.net/record/126211/files/wepik034.pdf (2017) , IPAC2017.

[9] ALICE Collaboration, M. Mager, *ALPIDE, the Monolithic Active Pixel Sensor for the ALICE ITS upgrade*, Nucl. Instrum. Meth. **A824** (2016) 434–438.

[10] ALICE Collaboration, G. Aglieri Rinella, *The ALPIDE pixel sensor chip for the upgrade of the ALICE Inner Tracking System*, Nucl. Instrum. Meth. **A845** (2017) 583–587.

[11] KLOE Collaboration, A. Calcaterra, *The KLOE drift chamber*, Nucl. Instrum. Meth. **A367** (1995) 104–107.

[12] MEG Collaboration, Y. Uchiyama, *Upgrade of MEG experiment*, PoS **EPS-HEP2013** (2013) 380.

[13] A. Mazzacane, *The 4th concept detector for the ILC*, Nucl. Instrum. Meth. **A617** (2010) 173–176.

[14] L. De Lorenzis, F. Grancagnolo, A. L'Erario, A. Maffezzoli, A. Miccoli, S. Rella, M. Spedicato, and G. Zavarise, *Analysis and Characterization of the Mechanical Structure for the I-Tracker of the Mu2e Experiment*, Nucl. Phys. Proc. Suppl. **248-250** (2014) 134–136.

Draft-v0.2

CHAPTER 4

TRACKING SYSTEM

Draft-v0.2

4.1 Vertex tracker detector

The identification of heavy-flavor (b- and c-) quarks τ leptons is essential for the CEPC physics program. It requires precise determination of the track parameters of charged particles in the vicinity of the interaction point (IP), permitting reconstruction of the displaced decay vertices of short-lived particles. This drives the need for a vertex detector with low material budget and high spatial resolution. The current design of the CEPC vertex detector adopts the same layout as the ILD vertex detector [1], but with special considerations for the sensors specifications.

4.1.1 Performance Requirements and Detector Challenges

As required for the precision physics program, the CEPC vertex detector is designed to achieve excellent impact parameter resolution, which in the $r\phi$ plane can be parameterized by:

$$\sigma_{r\phi} = a \oplus \frac{b}{p(GeV)sin^{3/2}\theta} \tag{4.1}$$

where $\sigma(r\phi)$ denotes the impact parameter resolution, p the track momentum, and θ the polar track angle. The first term describes the intrinsic resolution of the vertex detector in the absence of multiple scattering and is independent of the track parameters, while the second term reflects the effects of multiple scattering. a=5 and b=10 are taken as the design values for the CEPC vertex detector. The main physics performance goals can be achieved by meeting the following specifications on the system:

- Spatial resolution near the IP better than 3 μm;

By Copyright © 2018 HEP Community

- Material budget below 0.15% X_0/layer;
- First layer located at as close to beam pipe as possible;
- Detector occupancy not exceeding 1%.

Unlike like the ILD vertex detector, which operates in power-pulsing mode, the CEPC detector must operate in continuous mode. The power consumption of the sensors and readout electronics should be kept below 50 $\mathrm{mW/cm^2}$, if the detector is air cooled. The readout time of the pixel sensor needs to be shorter than 20 μs, to minimize event accumulation from consecutive bunch crossings. The radiation tolerance requirements, which are critical for the innermost detector layer, are driven by the beam related backgrounds as described in Chapter 10. The annual values of Total Ionising Dose (TID) and Non-Ionising Energy Loss (NIEL) are estimated to be X00 kRad and $\mathrm{X} \times 10^{10}$ 1 $\mathrm{MeVn_{eq}/cm^2}$, respectively.

4.1.2 Baseline design

The baseline layout of the CEPC vertex detector is exactly the same as that of ILD detector. As shown in figure 4.1, it consists of three cylindrical and concentric layers of double-sided ladders located at radii between 16 and 60 mm with respect to IP. The ladders, which are the main mechanical structure, support high spatial resolution pixel sensors on both sides. The CEPC vertex detector is designed to deliver six precise space-points for charged particle traversing the detector. The material budget of each detector layer amounts to $\sim$0.15% $\mathrm{X_0}$. Extensive simulation studies (see Section 4.1.3) show that the chosen configuration with the single point resolutions listed in table 4.1 achieves the required impact parameter resolution.

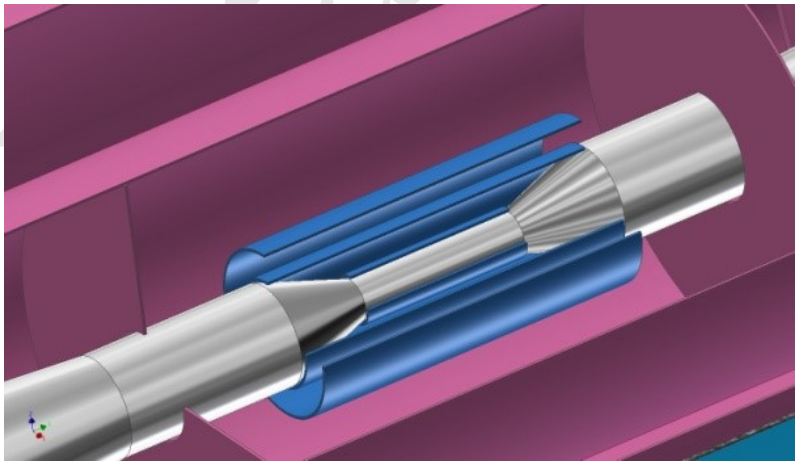

Figure 4.1: Schematic view of pixel detector (blue)

4.1.3 Detector performance studies

The identification of b/c-quark jets (called "flavor-tagging") is essential in physics analysis where signal events with b/c-quark jets in the final state have to be separated. Flavor tagging requires the precise determination of the impact parameter of charged tracks embedded in the jets. For CEPC operation at the center-of mass energy of 240 GeV, those

	$R(mm)$	$\|z\|(mm)$	$\|cos\theta\|$	$\sigma(\mu m)$	$Readout\ time(us)$
Layer 1	16	62.5	0.97	2.8	20
Layer 2	18	62.5	0.96	6	1-10
Layer 3	37	125.0	0.96	4	20
Layer 4	39	125.0	0.95	4	20
Layer 5	58	125.0	0.91	4	20
Layer 6	60	125.0	0.90	4	20

Table 4.1: Vertex detector parameters

tracks are often of low momentum, for which the multiple scattering effect dominates the tracking performance as illustrated by Eq. 4.1

The CEPC vertex detector layout has been fully implemented in the GEANT4-based simulations framework MOKKA [2]. In addition, as inspired by the detailed studies for the CLIC detectors [3], the LiC Detector TOY fast simulation and reconstruction framework (LDT) [4] have been used for detector performance evaluation and layout optimization. The preliminary studies for optimization to evaluate the sensitivity of the results on the chosen parameters have been done, for the purpose of assessing the impact of the detector geometries and material budgets on required flavor-tagging performance. However, beam-induced background was not included at the moment.

4.1.3.1 Performance of the Baseline Configurations

The impact parameter resolution following from the single point resolutions provided in the table 4.1 is displayed in figure 4.2 as a function of the particle momentum, showing that the ambitious impact parameter resolution is achievable.

4.1.3.2 Material Budget

The baseline design includes very small material budget for the beam pipe as well as for the sensor layers and their support. To assess the sensitivity of the performance on the amount of material, the material budget of the beam pipe and the vertex detector layers has been varied. The resulting transverse impact-parameter resolutions for low-momentum tracks are shown in Figure 4.3. When increasing the material of the detector layers by a factor of two, the resolution degrades by approximately 20%.

4.1.3.3 Dependence on Single-Point Resolution

The dependence of the transverse impact-parameter resolution on the pixel size was studied by worsening the single-point resolution of the vertex layers by worse of 50% w.r.t. the baseline values. The resulting impact parameter resolution for high and low momentum track as function of the polar angle θ is shown in Figure 4.4. The resolution for track momenta of 100 GeV is found to change by approximately 50% in the barrel region. Here they exceed the target value for the high-momentum limit of a$\approx$5 μm for both pixel sizes, as expected from the corresponding single-point resolutions. For 1GeV, where multiple-scattering effects dominate and the corresponding variation of the transverse impact-parameter resolution is only 10% larger. The target value for the multiple-scattering term of b$\approx$10 μm is approximately reached for both pixel sizes. It should be

Draft-0.2

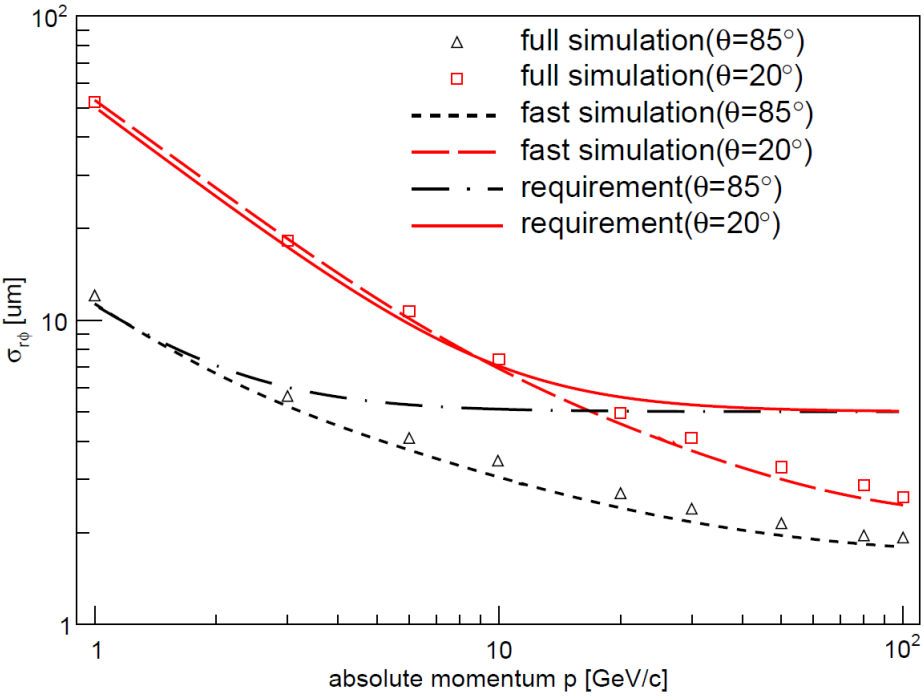

Figure 4.2: Transverse impact-parameter resolutions for single muon events as a function of the momentum for different polar angles.

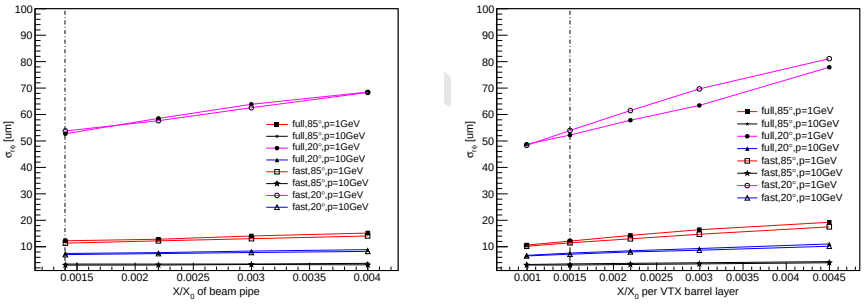

Figure 4.3: Transverse impact-parameter resolution as function of the amount of material inside the beam pipe (left) and inside the vertex barrel double layers (right), as obtained from the simulation. The results are shown for 1 GeV and 10 GeV tracks and for polar angles of θ=20 degrees and of θ=85 degrees. The material budget corresponding to the baseline configuration is indicated by dashed lines.

noted, however, that the pixel size is also constrained by the background occupancies (see Section 4.1.4) and the ability to separate adjacent tracks in very dense jets in the presence of such backgrounds.

4.1.3.4 Distance to IP

The distance of the first double vertex layer from the IP was varied by $\pm$4 mm relative to baseline geometry of the CEPC vertex detector. Figure 4.5 shows the resulting transverse impact parameter resolution at θ=85 degrees as function of the momentum and for different radial distance of the innermost barrel vertex layer from the IP. For low momentum

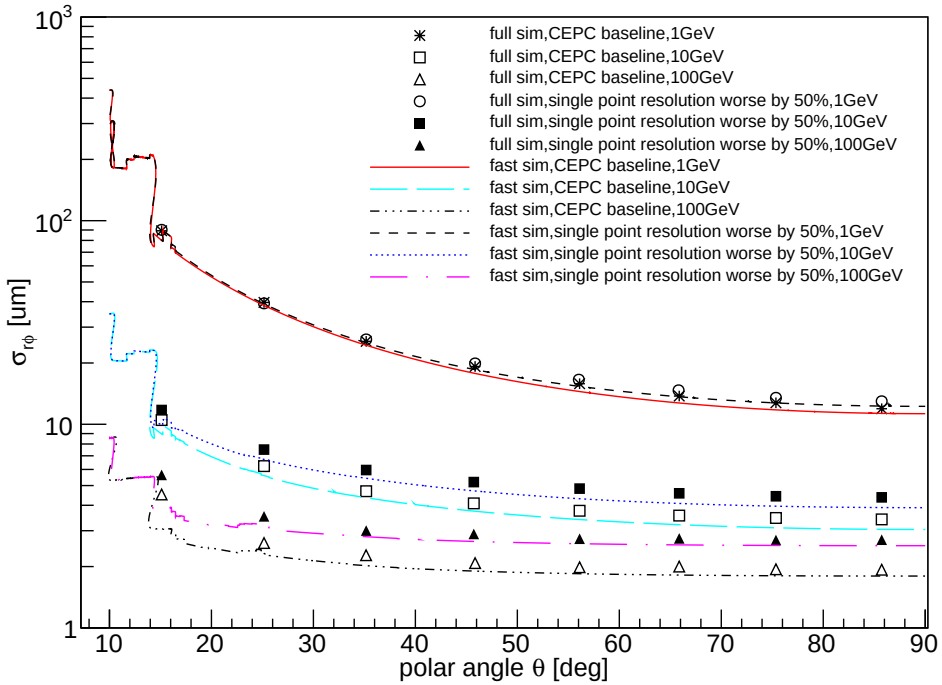

Figure 4.4: Transverse impact-parameter resolutions as function of the polar angle theta for different values of the single-point resolution of the CEPC barrel vertex detector. Shown are the resolutions for 1 GeV, 10 GeV and 100 GeV tracks.

tracks, the transverse impact-parameter resolution is proportional to the inner radius, as expected from the parameter formula.

4.1.4 Beam-induced Background in the Vertex Detector

To be updated with radiation tolerance and detector layer occupancy (1% reachable by estimating tolerable hit density, even a safety factor of 10 included) according to the background studies, with B=3 T

4.1.5 Sensor Technology Options

The first silicon pixel vertex detector was introduced in the DELPHI experiment [5] at LEP in 1995. Significant progress has been made over the last 20 years [6]. Considerable R&D efforts have taken place to develop pixel sensors for vertex tracking at future particle physics experiments [7], driven by track density, single point resolution and radiation level.

As outlined in Section 4.1.1, the detector challenges for the CEPC include high IP resolution, low material budget, low occupancy and sufficient radiation tolerance (mild comparing to ILC but not necessarily easy to achieve). To fulfill these requirements at system level, sensor technologies which achieve fine pitch, low power and fast readout must be selected. In fact the CEPC vertex detector is more demanding than previous applications. The power consumption for the ILC [1] and CLIC[8] vertex detectors is expected to be significantly reduced by choosing power pulsing operation, but it is not a

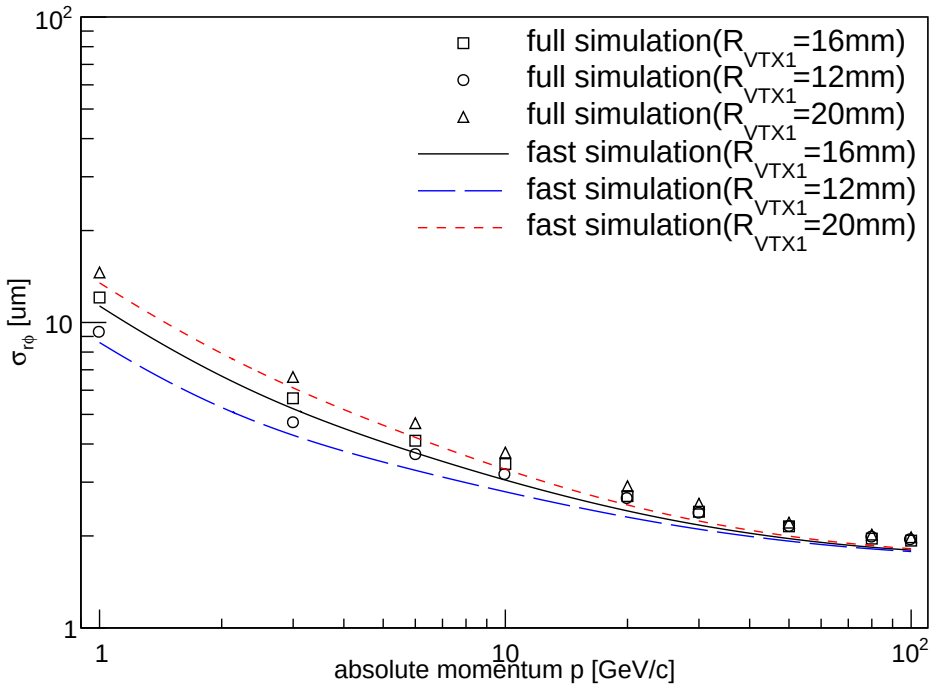

Figure 4.5: Transverse impact-parameter resolution at θ=85 degrees as function of the momentum for different values of inner most layer radius R_{min}. The black curve indicates the baseline configuration of R_{min}=20 mm.

practical option for the CEPC. Other experiments such as the STAR[9], BELLEII[10] and ALICE upgrade[11] readout continuously as the CEPC. However, they have less stringent requirements in terms of IP resolution and material budget. None of the existing sensor technologies fits perfectly the needs of the CEPC but there are a few that are close or/and have the potential to achieve the needed performance.

Driven by the requirements of low material and high resolution, the monolithic pixel sensor has been developing fast. The 1st generation MAPS-based vertex detector for STAR HFT upgrade [9, 12] just completed 3-year physics run successfully, while the new generation HR CMOS Pixel Sensor for ALICE-ITS upgrade [11] is in mass production. In the previous 0.35 μm double-well process, only N-MOS transistors can be used in the pixel design. This constraint is removed in the new 0.18 μm quadruple-well process. Both N and P-MOS transistors can be used in the pixel design. Combining with the smaller feature size, it becomes a very appealing technology. A good start point for the CEPC vertex would be the ALPIDE design [13], which is developed for the aforementioned ALICE-ITS upgrade and has achieved performances very close to the requirements of the CEPC. Further R&Ds are needed to shrink the pixel pitch to 16 μm (binary readout) in order to accomplish the required 2.8 μm single point resolution. Another monolithic option is the Silicon On Insulator (SOI) pixel sensor. After more than 10 years evolution, SOI has entered a new stage of maturity. Fundamental issues, including the transistor shielding [14] and the TID tolerance [15], have been addressed and wafer thinning [16] has been demonstrated. In the meanwhile, R&Ds for the ILC and the CLIC [17, 18] are progressing rapidly. The SOI has a unique feature of fully-depleted substrate as the active

silicon. And its 0.2 μm CMOS process provides the necessary density of transistors as the 0.18 μm CMOS in HR CMOS does. Therefore it is envisaged that the readout design for the CEPC vertex may be adapted for both processes and to exploit each one's potentials.

Depleted P-channel Field Effect Transistor (DEPFET) is referred to as semi-monolithic because it allows to integrate the first amplification stage into the pixel combined with subsequent processing circuit in separate readout ASICs. The BELLE II is anticipating its full detector operation with the DEPFET-based vertex [10] installed at the end of 2018. It is very helpful to have the readout ASICs located outside the detector acceptance area as the major heat sources, while keeping the sensors exceptionally low power and low material. The challenge is to periodically sample the modulated current over a large pixel array within required intervals, 20 μs/frame or even less.

Hybrid pixel has been used at hadron colliders for the past decades, and now CLIC R&D is pushing for 50 μm thinned sensors bump bonded on 25 μm pitch to 50 μm thinned ASICs [19]. The hybrid approach evolves constantly and profits from industrial technology developments. Apart from the Very Deep Sub-Micron (VDSM) ASIC technology that enables complex functionalities and superior performances, a close watch on industrial developments of the vertical and lateral inter-connection technologies will also be very helpful to meet the material budget.

4.1.6 Mechanics and Integration

The design of the vertex detector is conceived as a barrel structure, including six concentric layers. The preliminary layout of each layer is shown in table 4.2. The range of the radius covered by the detector is from 16 mm to 60 mm. The length of layers 3 to 6 is 125 cm, which is twice as long as the first two layers.

No. of layer	radius (mm)	length (cm)
Layer 1	16	62.5
Layer 2	18	62.5
Layer 3	37	125.0
Layer 4	39	125.0
Layer 5	58	125.0
Layer 6	60	125.0

Table 4.2: Preliminary layout of each layer

The detector may be realized by 3 double-sided layers. Each double-sided layer is equipped with pixel sensors on both sides, and has a common support frame. In the azimuthal direction, each layer is segmented in elements called ladders. The ladder, which extends over the whole length of the layer, is the basic building block of the detector. It contains all structural and functional components, such as chips, flex cable, support frame and cold plate if it is necessary. Pixel chips in a row are connected to flex cable by wire bonding or other bonding techniques, and then glued to the support frame, which is composed of low Z materials, such as carbon fiber and silicon carbide, providing stable mechanical support. The other side of the support frame is equipped with another layer of pixel sensors.

Draft-V02

The design of the ladders should take into account the specifications of the vertex detector. In order to reduce a small multiple Coulomb scattering contribution to the charged-track vertex resolution and control deformations from gravity and cooling forces for the sensors position stability, the ladder mechanical support must fulfill stringent requirements in terms of minimum material budget and highest stiffness. Ladder designs similar to the STAR pixel detector, the ALICE ITS, the BELLE II PXD, and the ILD double-sided ladder are under consideration.

The ladder mechanical support is inherently linked to the layout of the cooling system that will be adopted to remove the heat dissipated by the pixel sensors since the cooling system is integrated in the mechanical structure. The cooling system of the CEPC vertex detector must balance the conflicting demands of efficient heat dissipation with a minimal material budget. Therefore a suitable, high thermal conductivity and low material budget, cold plate coupled with pixel sensors should be implemented in the ladder design. There are two main types of cooling methods in particle physics experiments, air cooling and active cooling. Table 4.3 gives a list of cooling methods and the corresponding material of each layer of the aforementioned experiments. The upgrade of ALICE ITS [11] adopts water cooling with respect to a chips power dissipation value of 300 $\mathrm{mW/cm^2}$. Polyimide cooling pipes fully filled with water are embedded in the cold plate. STAR- PXL [20] uses air cooling according to its chips power consumption of 170 $\mathrm{mW/cm^2}$. For ILD [1] vertex system, two different cooling options are considered, depending on the sensor technology. The sensors and SWITCHER chips of BELLE II PXD [21] require air cooling, while active cooling will be used for readout chips on each end of the detector, which is out of the sensitive region of the detector. So for CEPC vertex detector, the suitable cooling method will be determined according to the sensor option and the power consumption.

Vertex detector	Power dissipation	Cooling method	Material budget requirement/layer
Alice ITS	300 mW/cm^2	water	0.3%
STAR PXL	170 mW/cm^2	air	0.39%
ILD vertex	<120mW/cm^2 (CPS and DEPFEET) 35W inside cryostat (FPCCD)	air or N_2 two-phase CO_2	0.15%
BELLEII PXD	20W for sensor and SWITCHER 180W on each end	Air CO_2	0.2%

Table 4.3: Cooling method of the vertex detector in each experiment

Simulation and module prototype studies should be carried out to find suitable designs that can meet requirements of stability, cooling and the performance of the vertex detector.

For the design of the whole mechanical structure of the vertex detector, some criteria must be taken into account. Firstly, minimum material has to be used in the sensitive region to reduce multiple Coulomb scattering. Secondly, to ensure high accuracy in the relative position of the detector sensors and provide an accurate position of the detector with respect to the central tracker of TPC and the beam pipe, a mechanical connector or locating pin at each end of the ladder should be considered to allow the fixation and alignment of the ladder itself on the end rings. Thirdly, cooling system should be arranged

reasonably to ensure stable heat dissipation. At last, to reduce the dead region caused by the boundary of each ladder, neighboring ladders should be partially superimposed.

In addition, the main mechanical support structures of the vertex should also meet the requirements of the integration with the other detectors, such as time projection chamber (TPC) and forward tracking disks.

4.1.7 Critical R&D

The inner most layers have to fulfill the most demanding requirements imposed by the physics program. In addition, the system is bounded by stringent running constraints. The technology options in Section 4.1.5 are able to meet each individual requirement, including single point resolution, low material budget, fast readout, low power consumption and radiation tolerance, but R&D is needed to select the specific design which can achieve the combination of all these criteria. Due to the limited manpower and availability of process, presently R&D efforts have been put into CMOS and SOI pixel sensor development to address the challenges concerning single point resolution and low power consumption. Further developments are foreseen to follow in the future, including enhancement of density, radiation hardness and ultra-light module assembling.

4.1.7.1 Current R&D activities

The current R&D activities have access to two advanced processes. The TowerJazz 0.18 μm quadruple-well process enables the full CMOS pixel circuit, while LAPIS 0.2 μm double-SOI process has properly solved the crosstalk between sensor and digital part, and improved TID tolerance significantly.

In order to exploit the potential of these new developments, two design teams have started chip designs using HR CMOS and SOI technologies respectively. Two designs have been submitted to the TowerJazz foundry. The first one uses simple three transistor (3T) analog amplification circuit to carry out the optimization of sensing diode and evaluate the influence of radiation damage [22]. The second one implements a well-proved rolling shutter readout as well as an innovative data-driven readout [23, 24]. Another two designs that adopt the SOI technology have also been submitted [25]. With the amplifier and discriminator integrated into each pixel, the pixel size has been shrunk to 16μm pitch. The chip has been thinned to 75 μm successfully and an infrared laser test has shown that 2.8 μm is achievable with that pitch [16]. All the designs for current R&D are in line with the same principle of in-pixel discrimination even though each one has its own implementation. An in-pixel discriminator can reduce analog current therefore lead to reduced power consumption.

4.1.8 Future R&D

Enhancements of the TowerJazz 0.18 μm process or Lapis 0.2 μm process are possible by migrating to a smaller production line, 0.13 μm for example, or combining with a micro-bump 3D integration process. The latter is able to attach a second layer of pixel circuit on top of the existing layer of the sensing diode and front-end circuit. The upper tier can be fully digital part that implements data-driven readout architecture, while the lower tier can be HR CMOS or SOI pixel matrix. A promising result has been demonstrated by the successful formation of 2.5 μm Au cone bump with NpD (Nano-particle deposition)

Draft-V0.2

technique [26]. However, the throughput needs further improvement and the thinning of sensors has to be compatible with micro-bump 3D integration.

The TowerJazz process is expected to be sufficiently radiation hard for the expected TID. An N-type plain implant has recently been added to improve the charge collection efficiency [27], which therefore will benefit the non-ionization radiation damage. In terms of SOI process, the weak point is the BOX layer of SiO_2. Although the TID tolerance of the SOI process has been improved dramatically by the introduction of Double-SOI and the optimization of transistor doping recipe (LDD, lightly doped drain) [15], SOI needs carefully study on the irradiation of large scale chip and of low power designs.

Sensor thinning and ultra-low material construction of modules are subject to the constraint of 0.15% X_0/layer. HR CMOS wafer thinned to 50 μm is routine in semiconductor industry nowadays. SOI wafers thinned to 75 μm with backside implant have also been demonstrated by current R&D. However, low material detector modules need to integrate mechanical support, power and signal connection, and sufficient stiffness to avoid vibration.

4.1.9 Summary

The basic concepts of the ILD Vertex detector, including the pixel sensors specifications required by the impact parameter resolution and radiation tolerance, the low-mass mechanical design, and the detector layout, are largely adapted to the baseline design of CEPC vertex detector. However, as power-pulsing will not be an option at the CEPC, it will be crucial to develop pixel sensors with lower power consumption and fast readout electronics. Detailed designs for mechanical supports and cooling, cabling, and power conversion are also necessary. Most of these issues will be addressed by R&D for the CEPC and by exploring synergies with experiments which have similar requirements.

4.2 Silicon tracker detector

As described in the PreCDR [28], the silicon tracker, together with the vertex detector and the TPC, forms the complete tracking system of CEPC. With sufficiently low material budget to minimize the multi-scattering effect, the silicon tracker provides additional high-precision hit points along trajectories of charged particles, improving tracking efficiency and precision significantly. In addition to complementary tracking, it also provides the following functionalities:

- monitoring possible field distortion in the TPC,
- contributing detector alignment,
- separating events between bunch crossings with relative time-stamping,
- potentially dE/dx measurement.

The transverse momentum resolution can be parameterized as [29]

$$\sigma_{1/p_{\mathrm{T}}} = a \oplus \frac{b}{p \sin^{3/2}\theta} \quad [\mathrm{GeV}^{-1}] \tag{4.2}$$

with p and p_{T} in GeV, θ the polar angle, a and b dimensionless numbers characterizing tracking resolution and multiple scattering effect separately. If a track is measured at N

Draft-V0.2

points equally distributed along the trajectory, we have

$$a = \frac{\sigma_{\mathrm{SP}}}{0.3BL'^2}\sqrt{\frac{720}{N+4}}$$

where B is in tesla, σ_{SP} in meter is the measurement resolution of each point and L' in meter is the projected length of the track onto the transverse plane. For multiple scattering and for relativistic particles, namely $\beta = 1$, there is

$$b = 0.053\frac{1}{BL'}\sqrt{\frac{L'}{X_0}}$$

where X_0 is radiation length in units of length. Assuming the CEPC baseline parameters and considering VTX as three layers, namely, $N = 6$, $B = 3.0\,\mathrm{T}$, $L = 1.795\,\mathrm{m}$, $\sigma_{\mathrm{SP}} = 7\,\mu\mathrm{m}$ and $L/X_0 = 2.85\%$, we have

$$a = 2.0 \times 10^{-5} \quad \text{and} \quad b = 1.7 \times 10^{-3}. \tag{4.3}$$

At low momenta, less than $50\,\mathrm{GeV}$ for perpendicular tracks, the resolution is dominant with the multiple scattering effect, and at high momenta, the resolution approaches to the tracking resolution, in turn determined by the single-point resolution. Hence, stringent constrain has to be put on material budget.

4.2.1 Baseline design

The main characteristic of the baseline design for the CEPC silicon tracker is a silicon envelope [30] around the TPC. It consists of four components: the Silicon Inner Tracker (SIT), the Silicon External Tracker (SET), the End-cap Tracking Detector (ETD) and the Forward Tracking Detector (FTD). The overall layout is shown in Figure 4.6, and the main parameters are summarized in Table 4.4.

Detector	Geometric dimensions			Material budget $[X/X_0]$
SIT	Layer 1:	$r = 153$ mm,	$z = 371.3$ mm	0.65%
	Layer 2:	$r = 300$ mm,	$z = 664.9$ mm	0.65%
SET	Layer 3:	$r = 1811$ mm,	$z = 2350$ mm	0.65%
FTD	Disk 1:	$r_{in} = 39$ mm, $r_{out} = 151.9$ mm,	$z = 220$ mm	0.50%
	Disk 2:	$r_{in} = 49.6$ mm, $r_{out} = 151.9$ mm,	$z = 371.3$ mm	0.50%
	Disk 3:	$r_{in} = 70.1$ mm, $r_{out} = 298.9$ mm,	$z = 644.9$ mm	0.65%
	Disk 4:	$r_{in} = 79.3$ mm, $r_{out} = 309$ mm,	$z = 846$ mm	0.65%
	Disk 5:	$r_{in} = 92.7$ mm, $r_{out} = 309$ mm,	$z = 1057.5$ mm	0.65%
ETD	Disk:	$r_{in} = 419.3$ mm, $r_{out} = 1822.7$ mm,	$z = 2420$ mm	0.65%

Table 4.4: Main parameters of the CEPC silicon tracker.

The barrel components SIT and SET provide precise hit points before and after the TPC, improving the overall tracking performance in the central region. The SIT helps the link between the vertex detector and the TPC, enhancing the reconstruction efficiency, particularly for low-momentum charged particles. The SET sits between the TPC and the

Draft-V0.2

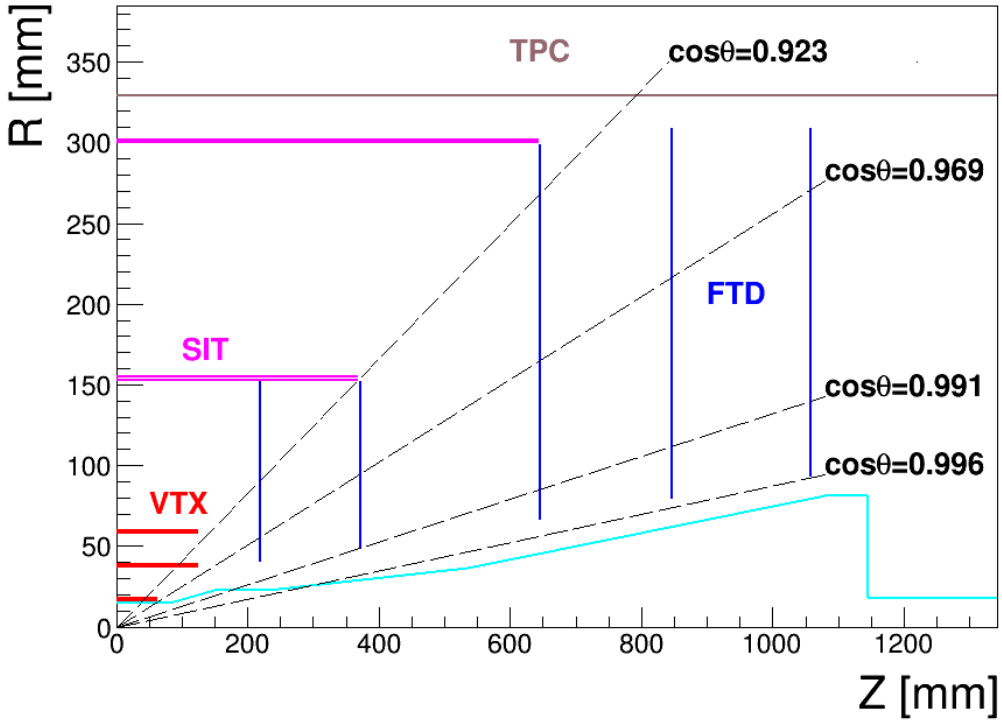

Figure 4.6: Preliminary layout of the CEPC silicon tracker. The red lines indicate the positions of the vertex detector layers and the blue lines the SIT and FTD for the silicon tracker. The SET and ETD, which sit outside the TPC, are not displayed.

calorimeter and helps in extrapolating from the TPC to the calorimeter. In addition, the good timing resolution of silicon sensors provides time-stamping for bunch separation.

The ETD is positioned in the gap between the endplate of the TPC and the end-cap calorimeter. It helps to reconstruct charged particles with a reduced path in the TPC. The SIT, SET and ETD covers the central tracking region. They form the complete silicon envelope and help in calibrating the tracking system.

The FTD is installed between the beam pipe and the inner cage of the TPC, covering the very forward region. It consists of five silicon disks on each side. The FTD is essential for precise and efficient tracking down to very small (or large) solid angles, where a number of challenges exist: the magnetic field approaching zero along the beam pipe, significantly larger occupancies due to forward going jets and high backgrounds from the interaction region. To achieve the best tracking performance, the FTD needs precise space points, a large lever arm, but low material budget. The baseline design would be a compromise among the constraints. Using highly granular pixel sensors for the first two disks can be foreseen to lower the occupancy and improve the $r\phi$ resolution.

4.2.2 Sensor technologies

The basic sensor technology is silicon microstrips for all tracker components except the two innermost FTD disks where silicon pixels are foreseen. Requirements of the single point resolution vary with positions of tracker components, but a general condition of $\sigma_{\mathrm{SP}} < 7\,\mu\mathrm{m}$ is required for high precision tracking. The microstrip sensors have proven to be capable of the resolution, taking into account material budget and power consumption. The baseline features of microstrip sensors will be a large detection area of $10 \times 10\ \mathrm{cm}^2$, a fine pitch of $50\,\mu\mathrm{m}$ and the thickness $< 200\,\mu\mathrm{m}$ to minimize the multi-scattering effect.

The alternative is a fully, or at least for inner components, pixelated silicon tracker. Although the choice of pixel technologies is open, the CMOS pixel sensors (CPS) have gained particular interest. The main advantages of the CPS comparing to the microstrip sensors are two folds:

- Granularity. The CPS provides better single-point spatial resolution and solves the problem of multiple hits.
- Material budget. The CPS can be thinned to less than $50\,\mu\mathrm{m}$, whereas the strip sensor is usually a few hundred microns.

As for the cost, because the CPS is based on the standard CMOS procedure in industry, production cost could be significantly reduced for fabricating large area sensors. In addition, the size of pixels used for the tracker can be comparatively large, hence it's possible to embed complicated circuits in the pixel to simplify the tracker readout circuitry. Initial R&D on large area CPS has been carried out.

4.2.3 Front-End electronics

The Front-End (FE) electronics will depend on the choice of sensor, namely microstrips or pixels.

For the microstrips, custom designed ASICs with deep sub-micron CMOS technology will be used. The chips will provide functions of the analogue to digital conversion (ADC), zero suppression, sparcification and possibly time stamping, together with nec-

Draft-V0.2

essary control circuitry. The high degree digitization is for relaxing the data processing pressure on downstream electronics.

As for the pixels, all FE functions can be realized in a pixel chip, even with some functions, e.g., ADC on pixels themselves. Particular concerns are readout time and electronic channels.

Commonly, the FE chip will be developed in mind with low noise, low power consumption and high radiation tolerance. New developments, such as in the SiLC collaboration and the LHC experiment upgrades, will be good references.

4.2.4 Powering and cooling

Powering and cooling are a challenge for the CEPC silicon tracker. It is important to investigate the novel powering scheme based on DC-DC converters, which has been already actively pursued by the ATLAS and CMS experiments for silicon detector upgrades [31–33]. It allows significant reduction in material budget for the low-voltage power cables and gives less power dissipation in the delivery system. Cooling is another critical issue. Although cooling based on forced cooled gas flow might be still feasible to efficiently conduct away the heat generated by the sensors, ASICs and other electronics, it is important to look into other cooling techniques, such as silicon micro-channel cooling [34], which are being investigated by several other experiments. The technique chosen will have to provide sufficient cooling without compromising the detector performance.

4.2.5 Mechanics and integration

There will always be additional challenging aspects of the mechanical design for a large area silicon tracker. A lightweight but stiff support structure can be built based on Carbon fibre Reinforced Plastic material [35]. The support structure, cable routing and electronics common to other sub-detectors need to be carefully designed to minimize the overall quantity of material and make easy construction and integration possible. Precise and quick system alignment might be achieved with dedicated laser monitoring systems, while the final alignment will be accomplished using tracks from well-understood physics events [36].

4.2.6 Tracking performance

While the tracking performance in the central region, which features the same layout as the ILD detector, has been extensively studied [37, 38], the performance in the forward region, which has been re-designed to cope with the rather short L^*, requires additional careful evaluation. Figure 4.7 shows the estimated transverse momentum resolution for single muon tracks for two polar angles $\theta = 20^\circ$ and 85°, and the analytical results from Eq. (4.2) and Eq. (4.3). Due the reduced lever arm of the tracks and fewer FTD disks in the forward region ($\theta = 20^\circ$), the resolution is worse than the required performance.

Tracking performance of the alternative pixelated silicon tracker has been studied with fast simulation, in which the microstrips are replaced with double-sided pixels with certain single point resolution and material budget reduced to $0.3\%X_0$, the same as VTX. Figure 4.8 shows the transverse momentum resolution for single muons with fixed momentum as a function of polar angle, comparing the pixelated tracker with various single point resolutions to the baseline microstrip tracker. Significant improvement can be ob-

Draft-v0.2

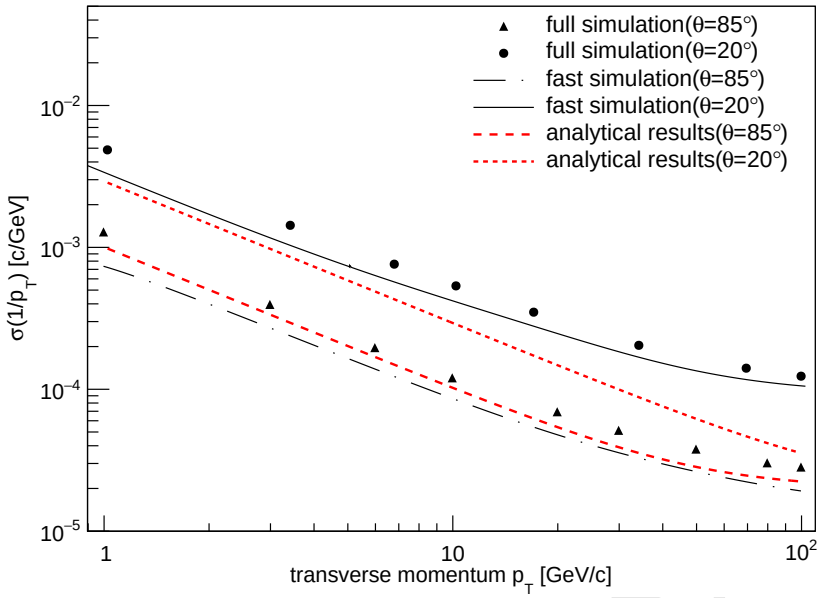

Figure 4.7: Transverse momentum resolution for single muon tracks as a function of the track momentum estimated for the CEPC baseline design with full simulation (dots) and fast simulation (black lines) compared to the analytical results obtained with Eq. 4.2 (red lines).

served when the polar angle is below about $20°$, in the tracking region of FTD. There is no, however, obvious difference for chosen pixel resolutions, all less than $10\,\mu\mathrm{m}$.

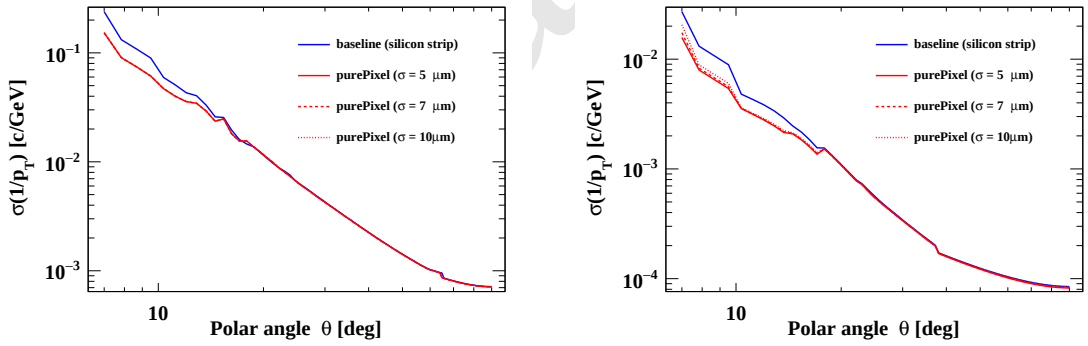

(a) $p = 1\,\mathrm{GeV}$ (b) $p = 10\,\mathrm{GeV}$

Figure 4.8: Transverse momentum resolution for single muons with momentum of $p = 1\,\mathrm{GeV}$ (a) and $p = 10\,\mathrm{GeV}$ (b) as a function of polar angle, obtained for the baseline CEPC silicon tracker with microstrips (in blue) and for pixelated tracker with various single point resolutions (in red).

Given the importance for heavy-flavor tagging, the impact parameter resolution, both transverse and longitudinal, is assessed, as shown in Figure 4.9 with muon momentum of $10\,\mathrm{GeV}$. Similar improvements can be observed, even in the high momentum range for the longitudinal impact parameter.

Further comparison is made for tracks at a fixed forward polar angle, $10°$, which pass all five FTD disks, as shown in Figure 4.10. Significant improvements can be observed in the whole momentum range for resolutions of transverse momentum and transverse

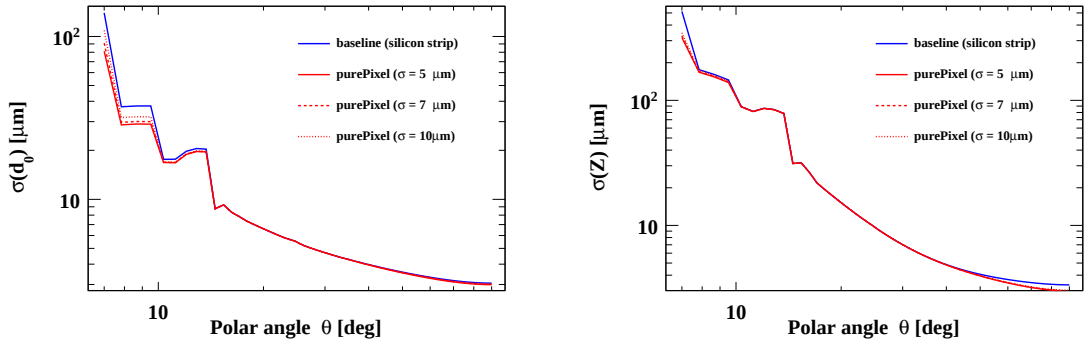

(a) σ_{d_0} (b) σ_z

Figure 4.9: Transverse (a) and longitudinal (b) impact-parameter resolution for single muons with momentum of $p = 10\,\mathrm{GeV}$ as a function of polar angle, obtained for the baseline CEPC silicon tracker with microstrips (in blue) and for pixelated tracker with various single point resolutions (in red).

impact parameter. As for longitudinal impact parameter, there is only slight improvement for high momenta, that is understandable because the z-resolution mainly depends on disk positions.

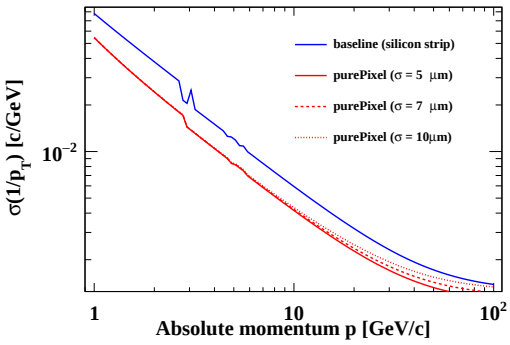

(a) σ_{1/p_T}

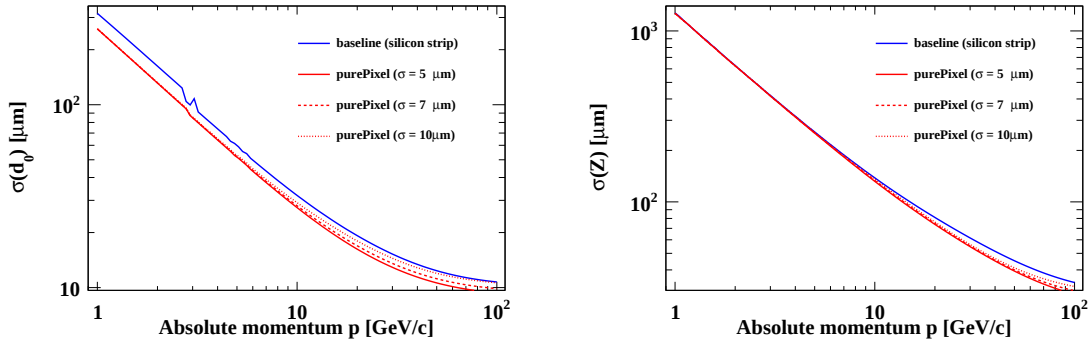

(b) σ_{d_0} (c) σ_z

Figure 4.10: Transverse momentum (a) and transverse (b) and longitudinal (c) impact-parameter resolution for single muons with the polar angle of 10° as a function of the track momentum, obtained for the baseline CEPC silicon tracker with microstrips (in blue) and for pixelated tracker with various single point resolutions (in red).

The studies are quite preliminary. There are spaces to optimize the performance of the pixelated tracker, particularly the pixel layout of FTD disks. Some other preliminary studies on the resolution of transverse impact parameter can be found in PreCDR [28].

4.2.7 Critical R&D

Silicon technology for large-area tracking detectors will continue to evolve over the next few years [39]. There are ongoing R&D activities conducted by the ATLAS and CMS experiments to develop advanced silicon detectors for the High Luminosity LHC as well as several pioneering R&D projects by the SiLC (Silicon tracking for the Linear Collider) collaboration. Despite the rather different operation conditions and requirements, it is always important to exploit synergies with existing R&D from other experiments to share expertise. During the preliminary studies, several critical R&D items have been identified for the CEPC silicon tracker. All of them, as listed below, will be pursued in the R&D phase of the CEPC project and made available for engineering construction.

- Alternative pixelated strip sensors with CMOS technologies;
- p^+-on-n silicon microstrip sensors with slim-edge structure;
- Front-end electronics with low power consumption and low noise, fabricated with CMOS technologies of small feature size;
- Efficient powering with low material budget and CO_2 cooling techniques;
- Lightweight but robust support structure and related mechanics;
- Detector layout optimization, in particular in the forward region.

It will be vital to develop necessary instrumentation for the module assembly and to verify the detector module performance with beam tests. Prototypes of support structures, including cooling solutions, shall be also built for mechanical and thermal tests.

4.3 TPC tracker detector

The tracking system are expected to affect the flying of the tracks as less as possible, which require it to be as light as possible. The particle ID ability is one of the feasibility of the tracking system, however for such energetic tracks, the classic method, such as dE/dx, TOF are not reliable. In CEPC, the inner tracking system should be sensitive in momentum measurement to charged particles, which transverse momentum ranged from 0 to 80GeV, with an accuracy compatible to the beam energy uncertainty of the accelerator[40].

The TPC (Time Projection Chamber) could be used as a main central tracker [41] [42], Time Projection Chambers (TPCs) have been extensively studied and used in many fields, especially in particle physics experiments, including STAR [43] and ALICE [44]. Their low material budget and excellent pattern recognition capability make them ideal for three dimensional tracking and identification of charged particles. They are also the only type of electronically read gaseous detector delivering direct three-dimensional track information. However, there has always been a critical problem with TPCs, especially in high

Draft-v0.2

background conditions, the space charge distortion due to the accumulation of positive ions in the drift volume [45].

TPC will be as a part of the detector concepts for the CEPC, it can measure the momentum of tracks of charged particles in the magnetic field. Micro Pattern Gas Detector (MPGD) such as Gas Electron Multiplier (GEM) and Micro-MEsh GAseous Structure (Micro MEGAS) or the Timepix chip are candidate for the readout technology [41]. Used the MPGD as readout, the $r\phi$ position resolution could be reach to 100 μm, even it's better in the high magnetic field(3.0T) [46]. Also, the TPC can reconstruct and identify particle species using energy loss (dE/dx) measured by the readout pad rows. In the reaction event of the electron-positron annhiliation in the CEPC experiment, it is required to identify charged particle species such as pion, kaon, electron, etc. and to reconstruct the events. For the CEPC-TPC, expected dE/dx resolution is less than 5% for clear identification.

Understanding the properties and achieving the best possible point resolution have been the object of $R\&D$ studies of Micro-Pattern Gas Detectors, GEM, MicroMEGAS, and pixel, and results from many years work in LC-TPC international collaboration group [47]. To improve on the performance, to optimize readout module and to control effectively ion back flow in circular machine (CEPC), these studies will continue for the next few years in order to understand and solve many critical technology challenges.

4.3.1 Principle of Time Projection Chamber

A TPC usually consists of a cylindrical drift volume with a central cathode and an anode at the two endplates. In the case of a colliding experiment, the TPC contains an inner radius in which the beam pipe and inner detectors are placed.

The anodes are at ground, while the cathode is at a potential high voltage to keep the rang of from 100V/cm to 1000V/cm in drift length. The walls of the volume are the field cage, which ensures a very homogeneous electrical field between the electrodes. The magnetic field is parallel to the electric field to suppress transverse diffusion. Without the magnetic field this diffusion would dominate, degrading the track and momentum reconstruction. The electrons are released after the ionization of the sensitive gas volume and drift along the electric field to the anodes, while the ions drift toward the cathode. An amplification device is placed in front of the anodes and creates an electron avalanche as the readout(GEM, MicroMEGAS or others).

All of TPC will be included some parts:

1. Chamber: TPC chambers are typically cylindrical and operate under the atmospheric pressure with the working gas filled inside. Chambers in high magnetic field close to the centre of the magnet, usually have a higher occupancy due to the curling low-energy tracks. Hence the material budget of stations inside the magnet is kept as low as possible. In the active area, the added the material due to the filled gas should be less than $1\%X_0$. The chambers are attached to the end-plate from the inside to minimise the dead area between neighbouring chambers. Special mounting technique is required to allow rotation and tilting of the chambers.

2. Field cage The cylindrical chamber's inner and outer composite walls hold field and forming strips, which are attached to a resistor divider chain network. The resistors must be no-magnetic. A central cathode will be held at approximately 50 kV when the

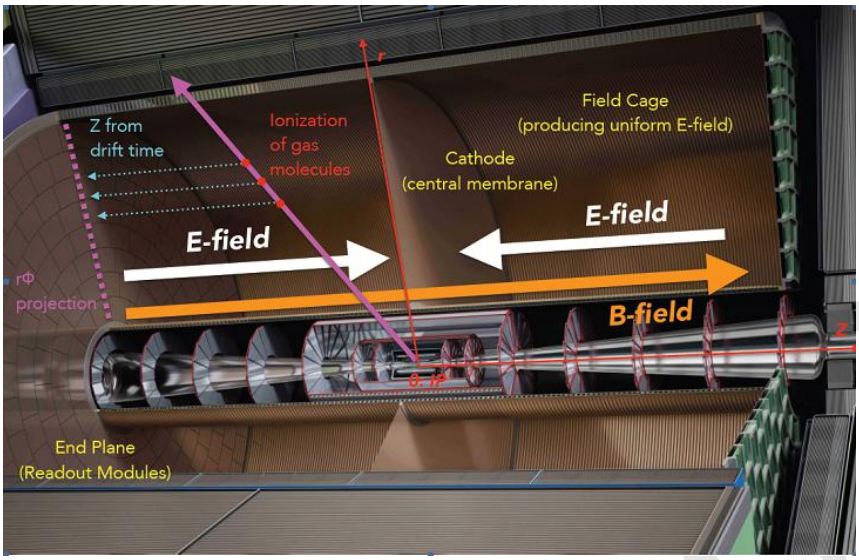

Figure 4.11: Sketch of the TPC structure.

drift field is 300 V/cm, with the end-plates and the other outer surfaces of the TPC at ground potential. Therefore the composite walls must self-stand the large potential of the central cathode. The mirror narrow strips will be arranged between the inner and outer walls to keep the electron field uniform in over the whole active TPC volume.

3. End-plate To obtain high position resolution, every end-plate is subdivided into many independent MPGD detector modules (GEM or Resistive/no Micromegas detector, so on), which can provide nearly full coverage of the end-plate. Power cables, electronic connectors, cooling pipes, PCB boards and support brackets wall are also mounted on the end-plate. In case the detector modules are damaged by the discharge or spark, they can be replaced and the end-plate should be kept stable during the replacement. In addition, the end-plate needs to built from lightweight material, not compromise the jet energy resolution in the forward region, but should be still sufficiently rigid to achieve stable positioning of the detector modules with a position accuracy better than 50 μm.The material budget of the mechanical structure accounts for $8\%X_0$. Additional materials for the readout planes, front-end electronics and cooling are estimated to be $7\%X_0$, and power cables and the connector up to $10\%X_0$.

The TPC could provide some physics information: First function is 3 dimensional track reconstruction, by getting the XY information from the anode segmented in pads and the Z coordinate delivered by the drift time. To obtain the Z coordinate from the drift time, the drift field has to be very homogeneous. Because this coordinate is obtained via the drift velocity of the electron, it should have a moderate dependence on the drift field for a given gas mixture. Second parameter is the total momentum of a charged particle, by measuring the radius, ρ, of the electron trajectory to get the transverse momentum, and adding this information to the knowledge of the trajectory in the Z plane. Final function is the particle identification, the energy loss can be extracted by measuring the charge deposited on the readout pads. The energy loss combined with the measurement of momentum in the magnetic field provides then the particle identification.

Draft v0.2

4.3.2 Baseline design and technology challenges

4.3.2.1 Main parameters of the detector geometry

In TPC parameters, the geometry will be limited with inner diameter, outer diameter, drift length, electric field, and the magnetic field. The transverse momentum resolution Δp_t of a tracking device - one of the basic figures of merit - is described by the Gluckstern formula

$$\frac{\Delta p_t}{p_t^2} \propto \frac{\sigma_{r\phi}}{BL^2}\sqrt{\frac{720}{n+4}} \tag{4.4}$$

where $\sigma r\phi$ denotes the spatial single-point resolution in the $r\phi$-plane, B is the magnetic field strength (which bends the particle trajectories depending on the momentum), L is the length over which the measuring points are distributed, and n is the number of single-point measurements that are used in the overall track fit.

From the formula [48], there is strong confidence that a TPC will be able to meet the performance goals of the CEPC tracker detector: with a single-point resolution of $r\phi$=100μm, with a magnetic field of 3T, with an inner radius of 0.3m and an outer radius of 1.5-1.8m, and with approximately 200 pad rows.

The resolution of the TPC is limited by the diffusion of the drifting electrons. An upper bound on the diffusion is calculated using the standard Gluckstern parameterization, assuming a large number of measurements along the length of the track

$$D < \frac{\sigma_p t}{p_t}\sqrt{\frac{n_T L}{720}}(L[m]^2)\frac{0.3B[T]}{p_t[GeV/c]}\frac{1}{\sqrt{L_{drift}}} = 100\frac{\mu m}{\sqrt{cm}} \tag{4.5}$$

where the diffusion component of the momentum resolution (σ_{pt}/p_t) is required to be less than 10^{-4} at p_t=1GeV/c, n_T=30 ionization electrons per cm of gas (mainly argon) for a track measured over L=1.8m and for a drift distance of L_{drift}=2.0m in the magnetic field of 3.0T [49].

A large volume TPC with about 200 points per track provides continuous tracking for a large volume (several meters level). The TPC is optimised for excellent three-dimensional point resolution and minimum material in the field cage and in the end plate. It also provides particle identification capabilities based on the energy loss of particles per unit of distance (dE/dx). The geometry baseline should be consider the following reasons: Sensitive to the track segment as long as possible, stronger enough magnetic field for track bending and as good as possible position resolution of the track measurement.

4.3.2.2 Modularization design

The figure4.12 shows that the diagram of large prototype module design in LC-TPC international collaboration group $R\&D$.

In the large collider machine, the readout structure is designed to be modularised to easily change and maintain. Each module will consist of gas amplification system, readout pad plane and following electronics. High density electronics make it possible to integrate the electronics directly on the back of the readout pad plane. The readout module will then have to provide all necessary high and low voltages and cooling for heat dissipation, however, especially because power-pulsing will not be available at the CEPC. To achieve the required performance, an MPGD-based gas amplification system will be developed.

Draft-v0.2

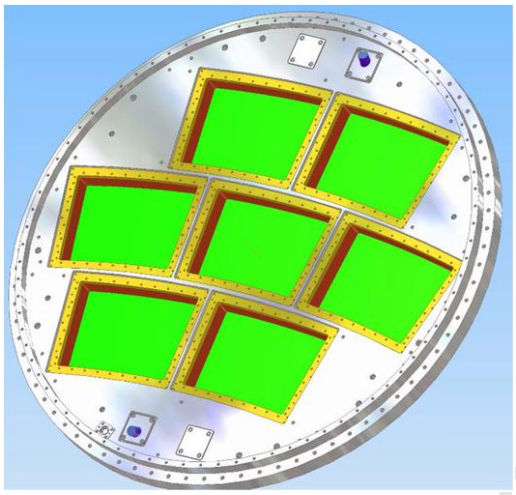

Figure 4.12: The diagram of large prototype module design.

The charge from the amplification system will be collected on a pad board. Each module size will be about 160mm-180mm of width and 190mm-210mm of highth.

To meet the physics performance basing on the modularization design, tt has been demonstrated that any amplification technologies combined with pad readout can be built as modules which cover large areas with little dead space.

4.3.2.3 Gas amplification detector module

For the detector module, the electron gas amplification is obtained in very high fields generated by modest voltages (300-400V) across $50-100\mu m$ structures suitable for large-area applications. Typically gains of $10^3 - 10^4$ are achieved with many gases under standard conditions. Gas Electron Multipliers and MICRO-Mesh GAseous structure are two example of MPGDs.

This gas amplification detector module for a pad-based TPC will be either GEM, MicroMEGAS or others structure, since they do not meet the ambitious performance goals. Two or three GEMs are stacked together to achieve sufficient charge amplification resistive MicroMEGAS have enough amplification in a single structure.

Micro-pattern devices for TPC provide:

1. Higher rate capability: MPGDs provide a rate capability over $10^5 Hz/mm^2$.
2. Intrinsic ion feedback suppression: The ions produced on these field lines do not go back to the drift volume and most of them will be neutralised on the mesh or GEM foil.
3. A direct electron signal, which gives a better time resolution.
4. A larger gain, by the specific operation high voltage.
5. Much smaller $E \times B$ effects than wires chamber for which the spacing of the wires is about a few mm.

4.3.2.4 Optimization readout pad size

Design of readout pad size is key parameter for the TPC detector module whether using GEM, MicroMEGAS or combination structure as the readout detector. Accurate posi-

Draft-v0.2

tion information require to process the adjacent pad's signal with the Center-of-Gravity Method(CGM).

The design of the two-dimensional readout strips has been developed with the triple GEMs of $100mm^2$ in IHEP. The readout strips in X direction are $193\mu m$ wide at $752\mu m$ intervals. There are pads with a size of 356 $\mu m \times 356\mu m$ connected with each other in Y direction and their strip pitch is $457\mu m$. The difference in strip widths is to improve signal sharing between X-axis and Y-axis strips, to ensure a homogeneous charge distribution between neighboring strips. The total number of strips in X and Y directions are 267 channels and 437 channels respectively. Each strip is connected with one electronic channel to process the signal.

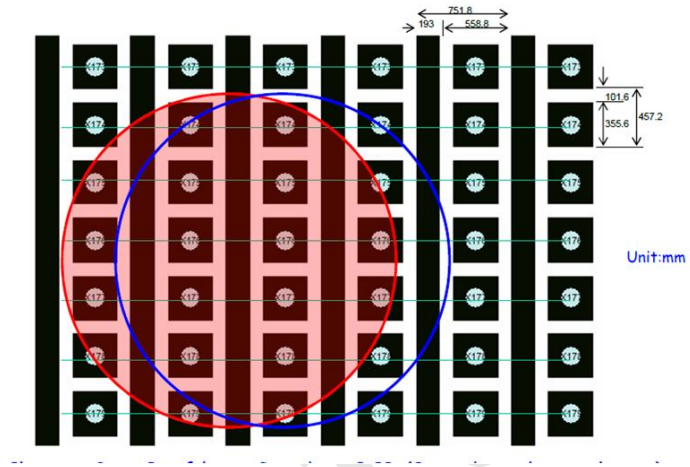

Figure 4.13: The profile of the electrons cluster in Triple GEMs.

In the figure4.13 of the typical profile of the electrons cluster in readout strips, the pink circle could be move to the blue circle and the profile is the Gaussian distribution. If there is a enough number pads to use Center-of-Gravity Method, the pad width should be designed to 1.0mm and the length of pad should be designed to 6.0mm to obtain the sufficient charge information when the amplifier gain is 10mV/fC.

4.3.2.5 Operation gas for the long drift

As with any gaseous detector, the choice of the chamber gas strongly affects the properties and eventually the performance of a TPC. Desirable characteristics are:

1. High drift velocity (to avoid accumulation of too many events inside the chamber)
2. A very low transverse and a low longitudinal diffusion coefficient (to prevent deterioration of the spatial resolution)
3. A sufficiently large specific energy loss $dE = dx$
4. A high enough stability against electrical breakthroughs (to allow reliable operation of the amplification device)
5. Nonhazardous chemical properties (to address safety concerns like in-flammability and damages to the hardware)

The gas mixture should be chosen to minimize the capture of electrons by the molecules of electronegative impurities. Due to the long drift distance of the several meters, and

the fact that ions are heavier and much slower than electrons, ions can accumulate in the chamber. This effect can lead to electric field distortions and should therefore be avoided. To decrease this effect, the structure of the readout chambers is generally designed to avoid ions from escaping into the gas volume. A gas with a large drift velocity is also chosen in experiments with large interaction rate.

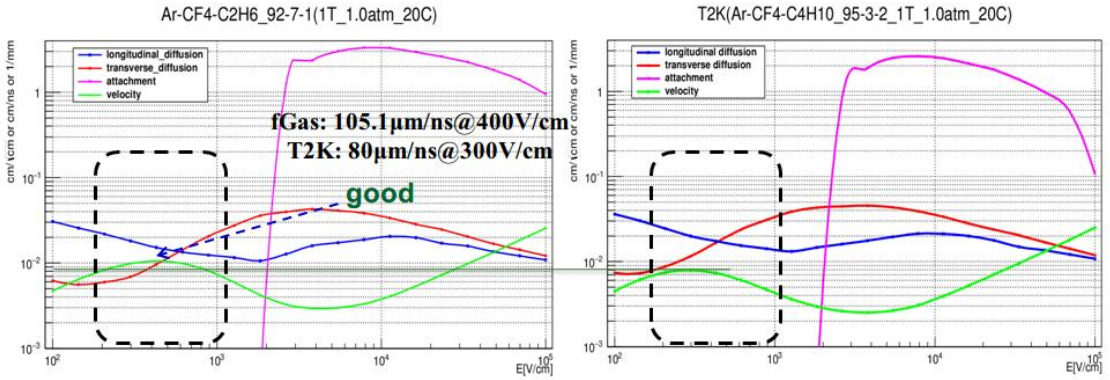

Figure 4.14: The drift velocity in different gas mixture.

In given the working gas and the electric field, the drift velocity of electron could be determined with Eq. 4.6

$$\mu_e = f(\frac{E}{P}) \tag{4.6}$$

where E denotes the electric field vector, P the gas pressure and μ_e the electron drift velocity. After reaching saturation (nearly maximum), the electron drift velocity depends slightly on the electric field. Fig. 4.14 shows that the drift velocity obtained in different mixture gases. For the CEPC TPC detector, it is required to be sensitive to as long as possible track segment. The working gas should be selected in such way to achieve high velocity in low drift field to lower the high voltage in all of the drift length, and small transverse diffusion in the magnetic field to decrease the electron cluster size on the readout pads.

The gas mixture of Ar/CF_4/iC_4H_{10} (95%/3%/2%) have been used for the Large Prototype of TPC Detector for the ILD TPC and the TPC chamber for the T2K experiment. The saturated drift velocity of the mixed gas reaches nearly 8 cm/μs in a drift field of 300 V/cm. In addition, the gas has a large parameter of $\omega\tau$ (same as the Eq. 4.6) and transverse diffusion coefficient of 30 μm/$\sqrt{\text{cm}}$ in the drift field of 300 V/cm. In the B-field, a reasonable transverse diffusion coefficient could be realised at 100 V/cm of the drift field. The bunch spacing at the CEPC is $\sim$ 3.6 μs. The working gas has an higher saturated drift velocity than the T2K mixed gas should be considered. In addition, the gas amplification needs to achieve approximately 6000 and the signal attenuation of the electron attachment should be kept below $1\%/m$.

4.3.2.6 Low power consumption electronics readout

Small readout pads of a few square millimeters (e.g. $1mm \times 6mm$)are needed to achieve high spatial and momentum resolution in TPC, demanding about 1 million channels of readout electronics per endcap.The total power consumption of the front-end electronics is limited by the cooling system to be several kilo-watts in practice and they have to

Total number of channels		1 million per endcap
APE	ENC	500e@10pF input cap
	Gain	$10mV/fC$
	Shaper	CR-RC
	Peaking time	100ns
ADC	Sampling rate	$\geq 20MSPS$
	Resolution	10 bit
Power consumption		$\leq 5mW$ per channel
Output data bandwidth		200 Mbps $\times$Occu. per channel*
Channel number		32
Process		TSMC 65nm LP
*Typical occupancy is less than 1% in CEPC-TPC		

Table 4.5: TPC readout electronics.

work continuously in CEPC.Hence the technique of so-called power pulsing cannot be applied. There are no current existing electronics readout system can fulfill the requirements of such high density and low power consumption. The architecture of the TPC readout electronics is shown in Fig.1, selected from a broad range of survey on current electronics installed or under development during past decades, including ALTRO/S-ALTRO and more recently SAMPA for ALICE,AFTER/GET for T2K and Timepix for ILC. It consists of the front-end electronics on the detector panel and the data acquisition system several meters away from the detector.

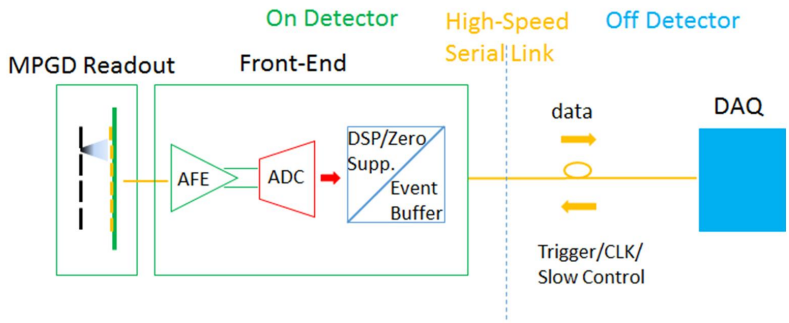

Figure 4.15: The architecture of the TPC readout electronics.

The waveform sampling front end is preferable, including a preamplifier and a shaper as the analog front-end (AFE), a waveform sampling ADC in 10MSPS, a dedicated digital signal processing (DSP) and zero-suppression unit and an de-randomize event buffer for each channel. In order to meet the stringent requirements on the integration and the power consumption, a front-end ASIC will be developed in advanced 65nm CMOS process. The key specifications of the front-end ASIC are summarized in Table 1.

CMOS scales down in favor of digital circuits in terms of power and density. The power consumption of the DSP circuits reported in $Ref.[3]$ was $4mW/ch$ in 130nm process and could be reduced by a factor at least of 2 by migrating the same design to 65nm. However

this is not the same for the analog circuits. The design strategy for the front-end ASIC is to keep the analog part as simple as possible. The block diagram of the analog front-end and the successive approximation (SAR) ADCare shown in Fig.2 and Fig.3 respectively. The CR-RC shaper and the SAR ADC instead of pipeline ADC will be used for their simplicity in analog circuits and hence the higher power efficiency.

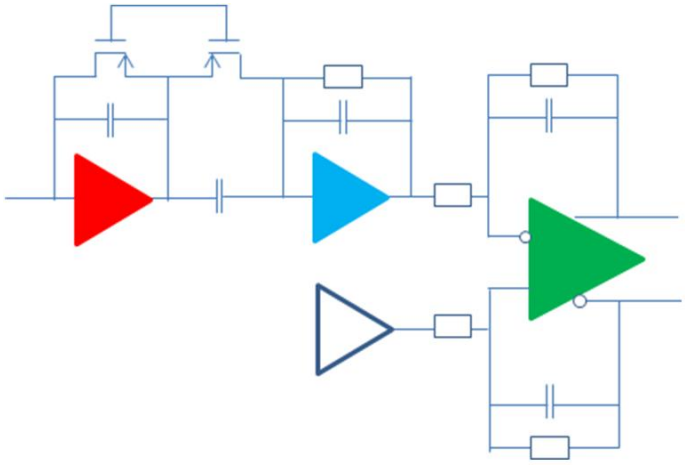

Figure 4.16: The block diagram of the analog front-end.

Dedicated digital filters will be applied to the continuously digitized input signals to suppress the pedestal perturbations caused by the non-ideal effects such as temperature variation and environment disturbance. Then the data will be compressed by only storing the data packets above a programmable threshold with a specified number of pre- and post-samples. A data head will be added to each packet with its time stamp and other information for reconstruction afterwards. The buffered data are readout through high speed serial links to the DAQ system. The front-end electronics can support for both external trigger and self-trigger mode.

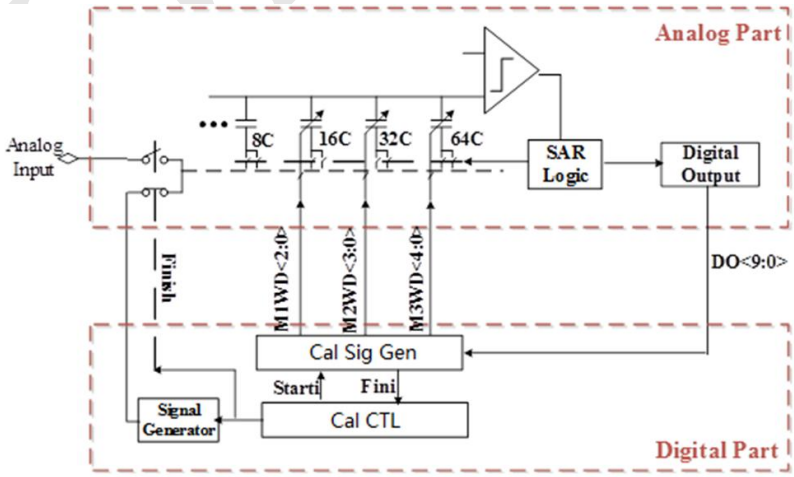

Figure 4.17: The block diagram of the SAR-ADC.

Even with the state of the art technology, the power density of TPC readout electronics for CEPC could still be several times higher than that for ILC-TPC. Two-phase CO_2 cooling[7] is a well-developed technology and can be used as a baseline solution to bring

out the heat generated by the front-end electronics and to keep the temperature of the TPC chamber stable at 20°C. More efficient micro-channel CO_2 cooling may be studied further and can be an alternative technique to copper pipes [8].

The TPC readout electronics are meters away from the collision point and the radiation dose is rather low ($< 1krad$) at CEPC, which allows us to use standard, radiation soft technologies. On the other hand, energetic particles can always produce instantaneous failure (SEU or SEL) from time to time. Hence radiation tolerant design needs to be considered that the overall system performance will not be affected or even irreversibly damaged by the rare events.

4.3.2.7 Critical technology challenges in the circular machine

The mechanical structure of the TPC consists of a field cage, which is made with advanced composite materials, and two readout end-plates that are self-contained including the gas amplification, readout electronics, supply voltage, and cooling. It will be challenging to design and build the TPC support structure with relatively light material, and at the same time very rigid. It is required to maintain accuracy, robustness in all directions, and stability over long time periods. As the field cage is not strong enough due to the limited material budget, the end-plates become the only choice, where the support structure connects to. In current stage of design, how the TPC end-plate should be supported is not fixed yet. A promising solution is to suspend from the solenoid, in which a number of spokes run radically along the faces of the calorimeter to the TPC end-plates. Bearing is not the most challenging issue.

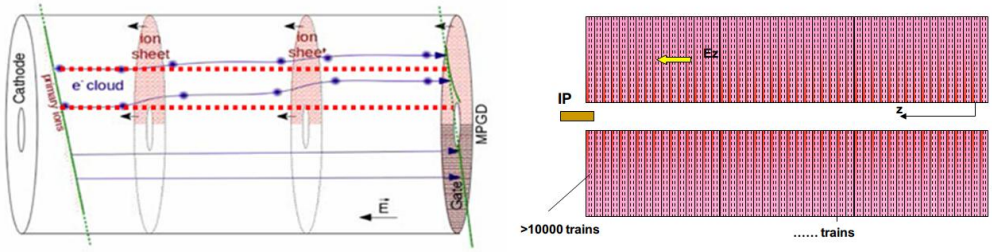

Figure 4.18: The diagram of distortion and ion disks in CEPC.

Any kind of amplification device creates not only secondary electrons, but also the same amount of ions. These ions move in the opposite direction away from the anode region into the main chamber volume - and furthermore have a much lower drift velocity, meaning that they could accumulate in the chamber gas and build up a significant space charge in the form of 'ion discs'. In CEPC, the majority of ions inside the drift volume are backflowing ions from the amplification region of the TPC readout devices. It is thus of great importance to limit ion backflow (IBF) from the amplification region. This might affect the drifting electron tracks through electrostatic attraction as well as inhomogeneities of the drift velocity (which depends on the electric field strength). In order to minimise this deteriorating influence on the spatial resolution of the chamber, the backflow of ions should be suppressed.

One possible mechanism of backflow suppression, often used together with wire mesh device, is a so-called gating grid. The critical problem with this relatively simple yet effective scheme is that it cannot be immediately applied to the timing structure of the CEPC: the bunch spacing of the machine is so small (μs or less, compared to the readout time) that tracks from many events are drifting through the chamber. It shows in the figure of the diagram of distortion and ion disks in CEPC. Another promising option is to exploit the 'built-in' ion backflow suppression of GEMs or MicroMEGAS. In next section, the $R\&D$ study of the hybrid detector module has been developed to control ions continuously and the update results will be described.

4.3.3 Simulation and estimation for the key issues

4.3.3.1 Occupancy requirement of Higgs and Z pole run

Using an sample of 9 thousand fully simulated $Z \rightarrow qq$ events at center of mass energy of 91.2 GeV, we studied the voxel occupancy and the local charge density of the CEPC TPC at Z pole operation for future circular electron positron colliders, with an instant luminosity of 2×10^{34} to 2×10^{36} cm^{-2} s^{-1}.

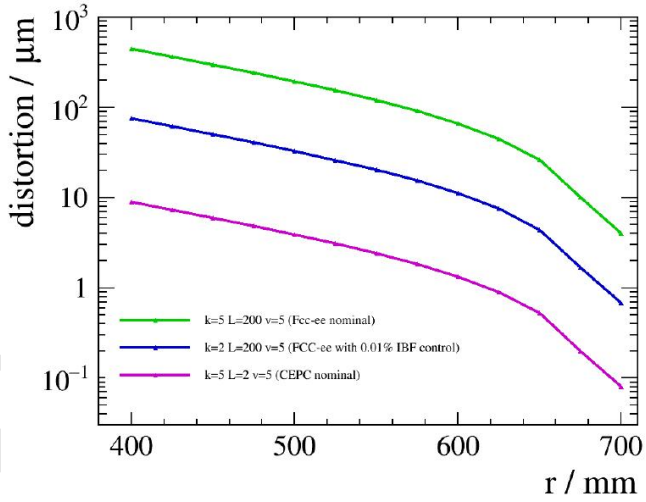

Figure 4.19: Distortion as a function of electron initial r position with different parameters.

Given the fact that the beam bunch is evenly distributed along the accelerator circumference, the voxel occupancy is extremely low ($1.4 \times 10^{-5}/1.4 \times 10^{-7}$ for the inner most layer and $3.4 \times 10^{-6}/3.4 \times 10^{-8}$ for average) and poses no pressure for the TPC usage. The distortion on TPC hit positions induced by the ion charges is estimated with dedicated program and calculation. At instant luminosity of 1×10^{36} and an ionback flow control of percent level, the distortion can be as large as 10 mm at the inner most TPC layer at the CEPC conceptual detector geometry, which is two orders of magnitude larger than the intrinsic TPC spatial resolution. A few approaches are proposed to reduce the effects caused by distortion:

1. Ion back flow control technology; the ion back flow should be controlled to per mille level, in other word, only $1-10$ back flow ions is allowed for each primary ionization.

2. Dedicated distortion correction algorithm, for the inner most layers, which should result in a mitigation of the hit position distortion by 1 order of magnitude.

3. Adequate track finding algorithm that could link the TPC track fragments to vertex tracks at high efficiency and purity.

Taking all of these approaches account, the distortion can be mitigated by approximately 2 orders of magnitude. To conclude, the pad occupancy and distortion stress no pressure to CEPC and if the above items can be achieved.

4.3.3.2 Distortion of Ions backflow in drift length

Early TPCs were equipped with multi-wire tional chambers (MWPCs) as gas amplification devices. The IBF ratio in a standard MWPC is $30 - 40\%$ so a gating grid is essential to prevent ions from reaching the drift volume. In the presence of a trigger, the gating grid switches to the open state to allow ionization electrons to travel into the gas amplification region. After a maximum drift time of about 100 μs (depending on the drift length, electric field and gas mixture), the gating grid is closed to prevent positive ions from drifting back into the drift volume. Since it must remain closed until the ions have been collected on the grid wires, the ionization electrons are also blocked during this time and the dead time consequently increases.

Triggered operation of a gating grid will therefore lead to loss of data. Thus, the TPC at the proposed circular collider will have to be operated continuously and the backflow of ions must be minimized without the use of a gating grid.

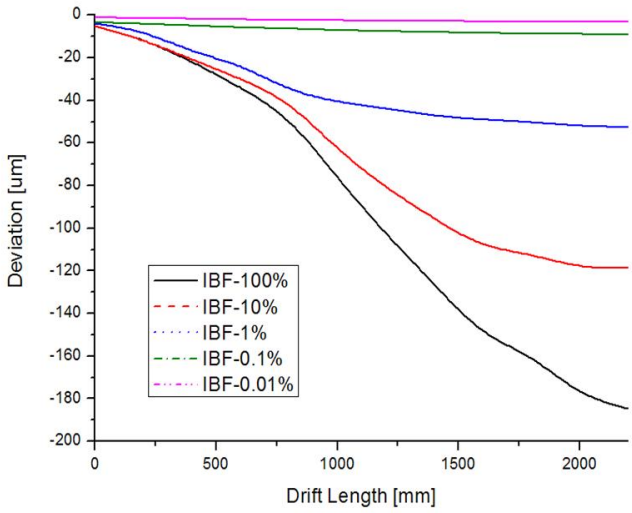

Figure 4.20: Evaluation of track distortions due to space charge effects of positive ions.

The ions generated from the ionisation in the drift volume or from the avalanche multiplication and have found their way into the drift region will not only introduce field distortion, but also deduce the TPC counting rate capability. This effect is called ion backflow, and should be fully suppressed in the TPC drift volume. With an averaged 300 eV required by per ion-electron ionisation and 2 keV energy loss per mili-meter, there will be roughly 12k primary electrons generated by a track with a typical length of 1.8 m in the TPC and there will be in total 240 k electrons in one event. With the electron drift velocity of 5 cm/μs, it takes $\sim$ 40 μs for all the electrons to drift 2 m to reach the end-plate.

With the expected bunch spacing of 3.6 μs at the CEPC, there will be about 11 events overlapping in the TPC volume. Therefore there will be 240k$\times 11/2 = 1.32$ M electrons continuously drifting toward the end-plate. On the other hand, ions drift much slower than electrons, with a velocity of only 500 cm/s in an electric field of 500 V/cm. This leads to ions from 110,000 events overlapping in the TPC volume. If the 1% of the ions are trapped by the gate and with the gas amplification factor assumed to be 10000, there will be 240k$\times 10000 \times 1\% \times 110,000 = 2.64$T ions drifting back continuously. With the TPC volume to be $\sim$20M cm^3 in size, there will be on average 0.13M ions/cm^3.

4.3.4 Feasibility study of TPC detector module and future work

4.3.4.1 Continuous IBF detector module

TPC readout with micro-pattern gaseous detectors (MPGDs), especially Gas Electron Multipliers (GEM)and micro-mesh gaseous structures (Micromegas), is very attractive, because the IBF of those detectors is intrinsically low, usually around a few percent. GEM detectors have been extensively proved in the last decade to be the prime candidate, as they offer excellent results for spatial resolution and low IBF. Several GEM foils can be cascaded, allowing multilayer GEM detectors to be operated at an overall gas gain above 10^4 in the presence of highly ionized particles. Micromegas is another kind of MPGD that is likely to be used as endcap detectors for the TPC readout. It is a parallel plate device, composed of a very thin metallic micromesh which separates the detector region into drift and amplification volumes. The IBF of this detector is equal to the inverse of the field ratio between the amplification and the drift electric fields. Low IBF therefore favours high gain. However, high gain will make it particularly vulnerable to sparking. The idea of combining GEM with Micromegas was first proposed with the goal of reducing the spark rate of Micromegas detectors. Preamplification using GEMa also extends the maximum achievable gain, so there have also been studies on gaseous photomultipliers with this hybrid configuration.

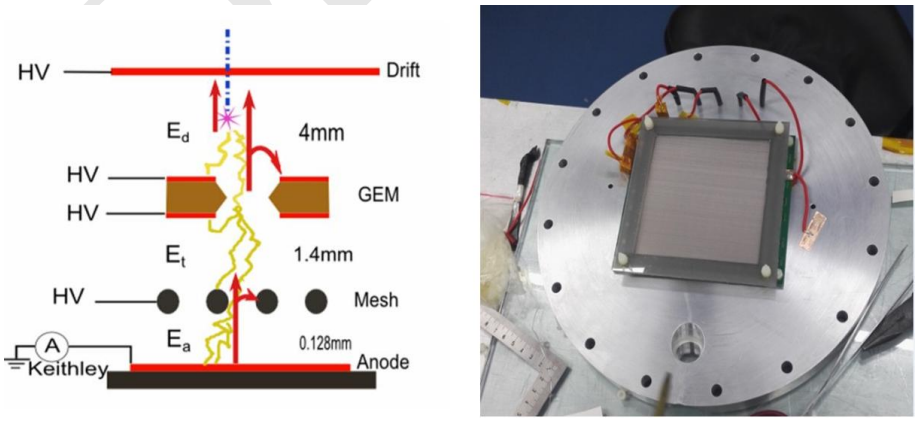

Figure 4.21: Schematic diagram of the detector module.

To fulfill the physics goals of the future circular collider, a TPC with excellent performance is required. MPGDs with outstanding single-point accuracy and excellent multi-track resolution are needed. We have proposed and investigated the performance of a novel configuration detector module: a combination of GEM and a Micromegas. The detector will be called GEM-MM for short throughout this paper. The aim of this study is

to suppress IBF continually by eliminating the gating grid. The design concept and some preliminary results of the detector module are described as following.

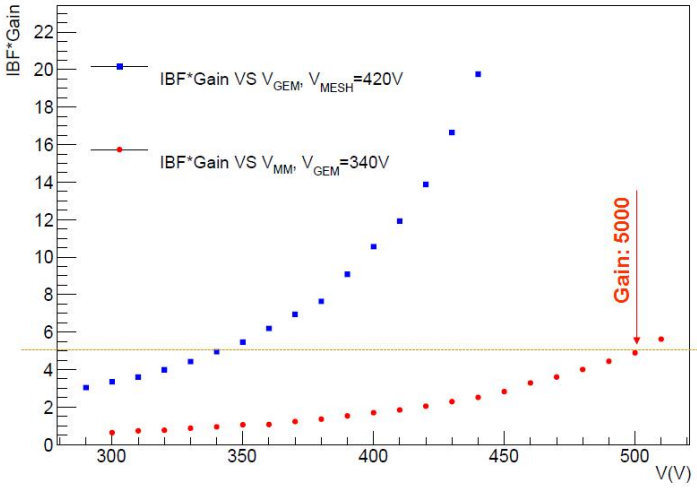

Figure 4.22: Result of the IBF TPC detector module.

A new concept of avalanche ion backflow reduction for a future MPGD readout based TPC, and a prototype has been developed. It is a hybrid structure with one GEM foil cascaded above the Micromegas detector. Tests of this detector have been carried out with an 55Fe X-ray source in $Ar/CO_2(90/10)$ gas mixture. The preamplification effect of GEM foil has been demonstrated in the energy spectrum measurement. With the novel hybrid structure, the effective gain of the GEM can be measured even when it is relatively low. The energy resolution of this hybrid structure gaseous detector is measured to be 27%(FWHM). The gain properties of this device were measured. A gain up to about 5000 can be achieved without any obvious discharge behaviour. The currents on the anode and drift cathode were measured precisely with an electro-meter. Out experimental measurements show that IBF can be reduced down to 0.19% at a gain of about 5000.

4.3.4.2 Laser calibration and alignment system

The laser calibration system could be used for the TPC detector, the narrow laser beams inside the drift volume of the TPC simulate ionizing tracks at predefined locations. The goal is to obtain a uniformity of the TPC drift field within a relative error of 10^{-4} corresponding to a spacial resolution of $\sigma_{r\phi} = 100\mu m$. The system can be used for tests and calibration either outside or during normal data taking with the aim of understanding the chamber performance. Of particular interest is the testing of electronics, alignment of the read-out chambers, and measurements of variations of the drift velocity due to mechanical imperfections and non-uniformities in the gas, temperature and the electric and magnetic fields.

The laser system would be used for calibration and for distortion measurement in the prototype with one module as readout or large, A Nd:YAG laser with a wavelength of 266nm shall be used to study the track distortions. An additional UV-lamp could generate additional ions. The complete optical path and the laser power will be split into $6-7$ laser tracks. The laser map coupling into the chamber and the planned laser tracks could

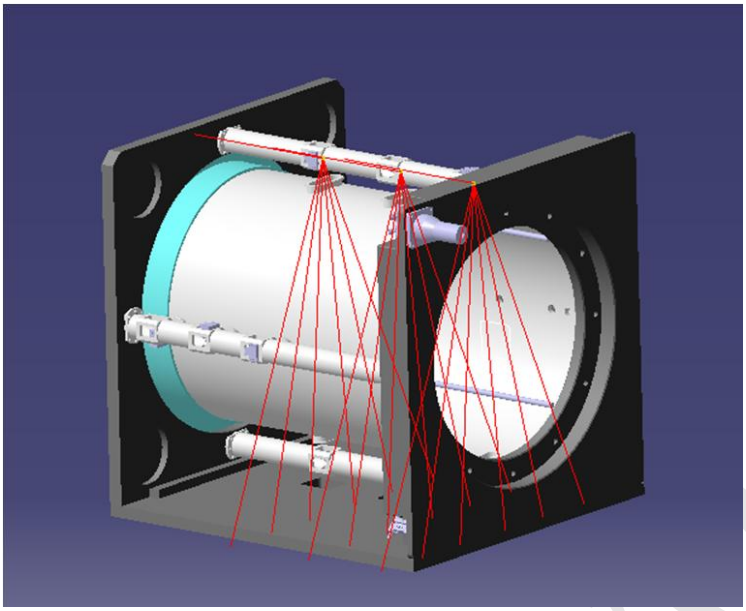

Figure 4.23: Schematic diagram of the detector module with the laser system.

be designed. The UV laser beam for calibration and alignment purposes to monitor the drift velocity, operation gas, gain uniformity and electric field. Nd:YAG laser device with 266nm wavelength could make the ionization in the gas volume along the laser path occurs via two photon absorption by organic impurities. The laser power should be reach $10J/mm^2$ to equal $10MIP$.

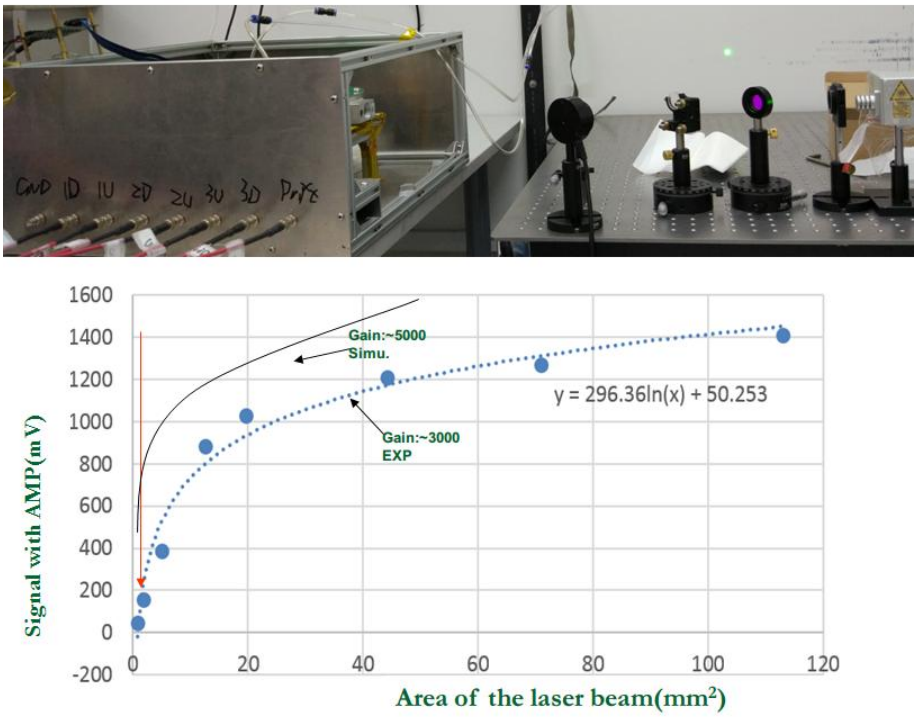

Figure 4.24: Signal with the different size of laser beam.

- Photoelectric laser source with UV light source: Enlights the cathode with UVs could produce photoelectrons to study and monitor distortions, the cathode with UVs to produce photoelectrons to study and monitor distortions, Deuterium lamp with $160nm - 400nm$ of the wavelength as UV light source and smooth Aluminum film as cathode. To mimic the bunch structure and the ions distortion with UV light lamp by the specific time structure shine controller, UV could create more than about 10000 $electrons/s.mm^2$.

- Calibration laser beam size: The shine and entrance window could use the fused silica as of $99\%\ trans.@266nm$. Provides a UV laser beam for calibration and alignment purposes to monitor the drift velocity, operation gas, gain uniformity and electric field. The ionization in the gas volume along the laser path occurs via two photon absorption by organic impurities. The study has been done using Nd:YAG laser device has the 266nm of wavelength(4.68eV). The optimization laser beam area of the laser device will be the range from $0.8mm^2$ to $1.0mm^2$ in the figure4.24.

To solve the critical technology problems in CEPC, the hybrid structure MPGD detector module has been developed and some preliminary results has been obtained and analyzed, the further study will be done from this combination detector module. Another small TPC prototype with 266nm laser calibration system and UV photoelectric function has been design and would be assembled, the calibration experiment would be further studied for CEPC.

4.3.5 Conclusion

The TPC designed following the LC-TPC concept provides a very good starting point for the CEPC TPC, but many modifications are foreseen due to the different performance requirements and experimental conditions. Several critical R&D issues have been identified in pre-studies. Possible solutions to those issues have been suggested and will have to be verified with a prototype TPC in future.

4.4 Full-silicon tracker detector

The design concepts for the tracking system at CEPC are similar to the ones studied for ILC [38, 50], which are required to provide excellent tracking efficiency and precision over a wide range of momenta for charged particles from the interaction point as well as from the decay of secondary particles. The tracking system must be built with minimal material to preserve the momentum resolution and being covered hermetically down to the dip angle of $|cos\theta| < 0.992$ from the beam pipe. There are two design options for ILC detectors, the large TPC+Silicon detector (ILD) and the compact full-silicon detector (SID), with very different approaches to achieve the same performances. The full-silicon tracker offers a well known technology that provides excellent space point resolution and granularity to cope track separation in dense jets and hits from the high luminosity beam related background. The drawbacks include the relative high materia density within the tracking system, less redundancy, and limited dE/dx measurements. Nevertheless, the purpose of this study is to demonstrate that the full-silicon tracking concept is a viable option for CEPC.

Draft v0.2

For designing a full-silicon tracker, we use the same detector boundary conditions considered in the CEPC v_4 detector, which are summarized in the following,

- the solenoid B field is set to 3 Tesla,
- the tracking envolope consists of a cylinder with a radius of 1.83 m and a length of 4.6 m,
- the tracker covers down to 7.25 degree from the beam pipe,
- the Be beam pipe has a radius of 1.45 cm and 14 cm long.

4.4.1 Full silicon tracker layout

The ILD-like detector relies on a mixture of Time Projection Chamber (TPC) and silicon tracking system. However, the tracker could be converted using full silicon if the TPC is replaced with additional silicon stereo-strip layers (SIT) in the central region with disks of silicon stereo-strip detectors (FTD) on each side. In this design, the outer tracking system consists of a full-silicon tracker arranged as a set of six nested SIT layers in the central region with five FTD strip endcap disks on each side as shown in Fig. 4.25. Details for design of SIT and FTD detectors can be found in the discussion of CEPC-ILD design [**?**] and we will use the same module design to build a full silicon detector as CEPC-SID. The pixel vertex detector (VTX) is kept the same as in CEPC v_4.

This new proposed tracking system provides at least 11 precisely measured points for all tracks down to a polar angle of about 15 degree and at least 7 measured points down to a polar angle of about 7.25 degree, as shown in Fig. 4.26. With three double pixel layers and forward disks covering a wide of polar angle, they are capable of providing excellent tracking on their own. The outer tracker adds additional track-finding constrains at large radii where hit density is low while improving the momentum measurement over a large level arm with excellent hit resolution in the transverse plane.

Alternatively, we could optimize the design of ILC-SID detector for CEPC by enlarging the outer silicon strip layers to fulfil the space up to a radius of 1.83 m and z at $\pm$ 2.3 m in order to achieve comparable momentum resolution using a lower solenoid B filed of 3 Tesla as shown in Fig 4.25. The pixel detectors again are kept the same as in the ILC-SID design. We will label this option as "SIDB", which provides an independent cross check on the tracking performance using a full-silicon tracker. The number of expected hits on the track from SIDB is also shown in Fig. 4.26.

Table 4.6 summarizes the geometry parameters of the proposed outer strip silicon trackers for CEPC between two full silicon options.

4.4.2 Toy simulation

For each layout, we use a toy simulation (Idres) to calculate the expected tracking resolution as function of track momentum for a given incident angle θ, in which the effect of multiple scattering due to the materia are taken into account correctly. Idres was developed by the ATLAS experiment [51]. The results are also cross checked using LDT program [52], which gives a consistent result.

The coverage of the full-silicon tracking system is shown in Fig. 4.26 as function of track pesudo-rapidity. At least 7 hits are measured for all tracks with a polar angle down to about 7.25 degree. The total radiation length for all-silicon tracking systems, including

Draft-V0.2

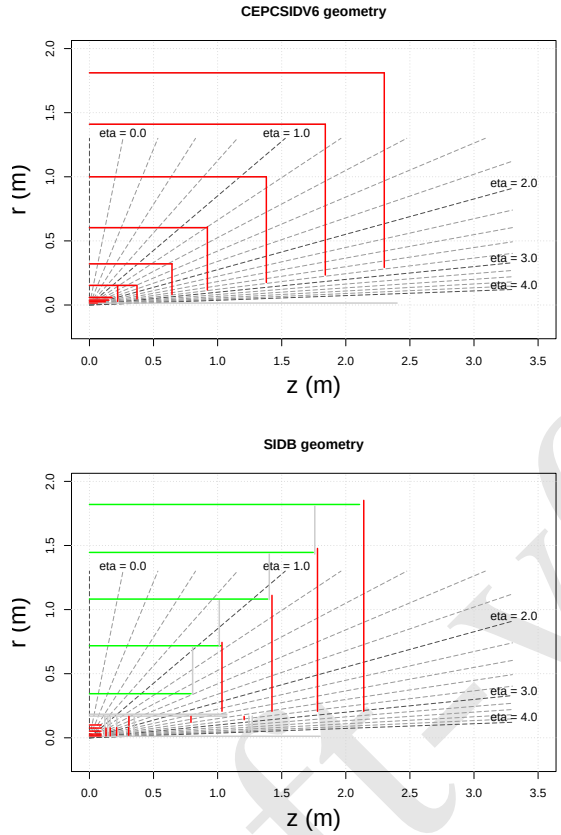

Figure 4.25: The R-Z view of the full silicon tracker proposed for CEPC (left) and the enlarged version of SID design (right).

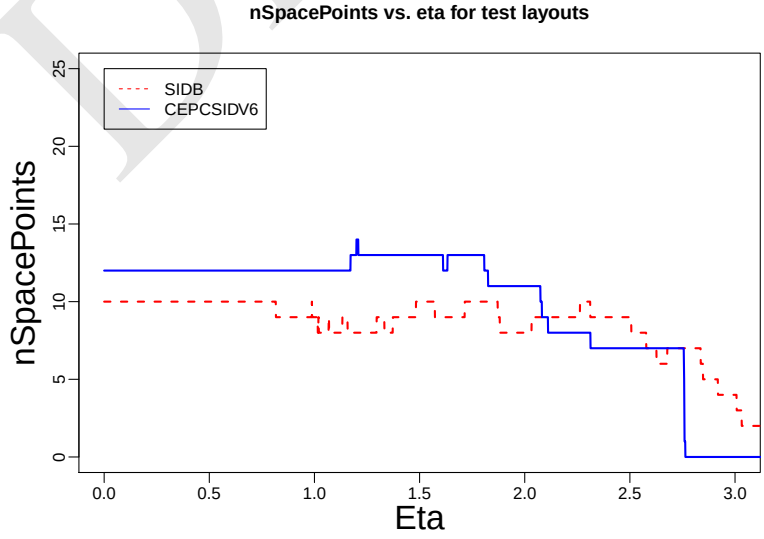

Figure 4.26: The number of expected hits are shown as function of track pesuro-rapadity.

Draft v0.2

	CEPC-SID				SIDB			
Barrel	R (m)		±z (m)	Type	R (m)		±z (m)	Type
layer 0	0.153		0.368	D	0.344		0.793	S
layer 1	0.321		0.644	D	0.718		1.029	S
layer 2	0.603		0.920	D	1.082		1.391	S
layer 3	1.000		1.380	D	1.446		1.746	S
layer 4	1.410		1.840	D	1.820		2.107	S
layer 5	1.811		2.300	D				
Endcap	R_{in} (m)	R_{out} (m)	±z (m)	Type	R_{in} (m)	R_{out} (m)	±z (m)	Type
Disk 0	0.082	0.321	0.644	D	0.207	0.744	1.034	D
Disk 1	0.117	0.610	0.920	D	0.207	1.111	1.424	D
Disk 2	0.176	1.000	1.380	D	0.207	1.477	1.779	D
Disk 3	0.234	1.410	1.840	D	0.207	1.852	2.140	D
Disk 4	0.293	1.811	2.300	D				

Table 4.6: The proposed geometry parameters for the outer strip barrel layers and disks, where D and S stand for double and single-strip layer.

dead material such as readout, cables and supports, is about 5-7% for CEPC-SID and 7-10% for SIDB, respectively.

The expected momentum (p_T) and impact parameters (d0, and z0) resolutions are compared as function of track p_T in GeV/c for tracks with $\theta = 85$ and 20 degree, respectively, as shown in Fig. 4.27. The z0 resolution is better for CEPC-SID than for SIDB due to extra stereo-strip layers while the p_T and d0 resolutions are similar.

4.4.3 Detector simulation and reconstruction

In order to optimize the full silicon tracker detector for CEPC, we generate several benchmark processes that include single muon events, $e^+e^- \to ZH \to \nu\nu\mu\mu$, and $e^+e^- \to ZH \to \nu\nu GG$ (two gluon jets). The events are then simulated and reconstructed using different detector geometries, which are then used for the tracking performance studies.

4.4.3.1 CEPC-SID detector

The implement of geometry of full-silicon-tracker is based on a simulation tool Mokka[53]. The CEPC group have create a version of database cepc_v4 to build the preliminary design of CEPC detector [28], in which the tracker is composed of VXD, SIT, TPC, SET and FTD. In order to implement the full-silicon-tracker, the TPC is considered to be replaced with a new silicon-based strip tracker. Similarly, the new silicon tracker is also called as SIT, and the SET is removed at the same time, since the type of the old SIT, the new silicon-based strip tracker and the SET are based on the same design. Finally, a full-silicon-tracker including VXD, SIT and FTD is built on the basis of cepc_v4, as described above.

Draft-v0.2

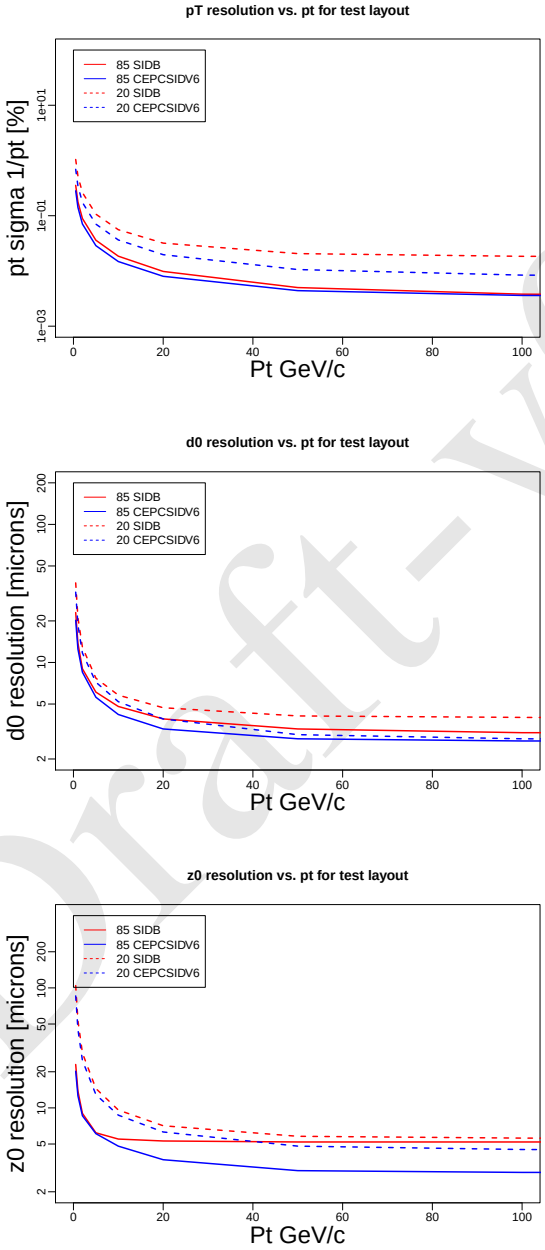

Figure 4.27: The expected p_T, d0, and z0 resolutions from the toy simulation (Idres) are compared as function of track p_T in GeV/c for tracks with $\theta = 85$ and 20 degree, respectively.

Draft-v0.2

In order to improve the flexibility of design, a new package of SiTracker is implemented in Mokka which represents the silicon tracker by planar structure, which consists of a. thin layer of silicon with 150 μm thickness and 50 μm pitch size. For VXD and SIT, they are composed by several layers, and each layer is composed by several ladders, and each ladder is divided to several sensors. The SIT layer consist of double silicon layers mounted back to back with a stereo-angle of 7 degree. For FTD, it is composed by several pixel disks FTD_PIXEL and several double-side strip disks FTD_STRIP that are composed by petals. The strip FTD disk has two sensitive silicon sub-layers on each side with a stereo-angle of 5 degree. The number of ladders/petals, the size and position of layers, and the sub-structure of layers can be modified easily in input file as globalModelParameter. In future, a XML structure is considered as the method to input parameters.

The lcio format is used to output the simulated signals from the full-silicon-tracker, same as other sub-detector system [54]. The digitization and clustering are done in reconstruction process. In the default version, a smearing technology based on truth information is used as a simple digitization and clustering, which is used for this study. Recently, a new digitization for silicon-based detector has been developed. It first finds out the pixel which the hit is located, and uses the center of the pixel or strip as the new position for the hit. And then those hits in same pixel or neighboring will be merged into single hit.

The silicon tracking algorithm is the same one used by CEPC-ILD [**?**], which are steered by a set of strategies. Each strategy represents a set of layers in the detector and tries to find combinations of hits that forms a helix within these layers. The algorithm starts by looking for a track seed by any combination of three hits that fulfils a helix fit. Once found, the track seed is extended by successively adding more hits that are consistent with the extrapolation of the seed helix. If fewer than the minimum required number of hits are found, the track candidate is discarded. If the tracks found in different strategies share more than one hit, only the track with the best fit is kept based on the χ^2 per degree of freedom and the number of hits on the track.

4.4.3.2 Optimized SID detector

For the SiD detector optimized for CEPC (or SIDB), events were simulated and reconstructed using a software developed for the International Linear Collider (ILC) [38, 50], but re-worked for the HepSim project [55, 56]. The response of the SiD detector to physics events is simulated using the "Simulator for the Linear Collider" (SLIC) 5.0 software [57] interfaced with the GEANT4 10.3p1 program [58]. The track reconstruction was performed with the LCSIM 4.0 package [54] using the "seed tracker" algorithm as for the SiD detector simulation. Track candidates with at least six hits in the silicon pixel and microstrip layers were considered. Only tracks with a minimum transverse momentum (p_T) of 100 MeV were accepted. The track-fitting was performed with the following requirements; maximum distance of closest approach (DCA) is $|DCA| < 6$ mm, $|z_0| < 10$ mm, and fit $\chi^2 < 10$. The reconstruction includes particle-flow algorithms (PFA) which enable identification and reconstruction of individual particles. The PFA objects can be reconstructed using the software algorithms implemented in the PANDORA package [59, 60].

The geometry of SIDB detector is implemented using the compact XML geometry description, which can load and built at runtime. The main changes over the ILC-SID detector include the reduced B-field from 5 Tesla to 3 Tesla. The outer tracker is scaled up by a factor of about 1.44 to the radius of 1.83 m and z of $\pm$ 2.3 m. The silicon module sizes were appropriately scaled. The first inner layer of the barrel vertex detector was

Draft-v0.2

positioned at 15 mm, just outside of the beam pipe. The outer barrel layer of the silicon vertex detector was moved to 100.3 mm (vs 59 mm for the SiD detector), while other barrel layers are equally spaced. The forward disks, together with the support structures, were appropriately scaled in z by a factor 1.37.

As for the SiD detector, the barrel tracker consists of five layers of silicon sensors with 50 μm pitch. The forward tracker has four disks of silicon sensors. The silicon pixel detector had 20 μm pitch, consisting of five layers in the barrel and six disks in the forward region. The hadronic and electromagnetic calorimeters, as well as the muon detector, were optimized for CEPC physics as described in [61].

4.4.4 Tracking performance

After the detector simulation and reconstruction, the tracking performances are measured in terms of efficiencies, fake rates, momentum resolution, and the impact parameter resolutions using single muons or $e^+e^- \rightarrow ZH$ events. The tracking efficiency is defined as a fraction of stable charged particles that can be matched to well reconstructed tracks. The stable particles are defined as those charged particles with p_T >1 GeV/c in the detector fiducial region ($9 < \theta < 170$ degree), originated from the interaction point, and lived long enough to reach the calorimeter. A well reconstructed track is defined as sharing more than 50% of its assigned silicon hits originating from a single particle (truth hits). We define a truth hit fraction as ratio of truth hits over total assigned hits of the track using silicon hits only. A poorly reconstructed track is defined to have the truth hit fraction less than 50%. The fake rate is defined as the fraction of poorly reconstructed tracks out of total reconstructed tracks, but this requires a realistic detector simulation, which we are not there yet. The tracking performance in the CEPC (v_4) detector is also shown as the reference.

4.4.4.1 Single muon particle

Figure 4.28 shows the tracking efficiency for single muons in CEPC-SID as function of p_T. The tracking efficiency is close to 100% at high p_T and slightly lower at small p_T. The trend is the same for CEPC v_4 , which indicate both trackers are capable of finding tracks efficiently in the detector fiducial region.

The number of silicon hits found on the track and the fraction of truth hits are shown in Fig. 4.29 where the hit purity is reached more than 90% for both detectors.

Since the track resolution depends on the track angle θ, we divide the tracks in the barrel region with $40 < \theta < 140$ degree and in the endcap region with $7.25 < \theta < 40$ degree or $140 < \theta < 172.75$ degree. Figure 4.30 shows the track resolutions of p_T, d0, and z0 as function of track p_T in the barrel and endcap region. The resolutions for the low momentum tracks seem slightly better in the CEPC v_4 detector (TPC+Silicon) than an alternative full silicon tracker due to extra materia in the detector while they are compatible at the high p_T. The resolutions from the SIDB detector are also included in the comparision, which has a compatible momentum resolution while the d0 and z0 are slightly worse.

4.4.4.2 Di-muon mass resolution

Figure 4.31 shows the di-muon invariant mass distributions from $ZH \rightarrow \nu\nu\mu\mu$ decay between different detector configurations. The higgs mass used in CEPC simulation is 125

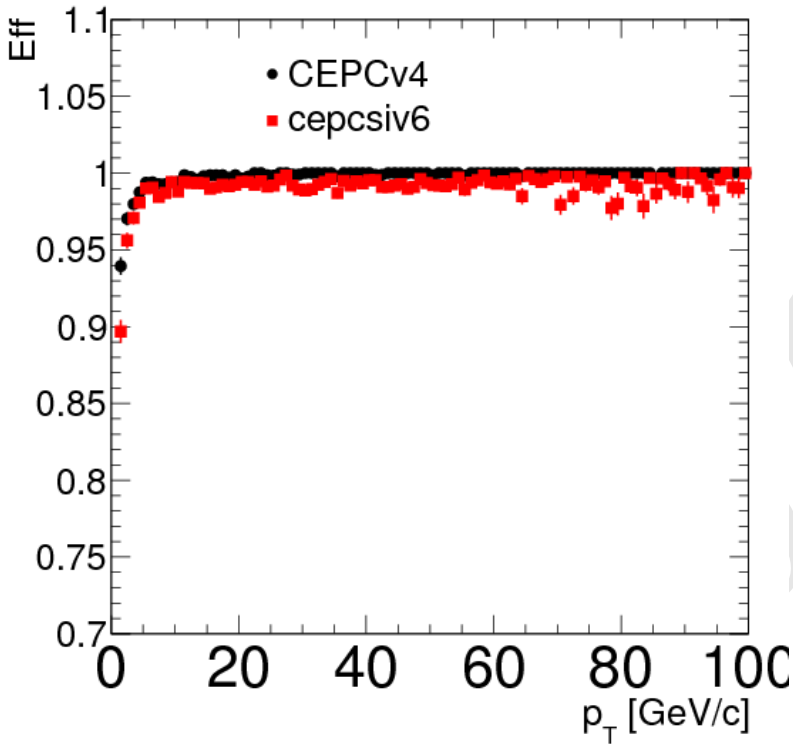

Figure 4.28: The tracking efficiencies are measured as function of p_T for single muons using CEPC v_4 and CEPC-SID detetcors.

GeV/c^2 while 125.09 GeV is used in the SIDB simulation. The di-mass from CEPC-ILD seems shifted by 0.2 GeV from the input Higgs mass of 125 GeV/c^2 while other masses from CEPC-SID and SIDB agree with the expectation. The di-muon mass resolution from CEPC-SID has $\sigma = 0.21$ GeV/c^2 and seems 20% and 25% better than ones obtained from CEPC-ILD and SIDB, respectively.

4.4.4.3 Tracking inside the jets

In order to study the tracking performance inside the jets, we generated and simulated some Higgs decaying into two gluon jets (GG) in $zH \rightarrow \nu\nu GG$ events. Figure 4.32 shows the tracking efficiency inside the jets as function of track momentum. The average efficiency of finding tracks inside the jets is about 90% for CEPC-SID while about 97% for CEPC-ILD due to the excellent tracking in TPC. The full silicon tracking inside the dense of jets is not fully optimized in dealing with outliers in the fit, which requires a realistic detector simulation and clustering. The work is in progress to improve the tracking inside the jets.

4.4.5 Conclusion

We present a preliminary study of full silicon tracker option as an alternative design for CEPC tracking. Two approaches are considered for the design: the first is to keep the silicon detectors (VXD, SIT, FTD) in the CEPC-ILD detector and replacing TPC with additional silicon detectors, the second is to optimize the ILC-SID tracker to fulfil the CEPC tracking volume in order to achive the excellent momentum resolution using 3

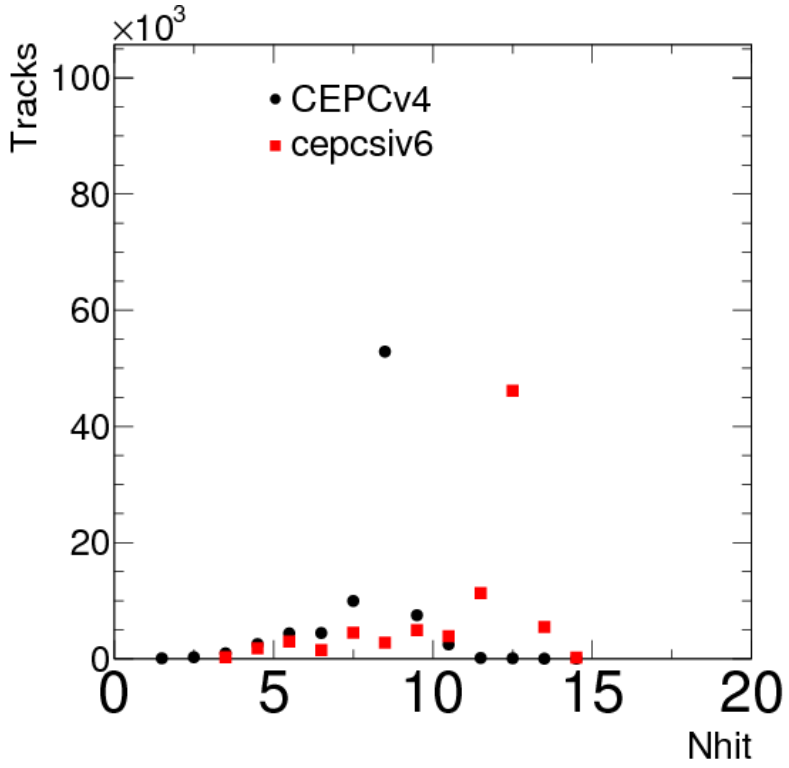

Figure 4.29: The distributions are shown for the number of silicon hits on the track (left) and the hit purity on (right).

Tesla B field. The new detector geometry has been implemented in the simulation and the track reconstruction has also been adoped for the full silicon tracker. The initial study of the tracking performance looks promising. There are still many improvements needed in the simulation and reconstruction in order to explore the full potential of the full-silicon tracker.

4.5 Drift chamber tracker detector

4.5.1 Introduction

The drift chamber (DCH) is designed to provide good tracking, high precision momentum measurement and excellent particle identification by cluster counting. The requirements imposed to the tracking system are high efficiency and state of the art momentum and angular resolutions for charged particles, respectively of the order of $\sigma(1/p_t) \approx 3 \times 10^{-5}\, GeV/c^{-1}$ and $\sigma(\theta, \phi) \approx 0.1\, mrad$ for 45 GeV muons.

Main peculiarity of this drift chamber is its high transparency, in terms of radiation lengths, obtained thanks to the novel approach adopted for the wiring and assembly procedures. The total amount of material in radial direction, towards the barrel calorimeter, is of the order of $1.6\%\, X_0$, whereas, in the forward and backward directions, the total amount of material is equivalent to about $5.0\%\, X_0$, including the front end electronics instrumented endplates.

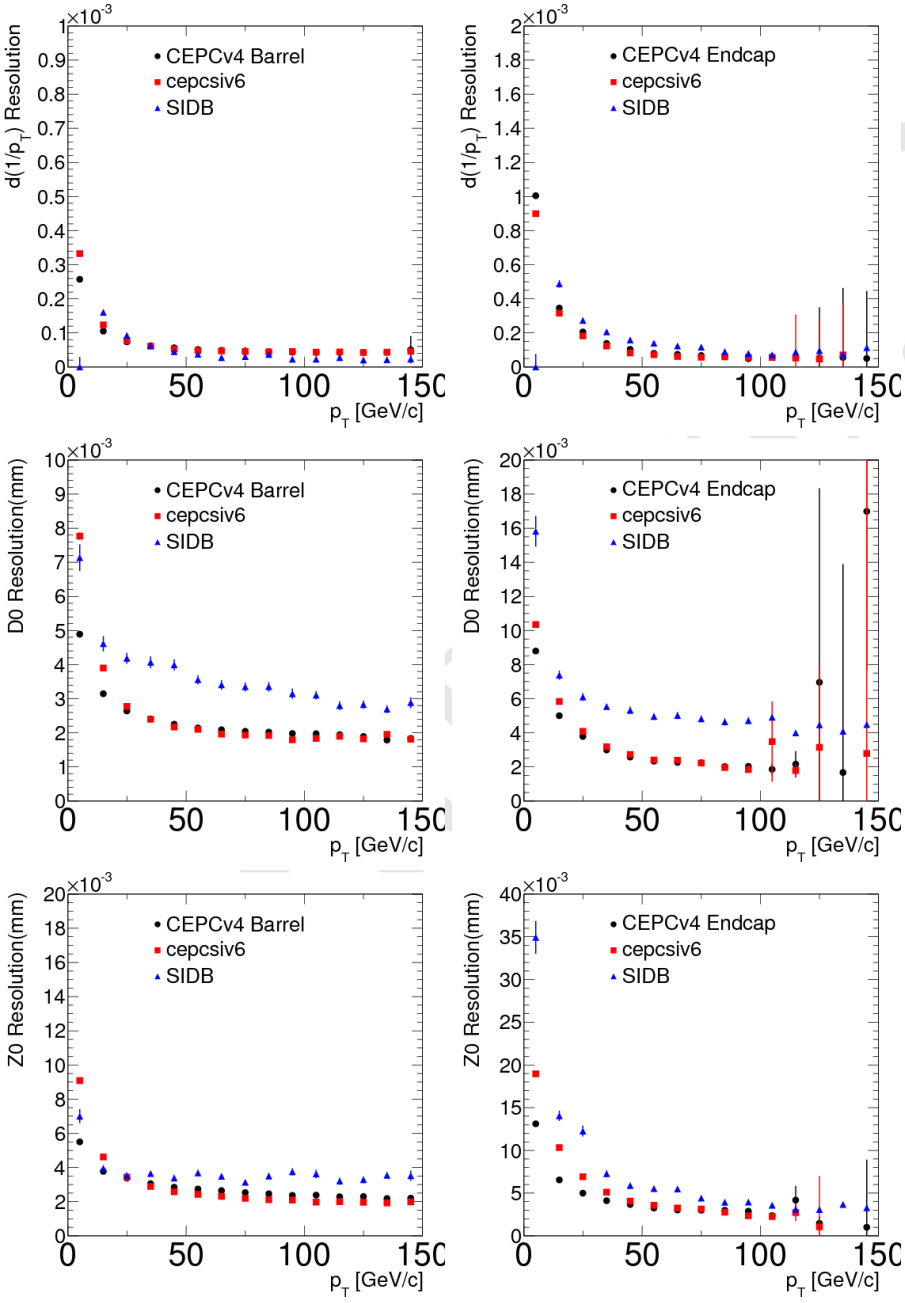

Figure 4.30: The tracking p_T, d0, and z0 resolutions are measured as function of p_T, ϕ, and θ using single muons, left in the barrel region and right in the endcap region. They are compared between CEPC v_4 and two full silicon detector concepts.

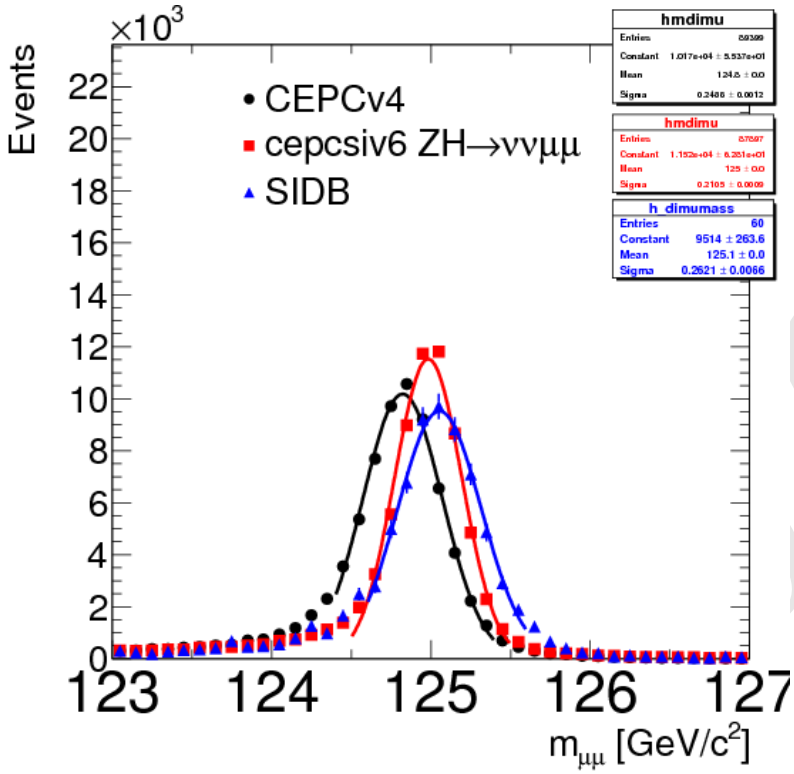

Figure 4.31: The di-muon mass distribution is compared from different detectors.

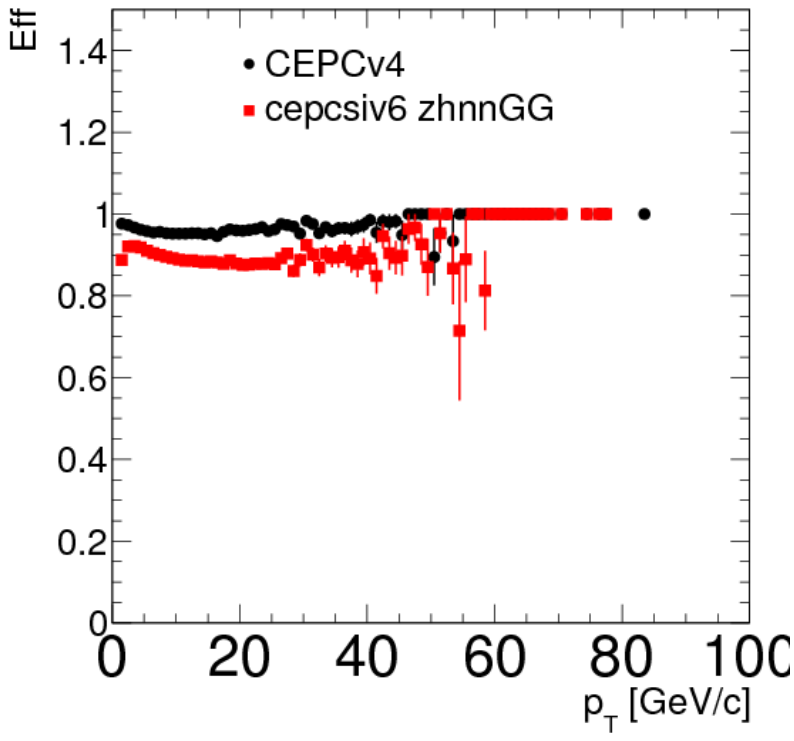

Figure 4.32: The tracking efficiencies for the stable particles inside the gluon jets as function of track p_T with CEPC v_4 and CEPCSID.

Original ancestor of the DCH design is the drift chamber of the KLOE experiment[62], more recently culminated in the realisation of the MEG2[63] drift chamber.

4.5.2 Overview

The DCH is a unique volume, high granularity, all stereo, low mass cylindrical drift chamber, co-axial to the 2 T solenoid field. It extends from an inner radius R_{in} = 0.35 m to an outer radius R_{out} = 2 m, for a length L = 4 m and consists of 112 co-axial layers, at alternating sign stereo angles (in the range from $50\,mrad$ to $250\,mrad$), arranged in 24 identical azimuthal sectors. The square cell size (5 field wires per sense wire) varies between 12.0 and 14.5 mm for a total of 56,448 drift cells. Thanks to the peculiar design of the wiring procedures, successfully applied to the recent construction of the MEG2 drift chamber, such a large number of wires poses no particular concern.

A system of tie-rods directs the wire tension stress to the outer endplate rim, where a cylindrical carbon fibre support structure bearing the total load is attached. Two thin carbon fibre domes, suitably shaped to minimise the stress on the inner cylinder and free to deform under the gas pressure without affecting the wire tension, enclose the gas volume.

The angular coverage, for infinite momentum tracks originated at the interaction point and efficiently reconstructed in space, extends down to approximately 13°.

In order to facilitate track finding, the sense wires are read out from both ends to allow for charge division and time propagation difference measurements.

The chamber is operated with a very light gas mixture, $90\%He - 10\%iC_4H_{10}$, corresponding to less than $400\,ns$ maximum drift time for the largest cell size. The number of ionisation clusters generated by a $m.i.p.$ in this gas mixture is about $12.5\,cm^{-1}$, allowing for the exploitation of the cluster counting/timing techniques for improving both spatial resolution ($\sigma_x < 100\,\mu m$) and particle identification ($\sigma(dN_{cluster}/dx)/(dN_{cluster}/dx) \approx 2\%$).

4.5.3 Expected performance

Figure 4.33 indicates a $100\,\mu m$ drift distance resolution, averaged over all drift times, measured in a MEG2 drift chamber prototype[64] ($7\,mm$ cell size), with very similar electrostatic configuration and gas mixture. A better resolution is expected for DCH, because of the longer drift distances. Cluster timing technique may further improve it. Analytical calculations for the expected momentum, transverse momentum and angular distributions are plotted in Figure 4.34.

Based on the assumption that one can, in principle, reach a relative resolution on the measurement of the number of primary ionisation clusters, N_{cl}, proportional to $1/\sqrt{N_{cl}}$, the expected performance relative to particle separation in number of units of standard deviations is presented in Figure 4.35 as a function of the particle momentum. Solid curves refer to cluster counting technique applied to a $2\,m$ track length with 80% cluster identification efficiency and negligible (a few percent) fake clusters contamination. Dashed curves refer to the best theoretical prediction attainable with the dE/dx technique for the same track length and same number of samples. For the whole range of momenta, particle separation with cluster counting outperforms dE/dx technique by more than a factor of two, estimating an expected pion/kaon separation better than three standard deviations for all momenta below $850\,MeV/c$ and slightly above $1.0\,GeV/c$.

Draft-v0.2

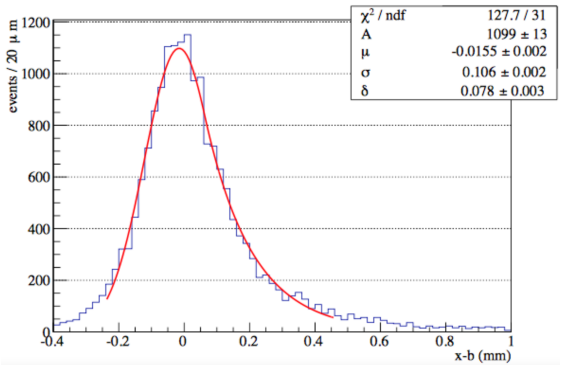

Figure 4.33: Measured drift distance residue distribution in the MEG2 drift chamber prototype under cosmic rays. $85\%\, He - 15\%\, iC_4H_{10}$ gas mixture.

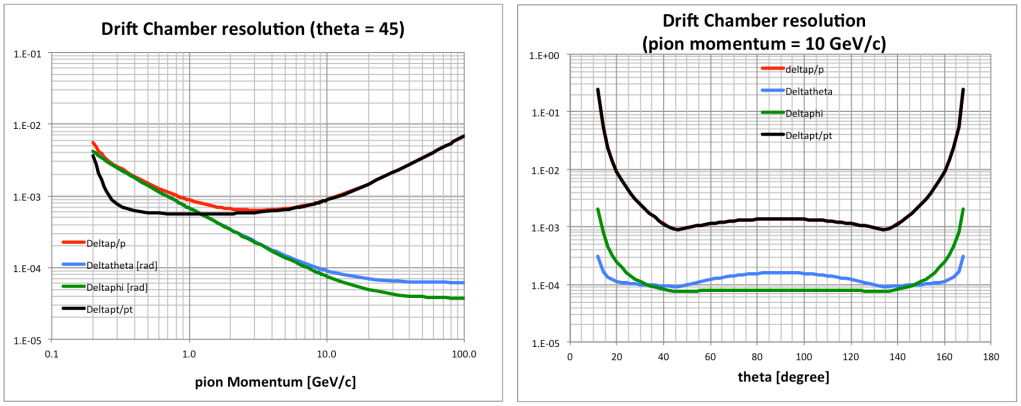

Figure 4.34: Momenta and angular resolutions as a function of the particle momentum for $\theta = 45°$ (left) and of the polar angle for $p = 10\, GeV/c$ (right)

4.5.4 Tracking system simulation results

For the purpose of optimising the track reconstruction performance, a seven layer cylindrical vertex detector and a two layer pre-shower counter, with $20\,\mu m$ pixel size, have been simulated, respectively, inside and outside the cylindrical drift chamber, together with a detailed geometrical description within a homogeneous $2\,T$ longitudinal magnetic field. Details of ionisation clustering for cluster counting/timing analysis have not been included in the simulations, limiting the drift chamber performance both in spatial resolution (a $100\,\mu m$ gaussian smeared point resolution has been assumed) and in particle separation (no dN_{cl}/dx analysis has been simulated). A simplified track finding algorithm at its preliminary stage of development has been used to feed the space points to the GenFit2 interface for the ultimate track fit. Figure 4.36 shows the momentum, angular and impact parameter resolutions obtained by the tracking system simulation. No optimisation has been tried yet. Momentum resolutions $\Delta p/p = 4 \times 10^{-3}$ at $p = 100\, GeV/c$, for $\theta = 65°$, and angular resolutions $\leq 0.1\, mrad$ for $p \geq 10\, GeV/c$, are within reach. Lastly,

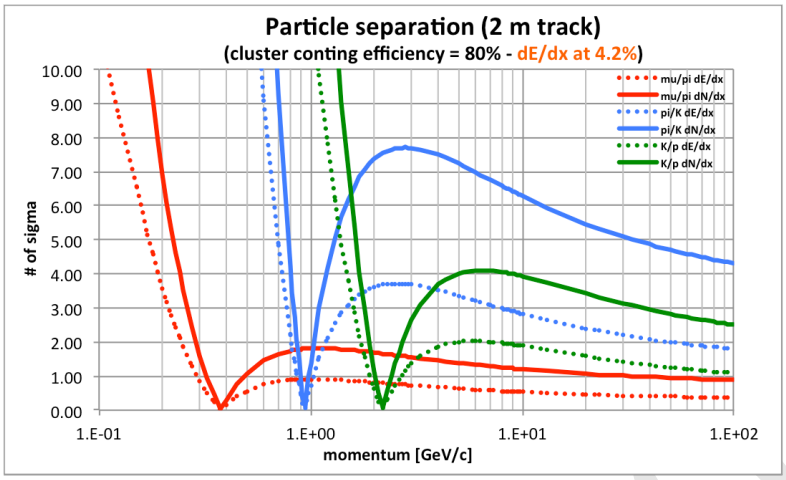

Figure 4.35: Particle type separation in units of standard deviations as a function of the particle momentum.

a fit to the bottom right plot in Figure 4.36 gives a d_0 impact parameter resolution:

$$\sigma_{d_0} = a \oplus \frac{b}{p \sin^{3/2} \theta}$$

with $a = 3\mu m$ and $b = 15\mu m \cdot GeV/c$.

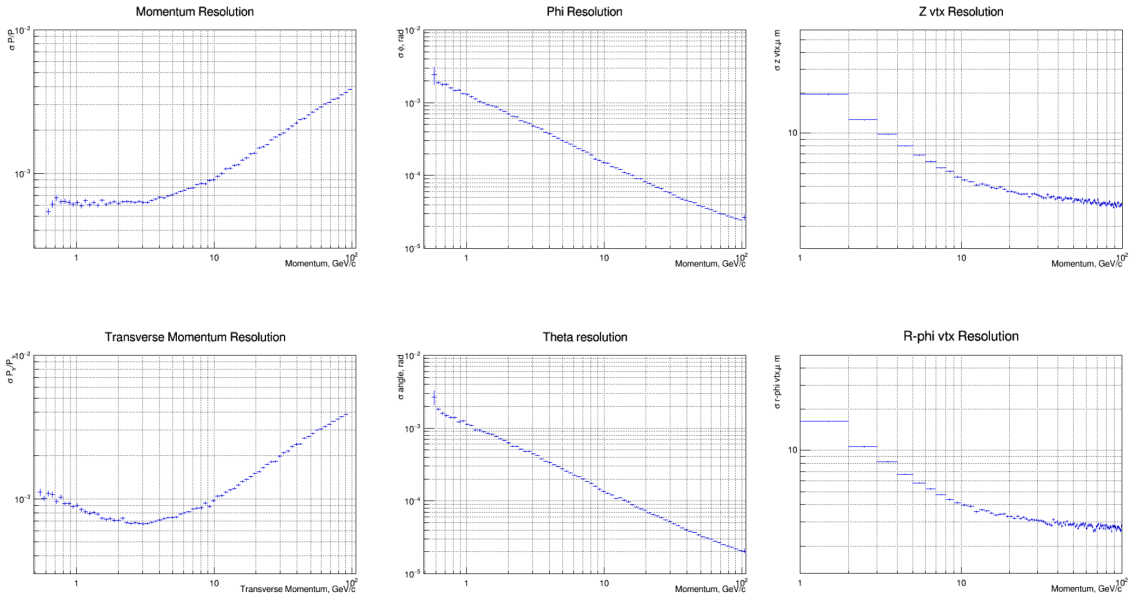

Figure 4.36: Momentum resolutions (top and bottom left), angular resolutions (top and bottom center) and impact parameter resolutions (top and bottom right) from simulation of isolated tracks.

References

[1] H. Abramowicz et al., *The International Linear Collider Technical Design Report - Volume 4: Detectors*, arXiv:1306.6329 [physics.ins-det].

[2] P. M. De Freitas and H. Videau, *Detector simulation with MOKKA/GEANT4: Present and future*, in *International Workshop on Linear Colliders (LCWS 2002), Jeju Island, Korea*, pp. 26–30. 2002.

[3] D. Dannheim and M. Vos, *Simulation studies for the layout of the vertex and tracking regions of the CLIC detectors*, , CERN, Apr, 2012. https://cds.cern.ch/record/1443503.

[4] M. Regler, M. Valentan, and R. Frühwirth, *The LiC detector toy program*, Nuclear Instruments and Methods in Physics Research Section A:Accelerators,Spectrometers,Detectors and Associated Equipment **581** (2007) no. 1, 553–556.

[5] A. Andreazza, G. Barker, V. Chabaud, P. Collins, H. Dijkstra, Y. Dufour, M. Elsing, F. Ledroit, C. Eklund, R. Orava, et al., *The DELPHI Silicon Tracker at LEP2*, .

[6] F. Hartmann, *The DELPHI Microvertex Detector at LEP*, in *Evolution of Silicon Sensor Technology in Particle Physics*, pp. 1–20. Springer, 2009.

[7] M. Battaglia, C. Da Viá, D. Bortoletto, R. Brenner, M. Campbell, P. Collins, G. Dalla Betta, M. Demarteau, P. Denes, H. Graafsma, et al., *R&D paths of pixel detectors for vertex tracking and radiation imaging*, Nuclear Instruments and Methods in Physics Research Section A:Accelerators,Spectrometers,Detectors and Associated Equipment **716** (2013) 29–45.

[8] L. Linssen, A. Miyamoto, M. Stanitzki, and H. Weerts, *Physics and detectors at CLIC: CLIC conceptual design report*, arXiv preprint arXiv:1202.5940 (2012) .

[9] G. Contin, E. Anderssen, L. Greiner, J. Schambach, J. Silber, T. Stezelberger, X. Sun, M. Szelezniak, C. Vu, H. Wieman, et al., *The MAPS based PXL vertex detector for the STAR experiment*, Journal of Instrumentation **10** (2015) no. 03, C03026.

[10] C. Lacasta, *The DEPFET pixel detector for the Belle II experiment at SuperKEKB*, PoS (2014) 005.

[11] B. Abelev, J. Adam, D. Adamova, M. Aggarwal, G. A. Rinella, M. Agnello, A. Agostinelli, N. Agrawal, Z. Ahammed, N. Ahmad, et al., *Technical design report for the upgrade of the ALICE inner tracking system*, Journal of Physics G: Nuclear and Particle Physics **41** (2014) no. 8, .

[12] I. Valin, C. Hu-Guo, J. Baudot, G. Bertolone, A. Besson, C. Colledani, G. Claus, A. Dorokhov, G. DoziÃĺre, W. Dulinski, M. Gelin, M. Goffe, A. Himmi, K. Jaaskelainen, F. Morel, H. Pham, C. Santos, S. Senyukov, M. Specht, G. Voutsinas, J. Wang, and M. Winter, *A reticle size CMOS pixel sensor dedicated to the STAR HFT*, Journal of Instrumentation **7** (2012) no. 01, C01102. http://stacks.iop.org/1748-0221/7/i=01/a=C01102.

Draft-v0.2

[13] G. A. Rinella, *The ALPIDE pixel sensor chip for the upgrade of the ALICE Inner Tracking System*, Nuclear Instruments and Methods in Physics Research Section A: Accelerators, Spectrometers, Detectors and Associated Equipment **845** (2017) 583 – 587. http://www.sciencedirect.com/science/article/pii/S0168900216303825. Proceedings of the Vienna Conference on Instrumentation 2016.

[14] Y. Lu, Q. Ouyang, Y. Arai, Y. Liu, Z. Wu, and Y. Zhou, *First results of a Double-SOI pixel chip for X-ray imaging*, Nuclear Instruments and Methods in Physics Research Section A: Accelerators, Spectrometers, Detectors and Associated Equipment **831** (2016) 44 – 48. http://www.sciencedirect.com/science/article/pii/S0168900216301851. Proceedings of the 10th International âĂIJHiroshimaâĂİ Symposium on the Development and Application of Semiconductor Tracking Detectors.

[15] I. Kurachi, K. Kobayashi, M. Mochizuki, M. Okihara, H. Kasai, T. Hatsui, K. Hara, T. Miyoshi, and Y. Arai, *Tradeoff Between Low-Power Operation and Radiation Hardness of Fully Depleted SOI pMOSFET by Changing LDD Conditions*, IEEE Transactions on Electron Devices **63** (2016) no. 6, 2293–2298.

[16] Z. Wu, *A prototype SOI pixel sensor for CEPC vertex*, https://indico.cern.ch/event/577879/contributions/2741627/attachments/1575067/2486910/A_prototype_SOI_pixel_sensor_for_CEPC_vertex.pdf.

[17] S. Ono, M. Togawa, R. Tsuji, T. Mori, M. Yamada, Y. Arai, T. Tsuboyama, and K. Hanagaki, *Development of a pixel sensor with fine space-time resolution based on SOI technology for the ILC vertex detector*, Nuclear Instruments and Methods in Physics Research Section A: Accelerators, Spectrometers, Detectors and Associated Equipment **845** (2017) 139 – 142. http://www.sciencedirect.com/science/article/pii/S0168900216303783. Proceedings of the Vienna Conference on Instrumentation 2016.

[18] M. Idzik, *SOI-Cracow*, https://agenda.linearcollider.org/event/7450/contributions/38595/attachments/31561/47538/2017_LCVertex_Idzik.pdf.

[19] S. Spannagel, *Silicon technologies for the CLIC vertex detector*, Journal of Instrumentation **12** (2017) no. 06, C06006. http://stacks.iop.org/1748-0221/12/i=06/a=C06006.

[20] H. Wieman, E. Anderssen, L. Greiner, H. Matis, H. Ritter, X. Sun, and M. Szelezniak, *STAR PIXEL detector mechanical design*, Journal of Instrumentation **4** (2009) no. 05, P05015.

[21] Belle-II Collaboration, T. Abe et al., *Belle II Technical Design Report*, arXiv:1011.0352 [physics.ins-det].

[22] Y. Zhang, H. Zhu, L. Zhang, and M. Fu, *Charge collection and non-ionizing radiation tolerance of CMOS pixel sensors using a 0.18Îijm CMOS process*, Nuclear Instruments and Methods in Physics Research Section A: Accelerators,

Draft v0.2

Spectrometers, Detectors and Associated Equipment **831** (2016) 99 – 104. http://www.sciencedirect.com/science/article/pii/S0168900216300481. Proceedings of the 10th International âĂIJHiroshimaâĂİ Symposium on the Development and Application of Semiconductor Tracking Detectors.

[23] Y. Zhou, *Development of highly compact digital pixels for the vertex detector of the future e+e- collider*, https://indico.cern.ch/event/577879/contributions/2740073/.

[24] Y. Zhang, *A Monolithic Active Pixel Sensor prototype for the CEPC vertex detector*, https://indico.cern.ch/event/577879/contributions/2740125/attachments/1574470/2485730/P15_ZY_POSTER_Final.pdf.

[25] Y. Lu, *Study of SOI Pixel for the Vertex*, http://indico.ihep.ac.cn/event/6433/.

[26] M. Motoyoshi, T. Miyoshi, M. Ikebec, and Y. Arai, *3D integration technology for sensor application using less than 5Îijm-pitch gold cone-bump connpdfection*, Journal of Instrumentation **10** (2015) no. 03, C03004. http://stacks.iop.org/1748-0221/10/i=03/a=C03004.

[27] W. Snoeys, G. A. Rinella, H. Hillemanns, T. Kugathasan, M. Mager, L. Musa, P. Riedler, F. Reidt, J. V. Hoorne, A. Fenigstein, and T. Leitner, *A process modification for CMOS monolithic active pixel sensors for enhanced depletion, timing performance and radiation tolerance*, Nuclear Instruments and Methods in Physics Research Section A: Accelerators, Spectrometers, Detectors and Associated Equipment **871** (2017) 90 – 96. http://www.sciencedirect.com/science/article/pii/S016890021730791X.

[28] CEPC-SPPC Study Group, *CEPC-SPPC Preliminary Conceptual Design Report. Volume I - Physics & Detector*, .

[29] Particle Data Group Collaboration, C. Patrignani et al., *Review of Particle Physics*, Chin. Phys. **C40** (2016) no. 10, 100001.

[30] J. E. Augustin et al., *A silicon envelope for the TPC*, .

[31] A. Affolder et al., *DC-DC converters with reduced mass for trackers at the HL-LHC*, JINST **6** (2011) C11035.

[32] S. Diez, *System Implications of the Different Powering Distributions for the ATLAS Upgrade Strips Tracker*, Phys.Procedia **37** (2012) 960–969.

[33] K. Klein et al., *DC-DC conversion powering schemes for the CMS tracker at Super-LHC*, JINST **5** (2010) C07009.

[34] A. Nomerotski et al., *Evaporative CO2 cooling using microchannels etched in silicon for the future LHCb vertex detector*, JINST **8** (2013) P04004, arXiv:1211.1176 [physics.ins-det].

Draft v0.2

[35] The ATLAS Collaboration, A. Affolder, *Silicon Strip Detectors for the ATLAS HL-LHC Upgrade*, Phys.Procedia **37** (2012) 915–922.

[36] V. Blobel, *Software alignment for tracking detectors*, Nucl.Instrum.Meth. **A566** (2006) 5–13.

[37] T. Abe et al., *The International Large Detector: Letter of Intent*, arXiv:1006.3396 [hep-ex].

[38] H. Abramowicz et al., *The International Linear Collider Technical Design Report - Volume 4: Detectors* , 2013. arXiv:1306.6329 [physics.ins-det].

[39] A. Savoy-Navarro, *Large Area Silicon Tracking: New Perspectives*, arXiv:1203.0736 [physics.ins-det].

[40] *CEPC project website*, http://cepc.ihep.ac.cn.

[41] I. Garzia et al., *GEM detector performance with innovative micro-TPC readout in high magnetic field*, EPJ Web Conf. **170** (2018) 01009.

[42] B. Mauss, T. Roger, J. Pancin, S. Damoy, and G. F. Grinyer, *MICROMEGAS calibration for ACTAR TPC*, EPJ Web Conf. **174** (2018) 01010.

[43] F. Shen, S. Wang, C. Yang, and Q. Xu, *MWPC prototyping and testing for STAR inner TPC upgrade*, JINST **12** (2017) no. 06, C06008.

[44] ALICE Collaboration, D. Rohr, *Tracking performance in high multiplicities environment at ALICE*, in *5th Large Hadron Collider Physics Conference (LHCP 2017) Shanghai, China, May 15-20, 2017*. 2017. arXiv:1709.00618 [physics.ins-det]. https://inspirehep.net/record/1621494/files/arXiv:1709.00618.pdf.

[45] P. Bhattacharya, S. S. Sahoo, S. Biswas, B. Mohanty, N. Majumdar, and S. Mukhopadhyay, *Numerical Investigation on Electron and Ion Transmission of GEM-based Detectors*, EPJ Web Conf. **174** (2018) 06001.

[46] ALICE Collaboration, S. Biswas, *ALICE TPC upgrade for High-Rate operations*, PoS **ICPAQGP2015** (2017) 094, arXiv:1511.04988 [physics.ins-det].

[47] LCTPC Collaboration, D. Tsionou, *Studies on GEM modules for a Large Prototype TPC for the ILC*, Nucl. Instrum. Meth. **A845** (2017) 309–312.

[48] J. Huth and D. Nygren, *Feasibility Tests of a High Resolution Sampling Radial Drift Chamber*, Nucl. Instrum. Meth. **A241** (1985) 375.

[49] DarkSide Collaboration, P. Agnes et al., *Electroluminescence pulse shape and electron diffusion in liquid argon measured in a dual-phase TPC*, Submitted to: Nucl. Instrum. Meth. A (2018) , arXiv:1802.01427 [physics.ins-det].

[50] C. Adolphsen et al., *The International Linear Collider Technical Design Report - Volume 3. II: Accelerator Baseline Design* , 2013. arXiv:1306.6328 [physics.acc-ph].

Draft v0.2

[51] N. Calace and A. Salzburger, *ATLAS Tracking Detector Upgrade studies using the Fast Simulation Engine*, J. Phys.:Conf. Ser. **664** (2015) 072005.

[52] M. Regler et al., *The LiC Detector Toy program*, J. Phys.:Conf. Ser. **119** (2008) 032034.

[53] P. Mora de Freitas and H. Videau, *Detector simulation with Mokka/GEANT4: Present and future, LC-TOOL-2003-010, 623-627 (2002).*, (2002) .

[54] N. Graf and J. McCormick, *LCSIM: A detector response simulation toolkit*, in *2012 IEEE Nuclear Science Symposium and Medical Imaging Conference Record (NSS/MIC)*, p. 1016. Oct, 2012.

[55] S. V. Chekanov, *Public repository with Monte Carlo simulations for high-energy particle collision experiments*, PoS **ICHEP2016** (2016) 229, arXiv:1609.04455 [hep-ex].

[56] S. V. Chekanov, M. Beydler, A. V. Kotwal, L. Gray, S. Sen, N. V. Tran, S. S. Yu, and J. Zuzelski, *Initial performance studies of a general-purpose detector for multi-TeV physics at a 100 TeV pp collider*, JINST **12** (2017) no. 06, P06009, arXiv:1612.07291 [hep-ex].

[57] N. Graf and J. McCormick, *Simulator for the linear collider (SLIC): A tool for ILC detector simulations*, AIP Conf. Proc. **867** (2006) 503–512.

[58] J. Allison et al., *Recent developments in Geant4*, Nuclear Instruments and Methods in Physics Research A **835** (2016) 186.

[59] M. J. Charles, *PFA Performance for SiD*, in *Linear colliders. Proceedings, International Linear Collider Workshop, LCWS08, and International Linear Collider Meeting, ILC08, Chicago, USA, Novermber 16-20, 2008* . 2009. arXiv:0901.4670 [physics.data-an].

[60] J. S. Marshall and M. A. Thomson, *Pandora Particle Flow Algorithm*, in *Proceedings, International Conference on Calorimetry for the High Energy Frontier (CHEF 2013)*, pp. 305–315. 2013. arXiv:1308.4537 [physics.ins-det].

[61] S. V. Chekanov and M. Demarteau, *Conceptual Design Studies for a CEPC Detector*, Int. J. Mod. Phys. **A31** (2016) no. 33, 1644021, arXiv:1604.01994 [physics.ins-det].

[62] M. Adinolfi et al., *The tracking detector of the KLOE experiment*, Nucl. Instrum. Meth. **A488** (2002) 51–73.

[63] A. M. Baldini et al., *MEG Upgrade Proposal*, arXiv:1301.7225 [physics.ins-det].

[64] A. M. Baldini et al., *Single-hit resolution measurement with MEG II drift chamber prototypes*, arXiv:1605.07970 [physics.ins-det].

Draft v0.2

CHAPTER 5

CALORIMETRY

Draft-v0.2

5.1 Introduction to calorimeters

Calorimeters of the CEPC detector, including electromagnetic calorimeter (ECAL) and hadron calorimeter (HCAL), are employed for precise energy measurements of electron, photon, tau and hadronic jets. To fully exploit the physics potential about Higgs, W, Z and related SM processes, the jet energy resolution σ_E/E is required to reach 3%-4%, or $30\%/\sqrt{E}$ at energies below about 100 GeV. This resolution is about a factor of two smaller than the calorimeters used for the LEP detectors and currently operating calorimeters at the LHC. It significantly improves the separation of the W and Z bosons which decay into two jets, as shown in Figure 5.1. The basic requirements for ECAL and HCAL resolution are $16\%/\sqrt{E}$ and $50\%/\sqrt{E}$, respectively.

To achieve the required jet energy resolution, many R&D researches are carried out within the CALICE collaboration since 2000 [1]. The majority of these studies aim to develop extremely fine granularity and compact imaging calorimeters with several technology options shown in Figure 5.2. Imaging calorimeter is a rapidly developing novel particle detector which has excellent spatial resolution. It is capable to provide enormous position information of incident and showering particles, which makes it possible to reconstruct every single particle cluster. This is vital for Particle Flow Algorithm (PFA [2]) and help to significantly improve the energy resolution of hadrons. The basic idea of PFA is to distinguish charged ($\sim$65%) and neutral particles ($\sim$35%) inside the calorimeters. Charged particles measured in the inner tracker with high momentum resolution are matched to their energy depositions in the calorimeters. Energy depositions without matched inner tracks are considered to originate from neutral particles inside jets, among

By Copyright © 2018 HEP Community

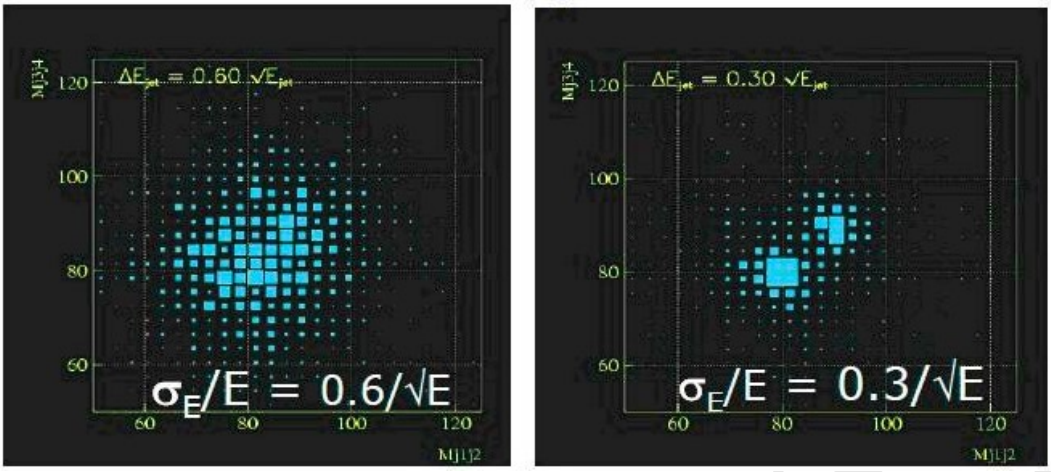

Figure 5.1: Separation of W and Z bosons with different jet energy resolutions.

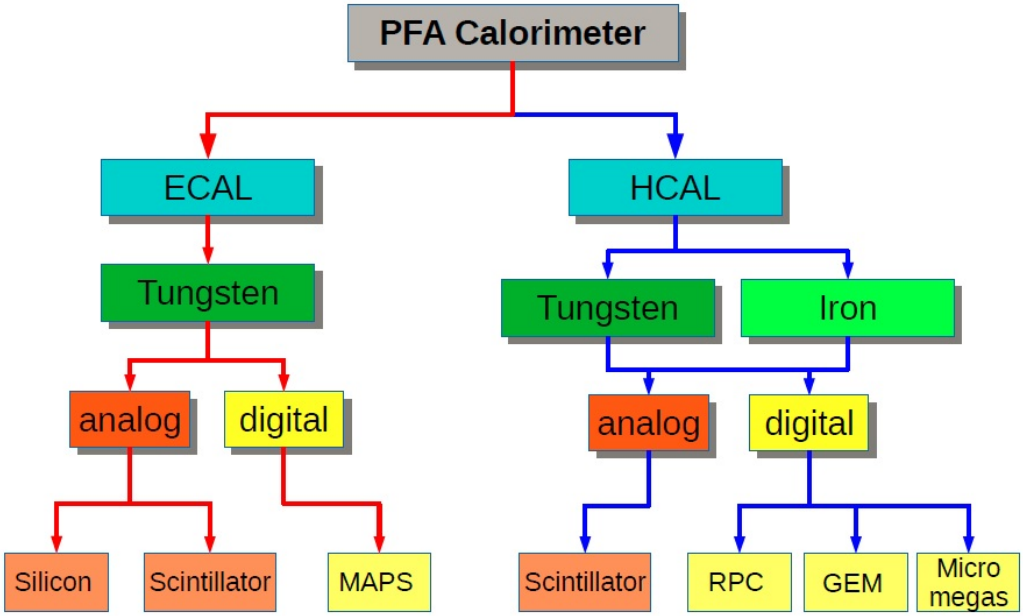

Figure 5.2: PFA: Imaging calorimeters being developed by the CALICE collaboration since 2000.

these neutral particles, about 25% of energy from photons are measured in the ECAL with good energy resolution, while the residual energy of merely 10% from neutral hadrons are measured by the calorimeters with poor energy resolution. Hence, the jet energy is determined by the charged track momenta of charged particles from inner tracker and energy depositions of neutral particles in the calorimeters. It has been demonstrated that significant improvement of the jet energy resolution is achievable based on MC simulations and test beam measurements. However, more efforts are needed to optimize the calorimeter design, to improve the PFA, and to develop the technologies for high granularity imaging calorimeters.

The calorimeter system includes two sub-detectors, an electromagnetic calorimeter (ECAL) which is optimized for the measurement of photons and electrons, and a hadronic

calorimeter (HCAL) which is employed to measure the energy deposit of the hadronic showers caused by the hadronic particles when they are absorbed in the HCAL detector. The two sub-detectors will be installed within the solenoid to minimize the inactive material in front of the calorimeters and to reliably associate tracks to energy deposits. The calorimeter system is divided into three parts, one cylindrical barrel and two end-caps.

The ECAL consists of layers of active sensors (such as silicon pads or pixels, or scintillator detector) interleaved with absorber tungsten plates. The digital HCAL (DHCAL) is expected to have stainless steel absorber plates with gaseous detectors such as glass Resistive Plate Chambers (gRPC) or GEM, or analog HCAL (AHCAL) using scintillator with SiPM readout as sensor. Both ECAL and HCAL are sampling detectors with very fine granularity and segmentations of electronic readout which is driven by excellent separations requirement between charged and neutral particles for the particle flow algorithms.

From Figure 5.2, there are more detector options with enormous worldwide R&D efforts ongoing within the CALICE collaboration.

An alternative approach for a combined, high-performance, electromagnetic and hadronic calorimeter aims at reaching even better resolutions by exploiting the dual-readout (DR) tecnique. Indeed the main limiting factor to the energy resolution in hadron calorimetry arises from the fluctuations of the electromagnetic component (f_{em}) that each hadronic shower develops as consequence of π^0 and η production. Since typically the detector response to the hadronic and em components is very different ($h/e \neq 1$), the reconstructed signal heavily depends on the actual value of f_{em}. By using two independent processes (namely scintillation and Čerenkov light production) that have a very different sensitivity to the hadronic and em components, it is possible to reconstruct f_{em}, event by event, and eliminate the effects of its fluctuations.

Among the possible DR implementations, a fibre-sampling DR calorimeter, based on either copper or lead as absorber material, looks the most suitable to provide the required performance in a cost-effective way. Preliminary results of Geant4 simulations point to possible resolutions better than 15% and around $30\% - 40\%$ (over $\sqrt{E}$), for electromagnetic and hadronic showers, respectively (see section 5.4.6).

Moreover, if the fibres are readout with SiPM, the high detector granularity and the possibility of longitudinal segmentation will make this solution easily compatible with Particle Flow Algorithms.

5.2 Electromagnetic Calorimeter for Particle Flow Approach

The particle flow paradigm has tremendous impact on the design of the electromagnetic calorimeter detector. Separating overlap showers from each other is principal requirement of the detector. A calorimeter used for particle flow thus needs to be able to do pattern recognition in the shower. The electromagnetic section has lots of tasks to fulfill. It should be able to select photons from close-by particles. It should be able to reconstruct the detailed properties of the shower, such as shower shape, starting point and energy distribution. It should be able to distinguish early starting electromagnetic showers from hadronic ones. The imaging capabilities of the calorimeter are more important than the intrinsic single particle energy resolution, although the latter is still important to the particle flow performance for electron, photons and jets. Due to the reason that about half of the hadronic showers will start development inside the electromagnetic calorimeter, a

Draft-v0.2

calorimeter with excellent three dimensional granularity is of utmost importance. In order to have the ability of separate close-by showers in the calorimeter, the detector with small Moliere radius is required. A large ratio between interaction length and radiation length of the detector is advantageous to the separation between electromagnetic and hadronic showers. A small radiation length will make the start of the electromagnetic shower earlier in the calorimeter, while a large interaction length will reduce the fraction of hadronic showers starting in the calorimeter. At the same time, the calorimeter with a compact structure is favorable.

In this section, we focus on two detector options for the ECAL, which consist of layers of active sensors (silicon pads or pixels, or scintillator detector) interleaved with absorber tungsten plates.

5.2.1 Silicon-Tungsten Sandwich Electromagnetic Calorimeter

5.2.1.1 Introduction

The study of the Higgs is not the only goal of a machine at 250 centre-of-mass energy. It can be generalised to the multi boson physics (Z, W and H). The best way to use the excellent luminosity foreseen at CEPC, consist to tag the boson through their mass in their decays into $q\bar{q}$ (2 jets). Taking into account the natural width of the Z and W, it has been shown that this goal required to achieve a jet energy resolution of $30\%/\sqrt{E_{\mathrm{Jet}}}$, thus a factor two better than the energy resolution achieved for a typical detector at LEP.

It has been shown [3] that a method consisting to fully reconstruct every single particle could reach this goal (Particle Flow Algorithm); it requires both a high performance tracker, typically achieving $\delta p/p$ of $10^5 p/GeV$ associated with high granularity calorimeters able to separate the contribution from individual particles down to the MIP level. As a typical jet is contains fractions in energy of 65%, 25% and 10% of charged particles, photons and neutral hadrons respectively, a moderate calorimetric resolution is then sufficient to achieve the goal. In this framework, the electromagnetic calorimeter (ECal), is first devoted to measure photon(s) and to a lesser extent electron(s) and to make a full pattern of the deposited energy of the hadron, i.e. shower of hadron interacting in the ECAL. To avoid "blind region", the entire calorimeter has to be put inside the super-conductive solenoid. The compactness is therefore an important criterion.

The design of the calorimeters have to take the following guidelines into account [4]:

- Optimisation of the number of calorimeter cells (cell size and number of layers)
- Choice of the absorber material in order to insure a high level of compactness and the infra-structural components such as cooling, power supplies, readout cables and the very front end electronics.

For the electromagnetic calorimeter these criteria has led to the choice of Tungsten with a radiation length of Xo=3.5mm, a Moli?re radius of RM=9mm and an interaction length of $\lambda_{\mathrm{I}} = 96mm$.

5.2.1.2 Silicon sensors

Among several sensor techniques, high resistivity silicon pin diodes offer several unique intrinsic advantages:

Draft v0.2

- stability: under a reasonable bias voltage, completely depleted pin-diode have a gain of one, and a signal response to MIP mostly defined by the thickness of the sensor, with a very low dependence on temperature, radiation, humidity, ...

- uniformity: for the same reason, the control of the thickness over large batches (typically to less than a percent) ensures a uniformity of response within a wafer and between them. The nonsensitive area between wafers has recently been reduced by the use of laser cutting, thinned guard-ring design [5], and would benefit from the use of larger ingot size (8" becoming the standard).

- flexibility: the dimension and geometry of the cells are defined by the readout pad on the PCB.

- High Signal-to-Noise ratio: with $\simeq 80$ electron-hole pairs created by linear mm of MIP track, MIPs tracks can easily be traced in the calorimeters, which is critical for the god performance of

The only real drawback of Silicon sensors remaining is their price, to be expected around $2 - 3\$/cm^2$.

By associating of Silicon sensors with Tungsten absorbers and Carbon Fibre structures, the SiW-ECAL offers an excellent option for PFA optimised calorimetry.

5.2.1.3 Constraints

High granularity calorimetry, and ECal especially, is technically challenging: the very number of channels calls for an embedded readout and zero suppression, to limits the amount of connections; in turn embedded readout power consumption should be as limited as possible to avoid large cooling systems which would degrade the capacity of the calorimeter. In the best case the cooling should stay passive at the heart of the calorimeters.

The design proposed for the CEPC SiW-ECal is very largely inspired by the one of the ILD detector for ILC as described in the Detector baseline Document [6]; it is influenced by the options studied for the CMS High-Luminosity upgrade endcap replacement HGCAL [7, 8], concerning cooling and electronics. In terms of luminosity and collision rates, the CEPC lies between the 2 options.

5.2.1.4 Mechanics & design

The geometry presented here reflects the current (october 2017) status on the realistic models developed for ILD. It differs slightly form the CEPC_v1 and CEPC_v4 models [9], mainly on ECAL thickness ($223mm$ vs $185mm$), and inner radius of the endcaps (226.8 and $245mm$ vs $400mm$).

5.2.1.5 Geometry

The geometry of the detector is based on ILD detector, where there is no blind zone between modules, but only "special zone", where it has been shown that performance of the reconstruction of jets or photon(s) is not downgraded significantly [10].
The figure below shows this octagonal geometry and the possible way to build the detector:

Draft-v02

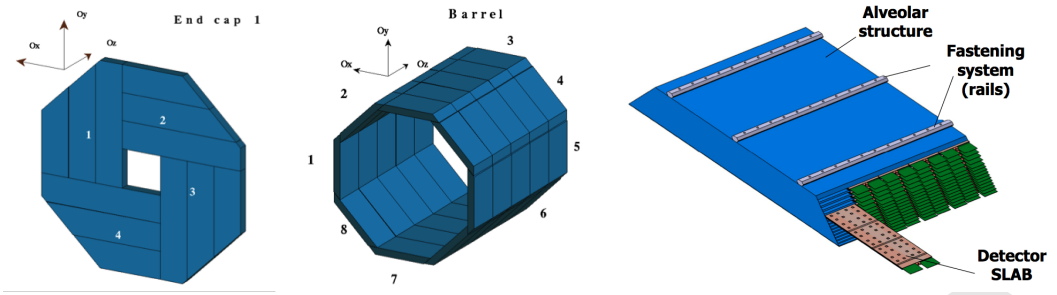

Figure 5.3: Left: Geometry of the SiW-ECAL Endcaps. Middle: Barrel Right: Geometry of the barrel modules.

ECal thickness For a baseline design featuring 30 layers – split in 2 sections of 20 and 10 layers, holding each an equal amount of $12Xo$ of W – $525microns$ thick wafers, and a base plate of $20mm$ of carbon, the ECal thickness is estimated at $223mm$.

For a reduced number of layers, at 22 (with section of 14 and 8), but thicker wafers ($725microns$), the thickness becomes $191mm$.

ECal dimensions The Barrel consist of 8 staves of 5 trapezoidal modules. Each barrel module contains 5 columns of alveoli. The number of modules and alveoli is even in order to avoid any special region at the azimuthal angle $theta = 0$. The alveolus size is fixed to $186mm$ by mechanical limits and by cost optimisation considerations, to contain exactly two 6-inch wafers or one-and-a-half 8-inch wafer. Integrating the alveolus size, walls of modules and contingencies, the barrel length amount to $4700mm$. ($4900mm$ in CEPC simulations). A gap of typically $70mm$ ($100mm$ in simulation) is left between the barrel sides and end-cap front parts, whose precise dimension will depend on the amount of ancillaries needed to service the ECAL and trackers (power and DAQ cables, cooling pipes, patch panels).

The end-caps are made of quadrants of 2 modules of 4 and 3 alveoli columns. Their inner radius is fixed by the ECal ring at $400mm$. With 7 alveoli columns, the end-cap outer radius is $1755mm$. An overshoot of $32mm$ is left between the outer radius of the barrel and of the end-caps, in order to contain the EM shower impinging the region of overlap. see figure 5.4. This fixes the inner radius size of the ECal barrel at $1498mm$ or $1530mm$.

For such a geometry, summing the barrel (200) and end-caps (56), 256 alveoli columns are needed. For 22 (resp. 30) layers, and this yields 5632 (7680) alveoli, and as many detector slabs.

Slab geometry In each alveola of the modules, a slab is inserted. Slabs contains 2 symmetric layers of Silicon sensors glued on PCB, equipped with readout ASICs, high voltage distribution by a Capton foil and copper layers for passive cooling. The elements are chained on both sides of a Carbon fibre cradle taking the shape of an H, with a core of Tungsten, and shielded by an aluminium cover. This so-called H-Structure is illustrated below.

To insure scalability and industrial production, the design has been made as modular as possible: the basic unit is the ASU (Assembly Single Unit), made of a $18x18mm^2$ PCB

Draft v0.2

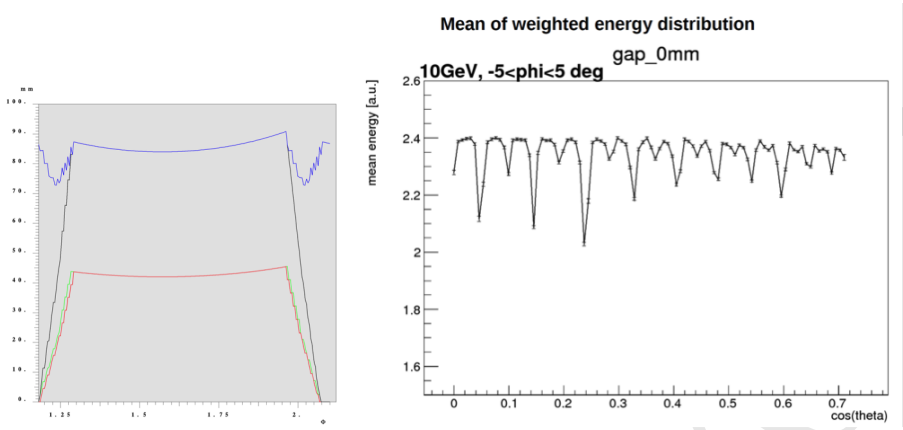

Figure 5.4: Left: Thickness of Tungsten seen as function of the polar azimuthal angle scan of one octant of the barrel. Right: Mean Theta angle scan

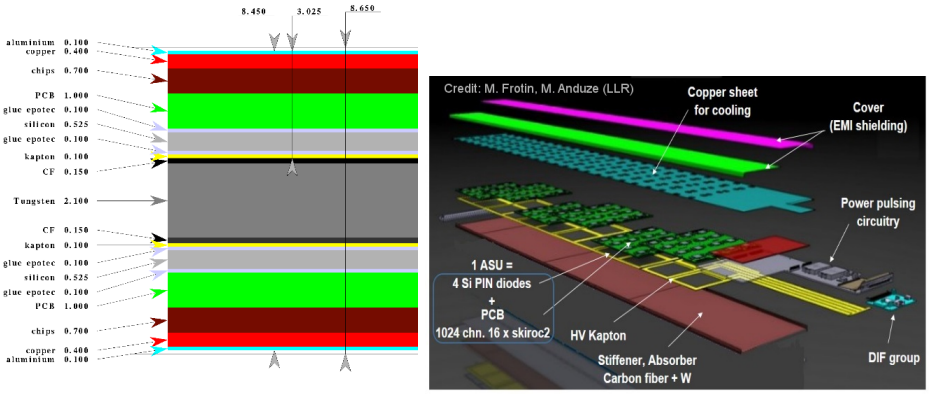

Figure 5.5: Left: Transverse cut through of a thin layer of the SLAB. Right: Exploded view of the top layer of a slab of the SiW-ECAL. The same structure is mirrored below the slab.

onto which 4 wafers of $90x90mm^2$ wafers are glued. Each ASU would handle 256 cells with 4 ASICs, for cell surfaces of $11.25x11.25mm^2$.

The ASUs are chained together for the clock and configuration distribution and data collection. For a radius of $1498mm$ the longest (shortest) barrel slabs measure $1146mm$ ($955mm$).

5.2.1.6 Electronics

One of the most critical element of the CEPC calorimeters is the readout electronics which is defined by the dynamic range, the effective digitisation, mode of trigger, the rate of working and power consumption per channel.

Dynamic range: A MIP going through a $725microns$ diode would produce $\simeq 60000$ electron-pairs holes or a charge of $9.6fC$ as the most probable value (MPV). To record MIPs with an efficiency higher than 95% this ports the low-end of the dynamic range to a 1/3 of the MPV. The high-end is determined by the number of MIP equivalent at the core of the high-energy EM showers, which can reach up-to 10000 MPV or $96pC$ for $11x11mm^2$ cells.

Timing: Time measurement of deposits in the calorimeters can be useful to Particle Flow algorithms to help disambiguate particle contributions. For the CMS HGCAL it is planned to distinguish particle stemming from different interactions [7], by achieving a timing of $50 - 20ps$ on EM showers. For e^+e^- colliders, with a single primary vertex, precision timing of individual cells – or group of cells – could still be useful to reduced the confusion and improve the resolution. The required precision is uncertain and should be studied further. Recent version of the SKYROC2a ASIC, could be operated [11] on test board with a measure of time close to 1.4ns. The performance has to be measured in an integrated design.

Rates: The running conditions a circular collider preclude any pulsed operation as is planned for the linear ones, where clocks, pre-amps, digital conversion are powered sequentially at a few Hz. A partial in-time shut-off or local on-demand switch-on of the ADC and TDC parts can be envisaged, leaving the pre-amp as the single major power consumer. As a point of reference, the current power consumption for SKIROC2 chips designed for the SiW-ECAL of ILD is of $5mW$ per channel in continuous mode.

Occupancy: The occupancy of the calorimeters should be very low. This pushes in the the direction of designing pre-amps with a very small consumption when there is no signal.

5.2.1.7 Power & Cooling

To the first order, the amount of power dissipates scales with the number of electronics channels. One important issue is to decide on the power scheme:

- a reduced number of channels using only passive cooling at the heart of the detector, such as planned at the ILD; a $400microns$-thick copper sheet will drain the heat to the end of the slab, where it is removed by a cooling system.
- keep a high granularity but include CO_2 cooling in the absorbers such as envisaged for the HGCAL.

The CEPC ECAL is at edge of both options, with a limit for the purely passive option of the order of $2x2cm^2$ cells for a increase of temperature limited to $\Delta T \sim 10°C$ at the remote-end of the slab.

Draft-v02

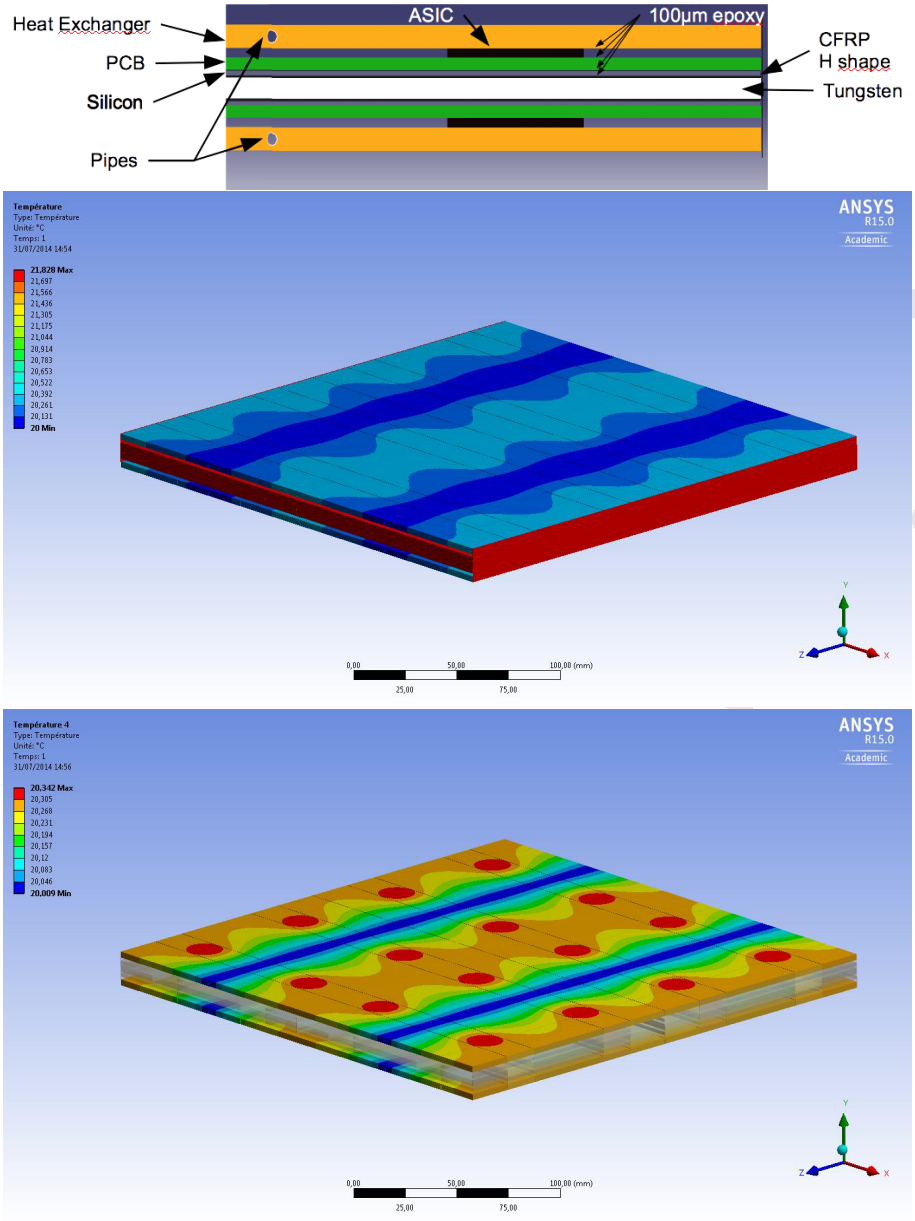

Figure 5.6: Top: Transverse section of slab equipped with CO_2 cooling pipes embedded in the cooling plates Left: Heat map over the full module. Right: heat map in the heat exchanger

Water cooling Current plans for the ILD SiW-ECAL is to use a leak-less water cooling system to extract the heat at the end of each slab from the copper. Details of implementation can be found in [12**?**].

CO_2 cooling HGCAL is preparing a biphasic CO_2 cooling system, with pipes circulating inside the absorber planes, made of an alloy of Tungsten and Copper.

A similar system adapted to the SiW-ECAL has been simulated [13]. The ILD $400microns$ passive colling are replaced by plates of $3mm$ of Copper, equipped with $1.6mm$ inner-diameter pipes for CO_2 circulation, glued on the ASICs, on both side of the slab. Assuming a fully transversally isolated system, with ASICs a sole heat source at equilibrium dissipating $0.64W$ ($10mW$ per channel times 64 channels), and a fixed working

point of $20°C$ for CO_2 (i.e assuming perfect heat absorption), a doubled sided module of $252x252mm^2$ holding 32 chips cooled by $2x2$ pipes was simulated.

Very preliminary simulations in "ideal conditions" show a difference of $\Delta T \sim 2°C$ mostly centered on ASIC's ($0.3°C$ in the exchanger itself only).

5.2.1.8 Status of R&D

The performances of a Silicon-Tungsten ECAL have beed explored using the "physical prototype" of the CALICE collaboration, on numerous beam tests during the years 2005-2011 [14–16].

Some ASU, similar to the one foreseen for the ILD detector have been operated in two beam test campaigns: first at CERN in 2015, where 3 ASU mounted on test boards behaved as expected [17]; a signal to noise ratio (SNR) - defined as the Most Probable Value of a Landau fit on data, divided by the Gaussian width of the noise – reached typical values of 15-18, with a very limited number of masked channels.

More recently a campaign at DESY using 1-5 GeV electrons, punching through "short slabs", featuring all the elements of the slabs described in section 5.2.1.5 but limited to a single ASU on a single side, could reach a SNR of $\simeq 20$ in average [18].

The collected data is still under analysis for estimated calorimetric performances, but they are expected to be similar to the physics prototype.

The building of a "long slabs" is being actively pursued, and should be completed toward the end of year 2019; the R&D involves all the power, cooling and FE issues for an ILD near the ILC.

The results and design will have to be adapted for a circular collider, where operation *a priori* forbid power-pulsed operations.

5.2.2 Scintillator-Tungsten Sandwich Electromagnetic Calorimeter

5.2.2.1 Introduction

Alternatively, a sampling calorimeter with scintillator-tungsten structure is proposed. It can be built in a compact and cost effective way. The structure of the ScW ECAL is similar to the SiW ECAL. The major geometry parameters of the ScW ECAL are also studied and optimized, with the similar results of the SiW ECAL. The active layers of the ScW ECAL are consisting of 5×45mm^2 scintillator strips. The scintillator strips in adjacent layers are perpendicular to each other to achieve a 5×5mm^2 effective transverse readout cell size. Each strip is covered by a reflector film to increase collection efficiency and improve uniformity of the scintillation light. Photons from each scintillator strip are read out by a very compact photo-sensor, SiPM, attached at the end of the strip. The SiPM and highly integrated readout electronics make the dead area in the ScW ECAL almost negligible.

Plastic scintillator is a robust material which has been used in many high energy physics experiments. Production of the scintillator strips can be performed at low cost by the extrusion method. Moreover, the number of readout channels can also be significantly reduced due to the strip structure. So the total construction cost of the ScW ECAL is lower than the SiW ECAL. Some key issues which might affect the performance of the ScW ECAL were studied and optimized.

Draft-v0.2

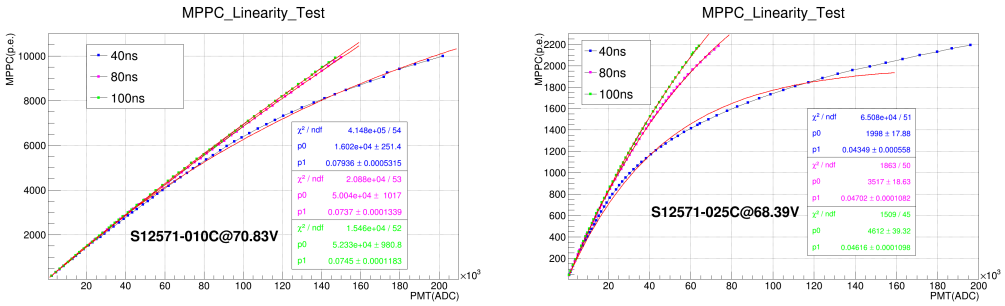

Figure 5.7: The response curve of 10000-pixel(left) and 1600-pixel(right) SiPM with different duration light.

5.2.2.2 SiPM dynamic range study

Because each pixel on a SiPM can only detect one photon at once and a few nanoseconds are needed before recovery, the SiPM is not a linear photon detection device, especially in the case of high intensity light input. The application of the SiPM in the CEPC ScW ECAL is a challenge to its dynamic range, which need to be studied.

For a short time light pulse, the response of the SiPM can be theoretically calculated as

$$N_{fired} = N_{pixel}(1 - e^{-N_{pe}/N_{pixel}}) \tag{5.1}$$

However, for the ScW ECAL, the width of the light pulse should not be ignored, and some pixels of the SiPM can detect more than one photon in an event. The response of the SiPM should be modified as

$$N_{fired} = N_{eff}(1 - e^{-N_{pe}/N_{eff}}) \tag{5.2}$$

The N_{eff} stands for the effective number of pixels on a SiPM, which is relative to the width of the input light pulse. Response curve of 10000 pixel (10μm pitch size)and 1600 pixel (25μm pitch size) SiPM with different duration light have been tested. As shown in Figure 5.7, the output linearity of the device is improved by the increase in the incident light width.

5.2.2.3 Scintillator strip test

Because the SiPM is coupled at one end of the scintillator strip, the light output will be non-homogeneous along the length of the scintillator, which will affect the performance of the ScW ECAL. By moving a Sr^{90} source along the length of the scintillator, we test the light pulses height read out by the SiPM to study the non-uniformity of the scintillator detector. Figure 5.8(left) is a typical test result of a scintillator module whose light output non-uniformity is 23%. The uniformity can be improved by optimizing the reflection material or the coupling methods of the SiPM to the scintillator strip. Figure 5.8(right) shows a result of a scintillator module with the SiPM embedded into the scintillator strip, and Figure 5.9 is the light output of another scintillator module with different reflector. Scintillators with ESR reflector can give much more light output. We have also test the light output of the scintillator coupled with the SiPM with different pitch size. Two kinds of SiPM have same sensitive area (1mm$\times$1mm), but have pitch size of 25μm and 10μm respectively. The light output of the scintillator with 25μm pitch SiPM is only about 1/3 of the scintillator with 10μm pitch SiPM, shown in Figure 5.10.

Draft-v0.2

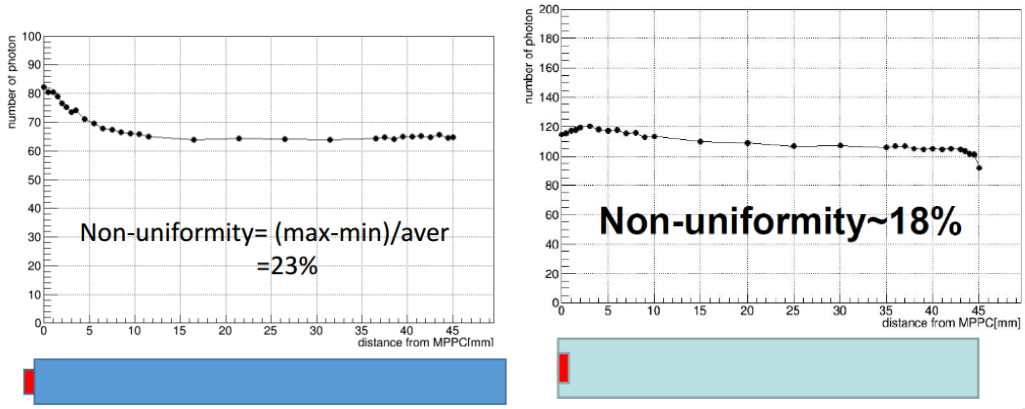

Figure 5.8: Scintillator module test results, with the SiPM coupled on the surface (left) or embedded into the strip(right).

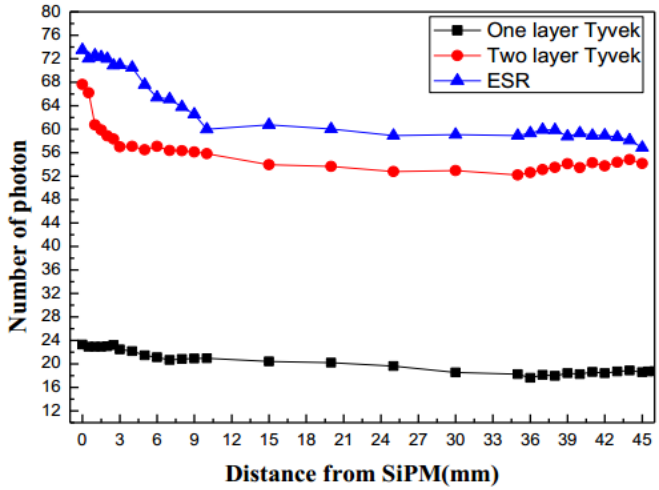

Figure 5.9: light output of scintillator with different reflector.

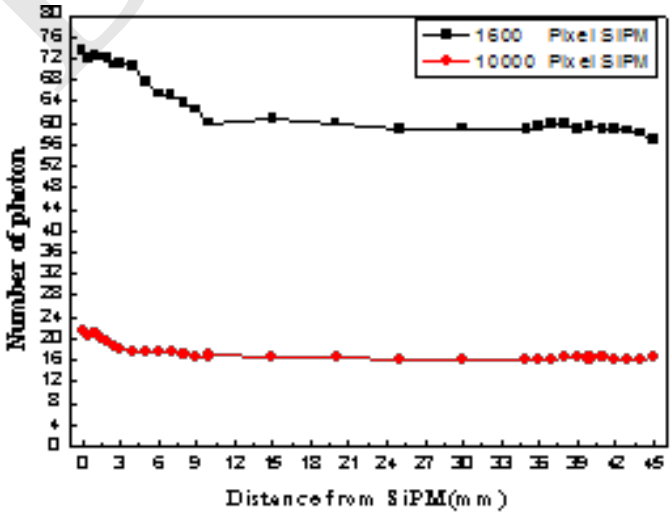

Figure 5.10: light output of the scintillator with different SiPM.

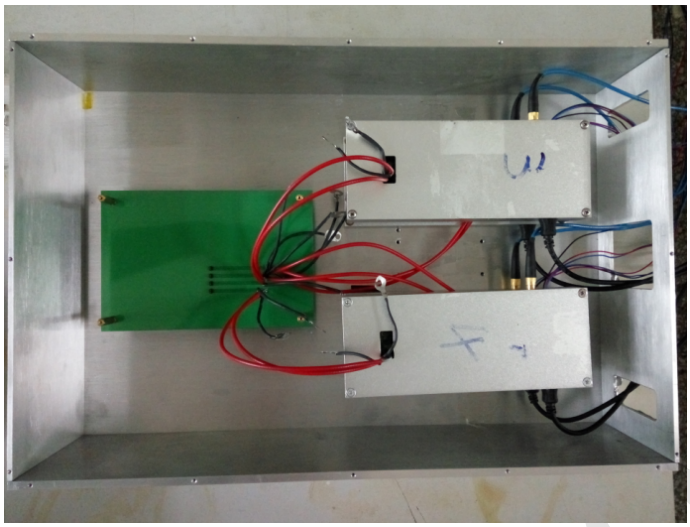

Figure 5.11: the picture of the prototype.

5.2.2.4 Beam test of a mini prototype

To study the layout, the coupling mode of the scintillator and the SiPM, and further test the minimum ionization particles (MIP). A mini prototype was constructed and tested by test beam. The test was carried out at the E3 beam at the IHEP, which could provide proton and pion mixed irradiation. The momentum of the particles was adjusted from 400MeV to 1.1GeV in the test.

The prototype includes four scintillator modules attached tightly to each other, as shown in Figure 5.11. Each module is composed of a BC408 scintillator with a dimension of 45mm×5mm×2mm, and a Hamamatsu S12571-025P SiPM coupled at the end of the scintillator as a photoelectric conversion device. The prototype is put into an aluminum box for electro-magnetic and light shielding. Figure 5.12 shows the detector layout in the test beam and the schematic of the readout. The beams first pass through two time of flight detectors (TOF) with the distance of 3m for particle identification, and then go through two scintillator counters with the same dimension of total of the four scintillator modules used to estimate the efficiency of the prototype. The prototype is located between the two scintillator counters. The signals from the TOFs and the scintillator counters are directly sent to a wave sampling digitizer (CAEN DT5751). The SiPM from each modules of the prototype is connected to a Hamamatsu driver board (C12332-01), which not only amplifies the signals from the SiPM, but also can eliminate the gain changes of the SiPM caused by the fluctuation of the temperature during the test thanks to its temperature compensation circuit. The signals from the four driver boards are sent to another CAEN DT5751 module to be digitized.

Figure 5.13 are the energy spectrums of pions and protons with momentum of 400MeV/c, 700MeV/c and 1000MeV/c respectively after the system calibration, which indicate the energy deposition in a module. The dE/dx as a function of the momentum of the particles can be got from the energy spectrums of the module, as shown in Figure 5.14. The values of dE/dx of protons and pions are consistent with the expected ones with respect to the momentum of the particles. Based on the dE/dx of pions, we can know the signal of the MIPs from the scintillator module is about 50 photoelectrons.

Draft v0.2

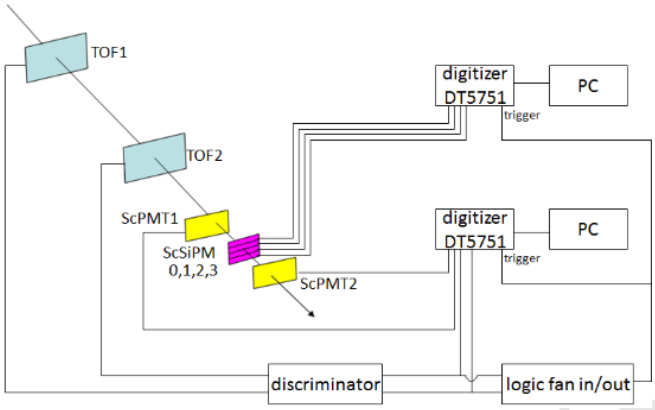

Figure 5.12: the schematic of the readout of the prototype.

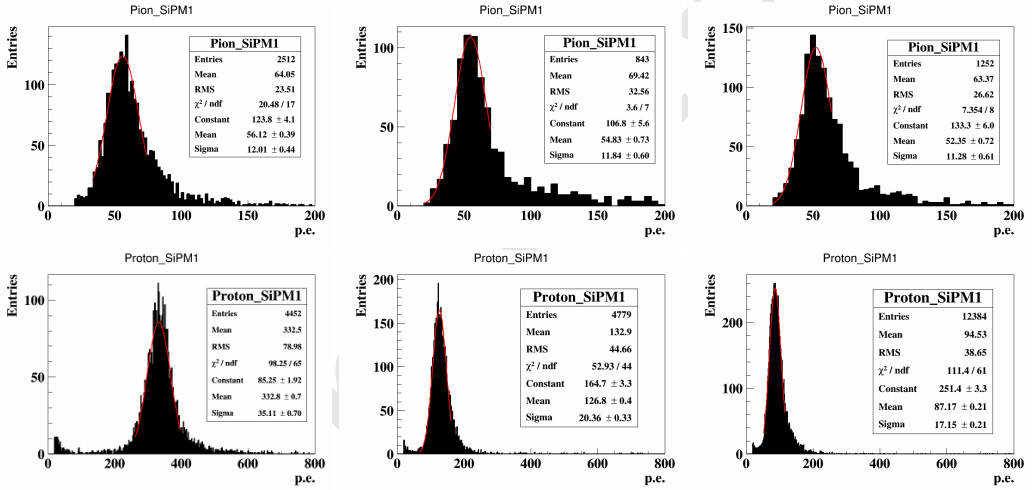

Figure 5.13: the energy spectrums of pions and protons with momentum of 400MeV/c, 700MeV/c and 1000MeV/c.

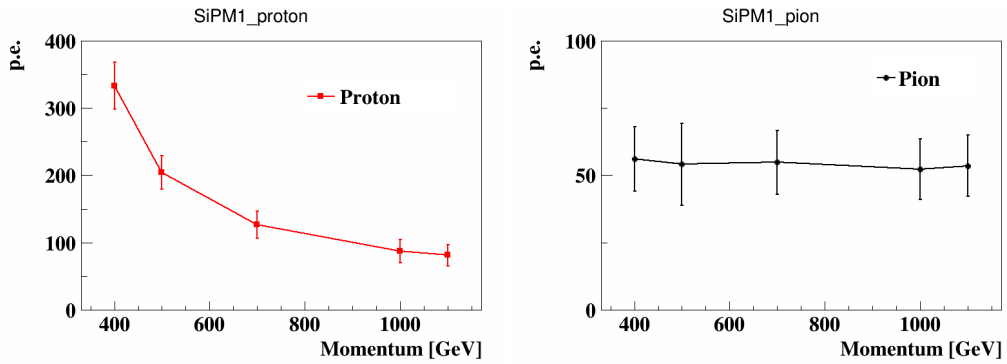

Figure 5.14: dE/dx of protons and pions change with the momentum.

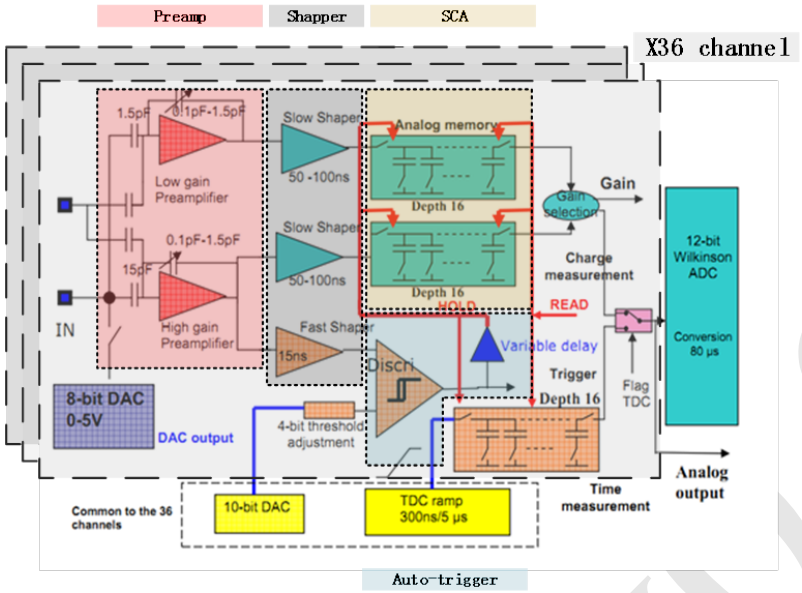

Figure 5.15: Schematic view of proposed readout ASIC.

5.2.2.5 Implementation Example for the Analog Calorimeter Readout

The readout electronics of the ECAL has to provide high dynamic range of energy, while showers of particle may deposit 1∼800 MIPs energy in single cell for 100GeV photon. As Particle Flow Algorithm (PFA) is being considered, high granularity requirement need be meet. Granularity of cells in ECAL need be finer than 10mm therefore a large amount of channels need be readout. So multiple-channels-readout-chip is considered.

Electronics consists of two parts: Front-End and Back-End. The Front-End-Electronics (FEE) is embedded into the layers of ECAL. It performs amplification, auto-triggering, digitization and zero-suppression, with local storage of data between the working phases. The Back-End-Electronics play the role of collecting data and configuring chip before system running.

Several studies and existing calorimeter readout electronics have shown that one can obtain optimized energy resolutions using a preamplifier-shaper and digitizing the pulse at peak. For instance, a preamp-shaper-SCA structure of analog circuit applied on ILC HCAL which implemented in ASIC. A similar approach can be applied at CEPC-ECAL. An ASIC named SPIROC2b is considered in present stage. The analog part is schematically depicted in Figure 5.15.

The basic principle consists of a readout chain with an amplifier-shaper using a RCn-CRp filter delivering a pulse length of about 50-200ns duration for a SiPM pulse signal. This signal is also shaped by a fast shaper in the same time to generate fast and narrow pulse for discriminating. Then the discriminator gives the trigger to Switched-Capacitor-Array (SCA) for locking the peak value of slow-shaped signal. The locked voltage value is corresponding to the charge that circuit received. A 12bits Wilkinson ADC is used for digitizing analog voltage in SCA. Future detailed implementations of the calorimeter front-end electronics for CEPC is still considered using ROC series ASIC but newer version.

The maximum data rate can be estimated as follows. Assuming signal keep coming consistently, SPIROC2b will be continuously switched between three states called Ac-

Draft-v0.2

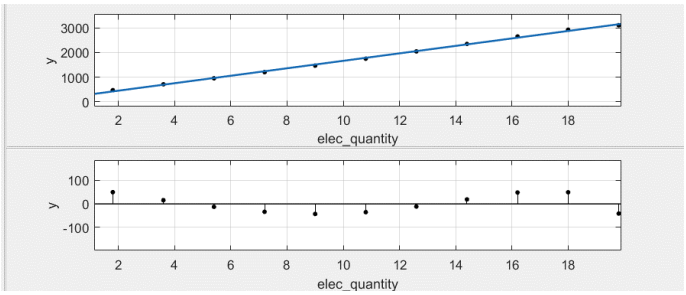

Figure 5.16: Pedestal noise.

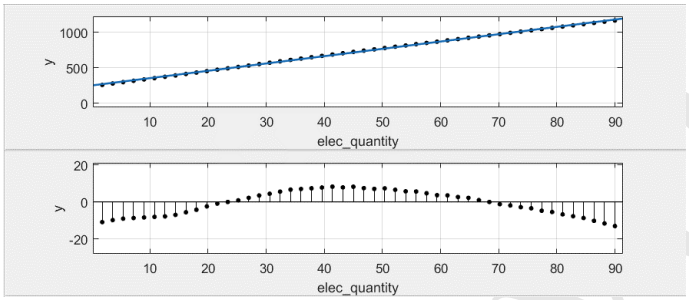

Figure 5.17: High gain calibration.

quisition, AD Converting and Readout. Only in Acquisition state can SPIROC2b receive signal from SiPM and stored in SCA in the rate of about 5MHz. Another two states should be seen as âĂIJdead-timeâĂİ status. There is 16 depth in SCA, so 4us for Acquisition, according to measurement, ∼4ms for ADC & Readout. So data rate is 16 events per 4ms which equals to 4 kHz. Each fulfilled data packaged is 2 Kbytes in size.

More chip in one layer will multiply the duration of Readout. Assuming that there are 4 chips in one layer. So there is 16ms for Readout. Maximum events rate is reduced to 1kHz and leads to about a transmission of 5Mbyte/s. This can easily be managed with 100M links.

The power consumption in the front-end will be dominated by ASIC and more specifically by analog part of ASIC. Opening all modules, one SPIROC2b is consuming 250.8mW of which about 150mW is consumed by analog part. In actual use, most of cycle is ADC and Readout. It leads to about 150mW power consumption per chip and 4mW per channels.

The electronic calibration and cosmic ray test have been done. From these electronic calibration Figure 5.16 - Figure 5.18, we can see that the noise of readout system is 46fC in RMS and high gain and low gain is 151/pC and 10.3/pC while maximum ADC range is 4096. So dynamic range that from 100fC-300pC of readout system is measured by electronic method. Cosmic ray results shows that the system can distinct MIPs signal from pedestal well and figure out that about 1pC.

5.3 Hadronic Calorimeter for Particle Flow Approach

5.3.1 Introduction

High-granularity hadronic calorimeter concept is to play an essential role in PFA-based experiments such as CEPC. It allows to separate the deposits of charged and neutral

Draft-v0.2

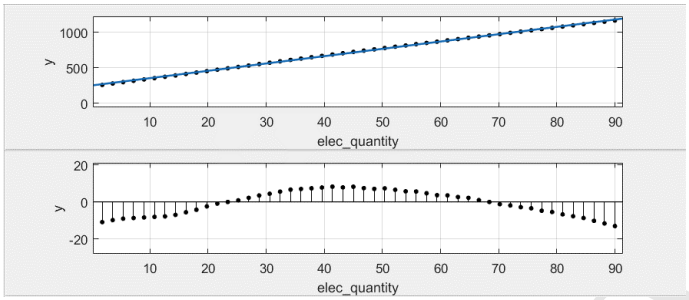

Figure 5.18: Low gain calibration.

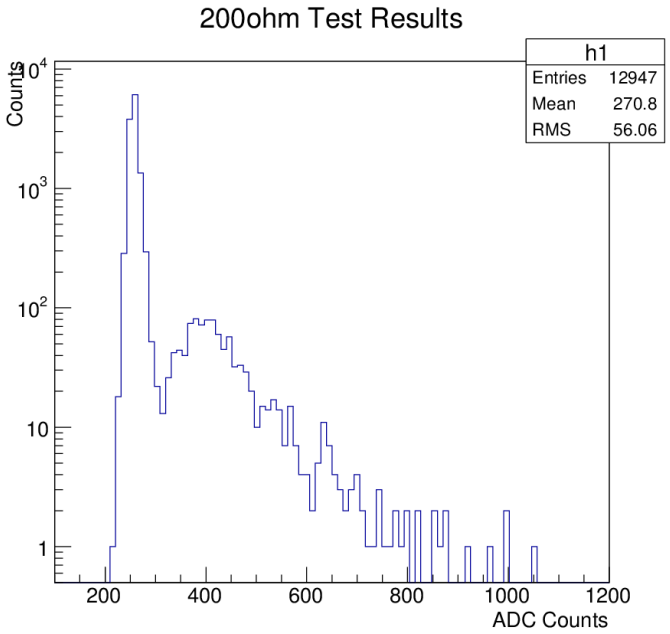

Figure 5.19: Cosmic Ray result.

hadrons and to precisely measure the energy of the neutrals. The contribution of the neutrals to the jet energy, around 10% on average, fluctuates in a wide range from event to event, and the accuracy of the measurement is the dominant contribution to the particle flow resolution for jet energies up to about 100 GeV. For higher energies, the performance is dominated by confusion, and both topological pattern recognition and energy information are important for correct track cluster assignment. High-granularity hadronic calorimeter is thus needed to achieve excellent jet energy resolution.

HCAL are sampling calorimeters with steel as absorber and scintillator tiles or gaseous devices with embedded electronics for the active part. The steel was chosen due to its rigidity which allows to build self-supporting structure without auxiliary supports (dead regions). Moreover, the moderate ratio of hadronic interaction length ($\lambda_I = 17$ cm) to electromagnetic radiation length ($X_0 = 1.8$ cm) of iron, allows a fine longitudinal sampling in terms of X_0 with a reasonable number of layers in λ_I, thus keeping the detector volume and readout channel count small. This fine sampling is beneficial both for the measurement of the sizable electromagnetic energy part in hadronic showers as for the topological resolution of shower substructure, needed for particle separation.

The active detector element has very finely segmented readout pads, with 1×1 cm^2 size, for the entire HCAL volume. Each readout pad is read out individually, so the readout channel density is approximately 4×10^5/m^3. For the entire HCAL, with $\sim$100 m^3 total volume, the total number of channels will be 4×10^7 which is one of the biggest challenges for the HCAL system. On the other hand, simulation suggests that, for a calorimeter with cell sizes as small as 1×1 cm^2, a simple hit counting is already a good energy measurement for hadrons. As a result, the readout of each channel can be greatly simplified and just record 'hit' or 'no hit' according to a single threshold (equivalent to a '1-bit' ADC). A hadron calorimeter with such kind of simplified readout is called a Digital Hadron Calorimeter (DHCAL). In a DHCAL, each readout channel is used to register a 'hit', instead of measure energy deposition, as in traditional HCAL. In this context, gas detectors (such as RPC, GEM) become excellent candidates for the active element of a DHCAL. Another technology option is Analog Hadron Calorimeter (AHCAL) which is based on scintillator with SiPM as active sensor.

A drawing of the HCAL structure is shown in Figure 5.20, the barrel part is made of 5 independent and self-supporting wheels along the beam axis. The segmentation of each wheel in 8 identical modules is directly linked with the segmentation of the ECAL barrel. A module is made of 40 stainless steel absorber plates with independent readout cassettes inserted between the plates. The absorber plates consist of a total of 20 mm stainless steel: 10 mm absorber from the welded structure and 10 mm from the mechanical support of the detector layer. Each wheel is independently supported by two rails on the inner wall of the cryostat of the magnet coil. The cables as well the cooling pipes will be routed outside the HCAL in the space left between the outer side of the barrel HCAL and the inner side of the cryostat.

5.3.2 Semi-Digital Hadronic Calorimeter (SDHCAL)

5.3.2.1 Introduction

For the CEPC, a SDHCAl based on gaseous detecor is proposed. This is motivated by the excellent efficiency and very good homogeneity the gaseous detectors could provide. Another important advantage of gaseous detectors is the possibility to have very fine lateral

Draft-V0.2

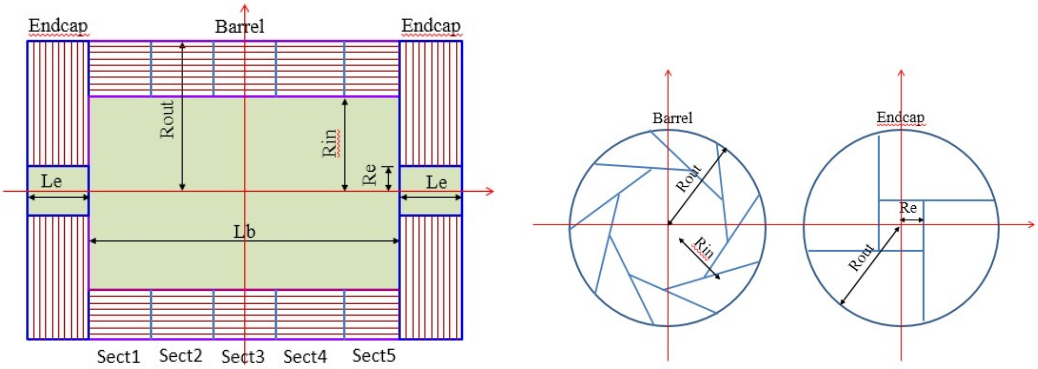

Figure 5.20: Longitudinal profile (Left) and transverse section (Right) of the HCAL.

segmentation. Indeed, in contrast to scintillator tiles, the lateral segmentation of gaseous devices is determined by the readout electronics and not by the detector itself. Active layer thickness is also of importance for what concerns the CEPC hadronic calorimeter to be placed inside the magnetic field. Highly efficient gaseous detectors can indeed be built with a thickness of less than 3 mm. Other detectors could achieve such performance. However, gaseous detectors have the advantage of being cost-effective and discharge free. They are also known for their fast timing performance which could be used to perform 4D construction of the hadronic showers. Such a construction can improve on hadronic showers separation by better associating the energy depots belonging to the same shower from those of other showers. It can also improve on the energy reconstruction by identifying the delayed neutrons and assigning them a different weight.

To obtain excellent resolution of hadronic shower energy measurement a binary readout of the gaseous detector is the simplest and most effective scenario. However, a lateral segmentation of a few millimeters is needed to ensure good linearity and resolution of the reconstructed energy. Such a lateral segmentation leads to a huge number of electronic channels resulting in a complicated readout system design and a too large power consumption. 1x1 cm^2 cells are found to be a good compromise that still provides a very good resolution at moderate energies. However, simulation studies show that saturation effects are expected to show up at higher energies ($> 40\,\mathrm{GeV}$). This happens when many particles cross one cell in the center of the hadronic shower. To reduce these effects, the choice of multi-threshold electronics (Semi-Digital) readout is chosen to improve on the energy resolution by exploiting the particle density in a more appropriate way. These elements were behind the development of a Semi-Digital Hadronic CALorimeter (SDHCAL) that we propose to equip one of the CEPC future experiments.

Even with a 1x1 cm^2 lateral granularity of the readout system, a huge number of electronic channels is still needed. This has two important consequences. The first is the power consumption and the resulting increase of temperature which affects the behavior of the active layers. The other consequence is the number of service cables needed to power, read out these channels. These two aspects can deteriorate the performance of the HCAL and destroy the principle of PFA if they are not addressed properly.

The R&D pursued by the CALICE SDHCAL groups has succeeded to pass almost all the technical hurdles of the PFA-based HCAL. The SDHCAL groups have succeeded to build the first technological prototype [19] of these new-generation calorimeters with 48 active layers of GRPC, $1m^2$ each. The prototype validates the concept of high-granularity

gaseous detector and permits to study the energy resolution of hadrons one can obtains with such calorimeter.

In order to find out an appropriate option for the active detector of the SDHCAL, two parallel detector schemes, the Glass Resistive Plate Chamber (GRPC) and the Thick Gaseous Electron Multiplier (THGEM) are proposed for the active layers of the SDHCAL.

5.3.2.2 GRPC based SDHCAL

The GRPC scheme The structure of GRPC proposed as an active layer of the HCAL proposed for CEPC is shown in Figure 5.21. It is made out of two glass plates of 0.7 mm and 1.1 mm thickness. The thinner is used to form the anode while the the thicker forms the cathode. Ceramic balls of 1.2 mm diameter are used as spacers between the glass plates. The balls are glued on only one of the glass plates. In addition to those balls, 13 cylindrical fiber-glass buttons of 4 mm diameter are also used. Contrary to the ceramic balls the buttons are glued to both plates ensuring thus a robust structure. Special spacers (ceramic balls) were used to maintain uniform gas gap of 1.2 mm. Their number and distribution were optimized to reduce the noise and dead zones (0.1%).

The distance between the spacers (10 cm) was fixed so that the deviation of the gap distance between the two plates under the glass weight and the electric force does not exceed 45 microns. The choice of these spacers rather than fishing lines was intended to reduce the dead zones (0.1%). It was also aimed at reducing the noise contribution observed along the fishing lines in standard GRPC chambers. The gas volume is closed by a 1.2 mm thick and 3 mm wide glass-fiber frame glued on both glass plates. The glue used for both the frame and the spacers was chosen for its chemical passivity and long term performance. The resistive coating on the glass plates which is used to apply the high voltage and thus to create the electric field in the gas volume was found to play important role in the pad multiplicity associated to a mip [20]. A product based on colloids containing graphite was developed. It is applied on the outer faces of the two electrodes using the silk screen print method, which ensures very uniform surface quality. The measured surface resistivity at various points over a 1m^2 glass coated with the previous paint showed a mean value of 1.2 $\text{M}\Omega/\square$ and a ratio of the maximum to minimum values of less than 2 ensuring a good homogeneity of the detector.

Another important aspect of this development concerns the gas circulation within the GRPC taking into account that for the CEPC SDHCAL, gas outlets should all be on one side. A genuine system was proposed. It is based on channeling the gas along one side of the chamber and releasing it into the main gas volume at regular intervals. A similar system is used to collect the gas on the opposite side. A finite element model has been established to check the gas distribution. The simulation confirms that the gas speed is reasonably uniform over most of the chamber area. The GRPC and its associated electronics are housed in a special cassette which protects the chamber and ensures that the readout board is in intimate contact with the anode glass. The cassette is a thin box consisting of 2.5 mm thick stainless steel plates separated by 6 mm wide stainless steel spacers. Its plates are also a part of the absorber.

The electronics board is assembled thanks to a polycarbonate spacer which is also used to fill the gaps between the readout chips and to improve the overall rigidity of the detector. The electronics board is fixed on the small plate of the cassette. Thanks to tiny screws and the new set is fixed on the other plate which hosts the detector and the spacers. The whole

Draft-V0.2

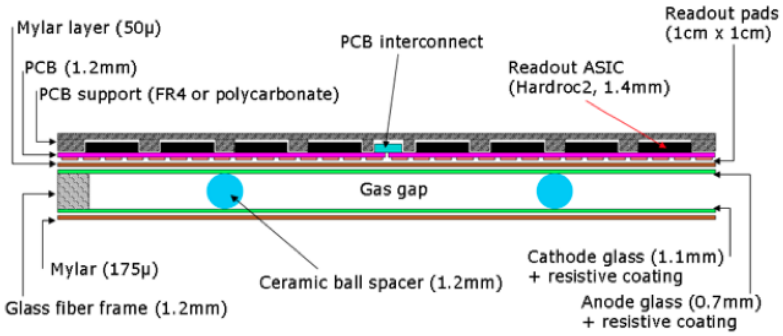

Figure 5.21: Cross-section through a 1 m^2 chamber.

width of the cassette is 11 mm with only 6 of them corresponding to the sensitive medium including the GRPC detector and the readout electronics.

GRPC technological prototype An SDHCAL prototype fulfilling the efficiency, robustness and the compactness requirements of the future PFA-based leptonic collider experiments [19] was built. 48 cassettes as the one described above were built. They fulfilled a stringent quality control. It is worth mentioning that 10500 HR ASICs were produced and tested using a dedicated robot for this purpose. The yield was found to be higher than 92%. The ASICs were then fixed on the PCBs to make a $1m^2$ and itself fixed on the cassette cover once successfully tested. The cassettes were inserted in a self-supporting mechanical structure that was conceived and built in collaboration with the Spanish group of CIEMAT. The structure is made of Stainless Steel plates of 1.5 cm each. The plates were machined to have an excellent flatness and well controlled thickness. The flatness of the plates was measured using a laser-based interferometer system. It was found that the flatness of the plates are less than 500 microns. This results guarantees that for the SDHCAL V structure proposed for ILD, a tolerance of less than 1mm is achievable. The prototype construction lasted less than 6 months. A commissioning test at CERN in 2011 allowed to understand the whole system behavior. In April 2012 the prototype was exposed to pion, muon, electron beams of both the PS and the SPS of CERN Figure (5.22). Power-pulsed mode was applied to the whole prototype using the beam cycle structure (0.3 ms time duration for the PS beam and 9 s for the SPS beam every 45s). The data were collected continuously in a triggerless mode. Figure 5.23 shows the efficiency (left) and pad multiplicity (right) of the prototype's GRPC chambers measured using the muon beam. Figure 5.24 shows a display of two events collected in the SDHCAL. One is a produced by a pion interaction (left) and the other by an electron interaction (right).

The SDHCAL prototype results obtained with a minimum data treatment (no grain correction) show clearly that excellent linearity and good resolution [21] could be achieved on large energy scale as can be shown in Figure 5.25 where results obtained in two different beam lines are obtained using the same detector configurations. Useless to mention that the high granularity of the SDHCAL allows one to study thoroughly the hadronic showers topology and to improve on the energy resolution by, among others, separating the electromagnetic and the hadronic contribution. The separation between close-by showers will also get big benefit thanks to the high granularity on the one hand and to to the very clean detector response (< 1 Hz/cm^2) on the other hand. The results obtained with the the SDHCAL [22] confirm the excellent efficiency of such separation thanks to the SD-

Draft-2018/07/19

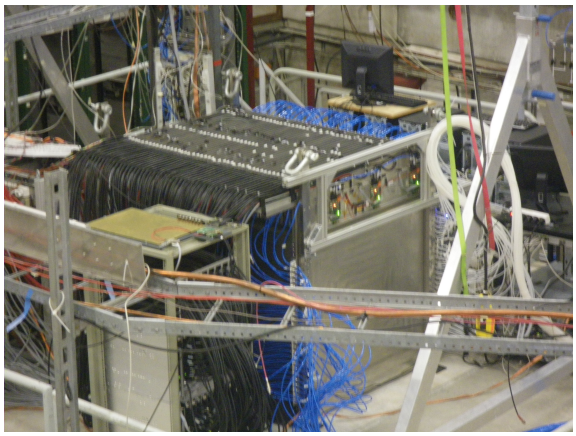

Figure 5.22: The SDHCAL prtototype in beam test at CERN.

HCAL performance. In addition, the high-granularity of the SDHCAL allows to extract the track segments of hadronic showers in a very efficient way [23]. The track segments (Figure 5.26) are then used to study the detector behavior in-situ. This is a simple but powerful control and calibration tool for a running calorimeter.

The quality of data obtained during several campaigns of data taking at the CERN PS and SPS beam lines validates completely the SDHCAL concept. This is especially encouraging since no gain correction was applied to the electronics channels to equalize their response. Still, improvement was further achieved by applying gain and threshold correction schemes in terms of the calorimeter response homogeneity.

A digitizer describing the response of the GRPC within the SDHCAL was developed [24]. It allows to study the SDHCAL behavior in a realistic manner in the future experiments.

In parallel to the prototype construction, a single cassette was tested in a magnetic field of 3 Tesla (H2 line at CERN) applying the power-pulsed mode. The TB results [25] indicated clearly that the use of the power-pulsed mode in such a magnetic field is possible. The behavior of the detector (efficiency, multiplicity..) was found to be similar to those obtained in the absence of both the magnetic field and the power-pulsed mode.

Preparation for future experiments A genuine self-supporting mechanical structure to host the hadronic calorimeter of future PFA-based leptonic collider experiments was fully studied. The structure (called V-structure) was conceived to eliminate the projective holes and cracks so none of the particles produced close to the detector centre could escape detection. The V-structure has additional advantages. It eliminates in principle the space between the barrel and the Endcaps avoiding the shower deformation which results not only because of this space but also of the different cables and services needed in CMS-like mechanical structures. In this structure the different services such as the gas tubes, data collection and electric cables of both the barrel and the Endcaps are taken out from the outer radius side.Detailed studies have shown that the deformation of this structure is extremely low and its robustness was verified experimentally with the SDHCAL technological prototype built with a self-supporting structure respecting the spirit of the V one. Services and Integration issues were also worked out. Besides, realistic costing was performed , based on the prototype experience.

Draft V0.2

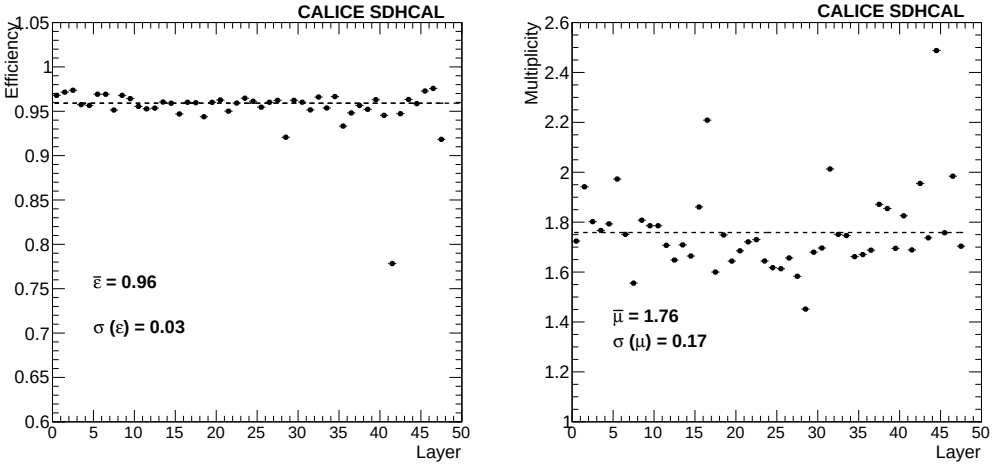

Figure 5.23: Left: Efficiency of the GRPC detectors of the SDHCAL. Right: the pad multiplicity of the GRPCs. One third of the chamber 42 was not instrumented.

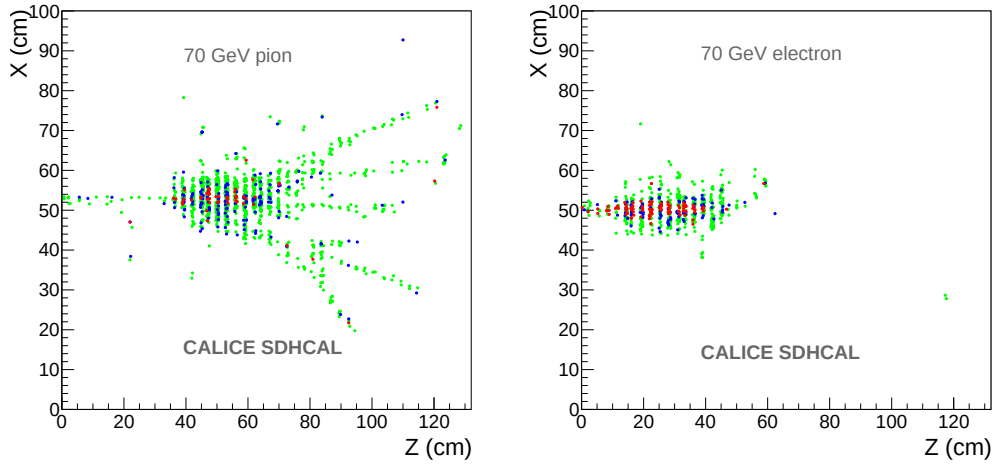

Figure 5.24: Left: event display of an 70 GeV pion interaction in the SDHCAL prototype. Right: Event display of a 70 GeV electron interaction in the SDHCAL prototype.

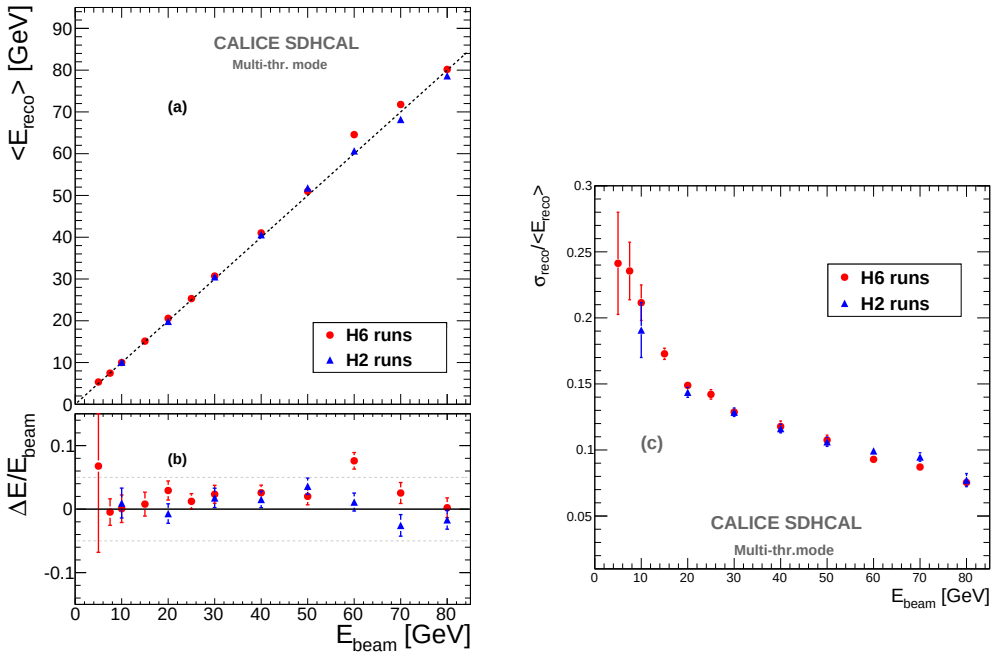

Figure 5.25: Left: a) Reconstructed energy of the hadronic showers collected in both H2 and H6 SPS beamlines. b) the relative deviation of the reconstructed energy with respect to the beam energy. Right: Relative energy resolution of the reconstructed hadronic shower.Pion beam of H6 beamline is largely contaminated by protons at high energy (>50 GeV).

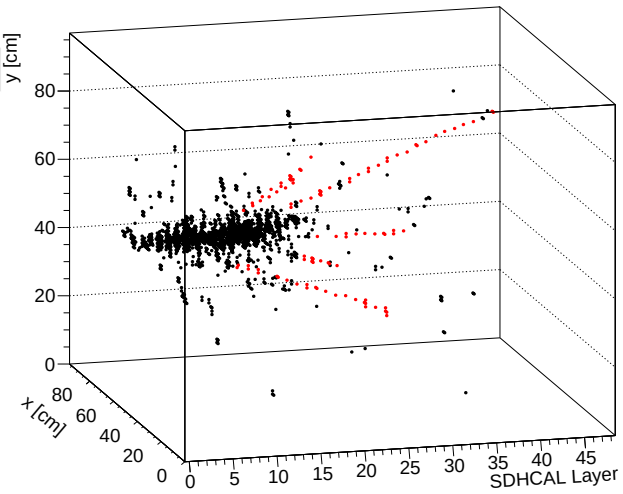

Figure 5.26: A 3D event display of a pion interaction event showing the track segments extracted by applying a hough transform technique.

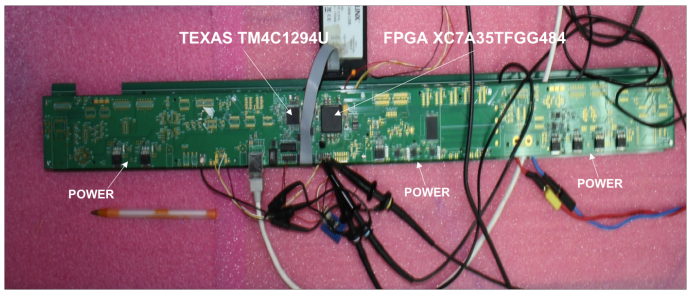

Figure 5.27: A new Detector InterFace (DIF) allowing to address up to 432 ASICs of 64 electronic channels each.

current SDHCAL R&D Large GRPC of $1m^2$ were developed and built for the technological prototype. However, larger GRPC are needed in the SDHCAL proposed for future leptonic collider experiments. These large chambers with gas inlet and outlet on one side need a dedicated study to guarantee a uniform gas gap everywhere notwithstanding the angle of the plate. It is necessary also to ensure an efficient gas distribution as it was done for the 1m2 chambers. To obtain this different gas distribution systems were studied. A new scheme with two gas inlets and one outlet was found to ensure an excellent homogeneity of the gas distribution. This system will be used in the near future to build large detectors exceeding $2m^2$. The readout of such chambers needs also to be as efficient as the one of the technological prototype $1m^2$. An upgrade of the HR ASIC allowing larger dynamic range (01-50 pC) was conceived, produced and successfully tested. The new ASIC (HR3) allows to be directly addressed and easily bypassed in case of failure thanks to the I2C protocol. In addition and contrary to the HR2, the 64 channels of the new ASIC are independent which allows a better calibration procedure. Furthermore, a new interface board (DIF) is conceived to control the ASICs synchronization and data transfer. Indeed, the space left between the active layer of one module and the cryostat maybe very short in future leptonic experiments (< 5 cm). This means that the DIF components should be optimized to cope with the volume availability. A new design with new functionalities of the DIF is proposed. A TPC/IP protocol is adopted for data transfer and a TTC one for the clock synchronisation. A microprocessor implemented on the new DIF is in charge of the communication between the ASICs and the DIF's FPGA. The new DIF shown in Fig. 5.27 is capable to address up to 432 ASIC. A new PCB design that allows to assemble few boards to cover up to 3 m^2 GRPC detector was also conceived. Care is taken to ensure robust and flexible but still tiny connection between the different PCB to build a large one. Fig. 5.28 shows a picture of such a PCB equipped with the HR3 ASICs. Finally a new technique based on electron beam welding is being tested to build a mechanical structure. This intends to reduce the steel quantity used to assemble the absorber plates while guaranteeing a minimum deformation. First attempts have taken place at CERN recently 5.29 and more study is ongoing to determine the best protocol one should follow to obtain optimal results. Finally, to cope with the heating produced by the embedded readout system in case of limited or even the absence of use of the Power Pulsing system, a new active cooling system is being studied. Figure 5.30 shows a study of a water-based cooling system to absorb the excess of heat in the SDHCAL. The cooling system is very simple but very effective as well. It allows to keep the average temperature as well as the temperature dispersion of the GRPC well under control.

Draft-V0.2

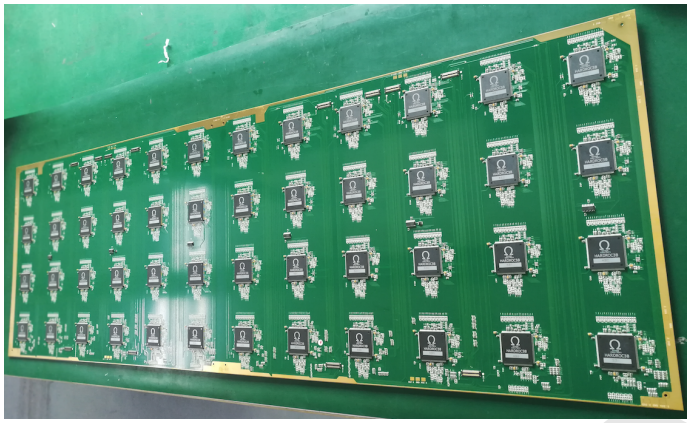

Figure 5.28: A new PCB equipped with he HR3 ASICs. The PCB is 100 cm $\times$ 33.3 cm. Several PCBs could be connected thanks to tiny flexible connectors to read out very large GRPC detectors.

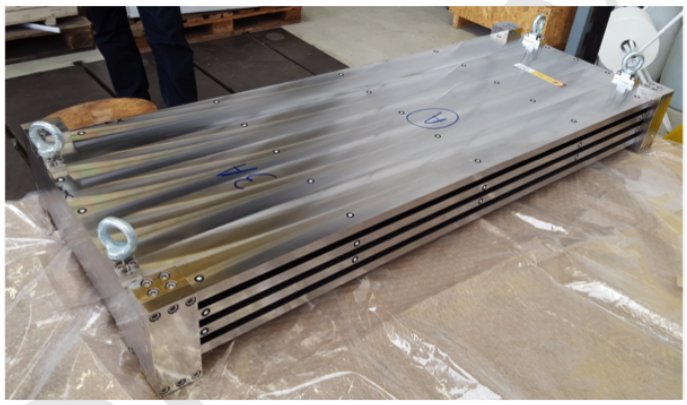

Figure 5.29: A prototype of an SDHCAL mechanical structure assembled using the electron beam welding technique.

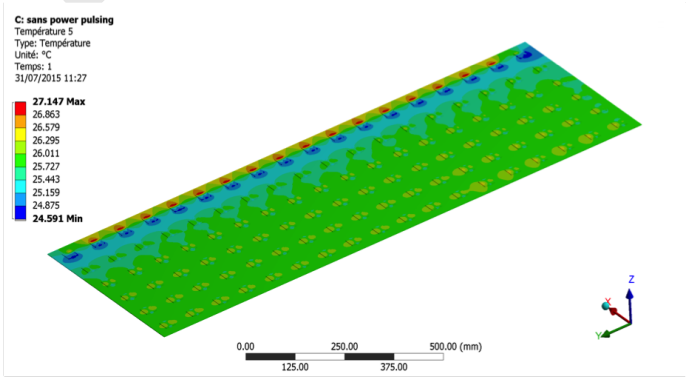

Figure 5.30: Temperature distribution in an active layer of the SDHCAL operated with no power-pulsing. The cooling system is made of a circulating water inside copper tubes in contact with the ASICs.

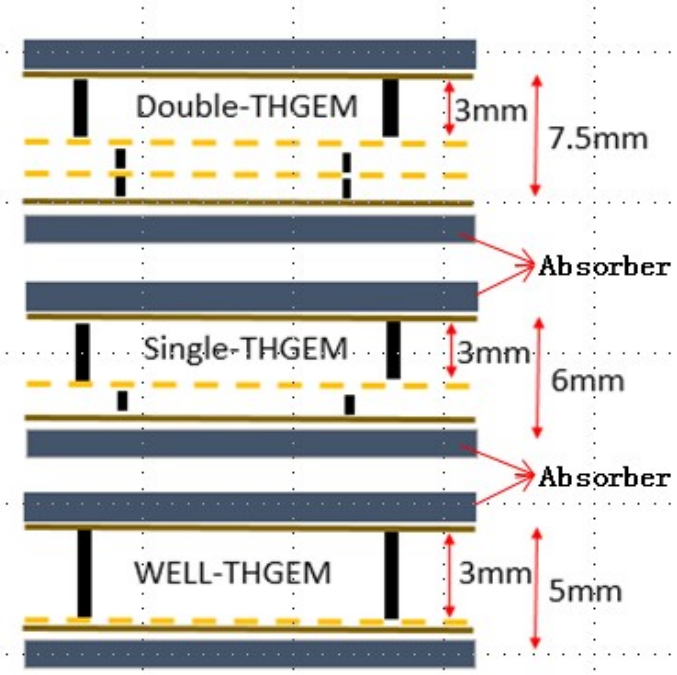

Figure 5.31: Structure of THGEM based detector for DHCAL.

5.3.2.3 THGEM-based DHCAL

The THGEM scheme The THGEM can be built in large quantities at low cost, which might make them suitable for the large CEPC HCAL. THGEM detectors can provide flexible configurations, which allow small anode pads for high granularity. They are robust and fast, with only a few nano-seconds rise time, and have a short recovery time which allows a higher rate capability compared to other detectors. They are operated at a relatively low voltage across the amplification layer with stable high gain. The ionisation signal from charged tracks passing through the drift section of the active layer is amplified using a sigle layer or WELL-type THGEM structure. The amplified charge is collected at the anode layer with pads at zero volts. As the HCAL is located within the coil, WELL-THGEM, a single layer structure with thinner thickness, as shown in Fig. 5.31, can be considered as the sensitive medium, to keep the HCAL compact.

Digital readout has been proposed to limit the total amount of data, which simplifies the data treatment without comprising the energy resolution performance. The readout electronics of the DHCAL will be integrated into the sensitive layer of the system, thus minimising dead areas. Large electronics boards are assembled together to form extralarge boards before being attached to the THGEM. The board assembly will utilise a mechanical structure made of 4 mm stainless steel plate. In addition, to keep the HCAL as compact as possible, the fully equipped electronic boards are designed to be less than 2 mm thick in total.

A THGEM based detector for DHCAL has been designed with 40 layers in total. Each layer contains 2.0 cm thick stainless steel, 0.8 cm thick THGEM and readout electronics with 1×1 cm^2 readout pads. As THGEM production technology matures, the maximum area of THGEM is limited only by the size of the CNC drilling area. Its low price, robustness against occasional discharges, high gain and count rate capability of up to

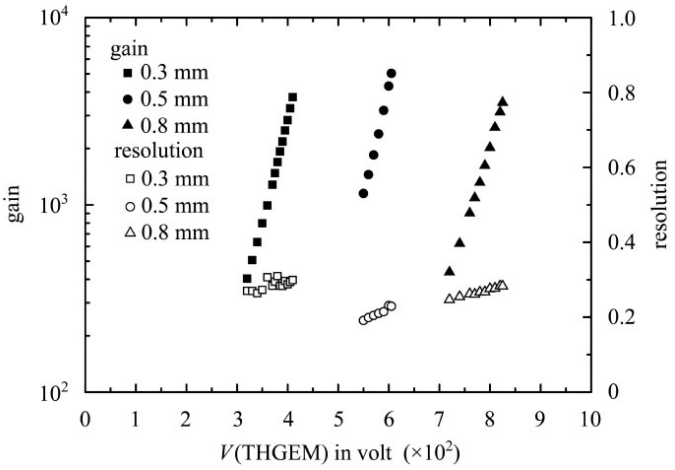

Figure 5.32: Gain and energy resolution of THGEM detector obtained with ^{55}Fe.

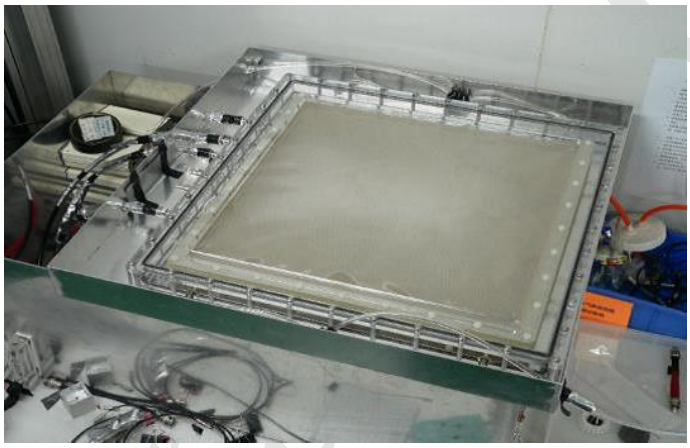

Figure 5.33: The maximum size of THGEM produced in domestic currently (40×40 cm^2).

10MHz/cm^2 make THGEM very attractive for building the DHCAL. THGEM is cheaper and more robust than GEM, and has a higher counting rate capability than GRPC. As illustrated in Fig. 5.31, the total thickness of the sensitive medium is 5 mm, which consists of 3 mm drift gap, 1 mm transfer gap and 1 mm induction gap. The absorber between the active layers is made of 20 mm thick stainless steel. The thickness of the readout electronics board is about 3 mm, and the total thickness of a single sensitive layer is less than 10 mm. Each layer corresponds to about 1.2 radiation length and 0.65 nuclear interaction length. The whole DHCAL detector is evenly divided into 40 layers, with a total stainless steel absorber thickness of 4.7 nuclear interaction lengths.

THGEM prototype A THGEM with an area of 40×40 cm^2 has been successfully fabricated, as shown in Fig. 5.33, and a gain of 2×10^5 has been achieved with a double THGEM, with an energy resolution of about 20%. The THGEM produced has the following features: 1)standard PCB processes are used, which keeps the cost low; 2) excellent performance in terms of energy resolution, gas gain and stability (as shown in Fig. 5.32); 3) Rim around the hole formed by full-etching process, the size of which can be varied between 10 μm and 90 μm, as depicted in Fig. 5.32 - this allows adjustment according to gas requirements.

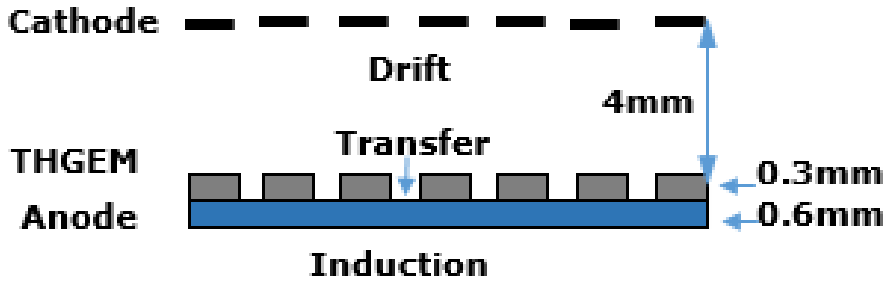

Figure 5.34: The schematic diagram of the WELL-THGEM.

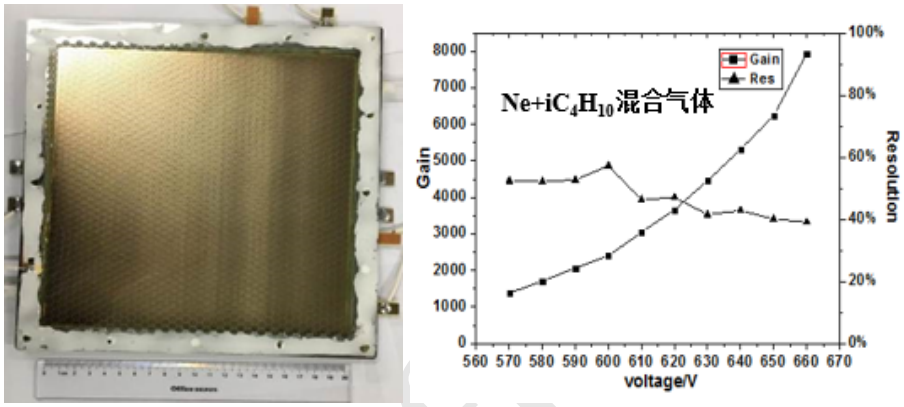

Figure 5.35: The photograph(left) and performance (right) of the WELL-THGEM detector.

Fig. 5.34 shows the schematic diagram of a new THGEM detector, where a micro-plate directly attached to the readout plate, since the micro-porous structure similar to a well, known as the well-type THGEM (WELL-THGEM). This structure contains of a single-layer THGEM, so that the thickness of detector can be reduced to $4 \sim 5$ mm, and the total thickness of the detector including ASIC electronics could be lowered to about 6 mm.

A $20cm \times 20cm$ WELL-THGEM detector using thin-type THGEM have been developed, and the basic performances such as the gain curve, uniformity and energy resolution were studied and shown in Fig. 5.35.

In addition, Researches on large THGEM detectors have been carried out. Single THGEM detectors and Well-THGEM detectors are being developed to reduce detector instability and inefficiency. Gas recycling systems are built to lower gas consumption and pollution. The achieved THGEM detection rate of 1 MHz/cm^2 with efficiency greater than 95% already meets the CEPC requirements.

THGEM digital readout system A MICRO-mesh gaseous structure Read-Out Chip (MICROROC), which is developed at IN2P3 by OMEGA/LAL and LAPP microelectronics groups was used to read out the THGEM-based SDHCAL. The MICROROC is a 64-channel mixed-signal integrated circuit based on 350 nm SiGe technology. Each channel of the MICROROC chip contains a very low noise fixed gain charge preamplifier which is optimized to cover a dynamic range from 1 fC to 500 fC and allow a input detector capacitance of up to 80 pF, two gain-adjustable shapers, three comparators for triple-threshold readout and a random access memory used as a digital buffer. Otherwise, it have a 10-bit DAC, a configuration register, a bandgap voltage reference, a LVDS receiver shared by 64

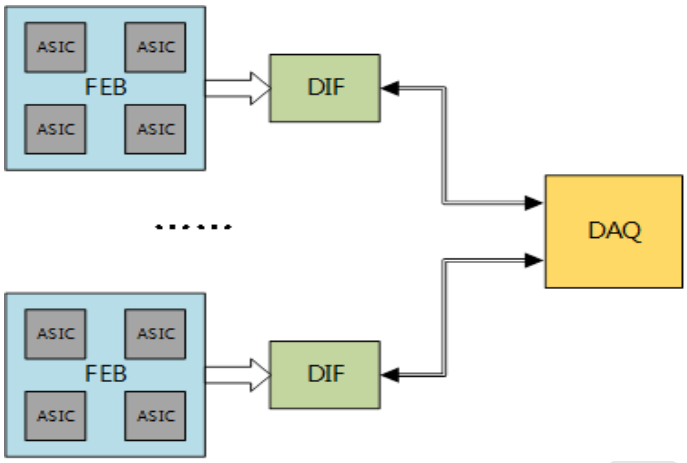

Figure 5.36: The schematic diagram of the readout system.

channels etc. A 1.4 mm total thickness is achieved by using the Thin Quad-Flat Packaging (TQFP) technology.

The readout system structure as shown in Fig. 5.36 is developed on the Scalable Readout System (SRS), which is proposed by the RD51 Collaboration. It is composed of a front-end board (FEB), a detector interface board (DIF) and a data acquisition card (DAQ). The FEB (also called ASU-Active Sensor Unit) carries all the front-end ASIC, together with the readout plane of GEM detector. The DIF in charge of ASIC control and data connection, plugs to the FEB using high density connector. The DAQ card is designed to serve several DIF boards. It distributes the clock, command and trigger to different DIF and gather the data from DIF boards.

The FEB is the combination of readout pads of GEM detector and readout ASICs. In order to minimize the dead-area of the detector, the FEB is designed to use blind and buried via technology. Considering the signal integrity and costs, $8 \sim 10$-layer PCB is a suitable choice. The thickness of this kind of PCB can be as thin as 1.2 mm. This means contain the 1.4 mm MICROROC, the total thickness of FEB can be made within 3 mm. Limited by PCB manufacturing technology, a well-performance FEB can be made as large as $50cm \times 50cm$. If a $1m^2$ prototype is made, it necessary to combine 4 FEB into one detector layer.

The DIF controls the FEB and gather the data of ASIC and can be tailored to the particular front-end ASIC with the particular application, giving the users the freedom of choice for the front-end circuit. Just changing the ASIC and DIF, the same design can be used both in ECAL and HCAL. Considering the data rate and costs, the master device of DIF can be some low-cost FPGA and the communication interface to the DAQ can be both USB type C or fiber-optical.

The DAQ card accesses the command from a server and controls several DIF. The design goal of the DAQ card is a universal controller for both ECAL and HCAL. Once a mature DAQ card is finished, it can be in common use even if we change the front-end ASIC.

Besides the readout ASIC and card, the clock synchronization design is an important block of the system. There are two kinds of clock source in the readout system, local clock and global clock (Usually, this kind of clock may be hundreds or thousands of meters from calorimeters). The local clock goes through the PLL and low-skew fan-out chip to the DIF,

Draft v0.2

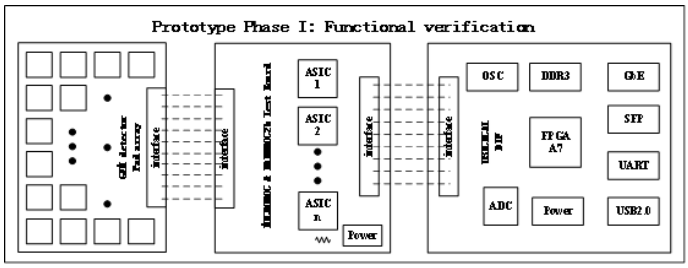

Figure 5.37: The diagram of the phase I design.

Figure 5.38: Pictures for the phase I design.

then the DIF distribute the clock to the FEB for local synchronization. If a global clock source is used, it is necessary to module there clock to optical signal and distribute the clock through fiber-optical. Another circuit call Clock and Data Recover (CDR) is needed for clock rebuild. The rebuild clock is global synchronized and can be used as local clock in one DAQ card.

A phase I design (in Fig. 5.37 and Fig. 5.38) is completed to verify this kinds of readout structure and to test the performance of the MICROROC chip. In this design we separate the front-end ASIC from the detector readout plane for single test the ASIC. It contains the readout array of the GEM detector, front-end ASIC board and DIF board. The structure of the design is shown in figure 2. The GEM detector is $30cm \times 30cm$, and the readout pad detector is 1 cm^2. To ensure signal integrity and low cross talk the readout plane is designed 8-layer PCB with 4 ground plane to separate the signal and shield. The pads signal is connector to the front-end ASIC board via soft-board made from kapton. The front-end ASIC board composed by 4 ASIC controlled in daisy chain. The DIF board controls the front-end ASIC board and transmit data to the upper monitor. The main controller of DIF is Xilinx A7 100T series, a low cost FPGA. The data can be readout via USB2.0 or fiber-optical or Giga-bit Ethernet. We also reserve an ADC on DIF for monitoring the analog test signal. Figure 3 shows the picture of these three board. The primary performance studies for this design have been carried out. For all the ASIC channel, the maximum noise is 0.35 fC, which means it beyonds the best performance of this ASIC distinguishing at least 2fC signal. The linear region of the high gain shaper reaches to $\sim$ 140 fC, and the low gain shaper is $\sim$ 500 fC. All the result shows that this ASIC can work well with the detector and the readout scheme is effective.

In order to optimize the design, a next stage design (shown in Figure 5.39) based on the test results have been proposed and put into effort. In this version, the MICROROC chips are planed to be mounted on the bottom side of the readout plane, utilizing blind buried via technology. A 10-layer PCB with 3 ground plane and 2 power plane will ensure good signal integrity and low crosstalk. Considering the cost and performance, we choose 2 kinds of blind via (Layer1 - Layer2 and Layer9 - Layer10) and 1 kinds of buried via

Draft-v0.2

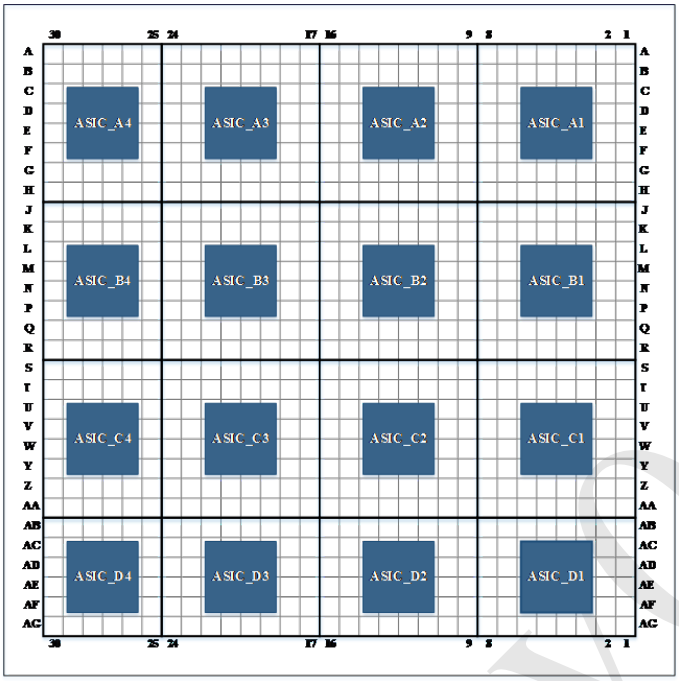

Figure 5.39: The Design scheme for next stage FEB.

(Layer2 - Layer9). This board is the real FEB in the system structure. The design diagram is shown in figure 4. Besides FEB, the design of the DIF board is going on the same time. The DIF can plug to FEB directly or through a soft-board made from kapton. After the DIF design, we will consider the design of DAQ board. We can share the same DAQ board with ECal readout system. The DIF is connected to DAQ through USB type C wire or fiber-optical. Besides the SRS readout structure, a new system name FELIX is under research, which can made the whole system trig less readout.

5.3.3 Analog Hadronic Calorimeter based on Scintillator and SiPM

A high-granularity hadronic calorimeter plays an essential role in PFA-based experiments such as CEPC. It allows separation of the energy deposits from charged and neutral hadrons. The contribution of the neutrals to the jet energy, around 10% on average, fluctuates over a wide range from event to event. The AHCAL (Analog Hadron CALorimeter) is a sampling calorimeter with steel as the absorber and scintillator tiles with embedded electronics. The moderate ratio of hadronic interaction length (I=17cm) to electromagnetic radiation length (X_0 = 1.8 cm) of steel, allows a fine longitudinal sampling in terms of X_0 with a reasonable number of layers.

Various calorimetry options are being developed to address challenges from the stringent performance requirements on future lepton collider experiments for precision measurements of the Higgs boson and for searches of physics beyond Standard Model. Within the CALICE collaboration, a large technological prototype [26] using scintillator tiles and SiPMs is currently being built to demonstrate the scalability to construct a final detector via automated mass assembly. Though this prototype is aimed for the future International Linear Collider (ILC), the outcome of CALICE-AHCAL R&D activities can be an essen-

Draft-V0.2

tial input for the conceptual design of the hadron calorimeter system at the future Circular Electron Positron Collider (CEPC).

5.3.3.1 AHCAL geometry and simulation

The AHCAL will consist 40 sensitive and absorber layers, and the total thickness is about 100cm. The AHCAL barral consists 32 supper module, each super module consists 40 layers, figure5.40 shows the AHCAL structure. Figure5.41 shows the AHCAL one layer structure. The scintillator tiles wrapped by reflective foil are used as sensitive medium, interleaved with stainless steel absorber. The thickness of active layer including the scintillator and electronics is 4mm to 5mm, but the baseline is 5mm. More studies of the scintillator thickness will be carried out.

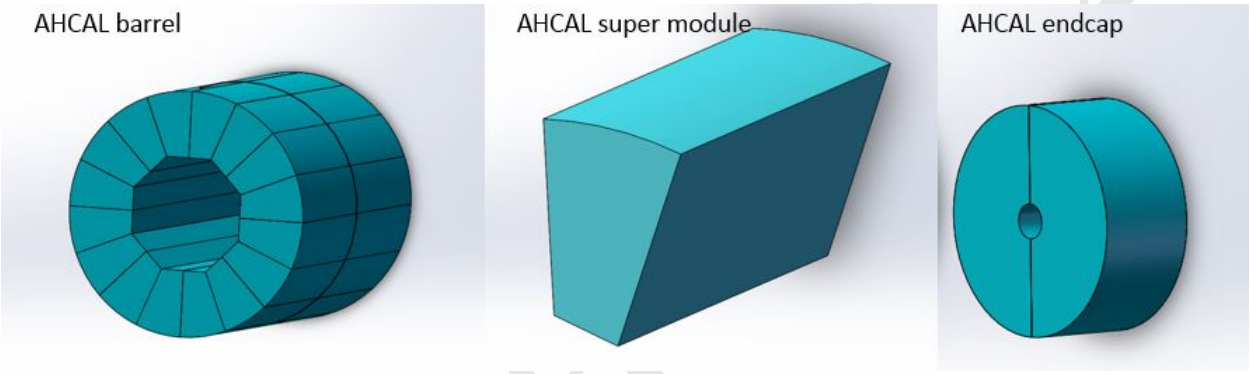

Figure 5.40: Side view of one layer in AHCAL

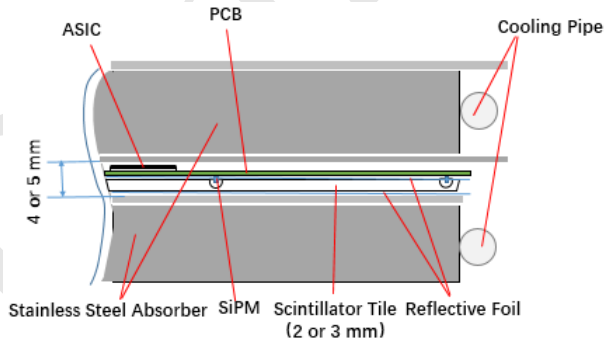

Figure 5.41: Side view of one layer in AHCAL

The structure of scintillator tiles is shown in Figure 5.42. A dome-shaped cavity was processed in the center of the bottom surface of each tile via mechanical drilling and polishing. The diameter and height of cavity [27] are 6mm, 1.5mm, respectively, as shown in Figure 5.42 (right). Good response uniformity and lower the dead area will be achieved by the design of cavity. More optimization of cavity structure will be done by geant4 simulation.

The AHCAL prototype detector simulated by Geant4 which was encapsulated in toolkit including several models. The detector model used here was CEPC_v1 detector model and the sub detector was SiCal. The geometry information was extract by Mokka at runtime and the generated events was stored in Slcio, which contains primary information regarding the energy deposition, hit position, time and Monte Carlo particle causing the

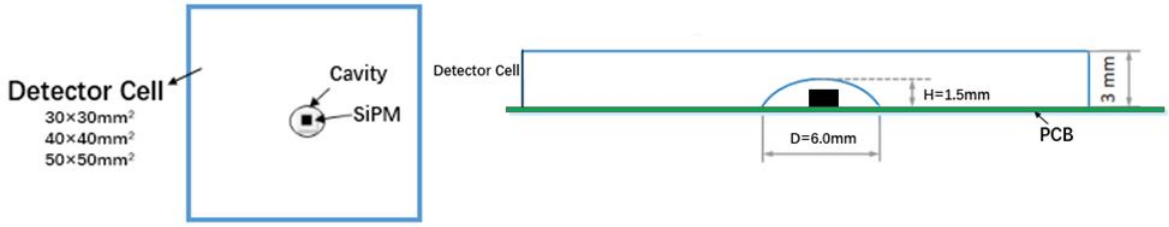

Figure 5.42: Top view of a detector cell (left) and sectional view of a detector cell with a dome-shaped cavity (right)

energy deposition. It can read out by Marlin and translate into Root files for analyzing. The ECAL was simulated 30 layers. The HCAL is a structure of 40 active layers interleaved with 20 mm steel absorber plates. Each active layer is assembled from 3mm plastic scintillator, also the readout layer thickness is 2mm PCB, detector cell size is 30×30×3 mm^3. Their structure is shown in Figure 5.43.

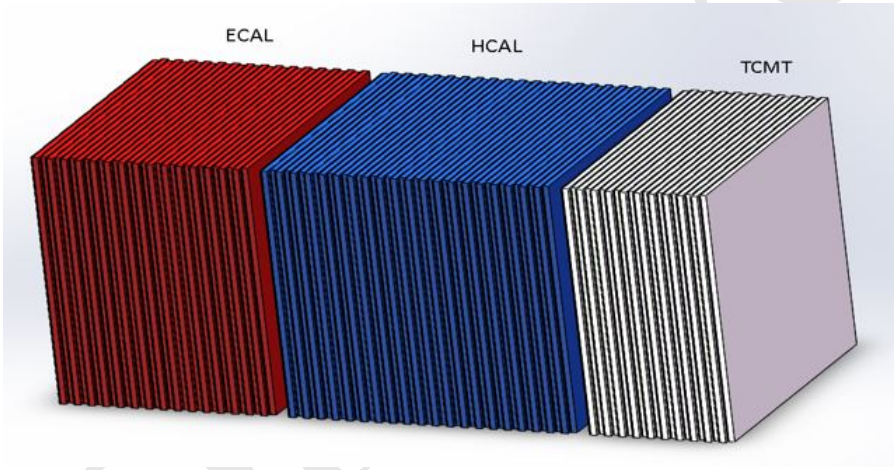

Figure 5.43: The structure of simulated calorimeters which is a part of the simplify geometry. Red part is the the Silicon ECAL, Blue part is the scintillator AHCAL

$$E_{REC} = a \times E_{ECAL} + b \times E_{HCAl} \tag{5.3}$$

For getting the resolution of calorimeters (ECAL and AHCAL) which structure was show in figure 5.43. Formula 5.3 is the energy reconstruction formula[28], the coefficients a and b in this formula represent ECAL and HCAl calibration constant. After optimization, the calibration constants are a=44.4 and b=44.2 respectively which were corrected by energy of 60GeV. Calibration constants can correct the energy leakage from the calorimeters. So it can be used formula 5.4 [28] for calculating the resolution. The energy resolution result shows in figure 5.44. For the resolution is better than the result of CALICE, the reason should be simulation ignore the response difference between detector cells. For the energy linearity, the slope value is 0.99, which means the reconstruction energy is essentially linear.

$$\frac{\sigma}{E} = \frac{p_0}{\sqrt{E}} + p_1 \tag{5.4}$$

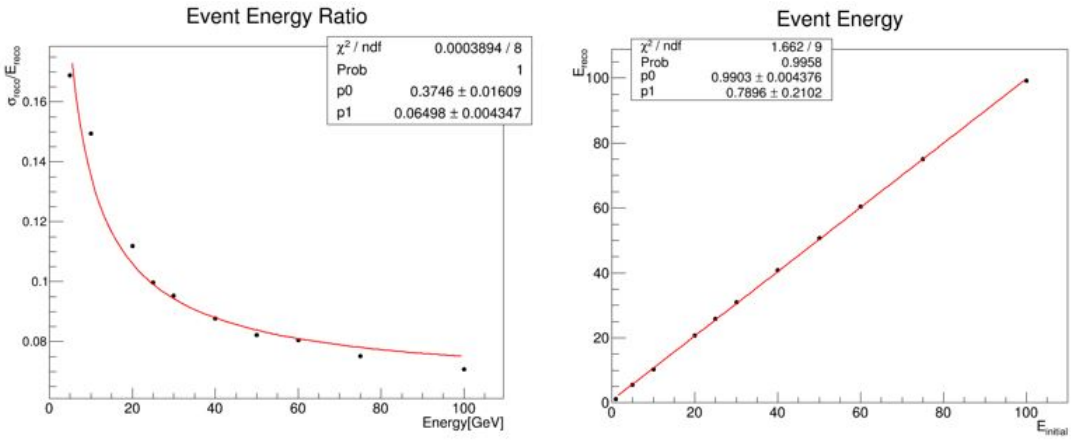

Figure 5.44: Left figure is energy resolution, right figure is the result of reconstruction energy linearity

5.3.3.2 Plastic Scintillator detector cell design and test

According the research results of CALICE collaboration, $30 \times 30\text{mm}^2$ scintillator detector cell size is optimized size. The simulation results of CALICE collaboration [29] also suggest that it is possible to use the detector cells of larger sizes. It will reduce nearly half electronics channels by using $40 \times 40\text{mm}^2$ size detector cell instead of $30 \times 30\text{mm}^2$ size. Therefore, the construction costs can be greatly reduced if the larger detector cells can meet the physics requirements. Two larger sizes of detector cells were considered. Four kinds of scintillator (Type: BC408) tiles with different sizes were fabricated and tested.

The SiPM is soldered onto a readout Printed Circuit Board (PCB) and the scintillator tile wrapped by ESR reflective foil is directly glued onto the PCB. A cavity design provides enough space for the SiPM package and improves collection efficiency of the light produced by incident particles penetrating the tile at different positions.

A strongly non-uniform tile response can lead to a distortion of the energy reconstruction in a complete calorimeter, and also compromises the calibration of the detector cells based on single particle signals. Three different sizes tiles ($30\times30\times3\text{mm}^3$, $30\times30\times2\text{mm}^3$ and $50\times50\times3\text{mm}^3$) were tested by the Hamamatsu MPPC S12571-025P and S13360-025PE. The spatial distribution of p.e. (photon equivalents) number with different detector cell areas are shown in Figure 5.45. The result shows that the number of p.e. in the center area is little higher than that of the surrounding area. The 100% of the cell signal amplitude is within 10% deviation from the mean value for $30\times30\text{mm}^3$ cell. The 94% of the cell signal amplitude is within 10% deviation from the mean value for $50\times50\times3\text{mm}^3$ cell. The three detector cells show good response uniformity.

Seven detector cells of different sizes, polishing methods and wrapping foil types were measured and summarized in figure 5.46. The larger the area of the cell is, the less p.e. are detected, and the results of same size cells varied greatly because of the polishing methods. As shown in the table that the ESR foil performs better than the TYVEK reflective foil.

The detection efficiency of $30\times30\times3\text{mm}^3$ and $50\times50\times3\text{mm}^3$ were measured by the cosmic ray test. The detection efficiency of $30\times30\times3\text{mm}^3$ and $50\times50\times3\text{mm}^3$ cells are 99%, 98.2%, respectively. According the cosmic-ray test result, the detection efficiency of $30\times30\times2\text{mm}^3$ with S13360-025PE MPPC also can reach to 98%.

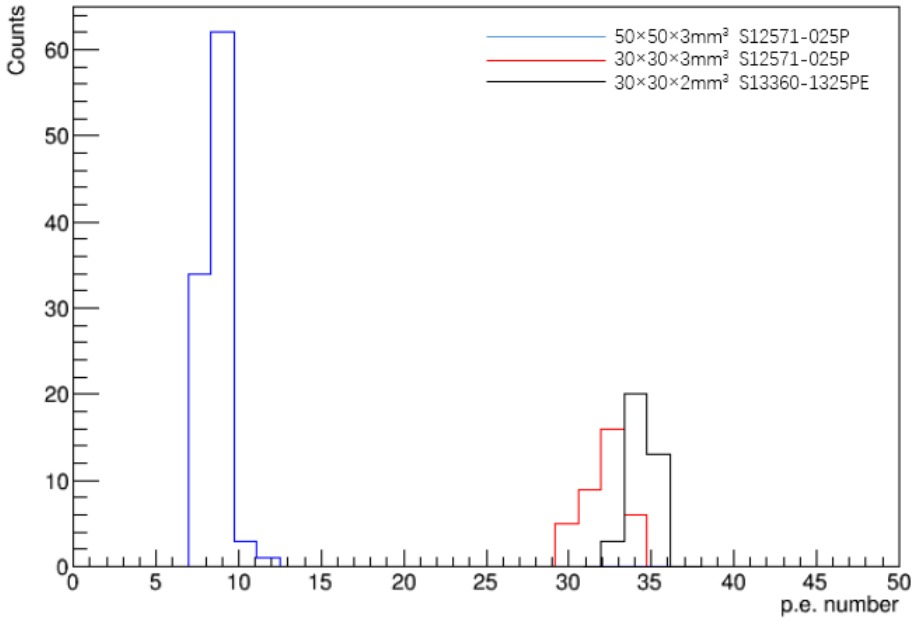

Figure 5.45: The uniformity measurement result of $30\times30\times3mm^3$, $50\times50\times3mm^3$ and $30\times30\times2mm^3$ detector cell

No.	Detector Cell	MPPC Type	Reflective Foil Type	Mean $N_{p.e.}$	Polishing Methods
1	$30\times30\times3mm^3$	S12571-025P	ESR	31.39±0.65	Ultra Precise Polishing
2	$30\times30\times3mm^3$	S12571-025P	ESR	22.55±0.7	Precise Polishing
3	$30\times30\times3mm^3$	S12571-025P	ESR	18.92±0.39	Rough Polishing
4	$30\times30\times3mm^3$	S12571-025P	TYVEK	13.63±0.33	Precise Polishing
5	$40\times40\times3mm^3$	S12571-025P	ESR	14.89±0.73	Precise Polishing
6	$50\times50\times3mm^3$	S12571-025P	ESR	9.87±0.43	Precise Polishing
7	$30\times30\times2mm^3$	S13360-1325PE	ESR	33.89±0.49	Precise Polishing

Figure 5.46: Cosmic-ray measurement results of detector cells with different sizes

Several size plastic scintillator detector cells of AHCAL were tested. The response uniformity, cosmic-ray responses and detection efficiency of detector cells were measured. The good response uniformity and high detection efficiency results show that scintillator detector cells are acceptable for AHCAL. The size of $30\times30\times3mm^3$ detector cell is the baseline of AHCAL and more optimization of the detector cell size will be done by the simulation and experiment.

5.3.3.3 NDL EQR-SiPM for CEPC AHCAL

Now, several kind SiPM was developed such as Hamamatsu MPPC, First Sensor SiPM and NDL EQR-SiPM, they have been introduced in scintillator ECAL. The SiPM with epitaxial quenching resistors (EQR SiPM) is one of the main SiPM technologies now under development. This kind SiPM was developed in China. As shown in Figure5.47, each APD cell (pixel) forms a high electric field, composing an enriched region between N-

type epitaxial silicon substrate and P++ cap layer, and it employs the un-depleted region in the epitaxial silicon layer below P/N junction as the quenching resistor. Compared to conventional SiPM configurations that employ poly-silicon quenching resistors on the device surface, it is easier to achieve high density and small micro APD cells, thus obtaining a small junction capacitor; it is also easy to realize low resistance for the quenching resistors, simply based on the resistivity of the epitaxial layer and the geometrical scale. As a result, a low RC time constant of the pixel, or a short recovery time and fast counting rate for the EQR SiPM, can be expected. In addition, thanks to the high geometrical fill factor of the EQR SiPM with a high density of micro APD cells, both wide dynamic range and adequate PDE can be realized at the same time, which satisfactorily resolves the conflict between dynamic range and PDE existing in most commercial SiPMs with poly-silicon stripes as quenching resistors.

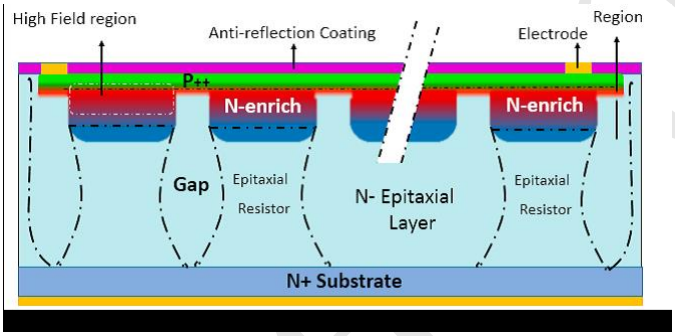

Figure 5.47: Schematic structure of EQR SiPM; APD cell consists of N-enriched regions forming high electric fields between the N-type epitaxial silicon wafer and the P++ surface layer, the un-depleted region in the epitaxial silicon layer below the P/N junction as the quenching resistor, and the APD cells are isolated from each other by the Gap depletion region.

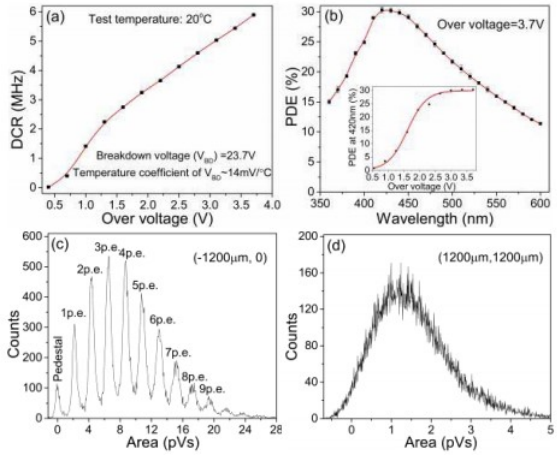

Figure 5.48: Characteristics of NDL EQR PS-SiPM. (a) DCR vs over voltages. (b) PDE vs the wavelength of 360nm-600nm at over voltage of 3.7V; peak PDE is at 420nm and is improved with the increase of over voltage as shown in the inset. (c), (d) show the pulse area distribution collected by cathode at the incident light positions of (1200um, 0) and (1200um, 1200um) respectively. Because of the pedestal electronic noise, the pulse area is starting at negative values.

Furthermore, the fabrication technology of NDL EQR-SiPM is simple, it omits the fabrication steps for producing quenching resistors on the surface; thus, the price of NDL

NDL EQR-SiPM VS Hamamatsu MPPC

	NDL SiPM		Hamamatsu MPPC	
Effective Active Area	11-3030 B-S	22-1414 B-S	S13360-3025PE	S13360-1325PE
	3.0×3.0 mm^2	1.4×1.4 mm^2 (2×2 Array)	3.0×3.0 mm^2	1.3×1.3 mm^2
Effective Pitch	10 μm	10 μm	25 μm	25μm
Micro-cell Number	90000	19600	14400	2668
Fill Factor	40%	40%	47%	47%
Breakdown Voltage (V_b)	23.7±0.1V	23.7±0.1V	53±5V	53±5V
Measurement Overvoltage (V)	3.3	3.3	5	5
Peak PDE	27%@420nm	35%@420nm	25%@450nm	25%@450nm
Max. Dark Count (kcps)	< 7000	<1500	1200	210
Gain	2×10^5	2×10^5	7.0×10^5	7.0×10^5
Temp. Coef. For V_b	17mV/° C	17mV/° C	54mV/° C	54mV/° C

Figure 5.49: Performance compare between EQR SiPM and Hamamatsu MPPC with similarly high micro-cell density.

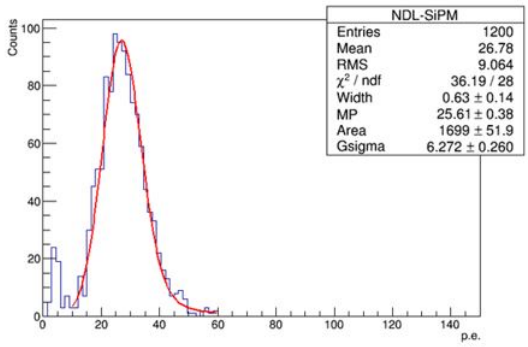

Figure 5.50: Sr-90 electron source test result of scintillator detector cell readout by NDL-SiPM

EQR-SiPM is low. Its good property and low price can meet AHCAL requirement, and it will be tried to be used on CEPC-AHCAL detector. Figure 5.48 show some performance of NDL EQR-SiPM, and figure 5.49 show the performance compare between NDL EQR-SiPM and Hamamastu MPPC. The NDL EQR-SiPM will be main option of CEPC AHCAL light sensor. The Sr-90 electron source test result of NDL EQR-SiPM (1.4×1.4mm^2) couple with scintillator have been shown in figure 5.50. The light output of detector cell reach to 25.6 p.e., and this result similar to Hamamatsu MPPC.

5.3.3.4 Electronics and DAQ

Front-end electronics ASIC: High-density electronics is indispensable to instrumentation of high-granularity calorimetry. An ASIC chip named SPIROC, developed by the OMEGA group, is capable to handle 36 SiPMs. For each channel, it can be operated in an auto-trigger mode and has a dual-gain charge preamplifier with high dynamic range. It allows to measure for each channel the charge from 1 to 2000 photo-electron and the time within 1 ns using a 12-bit digitizing circuit. With one 8-bit 5V input DAC per channel, the bias voltage for each SiPM can be adjusted to reach its optimum. In each channel, there are 16 analogue memory cells that can buffer both charge and timing signals to be

digitized afterwards consecutively. The digitization circuit is shared for both charge and timing measurements to minimize the power consumption, which needs to be as low as $25\ \mu W$ per channel. The latest version SPIROC2E has been improved in many aspects and its packaging has changed to a thinner BGA, which ensures a compact design for HBU and allows better automated mass soldering.

HCAL Base Unit: A merit of the AHCAL electronics is flexibility. One full AHCAL active layer can be constructed by connecting several base units (namely HBUs) via connectors, each with 12×12 channels in a square plate of $36 \times 36\ cm^2$. The exact granularity is being optimized for CEPC to balance between the detector performance and the number of total channels. To achieve a compact HCAL design, the PCB for each HBU should be thin enough and a 6-layer PCB within 1 mm thickness is proved to be feasible.

As a semiconductor detector, SiPM is intrinsically sensitive to environmental changes, especially temperature. Thus each SiPM needs on-site calibration, which requires an on-board LED circuit for each channel. There is an LED circuit at each channel of an HBU, which can emit UV light to a scintillator tile. Using these photons, the gain of a SiPM can be extracted and monitored.

Detector interface: ASIC chips are controlled by an interface board named DIF (Detector Interface). One DIF board handles a full HCAL active layer (a long slab with up to 6×3 HBUs), corresponding to 72 ASICs in total. The expected data rate per DIF can be estimated based on the event rate at HCAL, which depends on the beam structure at CEPC.

LED calibration board: A dedicated LED calibration board is needed to control all LED circuits in an HCAL active layer. It can send trigger signals for the proper SiPM calibration.

Power board: SiPM operation relies on a proper reversely bias voltage. Therefore, between power supplies and ASIC chips, a power board is required to distributing the bias voltage to each SiPM. This power board can also play an important role in regulating voltages for protection and smooth working of SiPMs. Like the DIF board, it would be feasible to use only one such board for an active HCAL layer (up to 6×3 HBUs).

DAQ system: DAQ system is also required to be compatible to the final detector layout, where two hardware parts are essential. One part is so-called LDA (Link to Data Aggregator), which collects all the data via DIFs from active layers in an HCAL segment and transmit them to a back-end PC for further processing or storage. Smart units like FPGAs are equipped on this board for data packaging and transmission. Modern FPGAs integrated with RAMs are an ideal option to have a capability of data buffering and some advanced feature like system on chip.

The other key hardware part is so-called CCC (Clock and Control Card), which provide a global clock signal and synchronize DIFs. Control signals are also sent to DIFs including starting and stopping acquisition.

5.3.3.5 Cooling system

The SPIROC ASIC chip will be used in CEPC AHCAL, the power consumption of SPIROC has been studied by CALICE collaboration [30]. Inside active layer, the total power consumption of SPIROC ASIC chip and SiPM is about 40μW/channel for ILD power pulsing mode. For CEPC continue mode, the power consumption is 40 mW/channel. The scintillator detector cell size is 30×30mm^2, and the total channel number is a bout 5

Draft-V02

million. For whole AHCAL, the total power consumption from ASIC chip is about 20kW. The copper cooling water pipes will be buried in stainless steel absorber. It is shown in layer structure just as figure 5.41.
The calibration system, the detector interface and the power board will be installed in gap between barrel and endcap. For CALICE collaboration, the total power consumption is about 28kW [31] for power pulsing mode. The estimation of total 18 HBUs power consumption is about 0.9kW for CEPC continue mode. For whole CEPC AHCAL, the total power consumption from electronics is about 1740kW. It is a big number. Of course, some optimize will be done to reduce the power consumption. A cooling system include water cooling pipe and cooling plate will be installed on this electronics system board. The cooling system will meet this requirement.

5.4 Dual-readout calorimetry

5.4.1 Introduction

Till now, the performance obtained in hadronic energy measurements has been by far worse than for the electromagnetic ones, since showers from single hadrons or jets develop an electromagnetic component, from π^0 and η production, that exhibits large event-by-event fluctuations and dependence on the particle type and energy [32].

As a matter of fact, the em fraction depends on the kind of particle initiating the shower (e.g., π, K, p) since, for example, impinging $\pi^{\pm}$ mesons can undergo a charge-exchange reaction with a nucleon as first interaction and generate a pure em shower, while a p cannot do that due to baryon number conservation.

Moreover, since π^0 production happens at any stage of shower development, the $< f_{em} >$ increases with the energy as well as with the depth ("age") of the shower.

The em and $non-em$ components of a hadronic shower are normally sampled with very different sensitivity, producing large differences in the measured signals, heavily affecting the energy resolution capability.

To overcome the problem two methods have been exploited: compensation and dual readout (DR). The first relies on equalising the detector response to electromagnetic and non-electromagnetic shower particles but requires the integration of the signals over large volumes (and long time) and leads to limited resolution for electromagnetic showers. The DR method avoids these limitations by measuring and accounting for the f_{em} on an event-by-event basis. The showers are sampled through two independent processes, namely scintillation (S) and Čerenkov (C) light emissions. The former is sensitive to all ionizing particles, while the latter is produced by highly relativistic particles only, almost exclusively found inside the em shower component. By combining the two measurements, energy and f_{em} of each shower can be simultaneously reconstructed. The performance in hadronic calorimetry may be boosted toward its ultimate limit.

The results obtained so far with prototypes, support the statement that fibre-sampling DR calorimeters may reach resolutions of the order of $10\%/\sqrt{E}$ for em showers and around $30-40\%/\sqrt{E}$ for hadronic showers, coupled with strong standalone particle-ID capabilities. This would allow $W \to jj$ separation from $Z \to jj$ by invariant mass, high-precision missing three-momentum reconstruction by subtraction, e-μ-π separation and tagging.

Draft V0.2

Indeed, while the DR concept has been extensively proven and experimentally validated in a series of beam tests, the use of standard Photo-Multiplier (PM) tubes to read out the S and C light has so far limited its development towards a full-scale system compliant with the integration in a particle detector at a colliding beam machine. These limitations should be overcome using SiPM, low-cost solid-state sensors of light with single photon sensitivity, magnetic field insensitivity and design flexibility.

5.4.2 Principle of dual-readout calorimetry

The independent sampling of hadronic showers, through scintillation and Čerenkov light emission, allows to fully reconstruct, at the same time, energy and f_{em} of hadronic showers. In fact, the total detected signals, measured with respect to the electromagnetic energy scale, can be expressed as:

$$S = E\,[\, f_{em} + \eta_S \cdot (1 - f_{em})\,] \tag{5.5}$$

$$C = E\,[\, f_{em} + \eta_C \cdot (1 - f_{em})\,] \tag{5.6}$$

where $\eta_S = (h/e)_S$ ($\eta_C = (h/e)_C$) is the ratio of the average S (C) response for the $non-em$ component of hadronic showers, and the one for the em component (the response being defined as the average signal per unit of deposited energy). The system can be easily solved giving:

$$\frac{C}{S} = \frac{[\, f_{em} + \eta_C \cdot (1 - f_{em})\,]}{[\, f_{em} + \eta_S \cdot (1 - f_{em})\,]} \tag{5.7}$$

$$E = \frac{S - \chi C}{1 - \chi} \tag{5.8}$$

where:

$$\chi = \frac{1 - \eta_S}{1 - \eta_C} = \cot\,\theta \tag{5.9}$$

This is the simplest formulation of hadronic calorimeter response: an em part with relative response of unity, and a $non - em$ part with relative response η.

There are two unknowns for each shower, E and f_{em}, and two measurements S and C. The electromagnetic fraction, f_{em}, is determined entirely by the ratio C/S, and the shower energy calculated as in Eq. (4). Both S and C h/e ratios have event-by-event fluctuations and should be considered stochastic variables, nevertheless the average $<h/e>$ values are essentially independent of hadron energy and species [33–35]. The global parameter χ can be extracted with a fit to calibration data:

$$\chi = \frac{E_0 - S}{E_0 - C} \tag{5.10}$$

$$S = (1 - \chi)E_0 + \chi C \tag{5.11}$$

where E_0 is the beam energy.

The geometrical meaning of the θ angle can be understood by looking at the scatter plor of C versus S signals. In Figure 5.51, there are both (a) a prediction for the normalised scatter plot for protons and pions, and (b) the observed scatter plot for 60 GeV pions, in the RD52 lead-fibre calorimeter.

Draft-v0.2

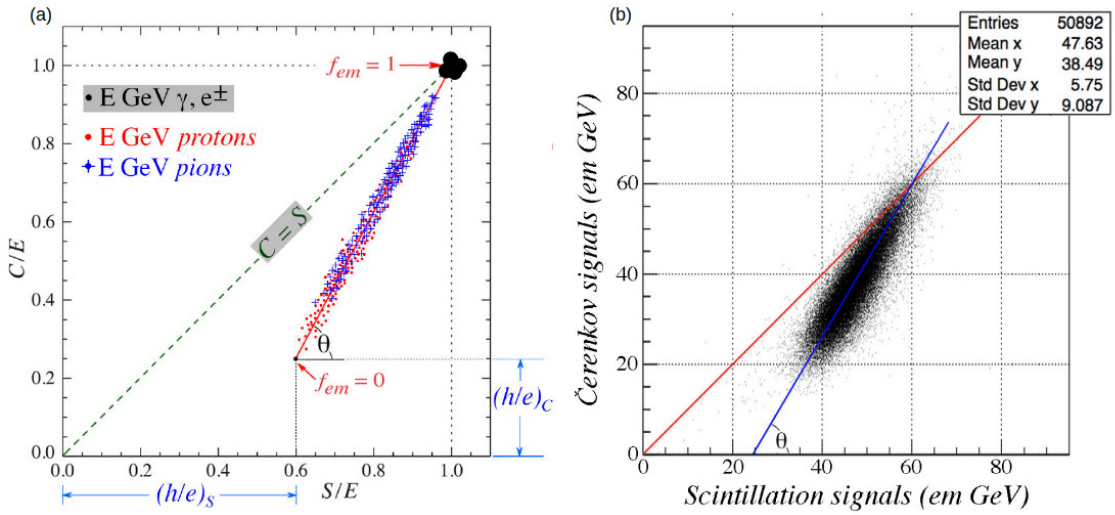

Figure 5.51: (a) Scatter plot of C/E versus S/E in a dual-readout calorimeter for p and π; (b) scatter plot of C and S signals for 60 GeV pions in the RD52 dual-readout lead-fibre calorimeter.

The plot in Figure 5.51(b) shows that the data points are located on a locus, clustered around a line that intersects the $C/S = 1$ line at the beam energy of 60 GeV. In first approximation, the signal generated in the Čerenkov fibres is produced only by the em components of the hadron showers. The smaller the em fraction f_{em}, the smaller the C/S signal ratio.

All signals are relative to the em scale meaning that both the Čerenkov and the scintillation responses are calibrated with electrons only, i.e. no hadronic calibration is required. This is one of the most qualifying points of dual-readout calorimetry.

The effectiveness of this approach has been probed by the DREAM/RD52 collaboration over a 15-year research program with a variety of detector solutions. Results and simulations [36–41] provide, so far, confidence that a fibre-sampling calorimeter, even without longitudinal segmentation, may meet the requirements of the CepC physics programme in a cost-effective way. Linearity and energy resolution, for both em and hadronic showers, $e/\pi/\mu$ separation, spatial resolution, all show adequate performance.

5.4.3 Layout and mechanics

5.4.3.1 Layout

A possible projective layout ("wedge" geometry, Figure 5.52) has been implemented. Based on the work done for the 4th Detector Collaboration (described in its Letter of Intent [42]), it covers, with no cracks, the full volume up to $|cos(\theta) = 0.995|$, with 92 different types of towers (wedges). A typical one in the barrel region is shown in Figure 5.53b, together with the fibre arrangement (Figure 5.53a): it has an acceptance of $\Delta\theta \times \Delta\phi = 1.27° \times 1.27°$, a length of about 250 cm ($\sim 10\lambda$) and contains a total of about 4000 fibres.

The sampling fraction is kept constant by fibres starting at different depths inside each tower.

This layout has been already imported in the simulations for the CepC detector. Preliminary results on performance are shown in the next chapters.

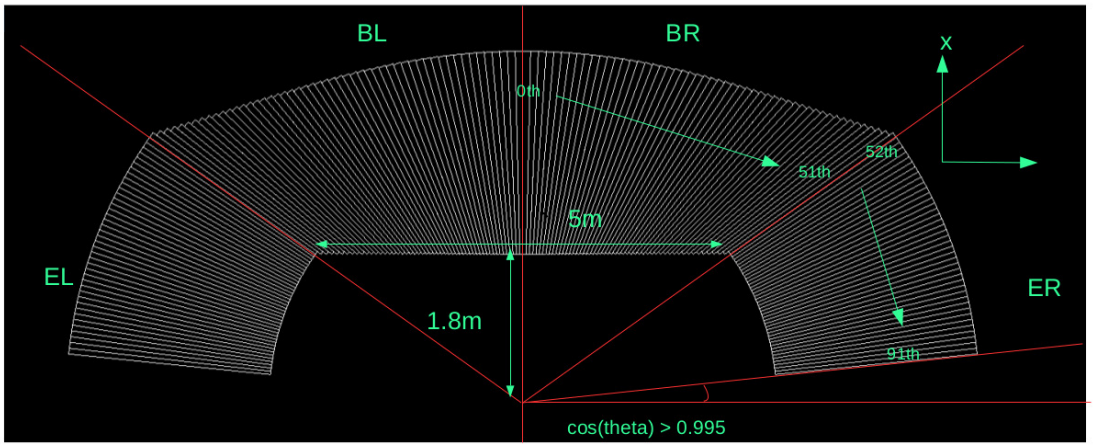

Figure 5.52: A possible 4π solution (called "wedge" geometry).

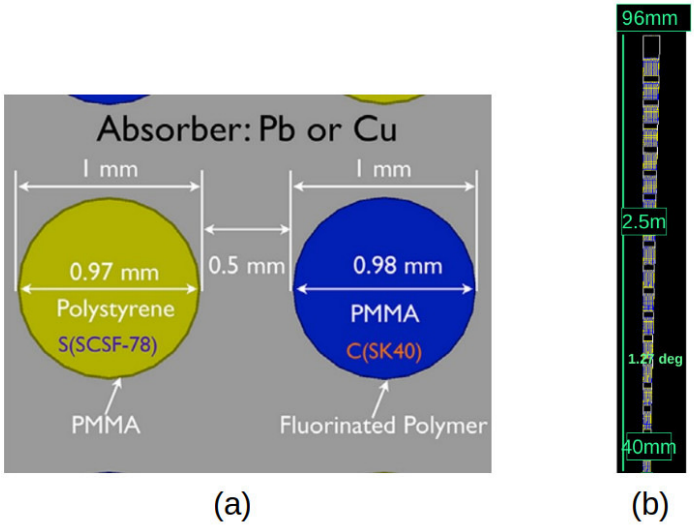

Figure 5.53: (a) Fibre arrangement inside the modules. (b) Dimensions of a module in the barrel region (at $\eta = 0$): from inside to outside the number of fibres more than doubles.

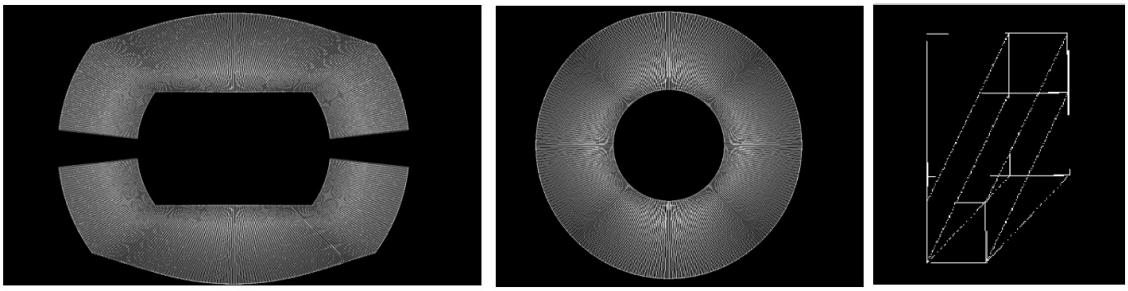

Figure 5.54: An alternative 4π solution (called "wing" geometry).

A different layout implementing the "wing" geometry (see Figure 5.54) is also under study and preliminary results on the em performance will also been shown in the next chapters. In this case, the calorimeter is made of rectangular towers coupled with triangular ones.

In both cases, the total number of fibres is of the order of 10^8.

5.4.3.2 Mechanics (material choice and machining)

Both lead and copper have been used as absorber materials by the DREAM/RD52 collaboration. Their main properties are:

$$Lead : \rho = 11.3\ g/cm^3,\ X_0 = 0.56\ cm,\ \rho_{Mol} = 1.60\ cm,\ \lambda_{int} = 170\ mm \quad (5.12)$$

$$Copper : \rho = 8.96\ g/cm^3,\ X_0 = 1.44\ cm,\ \rho_{Mol} = 1.56\ cm,\ \lambda_{int} = 151\ mm \quad (5.13)$$

meaning that, for hadronic showers, a full-coverage solution with lead will give broader and longer showers and a total mass 42% heavier than using copper. A full-containment $3 \times 3 \times 10\ \lambda^3$ prototype will need about 5 tons of material with lead and 2.8 tons with copper.

An possibly stronger reason in favour of copper is the fact that, being the Čerenkov light almost exclusively produced by the em shower components and the (e/mip) ratio 50% higher for copper than for lead, the Čerenkov light yield should be higher in copper, resulting in a better hadronic resolution.

On the other hand, copper extrusion, with the required tolerances in planarity and groove parallelism, is not yet an established industrial process. A variety of techniques (extrusion, rolling, scraping and milling) for machining the converter layers have been tested. None has been qualified for a large-scale production and identifying an industrial and cost-effective process, including moulding, is a key point.

Alternative copper alloys (brass, bronze) should be investigated as well, both for addressing the production process issues and for optimising the detector performance.

5.4.4 Sensors and readout electronics

To separately read out the signals from the S and C fibre forest and avoid oversampling of late developing showers is an issue that may be successfully addressed through the use of Silicon Photo-Multipliers (SiPM). They would allow the separate reading of each fibre and provide magnetic field insensitivity. In principle, assuming powering and cooling do not pose issues, the transversal segmentation could be made as small as possible.

SiPMs are low-cost solid state light sensors with single photon sensitivity that underwent an impressive development over the last years. Tests done in the last 2 years by the RD52 collaboration indicate that effective solutions for small-scale prototypes are very close already now. Thanks to their higher photon detection efficiency with respect to standard PM, the higher number of Čerenkov p.e. should result in an improved resolution for both em and hadronic showers. On the other hand, the scintillation light spans a very large dynamic range and saturation and non-linearity effects were observed already for low-energy em showers.

In Figure 5.55, the number of photoelectrons per GeV measured in July 2017, with a very small module ($1cm^2$ section, 32 + 32 fibres) is shown. The most relevant sensor

Draft-v0.2

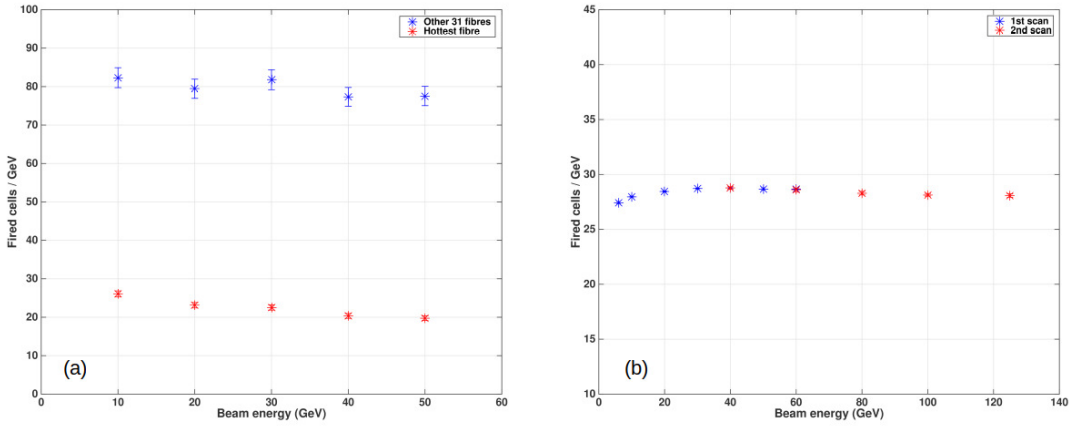

Figure 5.55: Number of p.e. per GeV for (a) the S (a) and the C (b) signal, as a function of the electron energy. In Figure a, the results, shown separately for the hottest fiber and for the sum of the signals measured by the other 31 scintillating fibers, were obtained at the (ultra low) PDE of $\sim 2\%$. The main sensor specifications are: 1600, 25×25 μm^2, cells, and a 25% nominal PDE.

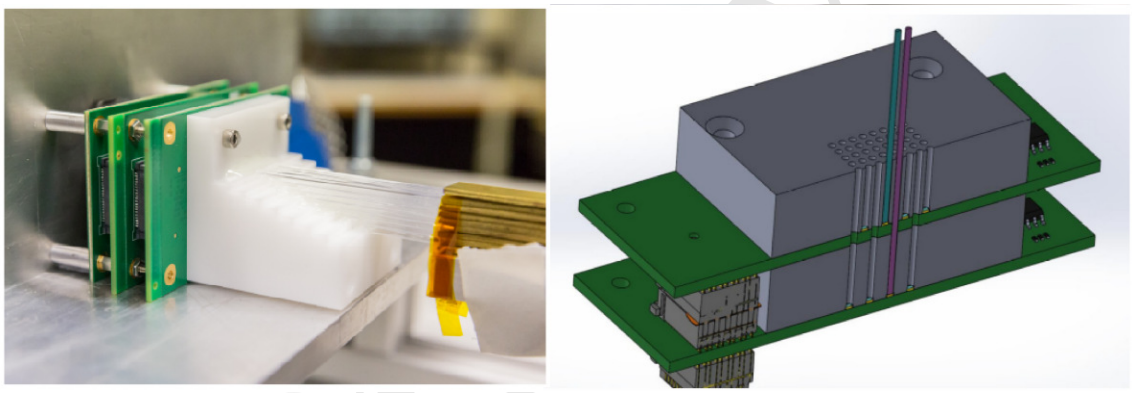

Figure 5.56: Staggered readout scheme: the scintillation and Čerenkov fibres are readout at different planes to avoid light leakage into neighbouring channels.

characteristics are 1600, 25×25 μm^2, cells, and a 25% nominal PDE. Due to the too large S light yield, the data for the S signal were obtained at the (ultra low) PDE of $\sim 2\%$, and corrected for non linearity. Rescaled to a 25% efficiency, the total number of S p.e. per GeV results to be $\sim 108 \times 12.5 = 1350$. By removing from the sum the hottest fibre, anyway suffering of non linearity effects, the estimate grows to ~ 1530 p.e. per GeV.

C signals show a linear response at ~ 30 p.e./GeV. It should be mentioned the fact that the shower containment was estimated to be $\sim 45\%$. Last but not least, the problem of large light leaks of the S signals to the neighbouring C SiPM, observed in the 2016 tests, looks largely attenuated - but not completely solved - thanks to a staggered readout of the S and C fibres (Figure 5.56). The contamination of the C signal was evaluated to be $\sim 16\% \pm 6\%$.

5.4.4.1 Sensor choice

As far as the scintillation light detection is concerned, saturation and non linearity should be solvable using higher density devices (e.g. with 10000, 10×10 μm^2, cells) in combination with some light filtering. The definition of the optimal dynamic range and the

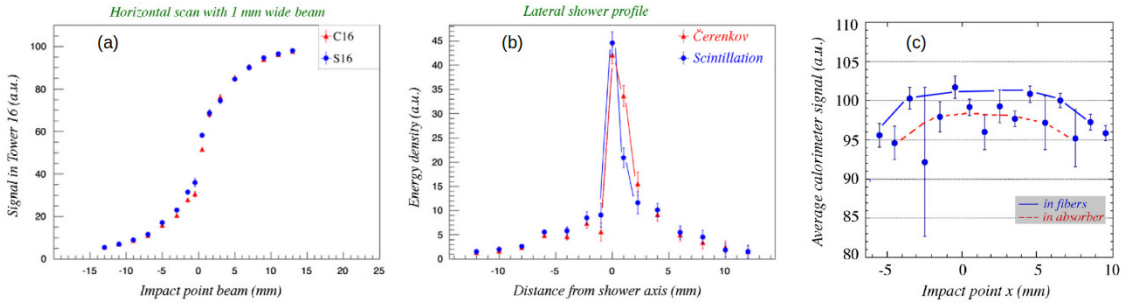

Figure 5.57: (a) The signal from a 1 mm wide beam of 100 GeV electrons, in a lead-fibre prototype, as a function of the impact point; (b) the lateral shower profiles derived from this measurement; (c) the dependence of the scintillation signal on impact point for a beam impinging parallel to the fibres.

qualification of existing SiPM in that regard, will be likely addressed in a short-term R&D phase.

For the Čerenkov light, improvements of the photon collection are possible with the use of aluminised mirror on the upstream end of the fibres. The acceptance cone may also be enlarged with the use of cladding with a different refractive index. Over some longer term, it could be possible that the R&D on new devices, such as Silicon Carbide (SiC) sensors, expected to provide exclusive UV sensitivity (i.e. visible-light blindness), will allow to obtain significantly larger p.e. yields.

5.4.4.2 Frontend electronics and readout

Concerning the frontend, the development shall certainly evaluate the use of Application Specific Integrated Circuits (ASIC), to handle and reduce the information to be trasferred to the DAQ system. A major question is finding the optimal way for summing signals from a plurality of sensors into a single output channel. A dedicated feature-extracting processor, capable of extracting timing information such as time-over-threshold, peaking, leading and/or falling times, may allow to disentangle overlapping em and hadronic showers without the need of longitudinal segmentation. With the present fibres, a resolution of the order of 100 ps corresponds to a spatial resolution of about 6 cm, along the fibre axis.

5.4.5 Performance studies with fibre-sampling prototypes

Different prototypes were built and studied by the DREAM/RD52 collaboration, with copper or lead as absorber and photomultipliers as light sensors [36–41]. With electrons and pions, in the range of $\sim 10 - 150\ GeV$, the response linearity was found at the level of 1% for both the em and the hadronic energy reconstruction (having applied the DR formula, equation 5.8, for hadronic showers). The em resolution was estimated to be close to $\sim 10\%/\sqrt{E}$, while the hadronic one was found at the level of $60 - 70\%/\sqrt{E}$, to be corrected for the fluctuations introduced by lateral leakage and attenuation length. More details can be found in the next paragraphs.

5.4.5.1 Electromagnetic performance

Figure 5.57a and 5.57b shows the radial shower profile and the sensivity to the impact point: the core of the signal spans just few mm. Figure 5.57c shows the dependence of the S signal on the impact point for particles entering parallel to the fibres. This introduces a constant term in the resolution that can be avoided with a small tilt of the fibre axis. In

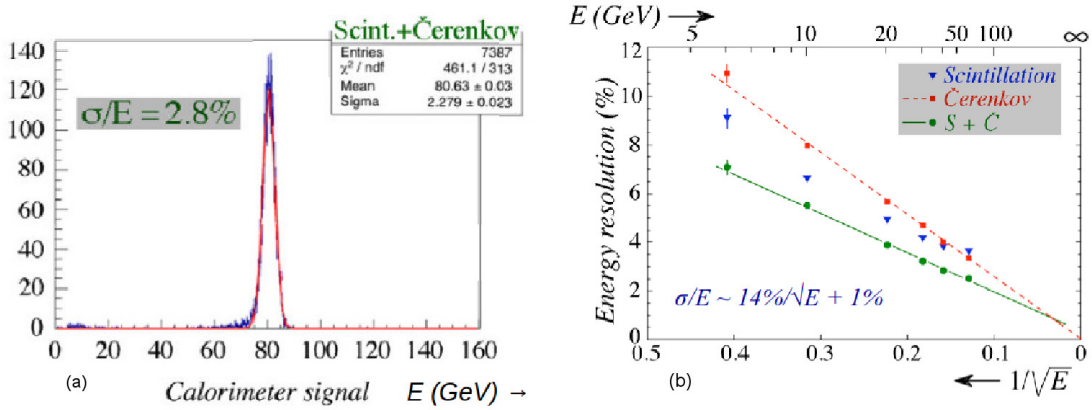

Figure 5.58: In a copper-fibre module: (a) signal distribution, with 40 GeV electrons, of the sum of all fibres; (b) the em energy resolution as a function of the beam energy. Shown are the results for the two types of fibres, and for the average combined signal.

the C fibres, the problem does not show up since the early (collimated) part of the shower produces photons outside the numerical fibre aperture.

For the reconstruction of the energy of em showers, S and C signals provide independent uncorrelated measurements, with different sensitivity of the response. They are affected by different problems: S signals have a photoelectron statistics of one or two order of magnitude higher than C signals, and their fluctuations are largely dominated by the sampling fluctuation of the energy deposits. C signal fluctuations are generally dominated by the limited photoelectron statistics, expecially at low energies. Nevertheless, at high energies, the constant term for C signals is negligible, giving a better resolution. Averaging the two measures improves the resolution up to a factor of $\sqrt{2}$. For the copper matrix, in Figure 5.58a the sum of S and C signals for 40 GeV electrons is plotted, while Figure 5.58b shows the em resolution, for S, C and the (average) combined signal.

5.4.5.2 Hadronic performance

The response of a lead-fibre matrix was studied with pion and proton beams [41]. The energy, reconstructed with the dual-readout relation (Eq. 5.8), shows a restored gaussian behaviour (Figure 5.59) and linearity of the response.

The comparison of p and π signals confirms that the DR method largely compensates for the differences in shower composition.

The limited lateral size of the matrix (about 1 λ) was allowing to collect, in average, $\sim 90\%$ of the shower energy so that leakage fluctuations were dominating the resolution capability (that was improving by a factor of ~ 2 while selecting well contained showers). The resolution was also affected by the finite light attenuation length of the fibres, causing early starting showers to be observed at lower signal values. The hadronic resolution, to be corrected for both effects, was reconstructed to be $\sim 70\%/\sqrt{E}$.

5.4.5.3 e/π separation

Four discriminating variables were identified for implementing e/π separation: the fraction of energy in the central tower, the C/S signal ratio, the signal starting time, the total charge/amplitude ratio, shown in Figure 5.60.

Draft-v0.4

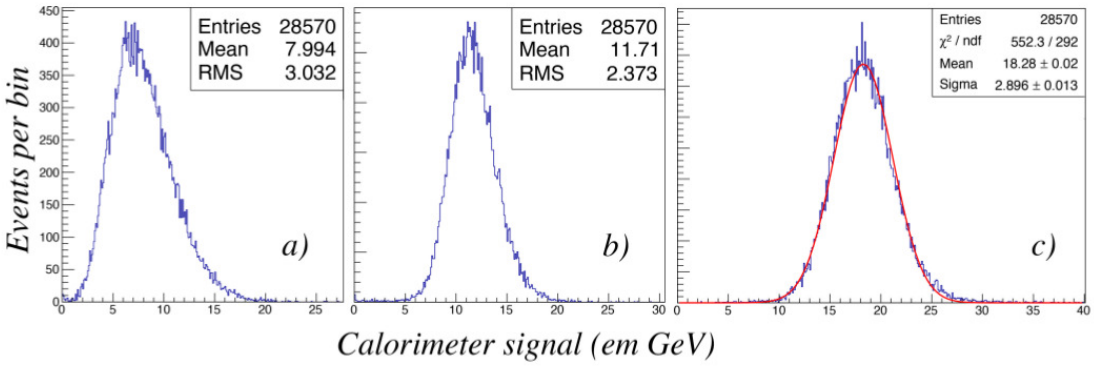

Figure 5.59: Signal distributions for 20 GeV π^- particles in a lead-fibre matrix. Shown are the measured (a) Čerenkov and (b) scintillation signal distributions as well as (c) the distribution obtained by combining the two signals according to Equation 5.8, with $\chi = 0.45$.

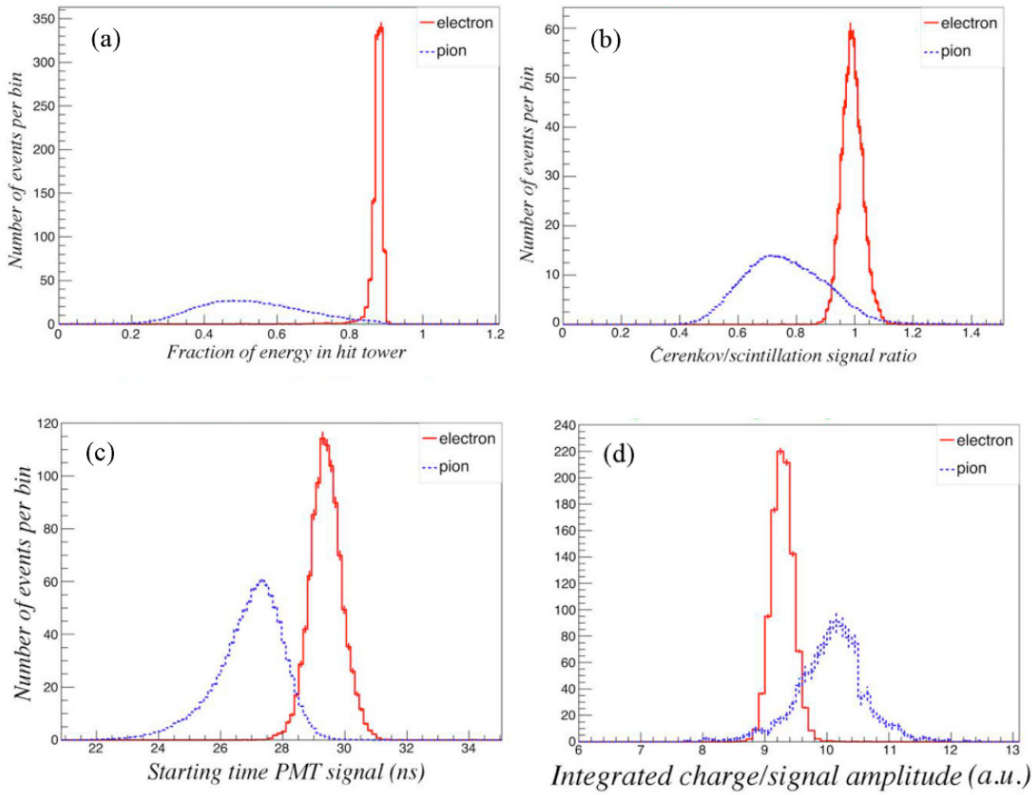

Figure 5.60: Distribution of four discriminating variables for 60 or 80 GeV electrons and pions: (a) energy fraction deposited in the hit tower; (b) C/S signal ratio in the hit tower; (c) starting time of the PM signal; (d) ratio of the integrated charge and the amplitude of the signals.

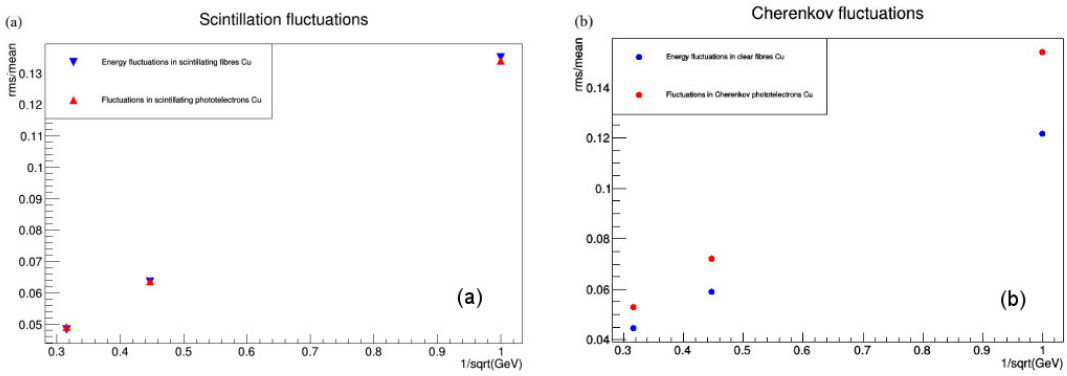

Figure 5.61: Relative fluctuation of the total signal detected in the (a) scintillating and (b) Čerenkov fibres, for both the energy deposit and the number of photoelectrons.

A multivariate neural network analysis showed that the best e/π separation achievable for 60 GeV beams was 99.8% of electron identification efficiency with 0.2% pion misidentification. Further improvements may be expected by including the full time structure information of the pulses, especially if the upstream ends of the fibres are made reflective.

5.4.6 Montecarlo simulations

Geant4 simulations (version 10.02.p01-10.03.p01, with FTFP_BERT_HP physics list) are under development and analysis for understanding the performance of both testbeam modules and a 4π calorimeter integrated in a detector, with magnetic field, tracking and preshower elements.

5.4.6.1 em performance

A $\sim 31 \times 31 \times 100\ cm^3$ Cu matrix, with 1 mm fibres at 1.4 mm distance, compatible with the RD52 prototypes, has been simulated for the evaluation of the electromagnetic performance. PMMA clear fibres and Polystirene scintillating fibres, with a 3% thick cladding (C_2F_2 Fluorinated Polymer for clear and PMMA for scintillating fibres), were the sensitive elements.

A small ($\lesssim 1°$) tilt angle was introduced to avoid large non gaussian tails in the scintillation signal due to channeling and oversampling.

The energy containment for 20 GeV electrons was estimated to be $\geq 99\%$, with sampling fractions of 5.3% and 6.0% for scintillating and clear fibres, respectively.

Given the integral sampling fraction of about 11.3% and the 1 mm thick fibres, the contribution to the energy resolution due to sampling fluctuations can be estimated to be $\sim 9\%/\sqrt{E}$, ultimate limit on the em resolution for this detector.

The scintillation light yield is so large (~ 5500 p.e./GeV) that the fluctuations of the S signals are dominated by the energy sampling process (Figure 5.61(a)). This is not true for the Čerenkov signals (Figure 5.61(b)), whose sensitivity is estimated to be ~ 100 p.e./GeV.

So, the propagation of the scintillation light has been switched off without biasing the detector performance while for the Čerenkov photons a parameterization has been introduced, convoluting the effect of light attenuation, angular acceptance and PDE.

Draft-V0.1

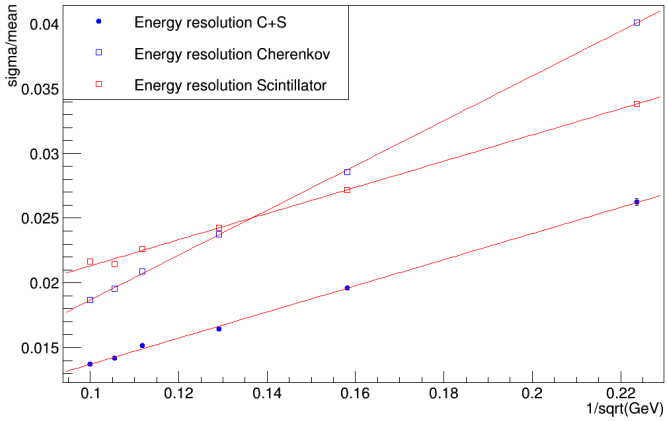

Figure 5.62: Relative resolution for em showers for the C and S signals, independently, and for the average of the two.

In Figure 5.62 the resolutions are shown for both C and S signals, separately, and for the unweighted average value of the two. The variable on the horizontal axis and in the formulae for the fitted resolutions is the beam energy.

The fit to the data points gives:

$$S\ only: \quad \frac{\sigma}{E} = \frac{10.1\%}{\sqrt{E}} + 1.1\% \tag{5.14}$$

$$C\ only: \quad \frac{\sigma}{E} = \frac{17.3\%}{\sqrt{E}} + 0.1\% \tag{5.15}$$

$$combined: \quad \frac{\sigma}{E} = \frac{10.1\%}{\sqrt{E}} + 0.4\% \tag{5.16}$$

A sligthly better result may be obtained with a weighted average.

5.4.6.2 Hadronic performance

A simulation of larger ($\sim 72 \times 72 \times 250\ cm^3$) matrices was implemented in order to get a hadronic shower containment of $\sim 99\%$. Calibration was done with 40 GeV electron beams.

In Figure 5.63 the Geant4 predictions for the hadronic energy resolution, with copper absorber, are shown. Fitting the curves give:

$$S\ only: \quad \frac{\sigma}{E} = \frac{30\%}{\sqrt{E}} + 2.4\% \tag{5.17}$$

$$C\ only: \quad \frac{\sigma}{E} = \frac{73\%}{\sqrt{E}} + 6.6\% \tag{5.18}$$

$$DR\ formula: \quad \frac{\sigma}{E} = \frac{34\%}{\sqrt{E}}\% \tag{5.19}$$

Draft-v0.2

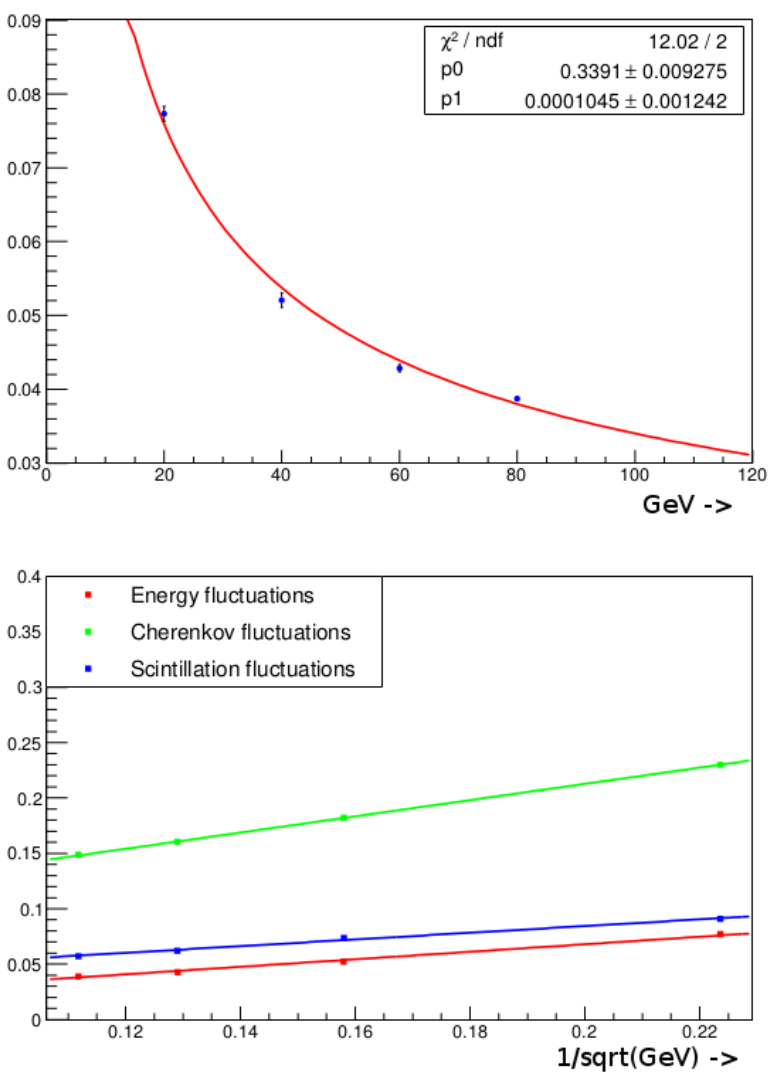

Figure 5.63: Relative resolution for hadronic showers as reconstructed with the DR formula (top). Relative hadronic resolution for the C and S signals, independently, and for the DR combination of the two (bottom).

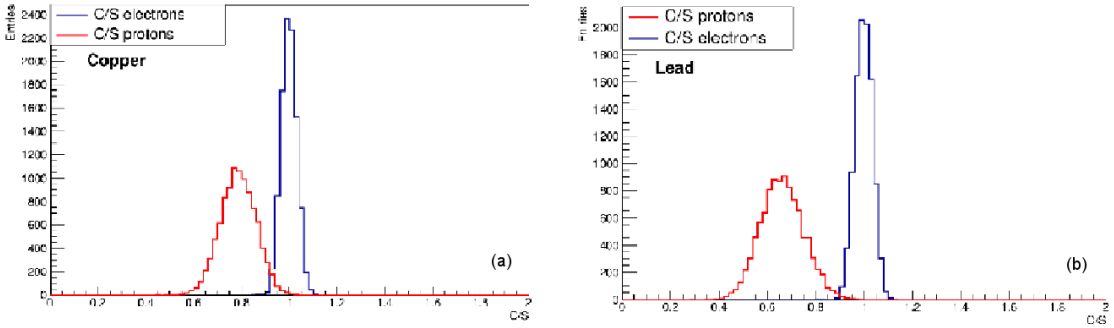

Figure 5.64: C/S ratio for 80 GeV e^- and protons in copper (a) and lead (b).

where the large constant terms, for both S and C signals, are generated by the f_{em} correlated fluctuations. Simulations with lead absorber give equivalent but even slighty better results. The energy E in the plot (and in the expressions for the fitted resolutions) is the beam energy, corresponding in average to the energy reconstructed with the Equation 5.8 when the containment is properly accounted for.

The correlation of the invisible energy with all the other components of hadronic showers was also analysed. Preliminary results seem to indicate that the most appropriate variable to account for the fluctuations of the invisible energy component is, by far, the f_{em}, with correlation coefficients of 90%, 92%, 94%, for copper, iron and lead respectively. The kinetic energy of the neutrons is predicted to be, at best, correlated at the 76% level. If confirmed, this would prove that compensation through neutron signal pickup or amplification will anyway give worse results than the DR method.

About particle id capabilities, in Figure 5.64 the C/S ratio is shown for 80 GeV e^- and protons in copper (top) and lead (bottom). For an electron efficiency of $\sim 98\%$, the rejection factor for protons is ~ 50, in copper, and ~ 600, in lead. Of course, this is an ideal detector and in reality is likely that the numbers will be worse. On the other hand, there are few other variables that can be easily used in order to enhance the particle id performance (namely the lateral shower profile, the starting time of the signal, the charge-to-amplitude ratio).

5.4.6.3 Projective geometry

Each tower, in the wedge geometry implementation, was exposed to 20 GeV electron beams, with an incident angle of $(1°, 1.5°)$, and the calibration constants calculated as the average deposit energy (in each tower) divided by the average C or S signal (of each tower). The response to an electron beam of the same energy is plotted in Figure 5.65. In the barrel region the response of all towers is within 0.2%, while in the forward the systematics are within 2%. All results were obtained with the quantum efficiency for the Čerenkov channel of each tower tuned to a light yield of ~ 30 p.e. per GeV, as estimated in the RD52 beam tests.

The performance of few towers was studied with electron beams in the range of 10-100 GeV. Figure 5.66 shows the linearity and em energy resolutions for the tower #0 and #45. In both cases, the combined S and C signal shows a resolution of $\sim 14\%/\sqrt{E}$ with a constant term of $\sim 0.1\%$ while the average response is constant within 0.4%.

The hadronic resolution was studied with pions in the same energy range. A χ value of 0.29, the value measured for the DREAM calorimeter [43], was used to reconstruct

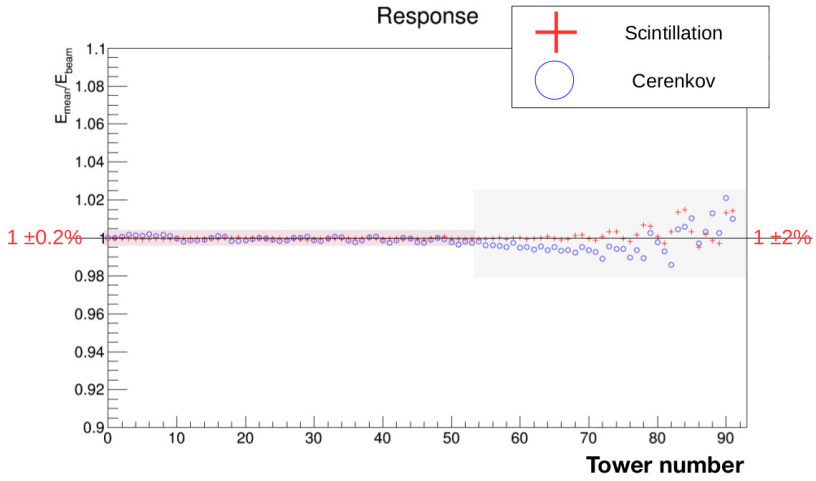

Figure 5.65: Ratio of reconstructed and beam energy for 20 GeV e^-, as a function of the tower number, in the wedge geometry.

the shower energy with Eq. 5.8. In the linearity plots for both tower #0 and #45 in Figure 5.67a, the C and S responses to single pions increase non-linearly as the pion beam energy increases. On the other hand, the value reconstructed with the DR formula shows a constant response to single pions, that is $\sim 8\%$ lower than that to electrons. This effect in the GEANT simulation is described in reference [44]. In addition, the energy resolution after the correction is $\sim 26\%/\sqrt{E}$ with a constant term of less than 1% for both tower #0 and #45 (Figure 5.67b). These results support the statement that the hadronic energy resolution and the response to single hadrons should be constant (and appropriate) over the full barrel region. We may reasonably expect to obtain good performance over the entire 4π detector.

For the wing geometry, the results, at present, are limited at the em performance of few towers and the results (linearity and em resolution) reproduce the ones obtained with the wedge geometry.

5.4.6.4 Short term planning and open issues

The performance for single hadrons, jets and τ leptons has to be understood and the work has just started. For validation, the comparison with a prototype with a non marginal hadronic shower containment, like the RD52 the lead matrix, will be pursued.

About em simulations, a program for the comparison with the 2017 RD52 data is ongoing. Some initial understanding of the absolute photoelectron scale for the Čerenkov light should be available in a very short time.

In general, light attenuation effects need also to be considered, for a $\sim 2-2.5m$ long detector, that may introduce a constant term in the hadronic resolution as a function of the shower development point (late starting showers will give bigger and faster signals).

The evaluation of pro/cons of filters (to dump the short attenuation-lenght components) and mirrors (to increase the number of photons that may reach the photodetectors) may be relevant in this context.

The effects of the integration of a preshower detector have to be evaluated and the e/π separation capability assessed and quantified, for both isolated particles and within jets.

Draft-v0.2

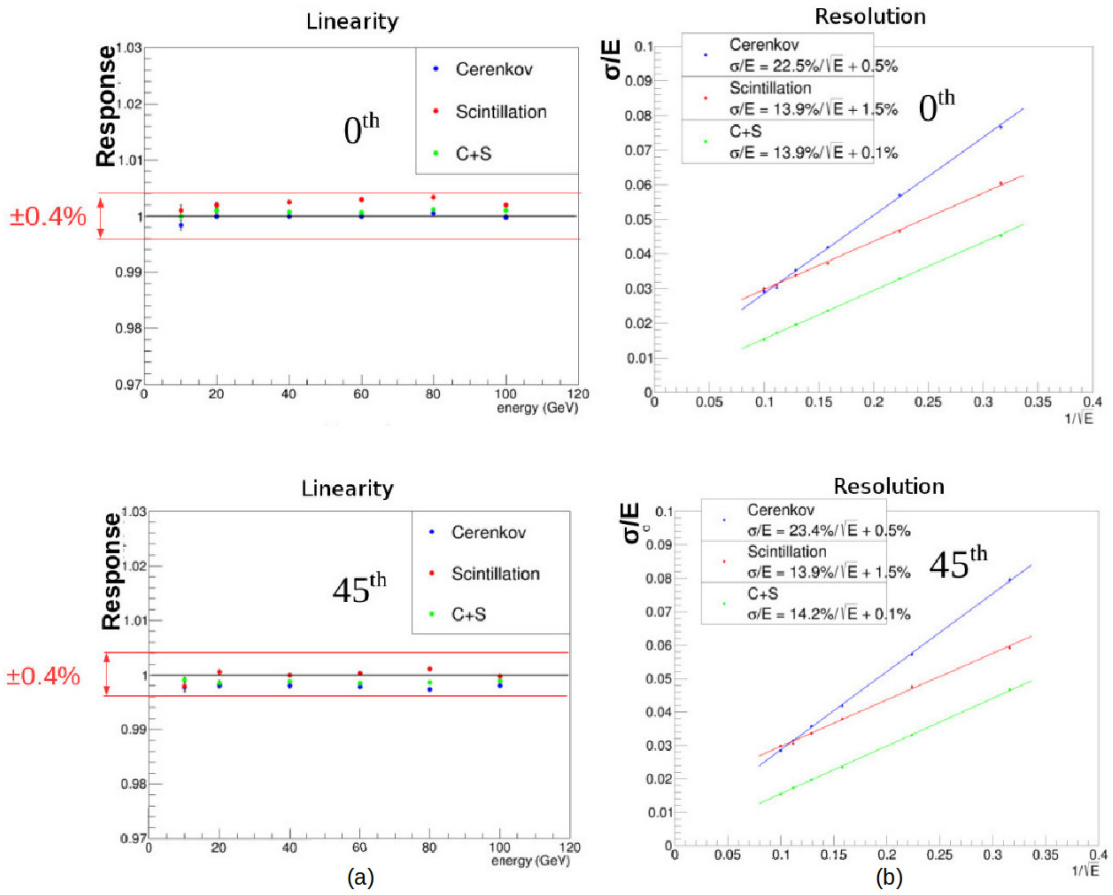

Figure 5.66: Linearity and *em* energy resolution for tower #0 (top) and #45 (bottom), in the wedge geometry.

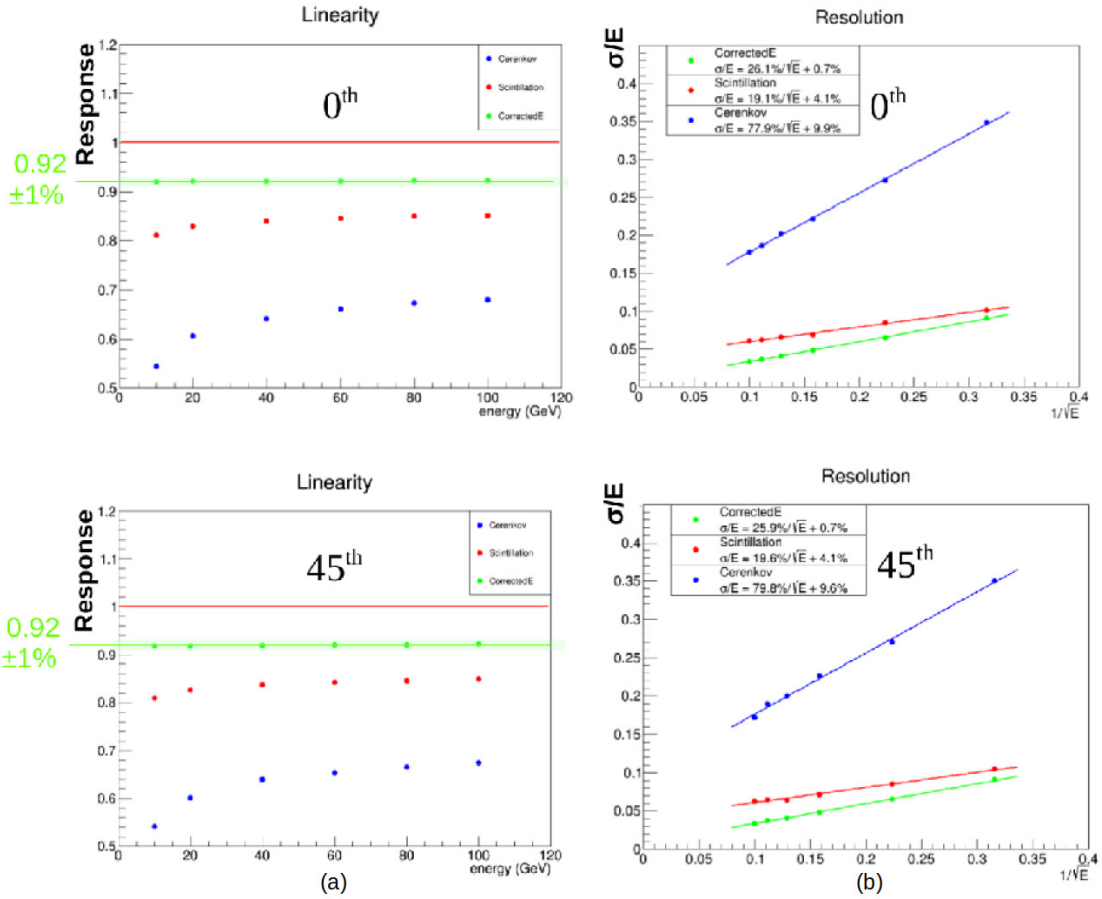

Figure 5.67: Linearity and energy resolution with pions, for tower #0 (top) and #45 (bottom), in the wedge geometry.

About physics, a (non exhaustive) list of benchmark channels to be studied is: $H \to \gamma\gamma$, $H \to \tau\tau$, $H \to gg$, $Z \to jj$, $W \to jj$, $H \to ZZ^* \to 4j$, $H \to WW^* \to 4j$.

5.4.7 Final remarks

Thanks to a 15-year long experimental research program on dual-readout calorimetry of the DREAM/RD52 collaboration, this technology looks mature for the application in future experimental programs. The results show that the parallel, independent, readout of scintillation and Čerenkov light, makes possible to cancel the effects of the fluctuations of the electromagnetic fraction of hadronic showers, dominating the energy resolution of most (if not all) the calorimeters built so far. In conjunction with high-resolution em and hadronic energy measurements, excellent standalone particle-id capability has been demonstrated as well.

Those results give increasing support to the conviction that a matrix of alternating scintillating and clear fibres, inserted in copper or lead strips and readout by Silicon PhotoMultipliers (SiPM), will be able to provide performance more than adequate for the physics programs at the proposed CepC collider.

Nevertheless, there is a series of technical and physics issues that needs to be solved, within the next 2-3 years in order to arrive up to the design of a realistic 4π detector.

A non-exhaustive list must include:

a) The industrial machining of foils of copper, lead or some other material, with the required precision.

b) The development of a mechanical integration design.

c) The readout of the high granularity matrices of SiPM that, in order to be effective, will require the development of a dedicated Application Specific Integrated Circuit (ASIC). Possible aggregations of more fibre outputs into a single channel have also to be implemented and studied.

d) The need and, in case, the way for a longitudinally segmented calorimeter system and the performance of Particle Flow Algorithms.

e) The development of a modular solution and the assessment, at all levels, of its performance, through beam tests of small modules and simulations. An intensive program of simulations is already ongoing, targeted at the CepC experimental program. The response to single particles and jets is under study, in standalone configurations. The work for understanding the behaviour of a 4π calorimeter integrated in a full detector, with a tracking and a magnetic system, has also started. This will include, as well, the evaluation of the combined performance with a preshower detector in front.

References

[1] CALICE Wikipage. https://twiki.cern.ch/twiki/bin/view/CALICE/.

[2] J.-C. Brient, *Improving the jet reconstruction with the particle flow method: An introduction*, 2004. Calorimetry in particle physics. Proceedings, 11th International Conference, CALOR 2004, Perugia, Italy,.

[3] H. Videau and J. C. Brient, *Calorimetry optimised for jets*, in *Proc. 10th International Conference on Calorimetry in High Energy Physics (CALOR 2002),*

Draft-v0.2

Pasadena, California [45].

[4] H. Videau and J. C. Brient, *A Si-W calorimeter for linear collider physics*, in *Proc. 10th International Conference on Calorimetry in High Energy Physics (CALOR 2002), Pasadena, California* [45], pp. 309–320.

[5] CALICE Collaboration, R. Cornat, *Semiconductor sensors for the CALICE SiW EMC and study of the cross-talk between guard rings and pixels in the CALICE SiW prototype*, in *Proceedings CALOR'08*, vol. 160, p. 012067. 2009.

[6] ILD Collaboration, T. Behnke et al., *International Linear Collider – Detector Baseline Document*, , DESY / FERMILAB / CERN, 2013. https://edmsdirect.desy.de/edmsdirect/file.jsp?edmsid=D00000001021295.

[7] CMS Collaboration, A. M. Magnan, *HGCAL: a High-Granularity Calorimeter for the endcaps of CMS at HL-LHC*, JINST **12** (2017) no. 01, C01042.

[8] CMS Collaboration, A. Martelli, *The CMS HGCAL detector for HL-LHC upgrade*, in *5th Large Hadron Collider Physics Conference (LHCP 2017) Shanghai, China, May 15-20, 2017*. 2017. arXiv:1708.08234 [physics.ins-det]. http://inspirehep.net/record/1620207/files/arXiv:1708.08234.pdf.

[9] H. Zhao, *PFA Oriented ECAL Simulation and Geometry Optimization for the CEPC*, in *proceeding of the International Conference on Calorimetry for the High Energy Frontier (CHEF 2017)*. 2017.

[10] D. Jeans, *Simalution of the SiW-ECAL for ILD*, in *proceedings of LCWS 2017*. 2017.

[11] T. S. et al., *Performance study of SKIROC2/A ASIC for ILD Si-W ECAL*, in *proceeding of the International Conference on Calorimetry for the High Energy Frontier (CHEF 2017)*. 2017.

[12] D. Grondin, J. Giraud, and J.-Y. Hostachy, *CALICE Si/W ECAL: Endcap structures and cooling system*, in *Proceedings, International Workshop on Future Linear Colliders 2016 (LCWS2016): Morioka, Iwate, Japan, December 05-09, 2016*. 2017. arXiv:1702.03770 [physics.ins-det]. http://inspirehep.net/record/1513187/files/arXiv:1702.03770.pdf.

[13] V. Boudry, *SiW ECAL R&D*, in *Fourth International Workshop on Future High Energy Circular Colliders (CEPC2014)*. 2014. http://indico.ihep.ac.cn/event/4338/session/2/contribution/35/material/slides/0.pdf.

[14] CALICE Collaboration, J. Repond et al., *Design and Electronics Commissioning of the Physics Prototype of a Si-W Electromagnetic Calorimeter for the International Linear Collider*, JINST **3** (2008) P08001, arXiv:0805.4833 [physics.ins-det].

Draft-v0.2

[15] C. Adloff et al., *Response of the CALICE Si-W electromagnetic calorimeter physics prototype to electrons*, Nucl. Instrum. Meth. **A608** (2009) 372–383.

[16] CALICE Collaboration Collaboration, R. Poschl, *A large scale prototype for a SiW electromagnetic calorimeter for a future linear collider*, in *Proceedings of International Workshop on Future Linear Colliders (LCWS11) 26-30 Sep 2011. Granada, Spain*. 2012. arXiv:1203.0249 [physics.ins-det].

[17] V. Balagura et al., *SiW ECAL for future e^+e^- collider*, in *Proceedings, International Conference on Instrumentation for Colliding Beam Physics (INSTR17): Novosibirsk, Russia*. 2017. arXiv:1705.10838 [physics.ins-det]. http://inspirehep.net/record/1601898/files/arXiv:1705.10838.pdf.

[18] A. Irles, *Latest R&D news and beam test performance of the highly granular SiW-ECAL technological prototype for the ILC*, in *proceeding of the International Conference on Calorimetry for the High Energy Frontier (CHEF 2017)*. 2017.

[19] G. B. *et.al.*, *Conception and construction of a technological prototype of a high-granularity digital hadronic calorimeter*, JINST **10** (2015) P10039.

[20] M. B. *et al.*, *Performance of Glass Resistive Plate Chambers for a high granularity semi-digital calorimeter*, JINST **6** (2011) P02001.

[21] C. Collaboration, *First results of the CALICE SDHCAL technological prototype*, JINST **11** (2016) P04001.

[22] C. Collaboration, *Separation of nearby hadronic showers in the CALICE SDHCAL prototype detector using ArborPFA*, CAN-054 (2016) .

[23] C. Collaboration, *Tracking within Hadronic Showers in the CALICE SDHCAL prototype using a Hough Transform Technique*, JINST **12** (2017) P05009.

[24] C. Collaboration, *Resistive Plate Chamber Digitization in a Hadronic Shower Environment*, JINST **11** (2016) P06014.

[25] L. Caponetto*et al.*, *First test of a power-pulsed electronics system on a GRPC detector in a 3-Tesla magnetic field*, JINST **7** (2012) P04009.

[26] F. Sefkow, *Prototype tests for a highly granular scintillator-based hadron calorimeter*, CHEF2017. https://indico.cern.ch/event/629521/contributions/2702990/.

[27] The CALICE Collaboration, Y. Liu et al., *A design of scintillator tiles read out by surface-mounted SiPMs for a future hadron calorimeter*, (NSS/MIC), IEEE (2014) 1–4.

[28] The CALICE Collaboration, C. Adloff et al., *hadronic energy resolution of a highly granular scintillator-steel hadron calorimeter using software compensation techniques*, Journal of Instrumentation **7(09)** (2012) 1–23.

[29] K. Krueger, *Software compensation and particle flow*, CHEF2017. https://indico.cern.ch/event/629521/contributions/2703038/.

Draft-v0.2

[30] M. Bouchel et al., *Second generation Front-end chip for H-Cal SiPM readout :SPIROC*, ILC website. https://agenda.linearcollider.org/event/1354/contributions/2542/attachments/1826/3054/SPIROC_presentation_13_02_2007.pdf.

[31] K. Krueger, *Cooling of ECAL and HCAL*, ILC website. https://agenda.linearcollider.org/event/7665/contributions/39698/attachments/32095/48580/Cooling_ILC-miniWS-2017Sep28.pdf.

[32] R. Wigmans, *Calorimetry, Energy Measurement in Particle Physics*, vol. 168 (second edition). International Series of Monographs on Physics, Oxford University Press, 2017.

[33] C. Patrignani et al. (Particle Data Group) Chin. Phys. C **40** (2016) 479–482.

[34] D. E. Groom, *Energy flow in a hadronic cascade: Application to hadron calorimetry*, Nucl. Instrum. Methods A **572** (2007) 633–653.

[35] D. E. Groom, *Erratum to "Energy flow in a hadronic cascade: Application to hadron calorimetry" [Nucl. Instr. and Meth. A 572 (2007) 633âĂŞ653]*, Nucl. Instrum. Methods A **593** (2008) 638.

[36] N. Akchurin et al., *Particle identification in the longitudinally unsegmented RD52 calorimeter*, Nucl. Instrum. Methods A **735** (2014) 120.

[37] N. Akchurin et al., *The electromagnetic performance of the RD52 fiber calorimeter*, Nucl. Instrum. Methods A **735** (2014) 130.

[38] N. Akchurin et al., *Lessons from Monte Carlo simulations of the performance of a dual-readout fiber calorimeter*, Nucl. Instrum. Methods A **762** (2014) 100.

[39] A. Cardini et al., *The small-angle performance of a dual-readout fiber calorimeter*, Nucl. Instrum. Methods A **808** (2016) 41.

[40] R. Wigmans, *New results from the RD52 project*, Nucl. Instrum. Methods A **824** (2016) 721.

[41] S. Lee et al., *Hadron detection with a dual-readout fiber calorimeter*, Nucl. Instrum. Methods A **866** (2017) 76.

[42] 4th Detector Collaboration Letter of Intent: http://www.4thconcept.org/4LoI.pdf.

[43] N. Akchurin et al., *Hadron and jet detection with a dual-readout calorimeter*, Nucl. Instrum. Methods A **537** (2005) 537.

[44] N. Akchurin et al., *Lessons from Monte Carlo simulations of the performance of a dual-readout fiber calorimeter*, Nucl. Instrum. Methods A **762** (2014) 100.

[45] *10th International Conference on Calorimetry in High Energy Physics (CALOR 2002), Pasadena, California, 25-30 Mar 2002*. March, 2002.

Draft-v0.2

Draft-v0.2

CHAPTER 6

DETECTOR MAGNET SYSTEM

Draft-v0.2

CEPC website [1]

6.1 General Design Considerations

The CEPC detector magnet system is designed with a diameter of 6.8 m and a length of 8.05 m. An axial magnetic field over the tracking volume is generated for particle detectors to measure the trajectories of charged tracks emerging from the collisions. Comparing to a 3.5 T solenoid field proposed in pre-CDR, a detector superconducting solenoid with 3.0 T central field is more reasonable to construct the compensation solenoid. It makes full cancelation to avoid disturbance to the beam with technologies to be demonstrated in coming years.

This chapter describes the conceptual design of CEPC detector magnet, including the design of field distribution, solenoid coil, specific superconductor, cryogenics, quench protection, power supply and the yoke. In this report, we explored the possibility of using HTS to build a large detector magnet for the first time. Compared to LTS (low temperature superconducting) coils, the ReBCO coil windings are expected to be more stable during operation, due to its high critical temperature.

We also discussed two candidate design options, including the iron yoke design and the dual solenoid scenario. The iron yoke design consists of the barrel yoke and the end yoke. Besides being used to shield the magnetic field, the iron yoke can also provide room for placing the muon detector between the iron plates and act as the main mechanical structure of the CEPC detector. The active shielding design has been widely used in commercial MRI magnets. It is iron yoke-free, however, it will bring unprecedented challenges to the muon detector design.

By Copyright © 2018 HEP Community

6.2 The Magnetic Field Requirements and Design

6.2.1 Main parameters

The main parameters of the CEPC detector solenoid are listed in 6.1. The 7.6 m long CEPC detector coil is designed with 5 modulus by taking into account the construction easiness and difficulties in superconducting wire selection, fabrication of the external support, winding and impregnation, transport and handling. This design enables the possibility to use short unit length of superconductors and make superconducting joints in low field regions. Compared to Pre-CDR, the designed central magnetic field for the CDR detector magnet drops from 3.5 T to 3.0 T. But the geometry size of the CDR detector magnet keeps the same as that of Pre-CDR detector magnet, as shown in Figure 6.1. The five coil modulus are all wound with 4 layers. The three middle coil modulus and the two end coil modulus are wound with 78 and 44 turns, respectively.Table 6.2 shows the coil parameters.

The solenoid central field (T)	3	Working current (kA)	15779
Maximum field on conductor (T)	3.485	Total ampere-turns of the solenoid (MAt)	20.323
Coil inner radius (mm)	3600	Inductance (H)	10.46
Coil outer radius (mm)	3900	Stored energy (GJ)	1.3
Coil length (mm)	7600	Cable length (km)	30.35

Table 6.1: Main parameters of the solenoid coil

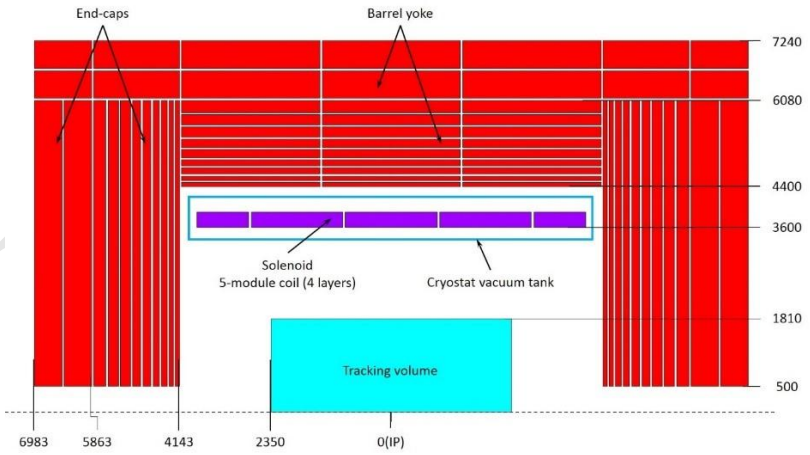

Figure 6.1: 2D layout of CEPC detector magnet (mm)

6.2.2 Magnetic field design

The cross-section of the superconducting cable used for magnet design is shown in Figure 6.2. The NbTi Rutherford cable is encompassed by the pure aluminum stabilizer and squeezed by the aluminum alloy reinforcement, the cross-section dimension of the cable is 72 mm x 22.3 mm. The cable configuration is used for the following magnetic field calculation, stress analysis of the coil and quench analysis of the magnet.

Figure 6.3 shows the magnetic field contour of the magnet. The central magnetic field is 3 T. The maximum field on the coil is 3.5 T. Figure 6.4 shows the main field component

Coil number	layers	Turns per layer
1	4	44
2	4	78
3	4	78
4	4	78
5	4	44

Table 6.2: Coil parameters

of BZ along the beam axis. Figure 6.5 shows the magnetic flux line distribution of the solenoid coil. The field non-uniformity within the Tracking Volume (diameter of 3.62 m, length of 4.7 m) is 9.11%. Figure 6.6 shows the magnetic field distribution of the Tracking Volume.

$$B_p = \frac{Bmax - Bmin}{Bcenter} = 9.11\%$$

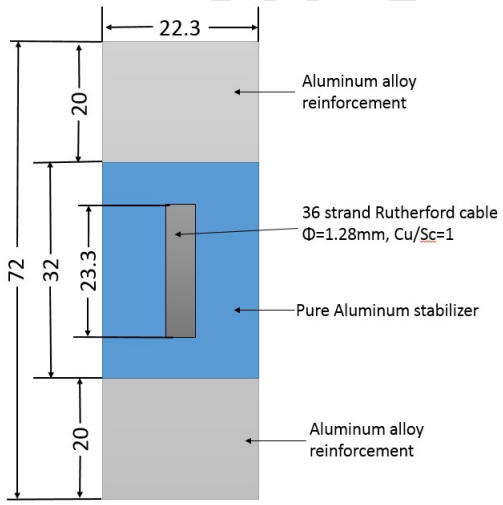

Figure 6.2: Sketch figure of cable cross section

<<<<< HEAD

The peak coil field of 3.5 T locates in the pure aluminum stabilizer, as shown in Figure 6.7. The magnetic field distribution on NbTi Rutherford cable is shown in Figure 6.8. The peak field on the NbTi cable is 3.485 T. Figure 6.9 shows the magnetic field distribution on the yoke. ======= The maximum magnetic field on the cable is 3.5 T located on the pure aluminum stabilizer. This can be seen in Figure 6.7 The magnetic field distribution on NbTi Rutherford cable is shown in Figure 6.8. The maximum field on the NbTi cable is about 3.485 T. Figure 6.9 shows the magnetic field distribution on the yoke. >>>>> ebc67f35d67e018d186dfe54b2a024c28d538543

The stray field of the detector magnet is shown in Table 6.3 and Figure 6.10. The stray field range of 50 Gs and 100 Gs are marked out.

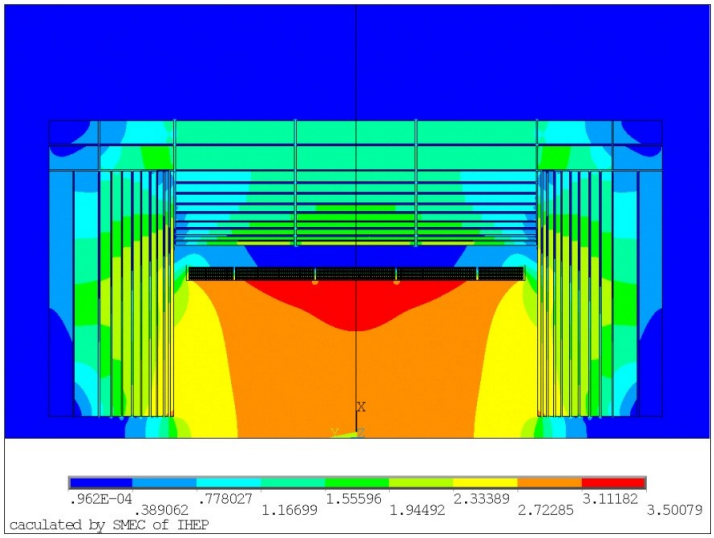

Figure 6.3: Field map of the magnet (T)

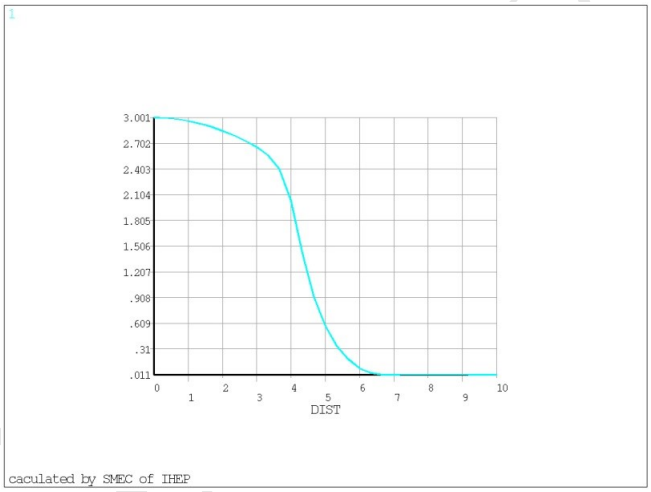

Figure 6.4: The calculated magnetic field Bz along the detector axis

Stray field	3 T
50Gs R direction	13.6 m
50Gs Z direction	15.8 m
100Gs R direction	10 m
100Gs Z direction	11.6 m

Table 6.3: Leak field parameters

6.2.3 Coil mechanical analysis

Introduction:

The coil stress is dominated by the cold shrinking force and the magnetic force after excitation. The stress analysis is followed by two load steps: coil at 4.2 K and coil excited to 15,779 A (3 T). A 2D magnetic FEA model is firstly created to calculate the

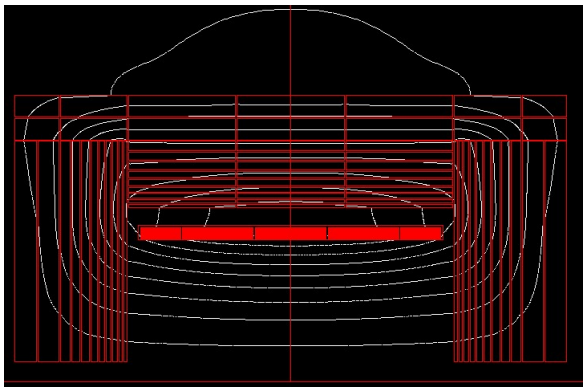

Figure 6.5: Magnetic flux line distribution of the magnet

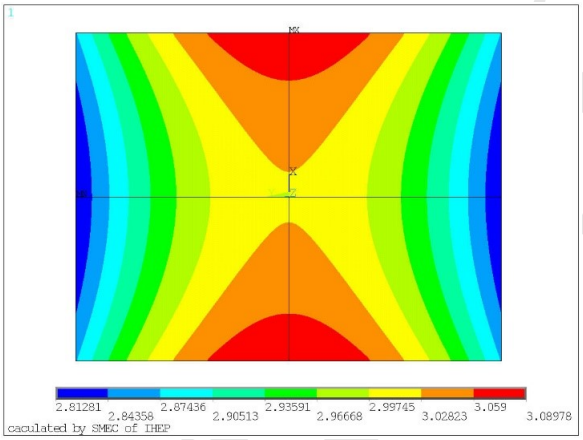

Figure 6.6: The magnetic field distribution of tracking volume

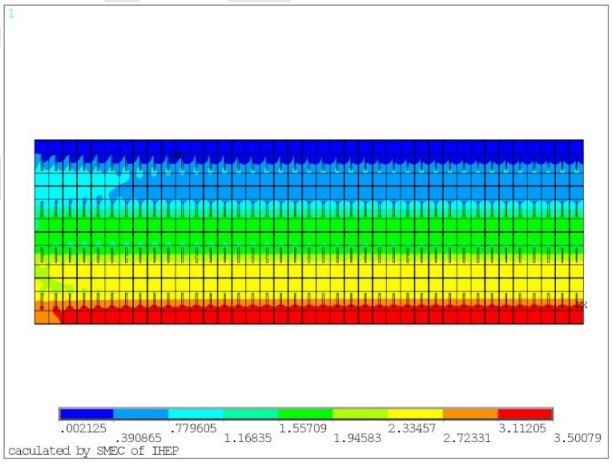

Figure 6.7: Magnetic field distribution on the cable of the center model

Lorentz force. After that, the 2D axisymmetric mechanical analysis was conducted by revising the generated magnetic model and using assumptions as follows: a) the barrel yoke and end-cap yoke are cylinders; b)the hole of the chimney in the barrel is neglected; c) the operating current of 15,779 A is uniformly distributed in the Rutherford cable. The thickness of the support is 50 mm, which is the same as al-alloy used in the cable.

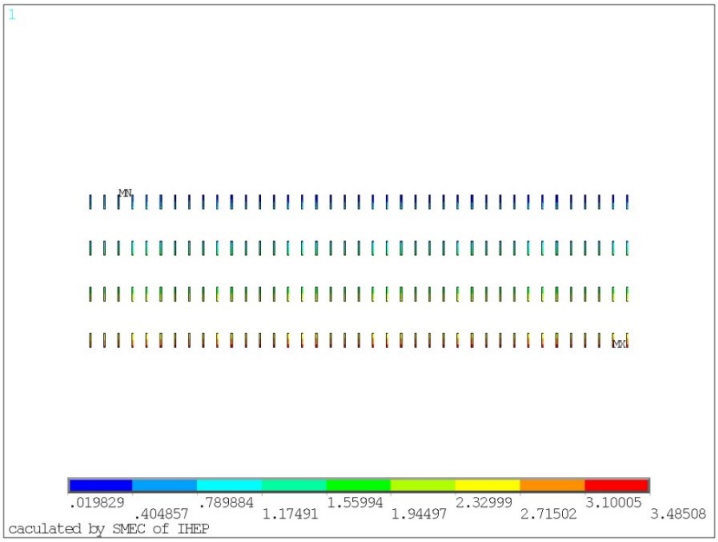

Figure 6.8: Magnetic field distribution on the center NbTi cable

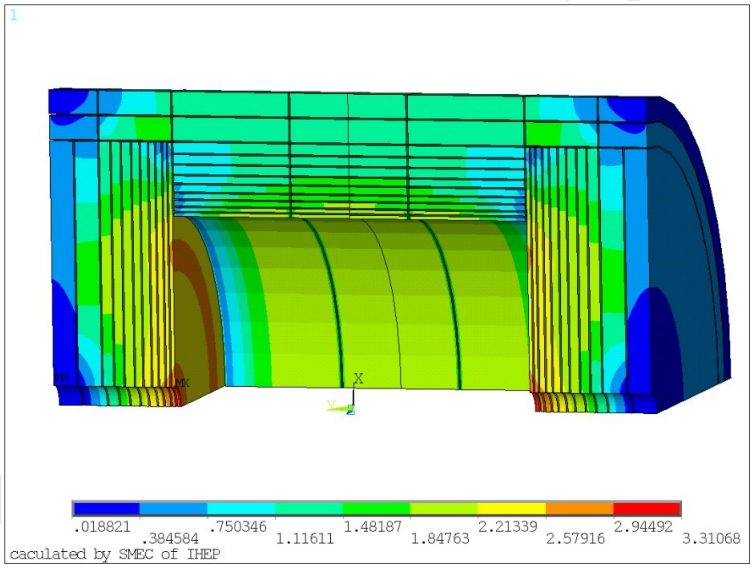

Figure 6.9: Magnetic field distribution on the yoke

The properties of different materials used for FEA simulation are given in Table 6.4 and Table 6.5. Figure 6.11 shows the coil with aligned turns. Different materials are marked with different colors. Figure 6.12 shows the mesh grid distribution of the model.

Material	Temperature(K)	Young's Modulus (GPa)	Poisson's ratio
Al	4.2	0.8	0.49
Al-Alloy	4.2	77.7	0.327
Sc strand	4.2	130	0.3
Fiber glass epoxy	4.2	12.5	0.21

Table 6.4: Material properties used in the FEA

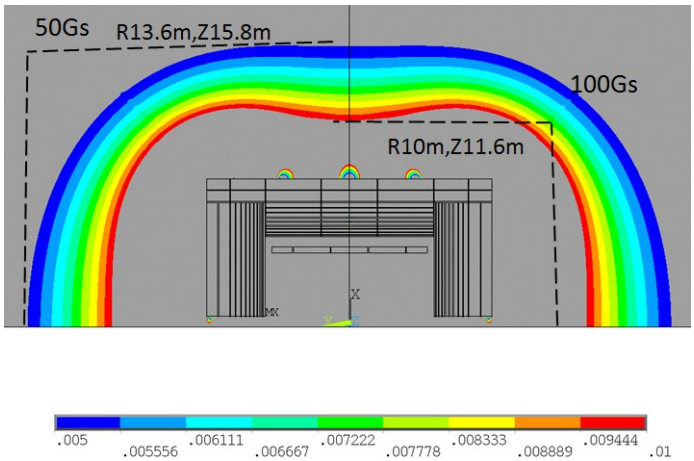

Figure 6.10: Stray field distribution outside the magnet (the field is given in T)

Material	Mean integral thermal expansion coefficient 293K-4.2K
Aluminum	14.23e-6
Al-alloy	14.16e-6
Sc strand	8.79e-6
Fiber glass epoxy	25.5e-6

Table 6.5: Mean integral thermal expansion coefficients used in the FEA

Figure 6.11: Coil with aligned turns

Stress FEA results:

The Von-Mises criterion is used for all ductile materials in the coil winding. A summary of analyzed results is given in Table 6.6 and Table 6.7. From Figure 6.13 to Figure

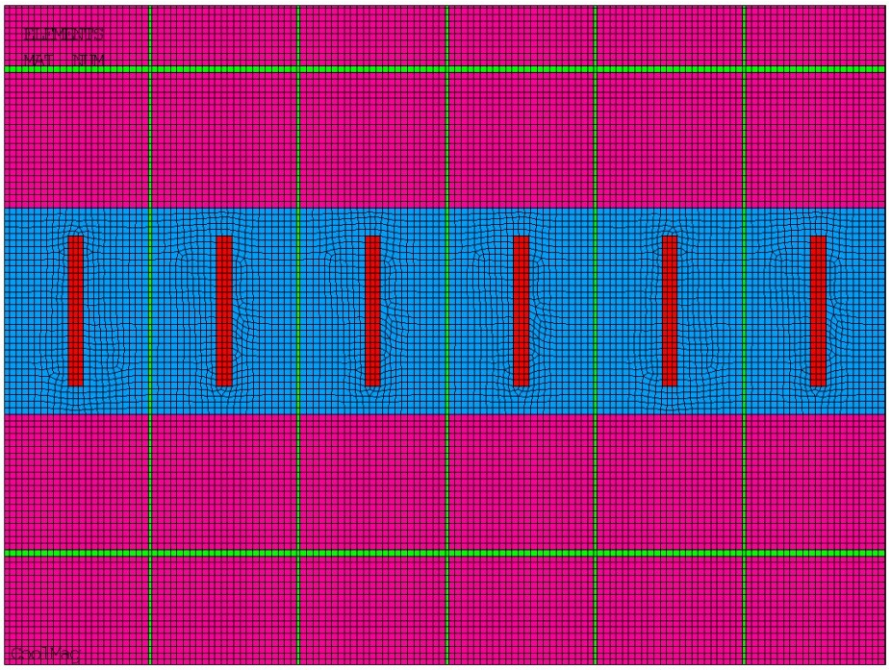

Figure 6.12: Mesh grid of the model

6.18, we show the Von-Mises stress of each part of the coil winding after cool-down (4.2 K) or excitation. It can be found that the load step of cool-down contributes to the major of the Von-Mises stress in SC cable and aluminum alloy.

Material	Von Mises stress MPa End coil	Von Mises stress MPa Middle coil	Von Mises stress MPa Central coil
Coil at 4.2 K			
Pure Aluminum	0-7.2	0-6.8	0-7
SC cable	189-205	190-201	189-200
Al alloy	2.2-44	5-39	5-43
Coil at 4.2 K, energized			
Pure Aluminum	0-9.3	0-8.5	0-9.3
SC cable	85-142	62-95	66-106
Al alloy	40-94	74-103	65-103

Table 6.6: Maximum Von Mises of conductors

6.2.4 Preliminary quench analysis

Figure 6.19 shows the quench protection system of the detector magnet, in which a dump resistor is employed. During quench, the energy is expected to be extracted mostly by the dump resistor. The coil quench is simulated by using Finite Volume Method (FVM) with Matlab, calculating the quench propagation, the hot-spot temperature and the terminal voltage in coils. Specifically, the coil winding is divided into four layers, with an inductance of 10.4 H and an operating current of 15,779 A. The thickness of insulation between layers and between turns is 1 mm and 0.5 mm, respectively.

Draft-V1.2

	End coil	Middle coil	Central coil
Coil at 4.2 K			
Von Mises(MPa)	21-60	19-59	21-59
Shear Stress(MPa)	1.2	8.8	1.3
Coil at 4.2 K, energized			
Von Mises(MPa)	29-85	30-84	29-79
Shear Stress(MPa)	12.4	9.0	13.1

Table 6.7: Shear stress and Von Mises of the insulation

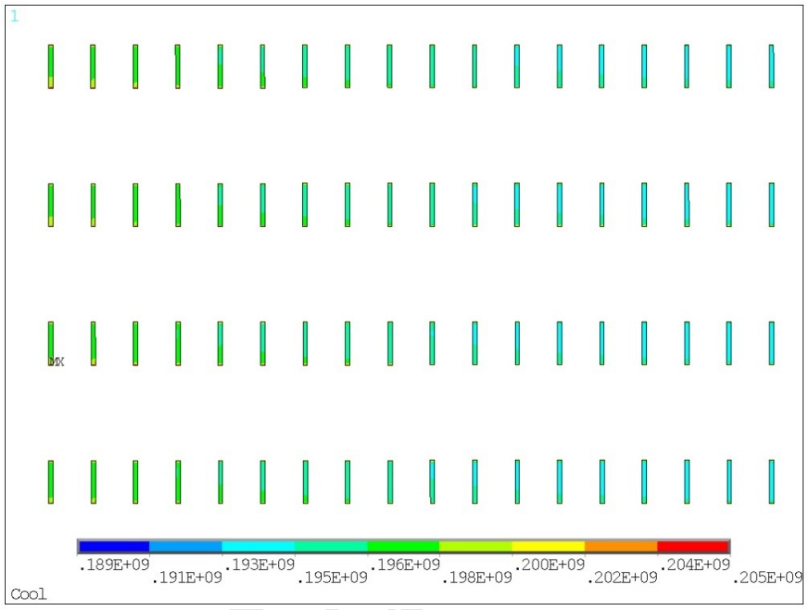

Figure 6.13: Coil at 4.2 K, Von Mises distribution of the end coil SC cable

Different cases have been considered in our quench simulation, including the normal external fast dumping (RP=0.05 Ω or RP=0.1 Ω) and the failure of the protection system (RP=0). Specially, we assume the quench starts at the end of first layer when given an initial temperature of 9 K.

The materials we used for simulation include G10 CR (fiber glass epoxy), 1100 pure aluminum, 6061-T6 aluminum alloy and Cu/NbTi (RRR=100). The curves of the magnet parameters (current, resistance, hot-spot temperature and voltage of the magnet) under different cases are shown in figures from Figure 6.20 to Figure 6.23. Table 6.8 summarizes the results of the quench simulation.

6.3 HTS/LTS Superconductor Options

6.3.1 HTS plan background

The central magnetic field strength of CEPC detector magnet is 3 T, which can be achieved by using LTS coil windings. Recent development of high temperature superconductors (HTS) result in significant R&D efforts towards high field solenoid coils and accelerator magnets. Compared to previously introduced LTS detector magnet, HTS detector magnet

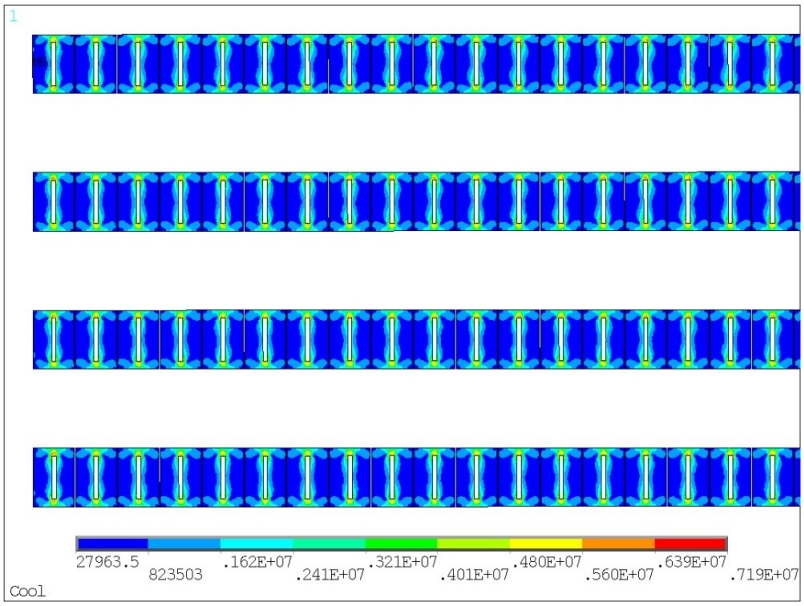

Figure 6.14: Coil at 4.2 K, Von Mises distribution of the end coil pure Aluminum

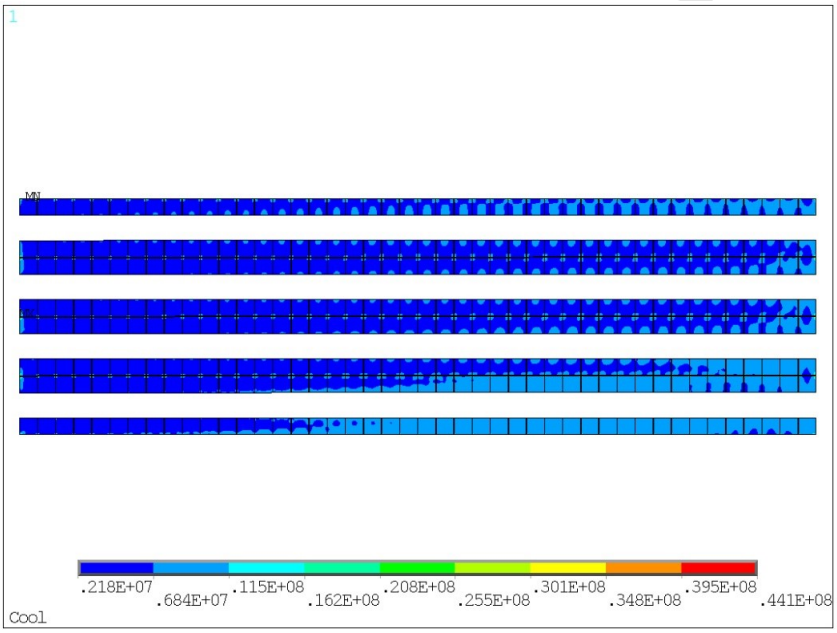

Figure 6.15: Coil at 4.2 K, Von Mises distribution of the end coil Aluminum alloy

has the following advantages: a) the HTS magnet is stable against external perturbation and not easy to quench; b) the critical current of ReBCO coated conductor will not degrade when exposed to irradiation environment; c) less amount of coil materials is required; d) the cooling system is cost-effective if ReBCO coils are operated at around 20 K; e) the performance of ReBCO coated conductor has the potential to be improved significantly while the price can be reduced in the coming years. And it will push the development of key technologies for large bore ReBCO magnet.

YBa2Cu3O7, the second generation of practical HTS conductor, is a candidate option in our design of the detector magnet. The coated conductor composite of YBCO

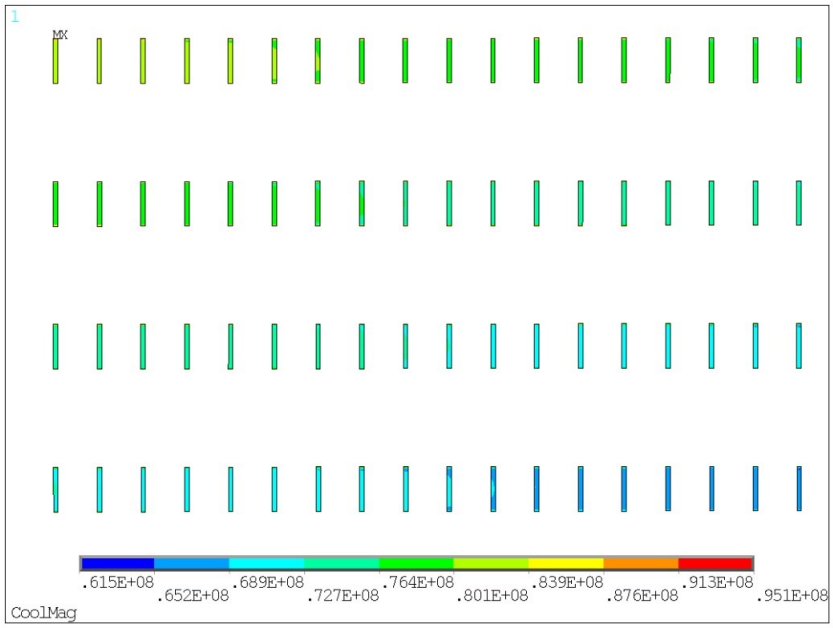

Figure 6.16: 6.16 Coil at 4.2 K, energized, Von Mises distribution of the central coil SC cable

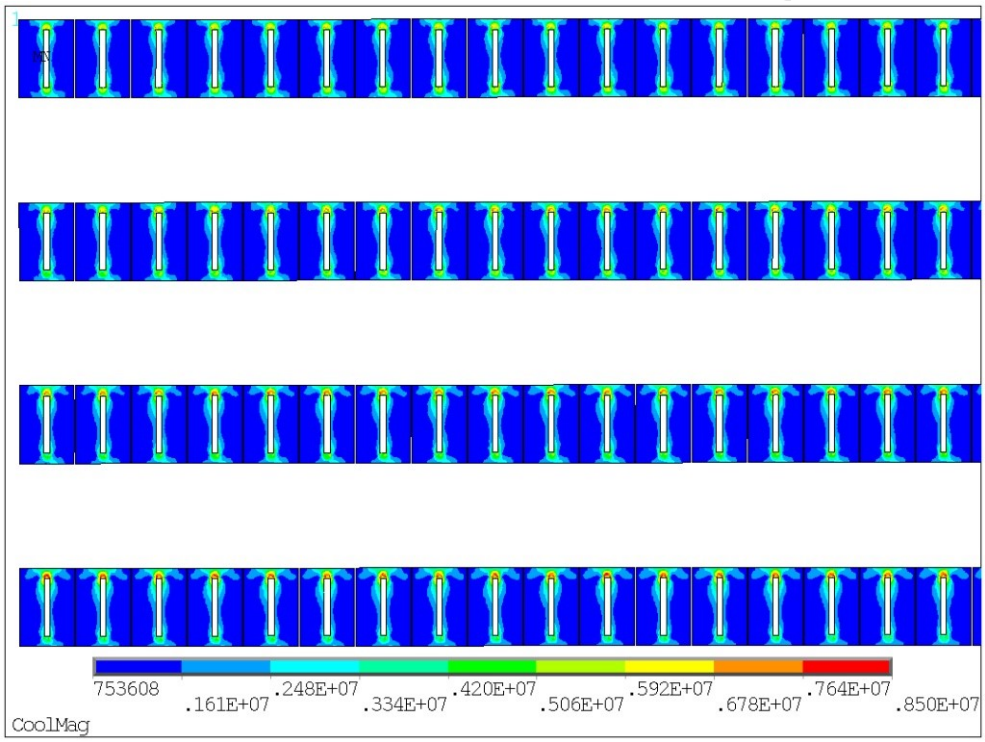

Figure 6.17: Coil at 4.2 K, energized, Von Mises distribution of the central coil pure Aluminum

is fabricated by using chemical deposition and physically coating the superconducting YBCO thin film on the alloy substrate. Figure 6.24 shows the cutaway view of YBCO (from Shanghai Superconductor Co Ltd).

The relationship between the whole-wire critical current density and the magnetic field for varied superconducting materials are plotted in Figure 6.25. HTS materials (YBCO & Bi-2212) show excellent Jc performance under the magnetic field strength of

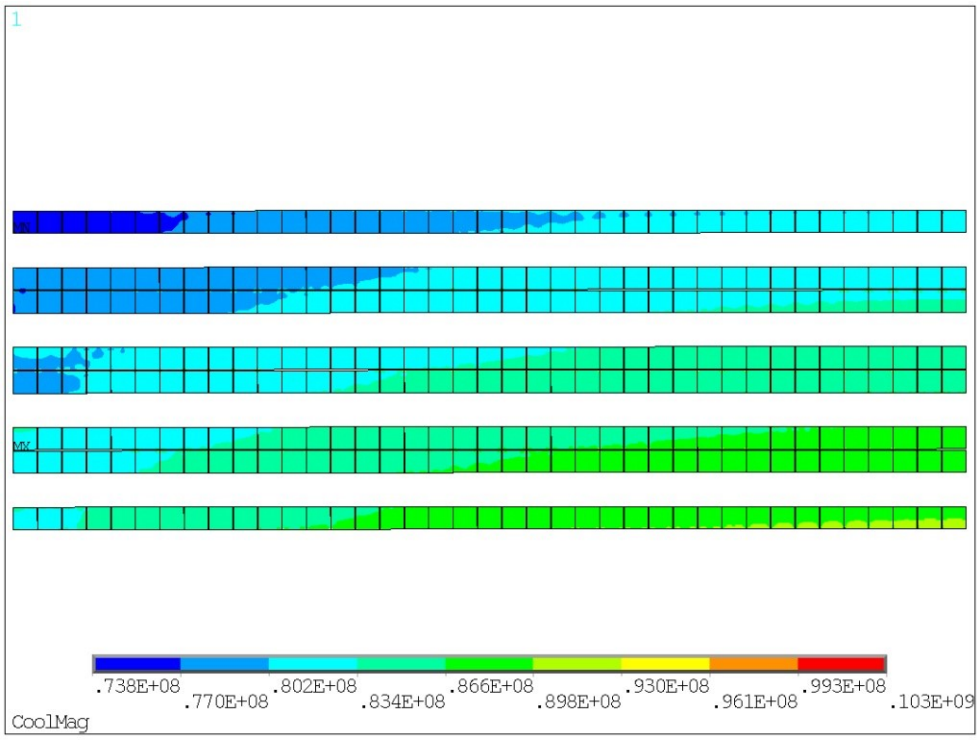

Figure 6.18: Coil at 4.2 K, energized, Von Mises distribution of the central coil aluminum alloy

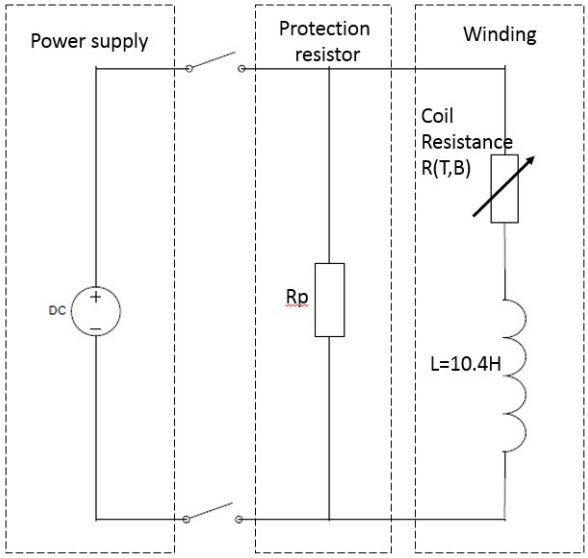

Figure 6.19: Equivalent electrical circuit of the quench protection of CEPC

over 20 T. For CEPC detector magnet, we take advantage of the high critical temperature of YBCO instead of its high Jc under high magnetic field. The HTS detector magnet will be operated at 20 K.

6.3.2 The latest development of high temperature superconducting cable

Superconducting cables are often used to wind coils for large detector magnet, accelerator magnet, fusion magnet, etc. They have the following advantages: a) improve the coil

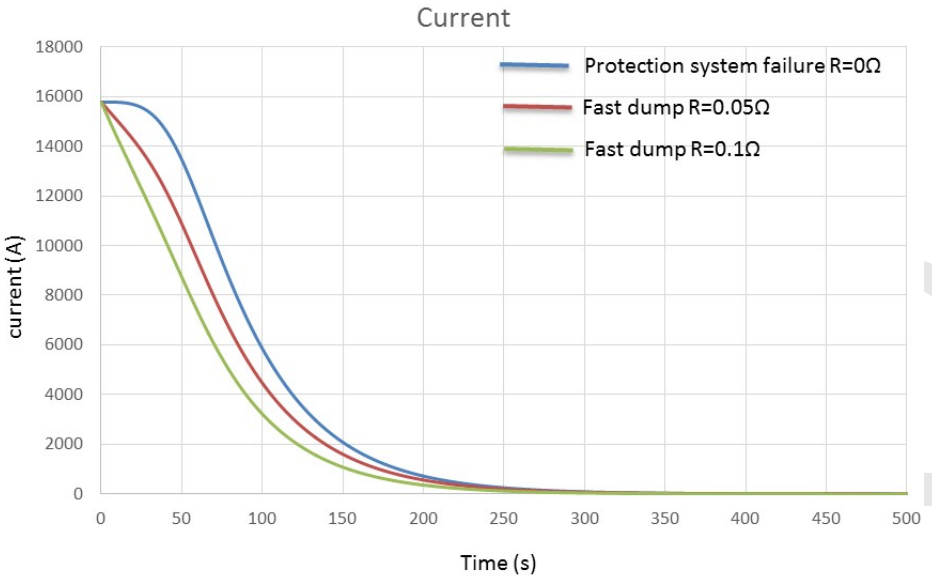

Figure 6.20: Comparison of the current profile with protection system failure and with different fast dump resistors

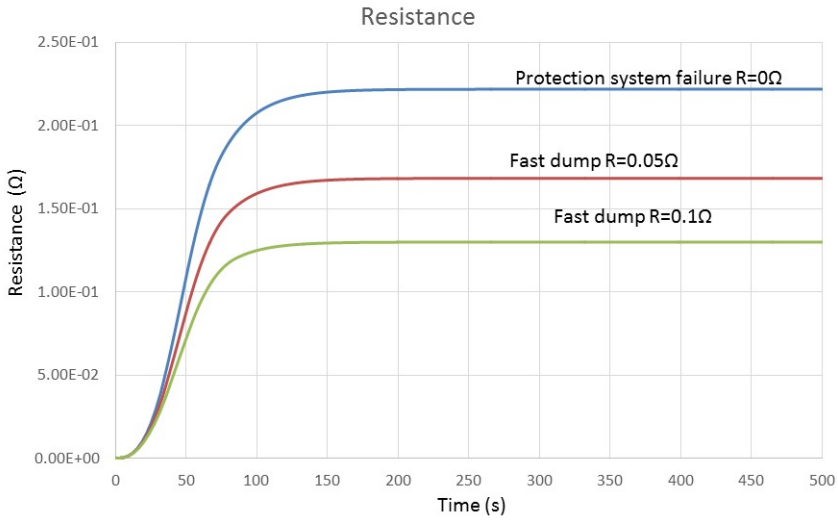

Figure 6.21: Comparison of the coil resistance profile with protection system failure and with different fast dump resistors

windingąŕs reliability ÍC the paralleled conductors can share the operating current when one wire or several wires reach the critical current due to premature quenches; b) coils winded by cables are with low inductance which lower the requirements for the voltage output of the power supply; c) the unit length of single superconducting wire is reduced to the level of 100-meter and the total material cost is reduced significantly.

Great R&D efforts towards ReBCO cables have been recently made in different application areas. Figure 6.26 shows three different types of ReBCO cables, including TSTC (Twisted Stacked-Tape Cable) developed by MIT (Massachusetts Institute of Technology), CORC (Conductor on Round Core) cable developed by ACT (Advanced Conductor Technologies LLC) and RACC (Roebel Assembled Coated Conductor) developed by KIT

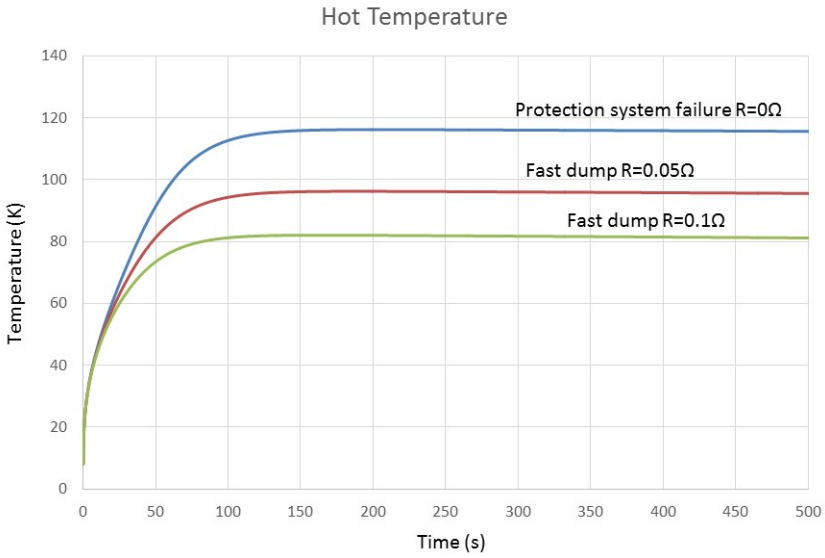

Figure 6.22: Comparison of temperature profile with protection system failure and with different fast dump resistors

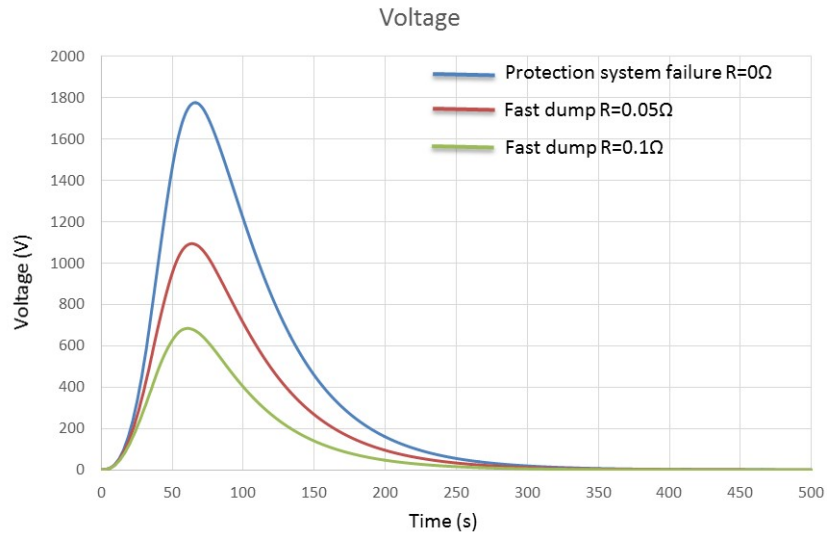

Figure 6.23: Comparison of the coil voltage profile with protection system failure and with different fast dump resistors

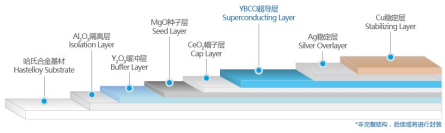

Figure 6.24: The structure diagram of YBCO

(Karlsruhe Institute Of Technology). All three types of ReBCO cables are still in the research stage and not widely used in superconducting applications.

TSTC can be easily fabricated with high engineering current density, high length ratio (cable length to tape length) and isotropic J(B). But it is not suitable for winding compact small size magnets. CORC is a round cable which can be bended freely with

Fast dump resistance Rp	0 Ω	0.05 Ω	0.1 Ω
Average final coil temperature	136 K	113K	96K
Effective time constant(the current is I=I0/e=6833A)	90s	80s	68s
Magnet final resistance	0.25 Ω	0.19 Ω	0.15 Ω
Max voltage	2323 V	1478 V	946 V
Extracted energy	0	8.27e8 J	1.279e9 J
Extracted energy ratio	0	46%	71%

Table 6.8: Influence of Rp on quench characteristics

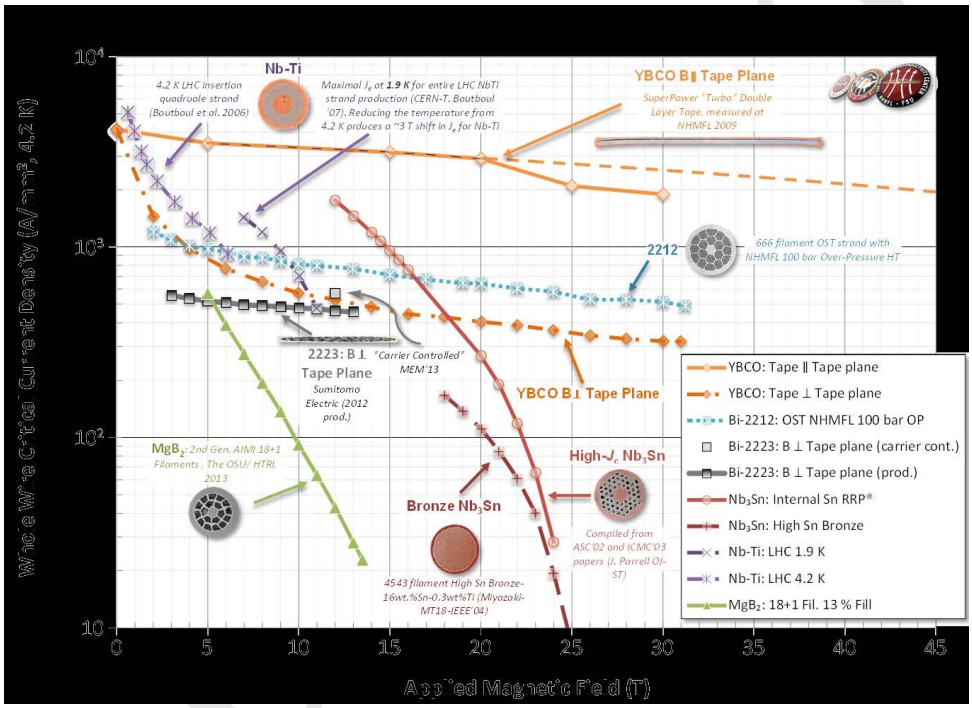

Figure 6.25: The relationship between critical current and applied magnetic field of different superconducting materials

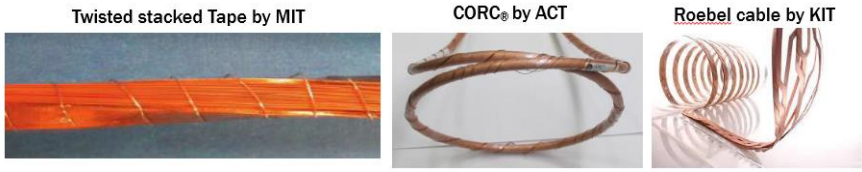

Figure 6.26: different YBCO cables

isotropic J(B). But it is with low cable length ratio and low engineering current density. RACC is a flat cable with high engineering current density, however, it is conductor-waste with anisotropic J(B).

Considering the first priority of long time stability requirement of CEPC detector magnet, several ReBCO tapes can also be soldered together as a rectangular cable neglecting its negative effects on AC loss. In this case, a 10 ReBCO tapes stacked cable is expected to carry 10 times higher operating current compared to a single tape. Specially, a slow ramping rate or de-ramping rate is required to reduce the AC loss when the stacked tapes are used in the coil windings. Figure 6.27 shows the cross-section of the YBCO stacked cable. Further investigation is required to study its winding-friendliness as the stacked cable is expected to harden after soldering.

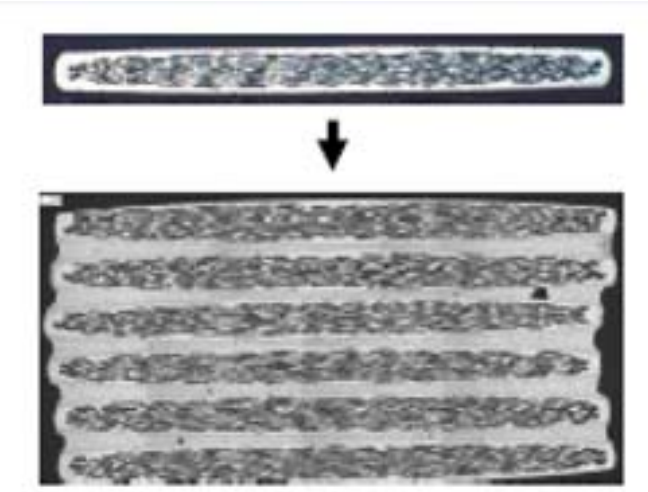

Figure 6.27: HTS stack cable

Further experiments are expected to be carried to determine which type of cable is most suitable to be used to wind CEPC detector magnet. The following calculation is based on the simplest stacked cable.

6.3.3 HTS magnetic design

The main parameters of commercial ReBCO coated conductors provided by Shanghai superconductor Co Ltd is shown in Table 6.9. Figure 6.28 shows the critical current of the 12 mm wide YBCO tape under varied temperature and magnetic field. As listed in Table 6.10, the critical current of the 12 mm wide YBCO tape at 4.2 K is 2000 A @ 2 T, 1700 A @ 3 T and 1200 A @ 5 T, respectively.

series	ST-02-E	ST-03-E	ST-04-E	ST-05-L	ST-05-E	ST-06-L	ST-10-E	ST-12-L
Post-processing	Copper-plated	Copper-plated	Copper-plated	Laminated	Copper-plated	Laminated	Copper-plated	Laminated
Average Ic (77K s.f.)	45-60A	75-100A	80-120A	45-120A	120-160A	120-160A	200-350A	200-350A
Wire Width	2mm	3/3.3mm	4mm	4.8mm	5mm	5.8mm	10mm	12mm
Wire Thickness	55-95 μm	55-95 μm	55-95 μm	175-350 μm	55-95 μm	175-350 μm	55-95 μm	175-350 μm
Crit.Tensile Stress	>400Mpa	>400Mpa	>400Mpa	>400Mpa	>400Mpa	>400Mpa	>400Mpa	>400Mpa
Crit.Tensile Strain	0.4%	0.4%	0.4%	0.4%	0.4%	0.4%	0.4%	0.4%
Current Uniformity	±5-10%	±5-10%	±5-10%	±5-10%	±5-10%	±5-10%	±5-10%	±5-10%
Min Bending Diameter	11-15mm	11-15mm	11-15mm	15-20mm	11-15mm	15-20mm	11-15mm	15-20mm

Table 6.9: Parameters of YBCO strip made by Shanghai superconductor Co.

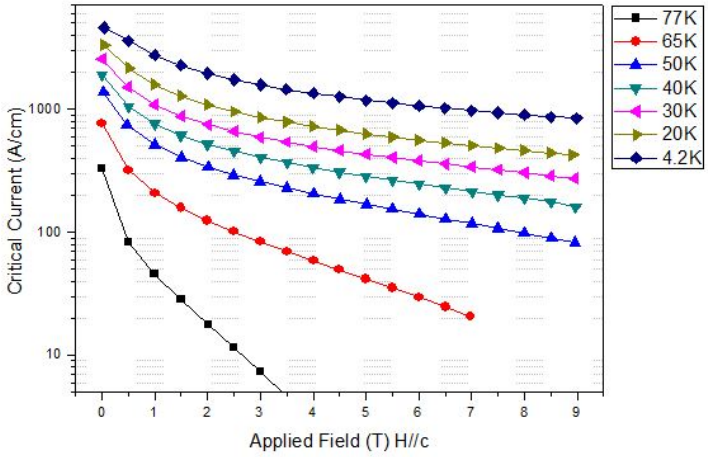

Figure 6.28: Critical current at different temperatures and magnetic fields

Magnetic field	Ic (4.2K)
2T	2000A
3T	1700A
5T	1200A

Table 6.10: critical current at different magnetic field

The cable used in the detector magnet design is stacked by ten 12 mm-wide YBCO tapes with a thickness of 5 mm, carrying a total operating current of 8000 A. The HTS superconducting detector magnet is composed of multiple double pancake coils, with 500 turns in the 7.5-m-long axial direction and 5 layers in 50-mm-thick radial direction. The detailed parameters of HTS detector magnet are listed in Table 6.11. Figure 6.29 and Figure 6.30 show the magnetic field distribution and the magnetic flux lines of the HTS detector magnet. The stray field distribution of the HTS magnet is shown in Table 6.12 and Figure 6.31.

Central magnetic field	3 T	Working current	7970 A
Maximum vertical field on cable	2.7 T	Ampere-turns	20000000
Inner diameter of coil	3.6 m	Inductance	38.36 H
Outer diameter of coil	3.7 m	Stored energy	1.2 GJ
Length of the coil	7.5 m	Operating temperature	Less than 20 K

Table 6.11: Parameters of CEPC detector magnet

Stray field distribution:

Draft v.2

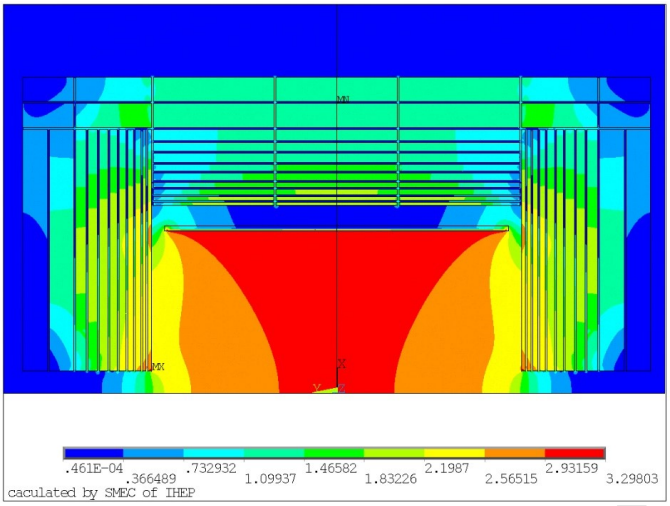

Figure 6.29: Magnetic field distribution

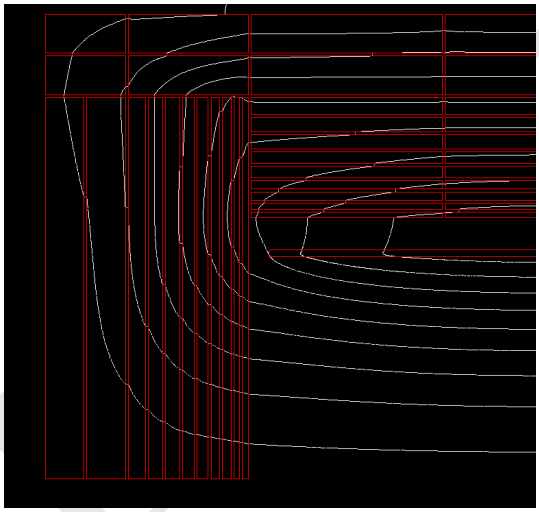

Figure 6.30: Magnetic flux distribution

	axial direction	radial direction
50Gs	15m	13m
100Gs	11m	9m

Table 6.12: Stray field region

6.3.4 Future work of HTS plan

In order to validate the feasibility of using HTS detector magnet, further work remains to be done: a) select appropriate ReBCO cable or design new cables to fit the requirements of large bore magnet; b) find a proper way to wind large HTS coils; c) study the quench

IDEA v0.2

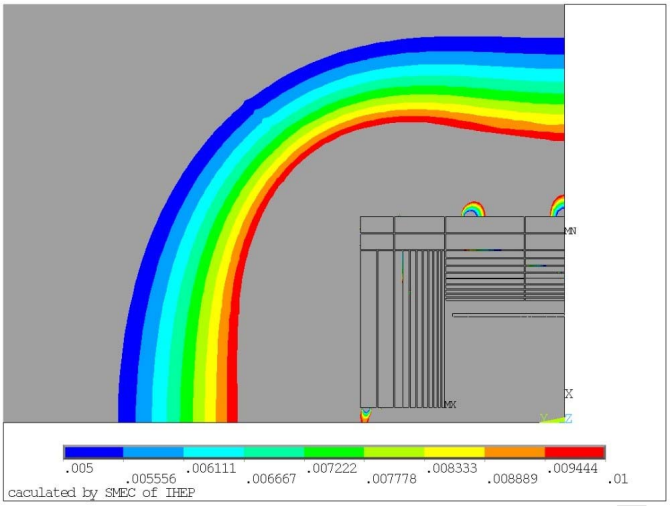

Figure 6.31: Stray field distribution of 50 Gs and 100 Gs

protection, quench propagation and quench protection of ReBCO coils by fabricate a prototype ReBCO coil.

6.4 Solenoid Coil Design

6.4.1 Solenoid Coil Structure

The coil windings of the LTS detector magnet is wound by using inner winding technique, with the aluminum-alloy cylinder acting as an external supporting mandrel and taking away the quench induced heat energy. In order to maintain the operating temperature of LTS detector magnet, the cooling tubes for circular flow of LHe are welded on the outer surface of the aluminum-alloy cylinder.

A horizontal cryostat, consisting of a vacuum tank, an inner thermal shield, an outer thermal shield. The stainless steel vacuum vessel is with a length of 8.05 m and an outer radius of 4.25 m. Two service towers are designed on the top of the cryostat to install the current leads and the helium phase separator. The vacuum tank is cantilevered from the central ring of the barrel yoke.

6.4.2 R&D of Superconducting Conductor

The stress level in pure aluminum stabilizer enclosing the NbTi Rutherford cable can exceed the materialąŕs yield point after cool-down and excitation. Thus, a mechanical strengthening structure is added and investigated to lower the stress level in the pure aluminum stabilizer. Specifically, two aluminum-alloy reinforcing blocks are bonded with the pure aluminum stabilizer by using electron beam welding. The LTS cable is expected to have similar characteristics with the cable used in CMS detector magnet. The designed parameters of the LTS cable are shown in Table 6.13.

Joint efforts have been made by IHEP and Toly electrical Co Ltd to fabricate the LTS cable for CEPC detector magnet. Test results of the LTS cable indicate that there is a 5% degradation of the critical current of the NbTi strands after cabling and there is a

Draft-v0.2

Superconducting strand in virgin state	
Strand diameter	1.2 mm
Cu/NbTi	1.3
SC strand critical current density	$\geq$ 2700A/mm2 @4.2K,5T
Filament diameter	About 55 um
RRR of copper matrix	$\geq$ 100
Twist pitch	1.3
Rutherford cable	
Number of strand	32
Cable transposition pitch	120mm
Compacting ratio	0.87
Final conductor	
Ic degradation during manufacturing	<10%
Nominal design current	16KA
Critical current at 4.2K and 5 Tesla	50KA
Total length of conductor	31km

Table 6.13: Superconductor characteristics

33.3% degradation of RRR value of the copper matrix of NbTi strands after cabling. The minimum shear strength between the copper and the pure aluminum is about 30 MPa after the inserting process. The tested samples are shown in Figure 6.32.

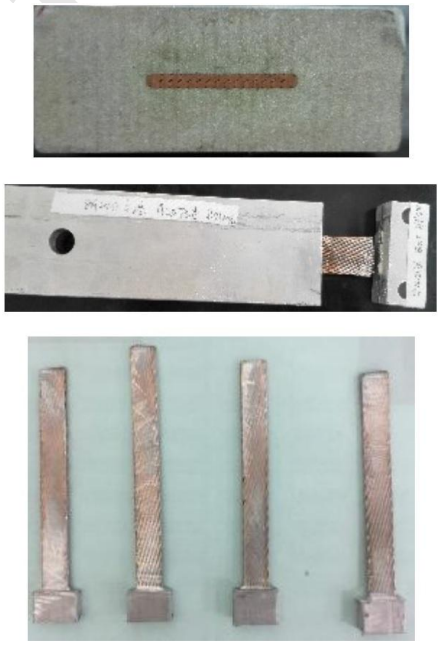

Figure 6.32: Samples of shear strength test

Draft-V0.2

6.4.3 Coil fabrication and assembly

1. Machining of aluminum-alloy cylinder

The coil supporting cylinder consists of three long central supporting modules and two short end supporting modules. All the five modules are made of Al-5083, with inner surfaces machined with high precision and outer surfaces enclosed with LHe tubes. Three long supporting modules are all designed with two flanges and two tube joints while two short supporting modules are both designed with one end flange and one tube joint.

2. Coil winding

The coils are winded along the inner surfaces of the aluminum-alloy, all the five coil modules are winded, impregnated and instrumented individually.

3. Coil assembly

The five coil modules are assembled together with the help from the assembly tooling in vertical direction. The assembling steps are as follows: i) the short end coil module is vertically placed onto the assembly tooling; ii) place the long central coil module onto the short end coil module and connect the two flanges by using bolts, then weld the tube and superconductor joints; iii)repeat the second step until the top short end coil module is connected, the tube and superconductor joint is welded.

6.5 Magnet Cryogenics Design

6.5.1 Preliminary Simulation of the Thermosyphon Circuit

6.5.1.1 Computational model and mesh

Thermosyphon principle is used to cool CEPC detector superconducting magnet by welding U-shaped tubes carrying LHe on the outer surfaces of the coil supporting cylinders. The thermosyphon circuit consists of the supplying pipe, the cooling pipe and the returning pipe. The liquid helium absorbs the heat transferred to the cooling pipe and then its phase changes, resulting in the pressure difference in the cooling pipe. A gas-liquid two-phase flow is then formed due to the pressure difference between the two sides of the circuit. In order to study the phase transition process of helium in the circuit, we start by simplifying the original circuit and assume it is constant mass flow instead of a pressure-driven flow. Thus, a single tube model is created as shown in Figure 6.33. The entire circuit, with an uniform diameter of 14 mm, is placed vertically and its gravity direction is downward vertically.

The finite element analysis mesh shape of the above three-dimensional model is shown in Figure 6.34. Actually, a fine mesh and small time step is required to simulate the phase transition process and obtain accurate simulation results. Specially, an extremely high mesh density near the wall of the tube is required to calculate the fluid boundary layer accurately, as shown in Figure 6.34. The distribution of the boundary layer will directly affect the heat transfer, phase change and two-phase flow process in the cooling pipe.

6.5.1.2 Computation settings for all scales

According to the data, set the inlet flow of 2.5g/s, using the flow calculation formula,

$$m = \rho V A$$

Draft-V0.2

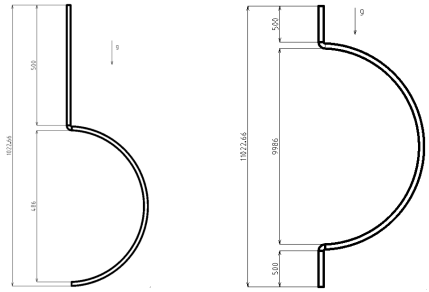

Figure 6.33: a. The 10:1 scale model b. The 1:1 scale model (schematic diagram) The computational model (mm)

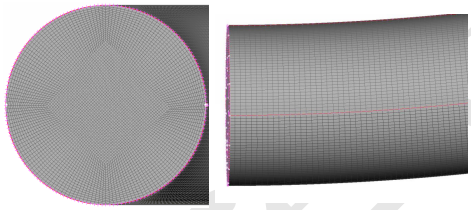

Figure 6.34: a. Cross-section mesh b. Lateral mesh The mesh shape

The fluid inlet velocity is 0.13 m / s. And then using Reynolds number calculation formula,

$$Re_D = \frac{\rho V D}{\mu}$$

The calculated Reynolds number Re_D of the flow in the thermosyphon circuit is 71830, much larger than the critical number ($Re_D, C = 2300$). Thus the helium flow in the thermosyphon circuit is turbulent flow, which can be simulated by suing turbulence model.

The phase transition of liquid helium and the two-phase flow process in the thermosyphon circuit are simulated by VOF method to capture the two-phase interface. The properties of liquid helium and gas helium are shown in Table 6.14. The difference between the standard state enthalpy (Hs) of gas helium and Hs of liquid helium represents the latent heat required for phase transformation of liquid helium.

The settings of the boundary conditions used in the simulation are shown in Table 6.15. The heat generation from the evaporator is firstly assumed to be with a constant heat flux density of $12.4W/m^2$. Then we adjust the heat flux density by referring to the status of the flow heat transfer, ensuring the gas mass fraction is less than 10% in the final stable gas-liquid two phase flow and maintaining the safety and stability of the entire thermosyphon circuit.

Draft-v0.2

The physical properties	Liquid helium	Gas helium
T(K)	4.18	4.21
$\rho(kg/m^3)$	124.972	16.627
H_s	-864.648	82709.986
Tboil(K)	4.2	
$\rho(mN/m)$		0.096

Table 6.14: The physical properties

Positions	Boundary conditions	Parameters
Inlet	Velocity inlet	$V = 0.13m/s, T = 4.18K$
Outlet	Pressure outlet	$P = 101325Pa, T = 4.18K$
The heat wall	Constant heat flux density	$q = 12.4W/m^2$
Other walls	Adiabatic wall	$q = 0$

Table 6.15: The physical properties

6.5.2 Preliminary results for 10:1 scale model

The transient numerical simulation of the two-phase flow in the cooling pipe has been carried out. Figure 6.35 and Figure 6.36 show the changes of the temperature distribution and the density distribution over the time, respectively. At t=1 s, the temperature of the cooling pipe rises gradually from the initial temperature of 4.2 K due to the constant heating source; all the working fluid in the circuit is still liquid helium. At t=5.042 s, the liquid helium reaches the boiling point (4.23 K) in the upper part of the cooling pipe; phase change occurs in the upper part of the cooling pipe as shown in Figure 6.36. The temperature in the upper part will keep rising as the heat cannot be taken away immediately.

Figure 6.37 shows the partial enlarged view of the blue box part of Figure 6.36. The helium bubbles emerged in the inner wall of the cooling pipe firstly and then moved outward because of the buoyancy. Some small bubbles gathered into a large bubble nearby the outer wall and were then washed by the fluid into the pipe outlet.

6.5.3 Experiment of a small-sized He thermosiphon

6.5.3.1 Experimental Set-up

Figure 6.38 shows the experimental set-up, which consists of one GM cryocooler (1.0 W@4.2 K), one phase separator, one 1-meter high vacuum container, one thermal shield connected with 1st stage cold head and one thermal shield connected with 2nd stage cold head. The U-shaped thermosiphon pipe is welded together with the phase separator, which is connected with the 2nd stage the cold head.

As shown in Figure 6.39, one thermometer is mounted on the phase separator and four thermometers are mounted on the U-shaped pipe to monitor the temperature distribution along the inner wall of the pipe, therefore, calculating the heat transfer coefficient. The thermometers are with a measurement accuracy of 0.1 K from 2.5 K to 25 K.

Draft-v0.2

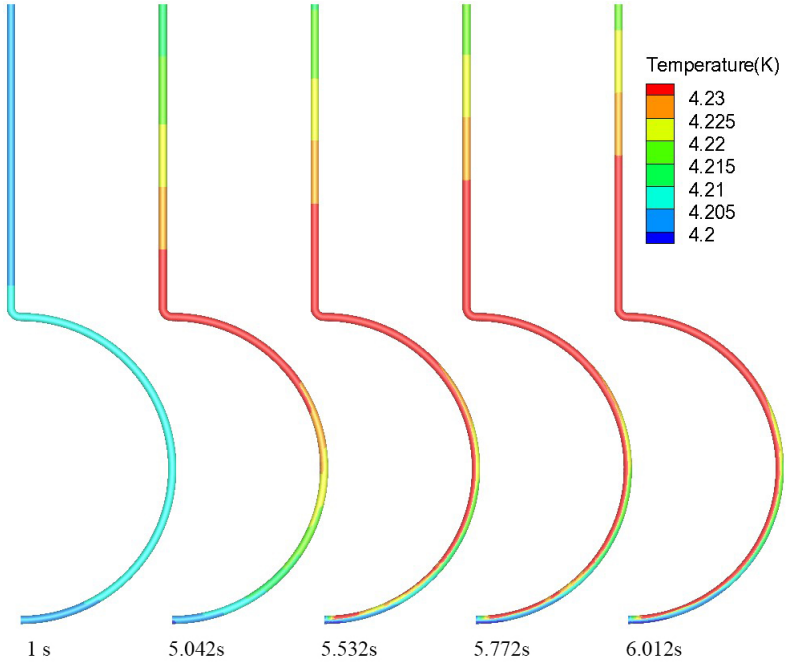

Figure 6.35: The comparison of the temperature distribution

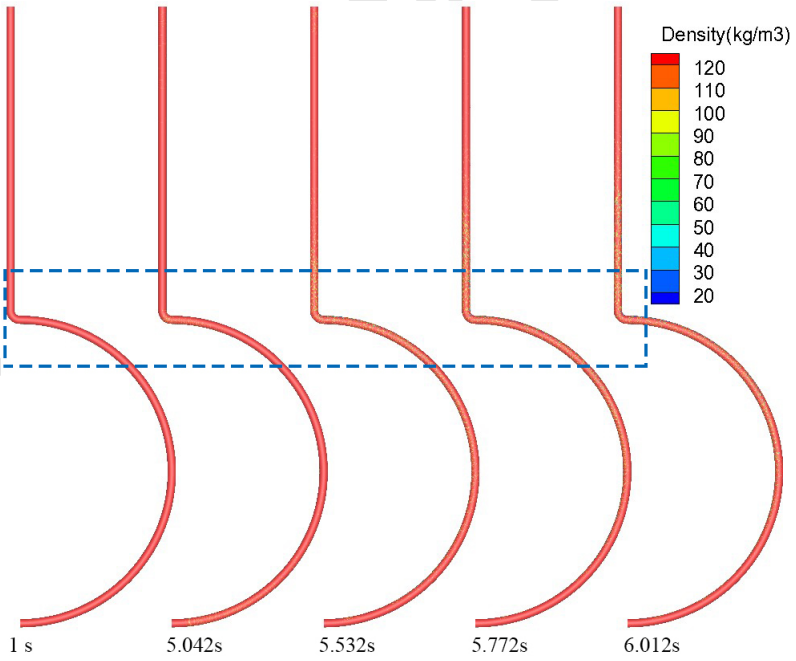

Figure 6.36: The comparison of the density distribution. (red: liquid helium, blue: gas helium)

6.5.3.2 Experimental result and analysis

As shown in Figure 6.40, when the heat flux is 137W/m2,the helium pressure increases from 0.3MPa to 1.8MPa,then descend to near 1.1MPa ,after that following up and down under the filling ratio of 26%.When the filling ratio is 52% and 87%,the pressure in thermosiphon maintain constant in general,as for ratio 87%,the pressure is a little higher than 52%.

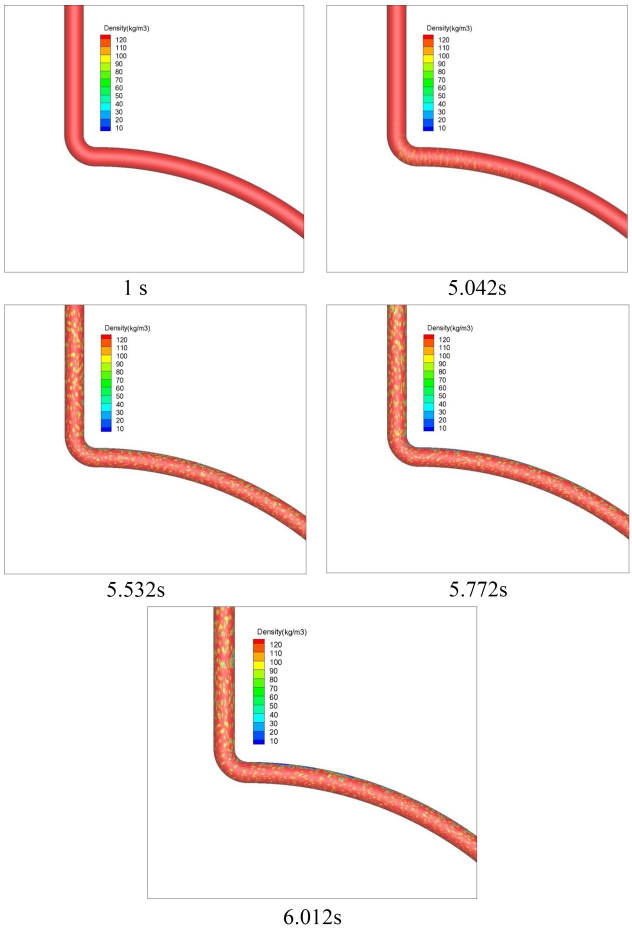

Figure 6.37: The comparison of the density distribution in the upper part of cooling pipe. (red: liquid he,blue: gas he)

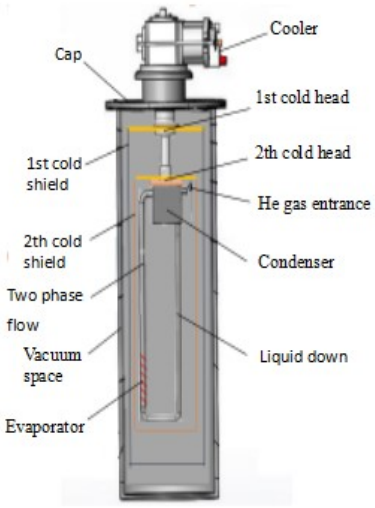

Figure 6.38: the main component structure of the experimental cryostat

Figure 6.40 shows the relation between saturation pressure and time under different filling ratios when given a heat flux of 137 W/m2. Specifically, for a given filling ratio of

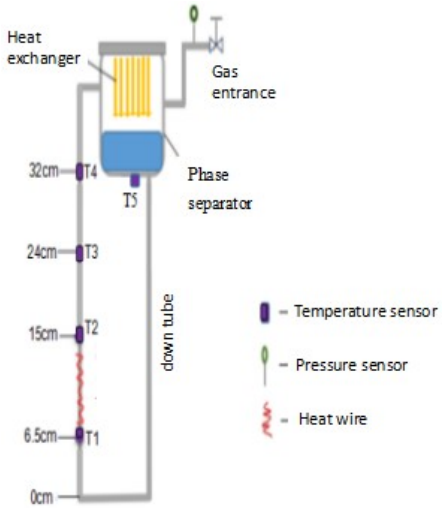

Figure 6.39: Schematic of the experimental measures circulation loop

26%, the helium pressure rises from 0.3 MPa to 1.8 MPa firstly, then drops to 1.1 MPa and finally keeps oscillating between 1.8 MPa and 1.1 MPa; for a given filling ratio of 52%, the helium pressure rises gradually from 0.3 MPa and then reaches a plateau at 1.125 MPa; for a given filling ratio of 87%, the helium pressure rises gradually from 0.3 MPa and then reaches a plateau at 1.325 MPa.

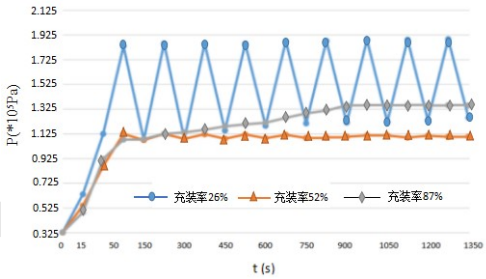

Figure 6.40: the saturation pressure of different filling ratio varies with time in heat flux $137W/m^2$

In the beginning of the experiment, ΔT_w increases linearly with heat flux at low heat fluxes. Before $q_A = 25W/m^2$ at point A on Figure 6.41 and Figure 6.42, the heat transfer is identified as single phase natural convection. After point A, the temperature difference show difference between Figure 6.41 and Figure 6.42,the reason is that heat transfer intensity in exit section is higher than that in entrance, this leads to the upper comes to dry out earlier, then develop to the bottom with heat increase. a) Before $q_A = 25W/m^2$ at point A, the heat transfer is identified as single phase natural convection. b) Between points A and C is in the developing nucleate boiling regime. c) The transition from nucleate boiling to film boiling occurs at point C. d) After point E helium enters its supercritical state.

Figure 6.41 shows the boiling curve at Z=6.5 cm in the entrance. Figure 6.42 shows the boiling curve at Z=32 cm in exit entrance. Before point A ($q_A = 25W/m^2$), ΔT_w increases linearly with the heat flux and the heat transfer is identified as single-phase natural convection in both Figure 6.41 and Figure 6.42. After point A, we can see a clear temperature difference between Figure 6.41 and Figure 6.42 because the heat transfer

effect in the exit section is higher than that in the entrance section which results in an earlier dry-out at the top. For both Figure 6.41 and Figure 6.42, between point A and point C is identified as the developing nucleate boiling regime and point C is identified as the transition point from nucleate boiling to film boiling. After point E, the helium reaches its critical state.

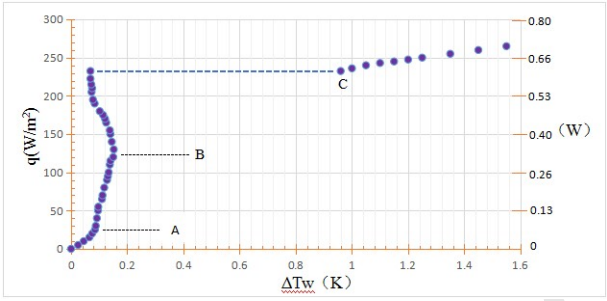

Figure 6.41: Boiling curve at $Z = 6.5cm$ in the entrance

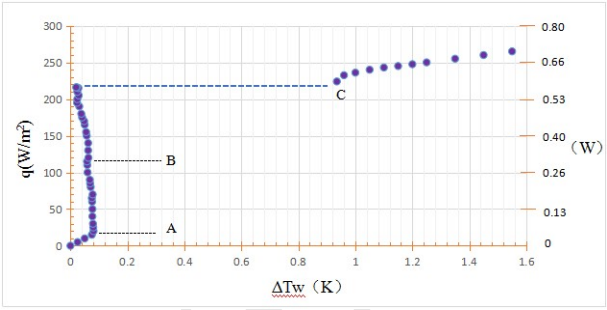

Figure 6.42: Boiling curve at $Z = 32cm$ in the exit section

Calculation formula of heat transfer:

$$h = fracqT_w - T_f$$

Figure reffig:510 shows the heat transfer coefficient at different locations in the tube. It can be summarized as follows: a) there is a linear relationship between the heat transfer coefficient (h) and the heat flux (q) at z=6.5 cm; b) compared to ąřz=6.5 cmąś, the heat transfer effect at z=24 cm (top area) is much stronger; c) the heat transfer effect drops quickly when the heat flux goes beyond point C because a large amount of the vapor cannot be liquefied immediately and the heating surface is covered by a film of vapor.

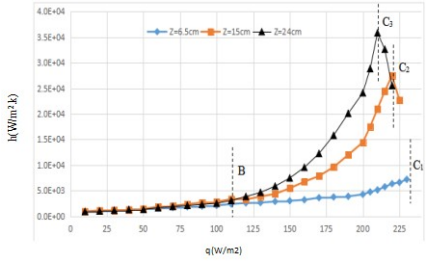

Figure 6.43: Heat transfer coefficient at different locations of the tube

6.6 Quench Protection and Power supply

6.6.1 power supply

A low ripple DC current-stabilized power supply, with low output voltage and high output current, is requested for CEPC detector magnet. The power supply is expected to have a free-wheel diode system and to be cooled with demineralized water. Figure 6.44 shows the main circuit topology diagram of a standard power supply, in which 12 pulse diode rectifiers and 4 IGBT chopper units with a switching frequency of 10 kHz are employed.Figure 6.45 is IGBT Performance schematic diagram.

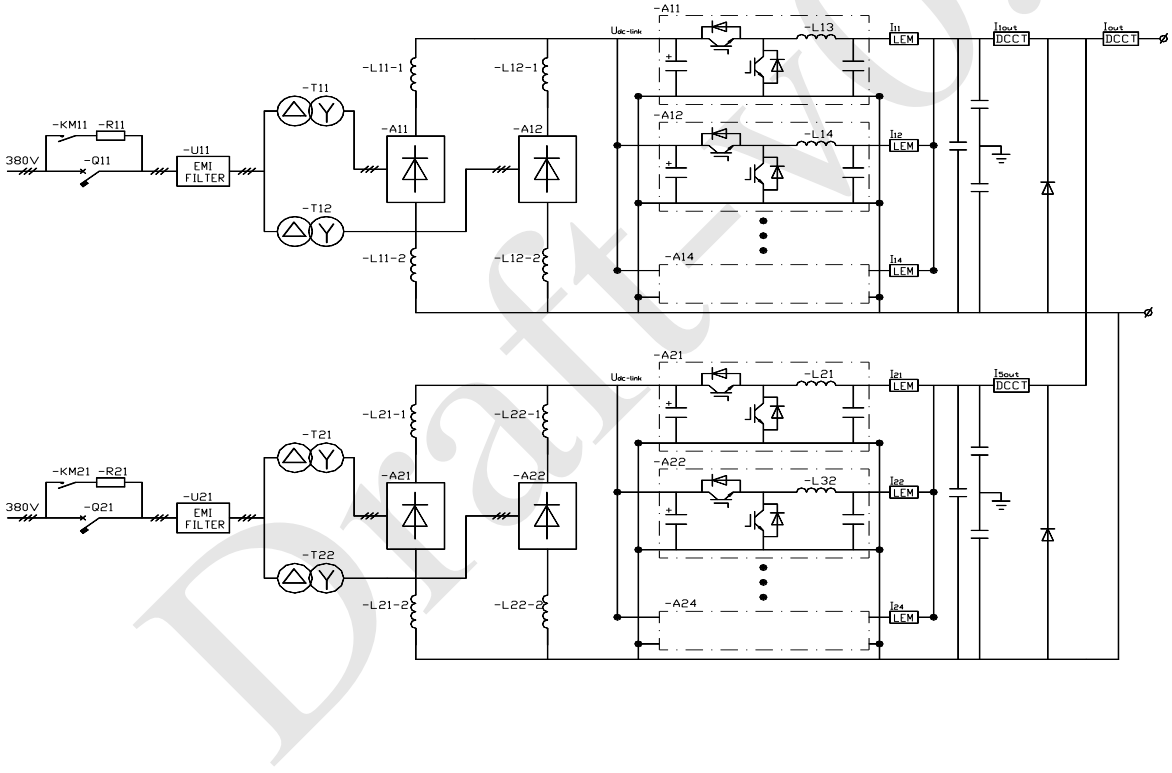

Figure 6.44: Main circuit topology diagram

6.6.2 Quench Protection

Selected voltage signals from the CEPC detector magnet coil and current leads are monitored by an FPGA board for quench detection. If a quench happened, the power supply is switched off and a dump resistor is switched into the electrical circuit, the huge stored energy will be extracted mainly by the dump resistor and partially by the coil itself. In order to monitor the status of the magnet, sensors or tools are added inside or outside to monitor temperature (busbar, current lead, valve box and etc), stress (tie rods), vacuum, coil current, liquid helium level, position (coil section) and etc.

Draft-v0.2

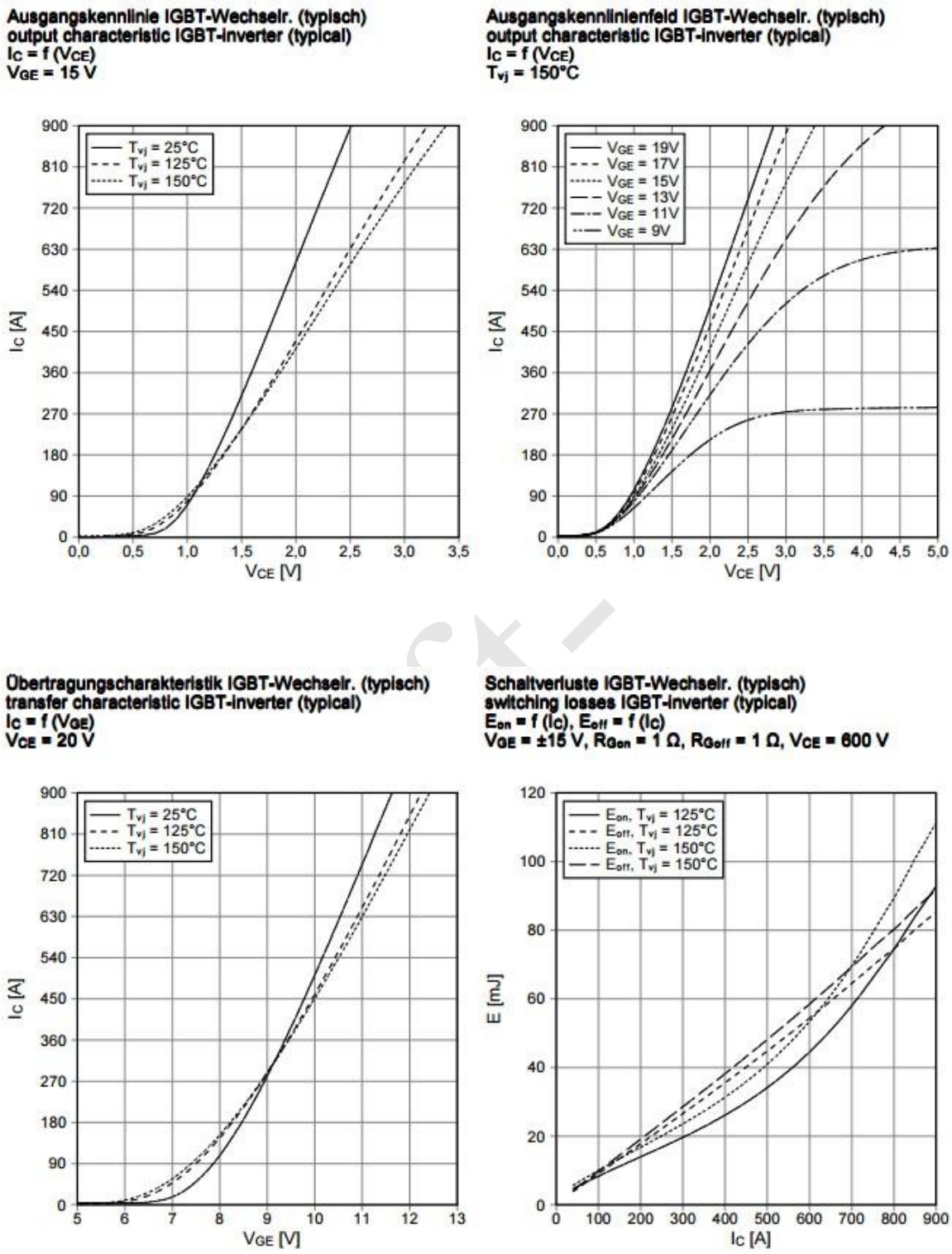

Figure 6.45: IGBT Performance schematic diagram

6.7 Iron Yoke Design

The CEPC detector magnet consists an assembly of iron yoke, as shown in Figure 6.46. The major functions of the iron yoke has been described in Section 7.1. According to

the general magnetic structure of large detector magnet, the yoke assembly consists of one cylindrical barrel yoke and two end cap yokes. High permeability material with high mechanical strength is requested for the yoke material by taking into accounts of requirements for both mechanical performance and magnetic field.

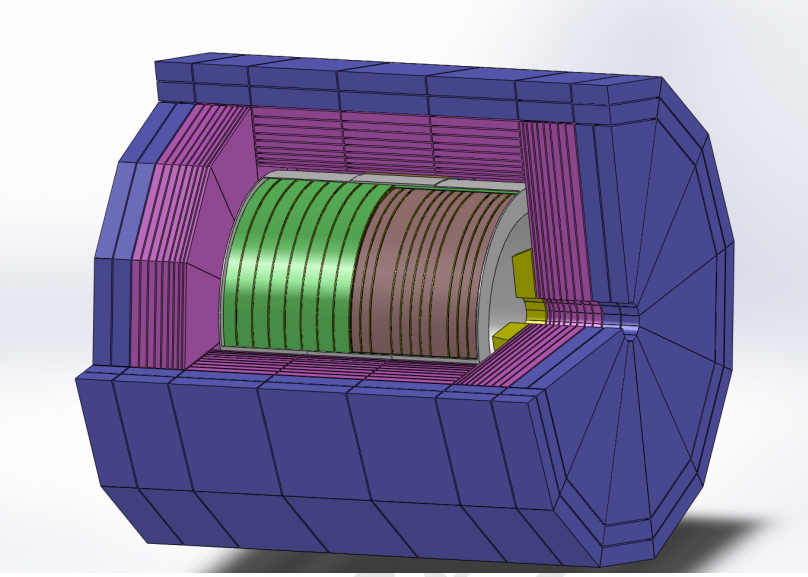

Figure 6.46: iron and magnet

6.7.1 The Barrel Yoke

As shown in Figure 6.47, the barrel yoke designed with a dodecagonal shape is with a length of 8,200 mm. The diameter of the inscribed circle for the outer dodecagon and the inner dodecagon is 13,300 mm and 7,800 mm, respectively. The barrel yoke are composed of 3 rings, with each ring consisting of 7 layers. A 100 mm gaps are designed between the rings to provide room for placing the electronics cables and services. And 100 mm space is designed between iron layers for placing the muon detector. Specially, the thickness of the inner 4 layers and the outer 3 layers is 100 mm and 450 mm, respectively.

6.7.2 The Endcap Yoke

Figure 6.48 shows the overall dimensions of the two dodecagonal end cap yokes. The diameter of the inscribed circle of the outer dodecagon is 13,300 mm. Each end cap yoke is with a thickness of 3,150 mm, consisting of 7 layers. The thickness of the innermost layer, the middle 3 layers and the outer 3 layers is 600 mm, 100 mm and 200 mm, respectively. A 100 mm space is designed between layers for placing the muon detector.

6.7.3 Yoke assembly

The total weight of the yoke assembly is about 10,000 tons. Each ring of the barrel yoke and each end cap yoke are both composed of 12 segments. The maximum weight of a single segment for the barrel yoke and the end cap yoke is 150 tons and 200 tons, respectively.

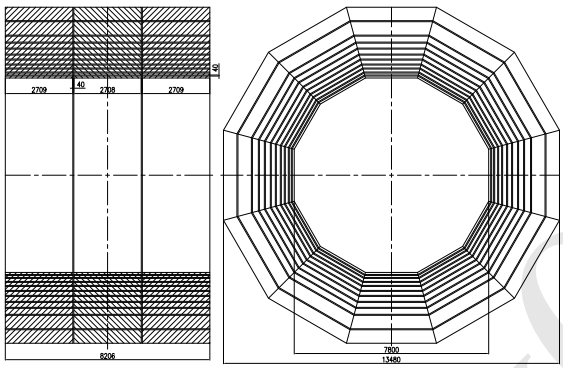

Figure 6.47: iron design

After pre-assembly at the manufacturer, the disintegrated yoke segments then are shipped to the detector lab. The yokes will be assembled at the underground IR cavern if possible, otherwise they will be assembled in the surface building around the IR area. The middle ring of the yoke is firstly assembled together with the detector solenoid and then lowered into the IR carven as the heaviest component which estimated 3000 tons. In this case, a gantry crane will be employed temporarily. Generally, it takes longer time to assemble the yokes at the underground cavern than in the surface building.

6.8 Dual Solenoid Scenario

The active shielding design is iron-yoke free which has been studied by FCC conceptual design [1-2]. The main challenge for this dual solenoid scenario design is that we need to confirm its ability to allow high-quality muon tracking which is crucial for studying Higgs boson and hunting for new fundamental particles.

The active shielding design contains two series connected superconducting solenoids which carry the operating current of opposite current direction to the main superconducting solenoid. Figure 6.49 shows the sketch for the half cross section of the active shielding magnet. The main detector solenoid provides 5 T central field within an obstruction-free room temperature bore (radius of 3.6 m, length of 7.6 m). The outer shielding solenoid provides -2 T central field within the bore (radius of 6.5 m, length of 10 m). Two supporting cylinders are requested for the main solenoid and the shielding solenoid. The available areas for placing muon chambers are marked in Figure 6.49. The field map of the active shielding detector magnet is shown in Figure 6.50.

Draft-v0.2

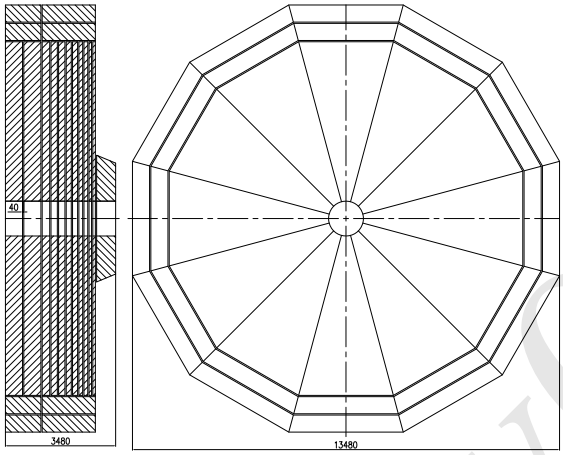

Figure 6.48: iron design

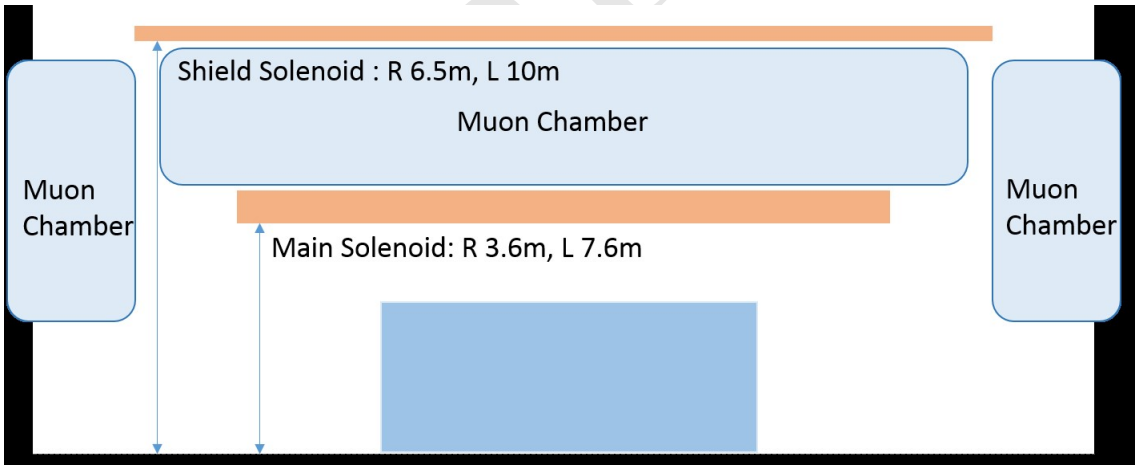

Figure 6.49: Sketch figure for the half cross section of the active shielding magnet, with the available areas for muon chambers

6.9 The low magnetic field detector magnet

A 2 Tesla solenoidal magnetic field scheme is proposed to match different options of the detector.

In this scheme, the tracker is located inside the room temperature bore of the magnet, however the calorimetry will locate outside the magnet coil, then the size of the coil getting smaller to about 2.1 m in radius, but it should be built thin enough to reduce the material.

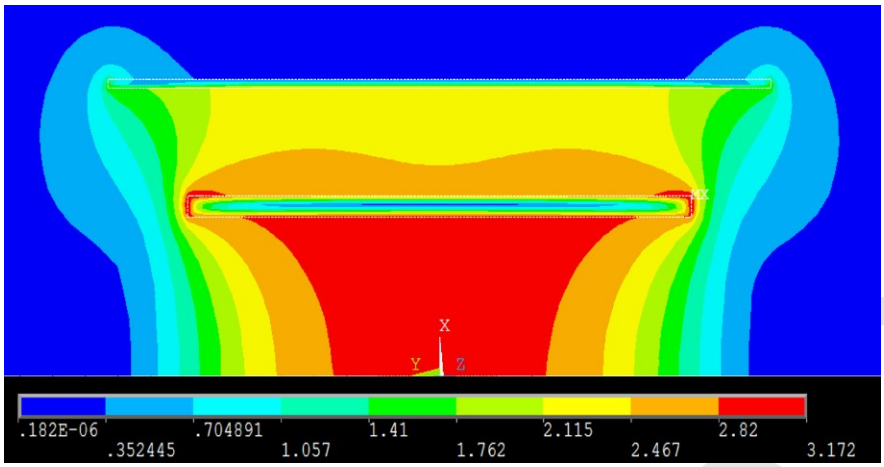

Figure 6.50: Field map of the active shielding magnet

The solenoid magnet will be around 30 cm in thickness and less than 0.8 Xo in radiation length.

References

[1] CEPC project website. http://cepc.ihep.ac.cn.

Draft-v0.2

Draft-v0.2

CHAPTER 7

MUON SYSTEM

Draft-v0.2

As described in pre-CDR [1], the CEPC muon system acts as the muon identifier, the solenoid flux return yoke and the support structure for the whole spectrometer. High muon detection efficiency, low hadron mis-identification rate, modest position resolution and large coverage are the main concerns of the design. The muon system plays an important role in measuring physics processes involving muon final states, e.g. $e^+e^- \to ZH$ with $Z \to e^+e^-$ or $\mu^+\mu^-$. In addition, it compensates for leaking energetic showers and late showering pions from the calorimeters, which is important to improve the relative jet energy resolution[2].

7.1 Baseline Design

The CEPC muon system is the outermost component of the whole detector. It is divided into barrel and end-caps, as shown in Fig. 5.1. Both the barrel and end-caps consist of segmented modules. The segmentation is constrained by the maximum sizes of the module and sensitive unit (more segments are required for a larger detector), dodecagon segmentation is selected for the baseline design of the CEPC muon system. All baseline design parameters are summarised in Table 7.1. These parameters will be further optimised together with the inner detectors, in particular the ECAL and the HCAL.

The number of sensitive layers and the thickness of iron (or tungsten) in the absorbers are two critical parameters. For the baseline design, the total thickness of iron absorber is chosen to be 8λ (the nuclear interaction length of iron) distributed in 8 layers, which should be sufficient for effective muon tracking. Gaps of 4 cm between neighbouring iron layers give adequate space for installing sensitive detectors.

By Copyright © 2018 HEP Community

Table 7.1: The baseline design parameters of the CEPC muon system

Parameter	**Possible range**	**Baseline**
Lb/2 [m]	3.6 – 5.6	4.0
Rin [m]	3.5 – 5.0	4.4
Rout [m]	5.5 – 7.2	7.0
Le [m]	2.0 – 3.0	2.6
Re [m]	0.6 – 1.0	0.8
Segmentation	8/10/12	12
Number of layers	6 – 10	8
Total thickness of iron	6 – 10λ ($\lambda = 16.77$ cm)	8λ (136 cm) (8/8/12/12/16/16/20/20/24) cm
Solid angle coverage	(0.94 – 0.98)$\times 4\pi$	0.98
Position resolution [cm]	$\sigma_{r\phi}$: 1.5 – 2.5	2
	σ_z : 1 – 2	1.5
Detection efficiency ($E_\mu > 5$ GeV)	92% – 99%	95%
Fake($\pi \to \mu$)@30GeV	0.5% – 3%	$< 1\%$
Rate capability [Hz/cm^2]	50 – 100	$\sim$60
Technology	RPC	RPC (super module, 1 layer readout, 2 layers of RPC)
	μRWell	
Total area [m^2]	Barrel	$\sim$4450
	Endcap	$\sim$4150
	Total	$\sim$8660

Draft-v0.2

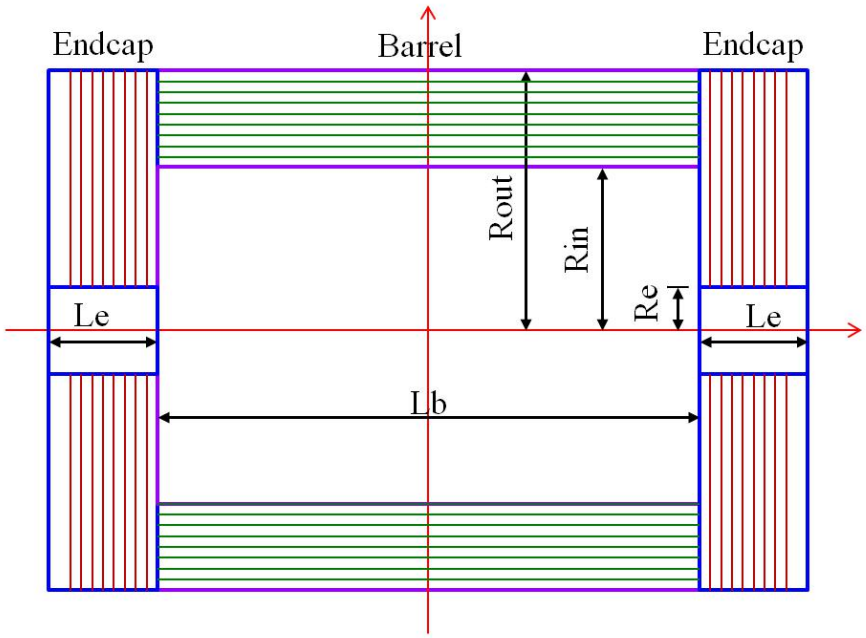

Figure 5.1: The basic layout of the muon system.

The solid angle coverage of the CEPC muon system should be up to $0.98 \times 4\pi$ in accordance with the tracking system. Position resolutions of $\sigma_{r\phi} = 2.0$ cm and $\sigma_z = 1.5$ cm are also required. Since the particle flow algorithm calorimetry provides very good particle identification capabilities, the detection efficiency of 95% ($E_\mu > 5$ GeV) of the CEPC muon system should provide enough redundancy in muon detection for most physics processes related to muons. Based on the dimensions and segmentation of the baseline design, the total sensitive area of the muon system amounts to 8600 m^2.

7.2 The Resistive Plate Chamber technology

Resistive Plate Chamber (RPC) is suitable for building large area detectors with milimeter spatial resolution. It has been applied in muon systems for experiments including BaBar [3], Belle [4], CMS [5] , ATLAS [6], BESIII [7], and Daya Bay [8]. It provides a common solution with the following advantages: low cost, robustness, easy construction of large areas, large signal, simple front-end electronics, good time and spatial resolution. It is chosen as the baseline design of the CEPC muon system.

RPCs can be built with glass or Bakelite, and run in avalanche or streamer mode. Bakelite RPCs of about 1200 m^2 and 3200 m^2 were produced for the BESIII and Daya Bay muon systems, respectively. Compared with glass RPC, Bakelite RPC has the advantages of easier construction, lower density, larger cell size and lower cost, especially if the event rate is below 100 Hz/cm^2 as required by the CEPC muon system. The characteristics of Bakeliete and glass RPCs are compared in Table **??**. Further improvements are required for Bakelite RPCs, however, in terms of long-term stability, detection efficiency, readout technologies, lower resistivity ($< 10^{10}$) and higher rate capability.

Table 7.2: Comparison of Bakelite and glass RPC.

Parameters		Bakelite	Glass
Bulk resistivity [$\Omega\cdot$ cm]	Normal	$10^{10} \sim 10^{12}$	$> 10^{12}$
	Developing	$10^{8} \sim 10^{9}$	
Max unit size (2 mm thick) [m]		1.2×2.4	1.0×1.2
Surface flatness [nm]		< 500	< 100
Density [g/cm^3]		1.36	2.4∼2.8
Min board thickness [mm]		1.0	0.2
Mechanical performance		Tough	Fragile
Rate capability [Hz/cm^2]	Streamer	100@92%	
	Avalanche	10K	100@95%
Noise rate [Hz/cm^2]	Streamer	< 0.8	0.05

7.3 The μRWell technology

The μRWell is a compact, spark-protected and single amplification stage Micro-Pattern Gas Detector (MPGD). In the μRWell technology an additional discharge resilience with respect to the triple-GEM detectors is foreseen as well as a simplified assembly geometry. A μRWell detector [**?**] is composed of two PCBs: a standard GEM Drift PCB acting as the cathode and a μRWell PCB that couples in a unique structure the electron amplification (a WELL patterned matrix) and the readout stages 7.2a). A standard GEM 50 μm polyimide foil is copper clad on one side and Diamond Like Carbon (DLC) sputtered on the opposite side. The thickness of the DLC layer is adjusted according to the desired surface resistivity value (50-200 M$\Omega/\square$) and represents the bottom of the WELL matrix providing discharge suppression as well as current evacuation. The foil is then coupled to a readout board 7.2b). A chemical etching process is then performed on the top surface of the overall structure in order to create the WELL pattern (conical channels 70 um (50 um) top (bottom) in diameter and 140 μm pitch) that constitutes the amplification stage 7.2c). The high voltage applied between the copper and the resistive DLC layers produces the required electric field within the WELLs that is necessary to develop charge amplification. The signal is capacitively collected at the readout strips/pads. Two main schemes for the resistive layer can be envisaged: a *low-rate* scheme (for particles fluxes lower than 100 kHz/cm^2) based on a simple resistive layer of suitable resistivity; and an *high-rate* scheme (for a particle flux up to 1 MHz/cm^2) based on two resistive layers intra-connected by vias and connected to ground through the readout electrodes. Finally, a drift thickness of 3-4 mm allows for reaching a full efficiency while maintaining a versatile detector compactness.

A distinctive advantage of the proposed μRWell technology is that the detector does not require complex and time-consuming assembly procedures (neither stretching nor gluing), and is definitely much simpler than many other existing MPGDs, such as GEMs or MicroMegas. Being composed of only two main components, the cathode and anode PCBs, is extremely simple to be assembled. The engineering and the following industri-

Draft-v0.2

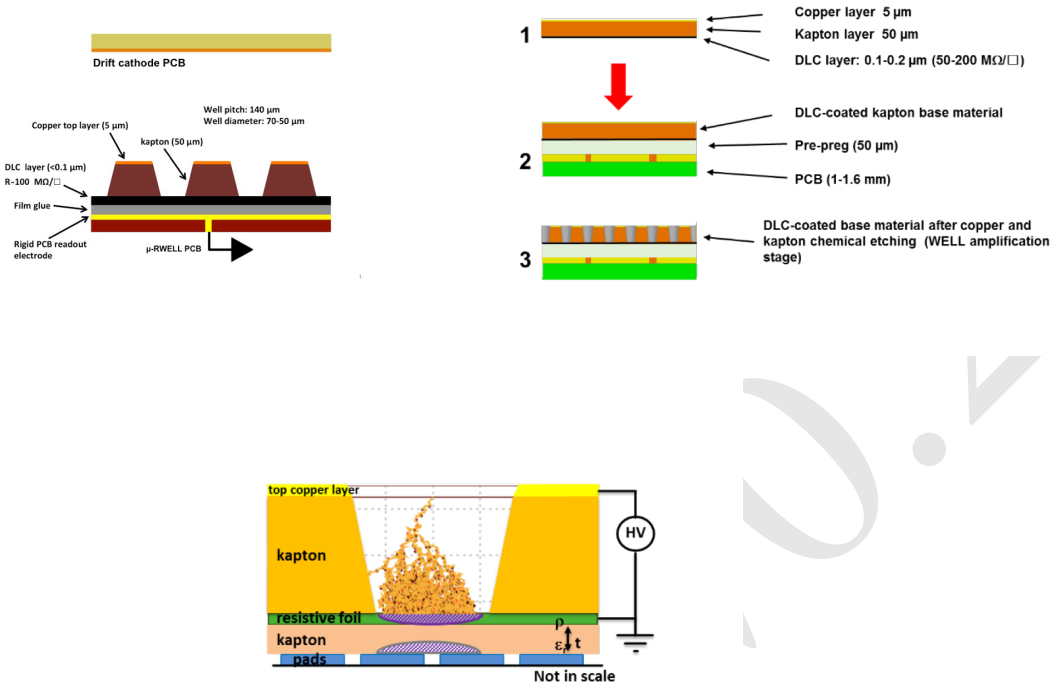

Figure 7.2: a) Layout of a μRWell detector module; b) Coupling steps of the μRWell PCB c) Amplification stage directly coupled with the readout.

alization of the u-RWell technology is one of the most important goals of the project. The technology is suitable for large area tracking devices and compact digital hadron calorimetry in HEP experiments; for X-ray and neutron imaging in industrial applications, medical and in particular for homeland security, where muon tomography requires very large area coverage.

7.3.1 Large size μRWell detectors

Modern HEP experiments, as well as some specific applications of gaseous detectors, require for large area coverage. In particular the upgrade of the experiments at the HL-LHC at CERN needs to cover large regions with high precision rad-hard tracking devices.

The single-resistive layer μRWell is a mature technology that has been proposed as tracking device for the CMS Phase2 upgrade of the muon detector. In this framework an R&D for the engineering, construction and test of large size single-resistive layer μRWells has been pursued. The task has been accomplished in strict collaboration with an Italian PCB Company (ELTOS SpA, http://www.eltos.com/).
As a first step a $\sim 1.2 \times 0.5$ m^2 μRWell (GE1/1-μRWell prototype) was designed, built and characterized in a beam test at the H8-SPS area at CERN, smaller than the final GE2/1, but $\sim$40 times larger than every μRWells prototype previously built (fig. 7.3 Top).

Figure 7.3: Top) Picture of the CMS GE1/1-μRWell prototype. Bottom) Picture of the CMS GE2/1 sector with two M4 μRWell prototypes.

The GE1/1 prototype had a resistive DLC surface resistivity of about 70 M$\Omega\square$ (in the *low-rate* schema configuration). The strips pitch was 800 μm and the chamber was equipped with VFAT2 front-end electronics. The gas mixture used was Ar/CO_2/CF_4 (45/15/40), with a drift gap of 7 mm. Due to the different used geometries for the amplification stage, the prototype was divided into two sectors (left and right) of slightly different gain. Both sectors were tested for efficiency and time resolution and the results compared with the performance of small μRWell prototypes (10 cm x 10cm, built in the *high-rate* configuration) used into the same experimental setup and equipped with the same electronics. Figure 7.4a) shows the efficiency as a function of gain for the GE1/1 size prototype and two small (10x10 cm^2) μRWell prototypes: one can observe that the three detectors have an identical behavior. Figure 7.4b) shows the time resolution as a function of gain: a resolution better than 6 ns is obtained for all three μRWell prototypes for a gain of about 10000.

In July 2017, the first GE2/1 20 degree sector equipped with two large area M4 μRWell detectors (each of dimensions $\sim$50x60 cm^2) was assembled. It was subsequently

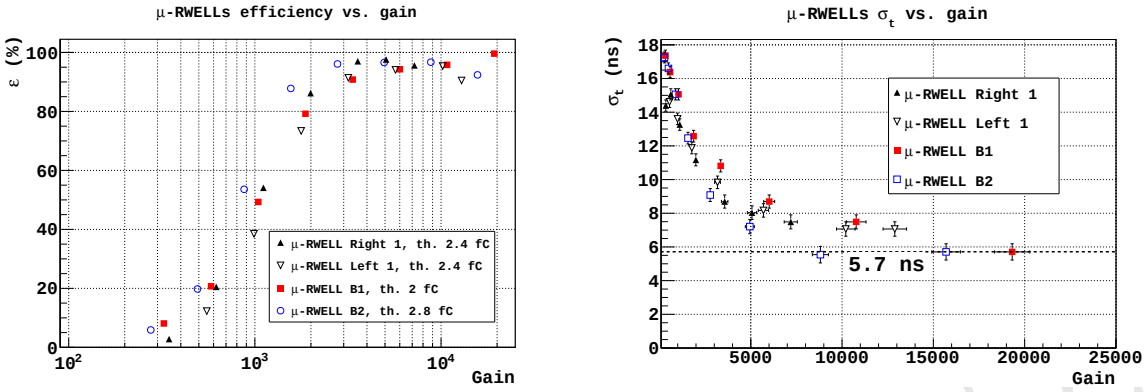

Figure 7.4: a) Efficiency vs Gain. b) Time resolution vs Gain.

exposed to a muon beam at the H4 test beam at CERN. The detector was placed on a remotely controllable moving platform in order to allow to scan the surface of the detector across the muon beam, as can be seen in figure 6. Only one half of one M4 was equipped with readout electronics and horizontal scans across one half of the M4 at the time were performed. The GE2/1 sector was flushed with an $ARCO_2$ 70-30 gas mixture. The beam line was equipped with a tracker composed of two GEM detectors and two small size μRWell prototypes. The efficiency of the GE2/1 sector was defined as the number of triple coincidences GE21xGEM1xGEM2 divided by the double coincidence GEM1xGEM2. In figure fig. 7.3 Bottom) a picture of the GE21 sector equipped with two large are M4 detectors is shown in the H4 beam line at CERN.

An operating voltage of 530 V was chosen, that is in the middle of the HV plateau. The nominal gain at this operating voltage is about 10000. Two horizontals scans were then performed at this voltage across the whole surface of one M4 detector: the two scans were performed at two vertical positions separated by 20 cm in height, in order to illuminate the whole surface of the detector. Figure 7.5 shows the efficiency obtained in the various points of the two horizontal scans. All points are within 98-99% efficiency, therefore showing the excellent uniformity achieved by the detector over all its surface.

7.3.2 Applications for a Muon detection system for a CepC experiment

The μRWell technology, especially in its *low-rate* version, is a mature solution, with whom single detectors of a 0.5 m^2 have been realised and succesfully operated in the laboratory as well as in test beams. They can withstand particle rates up to a few tens of kHz/cm^2, providing a position resolution as good as $\sim$60 μm with a time resolution of 5-6 ns. Moreover the μRWell technology is a robust solution, intrinsically safer against sparks than, for example, the widely used GEM detectors. In comparison with the GEM detectors the construction is much simpler, involving no stretching of the kapton foils and only one amplification stage instead of the three stages of the triple-GEM solution. This makes the cost of a μRWell detector typically less than half the cost of a triple-GEM detector of the same size and the same strip pitch. A few industries have already started collaborating and producing some of the components of the μRWell detectors, and in a very short time, all the needed μRWell detector components will be produceable by industry. This technology could therefore be very effectively used for realizing a muon detection system for CepC. In particular this detector, which would have dimensions of a few thousand m^2

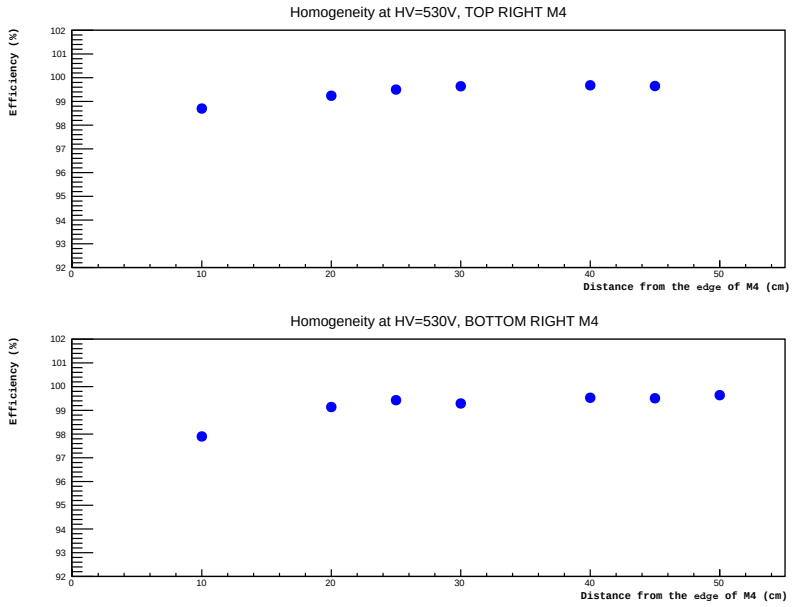

Figure 7.5: GE21 efficiency across the whole surface of one M4 detector. Two horizontal scans were performed in two vertical positions separated by 20 cm in height. All points are within 98-99% efficiency providing an excellent uniformity.

could be realised by using tiles of μRWell detectors of a size 50x50 cm^2. Each tile woud have a relatively small gas volume of $\sim$1 l. This would make the whole muon detector very modular with components bought directly from industry. The needed assembly and quality control of the μRWell detectors could then be efficiently realised by the collaborating institutes. A CepC muon detector made of μRWell tiles could consist of the three successive muon stations, each equipped with a couple of layers of μRWell detectors in order to provide a very precise, of the order of 200μm, position resolution on the coordinates of a muon track. This precise position resolution, together with the three stations, would allow to have an independent muon tracking that could then also be associated back to the tracks measured by the central tracker. This would make for a very robust and efficient muon detection system. A muon trigger system, albeit probably not essential for a CepC detector, could be easily implemented. A similar muon detection scheme, could be envisaged also for a SppC detector, eventually using the *high-rate* μRWell detectors in the regions where the highest particle rates are foreseen.

7.4 Future R&D

The baseline conceptual design and most promising technologies for the CEPC muon system have been discussed. Future R&D requires detailed studies of different technologies and further optimization of baseline design parameters. Several critical R&D items have been identified, including:

- **Long-lived particles optimization**: Explore new physics scenario of long-lived particles and exotic decays. Optimize detector parameters and technologies.
- **Layout and geometry optimization**: Detailed studies on the structure of the segments and modules need to be carried out to minimise the dead area and to optimise

the interface for routing, support and assembly. The geometry and dimensions need to be optimized together with the inner detectors, in particular the ECAL and the HCAL.

- **Gas detectors**: Study aging effects, improve long-term reliability and stability.
- **All detectors**: Improve massive and large area production procedures, readout technologies.

References

[1] CEPC-SPPC Study Group, *CEPC-SPPC Preliminary Conceptual Design Report. 1. Physics and Detector*. IHEP, 2015. http://cepc.ihep.ac.cn/preCDR/volume.html.

[2] CALICE Collaboration, *Construction and performance of a silicon photomultiplier/extruded scintillator tail-catcher and muon-tracker*, JINST **7** (2012) no. 04, P04015, arXiv:1201.1653. http://stacks.iop.org/1748-0221/7/i=04/a=P04015.

[3] Babar Collaboration, *The BaBar detector*, Nucl. Instrum. Meth. **A479** (2002) 1–116, arXiv:hep-ex/0105044.

[4] A. Abashian et al., *The Belle Detector*, Nucl. Instrum. Meth. **A479** (2002) 117–232. KEK-PROGRESS-REPORT-2000-4.

[5] CMS Collaboration, *The CMS muon project: Technical Design Report*. Technical Design Report CMS. CERN, Geneva, 1997. http://cds.cern.ch/record/343814.

[6] ATLAS Collaboration, *ATLAS muon spectrometer: Technical Design Report*. Technical Design Report ATLAS. CERN, Geneva, 1997. http://cds.cern.ch/record/331068.

[7] Y.-G. XIE, J.-W. ZHANG, Q. LIU, J.-F. HAN, S. QIAN, N. YAO, J.-B. ZHAO, J. CHEN, and J.-C. LI, *Performance Study of RPC Prototypes for the BESIII Muon Detector*, Chinese Physics C **31** (2007) no. 01, 70–75. http://cpc-hepnp.ihep.ac.cn:8080/Jwk_cpc/EN/abstract/abstract7618.shtml.

[8] J.-L. Xu, M.-Y. Guan, C.-G. Yang, Y.-F. Wang, J.-W. Zhang, C.-G. Lu, K. McDonald, R. Hackenburg, K. Lau, L. Lebanowski, C. Newsom, S.-K. Lin, J. Link, L.-H. Ma, and P. Viktor, *Design and preliminary test results of Daya Bay RPC modules*, Chinese Physics C **35** (2011) no. 9, 844. http://stacks.iop.org/1674-1137/35/i=9/a=011.

Draft-v0.2

Draft-v0.2

CHAPTER 8

READOUT ELECTRONICS AND DATA ACQUISITION

Draft-v0.2

This [1] is an example with plots, please edit ...

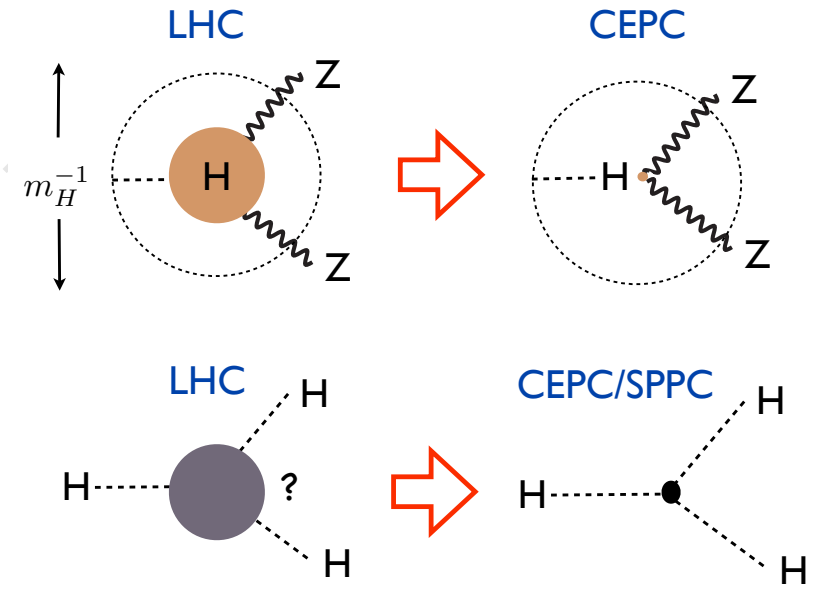

Figure 8.1: A sketch of two of the central goals of the CEPC and SPPC. The CEPC will probe whether the Higgs is truly “elementary", with a resolution up to a hundred times more powerful than the LHC. The SPPC will see, for the first time, a fundamentally new dynamical process — the self-interaction of an elementary particle — uniquely associated with the Higgs.

By Copyright © 2018 HEP Community

8.1 New Colliders for a New Frontier

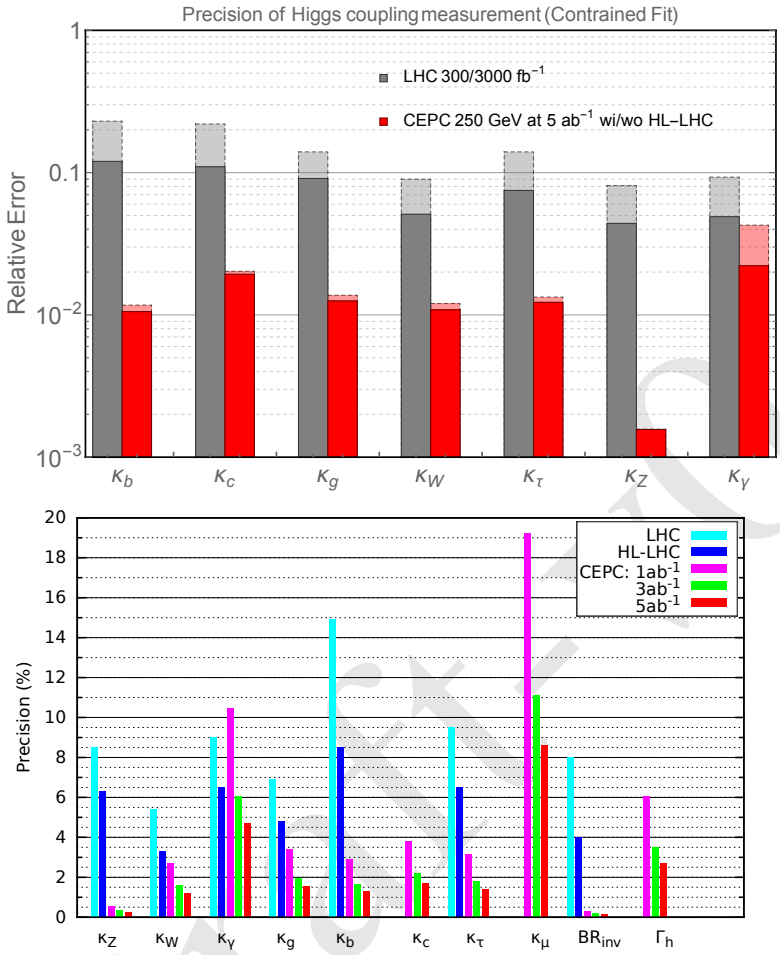

Figure 8.2: Top: The 7 parameter fit, and comparison with the HL-LHC, discussed in detail in Chapter 10. The projections for CEPC at 250 GeV with 5 ab^{-1} integrated luminosity are shown. The CEPC results without combination with HL-LHC input are shown with dashed edges. The LHC projections for an integrated luminosity of 300 fb^{-1} are shown in dashed edges. Bottom: Comparison between the LHC and several benchmark luminosities of the CEPC.

References

[1] CEPC project website. http://cepc.ihep.ac.cn.

Draft-2018/07/19

CHAPTER 9

CEPC INTERACTION REGION AND DETECTOR INTEGRATION

Draft-v0.2

The Machine-Detector Interface (MDI) represents one of the most challenging topics for the CEPC projects. In general, it has to cover all common issues relevant to the machine and the detector. Topics summarized in this chapter include design of the interaction region, design of the final focusing magnets, estimate of the detector backgrounds, design of the luminosity instrumentation, and integration of the machine and detector components in the interaction region. Comprehensive understandings are vital to address all such MDI issues and achieve the optimal overall machine and detector performance, yet always with lots of compromises to be made.

9.1 Interaction region

Figure 9.1 shows the current layout of the interaction region (IR). Its design receives several updates, with respect to the published PreCDR [1], to cope with the evolving double-ring design and a beam crossing angle of 33 mrad. It features an increased focal lengthen ($L^* = 1.5$ m $\rightarrow$ 2.2 m), defined as the distance between the final focusing magnet (QD0) and the interaction point (IP). This allows enlarged separation between the two single apertures of the QD0. Compensating magnets are positioned in front of the QD0 and surrounding both QD0 and QF1 magnets. They are introduced to cancel out the detector solenoid field and minimize the disturbance on the focusing beams. Furthermore, the outer radius of the compensating magnets defines the detector acceptance of $|\cos\theta| \leq 0.993$. The luminosity calorimeter ("LumiCal"), located right in front of the compensating magnets, is designed to measure the integrated luminosity to a precision of 10^{-3} or even higher. Tracking disks, labeled as FTD, are designed to measure charged particle trajectories in the forward region.

By Copyright © 2018 HEP Community

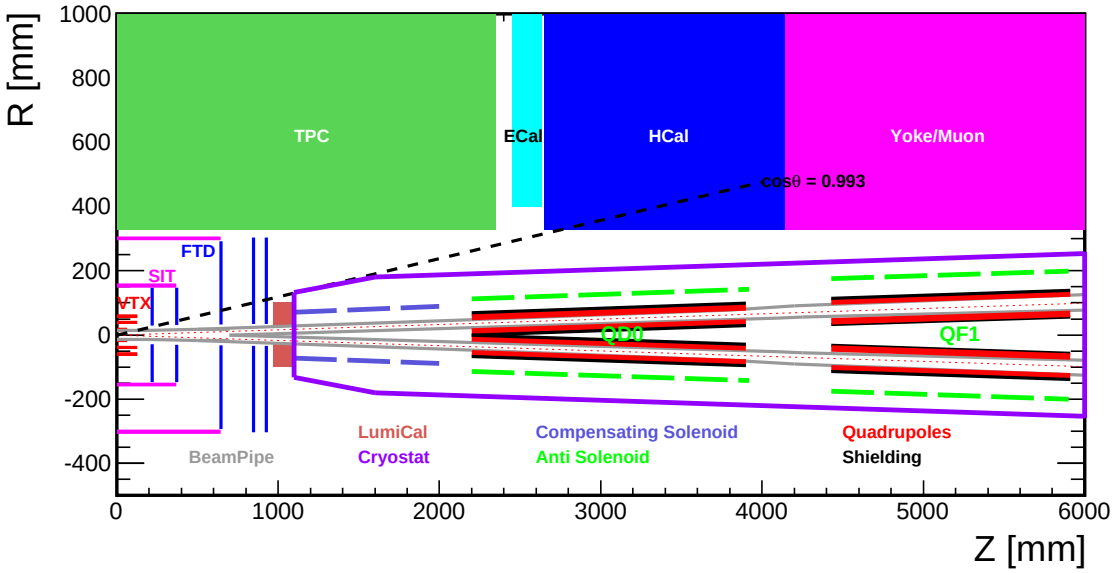

Figure 9.1: Current layout of the CEPC interaction region.

9.2 Final focusing magnets

Compact high gradient quadrupole magnets are required to focus beams. The two final focusing quadrupoles, named QD0 and QF1, are placed inside the CEPC detector, and must operate in the background field of the detector solenoid. Their basic requirements are listed in Table 9.1. QD0 is the quadrupole magnet close to the interaction point, with a distance of 2.2 m to the IP. It is designed as a twin aperture superconducting magnet and can be realized with two layers of Cos-Theta quadrupole coil using NbTi Rutherford cables without iron yoke. Two shield coil layers are introduced just outside the quadrupole coil to improve the field quality. The total four coils are clamped with stainless steel collars. It is designed to deliver a gradient field of 136 T/m and control the filed harmonics in the sensitive area to be below 3×10^{-4}. The cross-sectional view of the single aperture of the QD0 is depicted in Fig. 9.2. The design of QF1 magnet is similar to that of the QD0, except that there is iron yoke around the quadrupole coil for QF1.

Table 9.1: Basic requirements of the QD0 and QF1.

Magnet	Central Field Gradient (T/m)	Magnetic Length (m)	Width of GFR (mm)
QD0	136	2.0	19.51
QF1	110	1.48	27.0

In addition, compensating magnets are designed to cancel out the detector solenoid, resulting in zero integral longitudinal field. Based on wound of rectangular NbTi-Cu conductor, the compensating magnet is segmented into 22 sections with different inner coil diameters and reduces effectively the magnet size.Inside the first section, the central

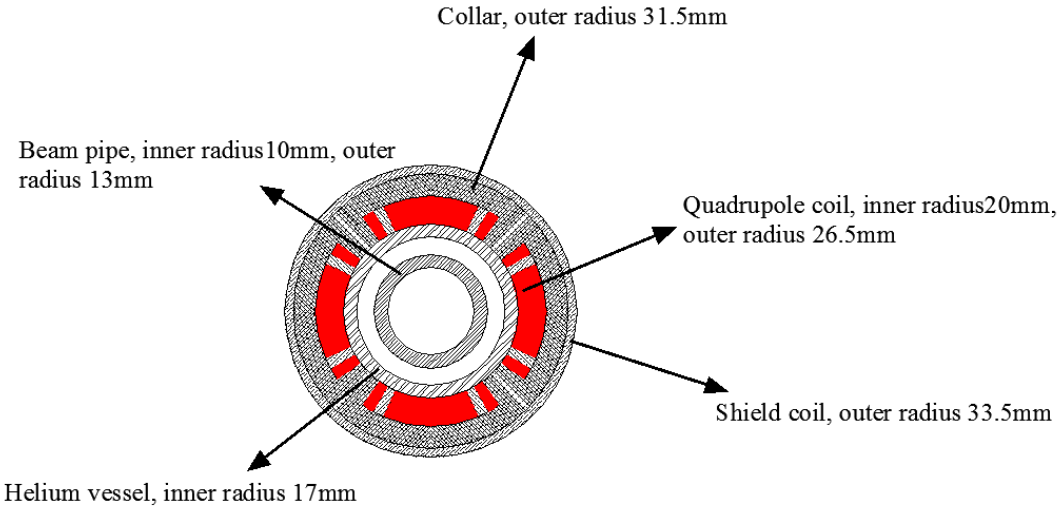

Figure 9.2: Schematic view of the single aperture of the QD0 superconducting magnet.

field reaches the peak value of 7.26 Tesla. Such high field introduces coupling and leads to significant vertical emittance growth, thus limits the machine luminosity that can be achieved, in particular for the operation at the Z pole.

9.3 Detector backgrounds

Machine induced radiation backgrounds can be always the primary concern for the detector design [2–5]. They can cause radiation damages to the detectors and associated electronic components, and degrade their particle detection performance. To make things even worse, high rate backgrounds can increase the detector occupancy, and may exaggerate the data-taking capability of the impaired detector. Therefore it is desirable to characterize the potential backgrounds and mitigate their impacts with effective and sufficient measures. Detailed Monte Carlo simulation, and more importantly lessons and experience learned from previous and current experiments, serve the basis for such studies. Discussion of the background sources and predicted background levels are presented below. Main radiation backgrounds originate from synchrotron radiation, beam-beam interactions, and off-energy beam particles.

9.3.1 Synchrotron radiation

Synchrotron radiation (SR) photons can be produced in the closest bending magnets and in quadrupoles in the straight sections on either side of the IP. The innermost precision detectors are typically sensitive to photons above 10 keV and vulnerable to high levels of soft photon radiation. It should be noted that the SR background increases rapidly with beam energy and additional measure must be introduced to allow detector operation at higher energies. In order to reduce the energy and flux of synchrotron radiation photons that enter the straight sections, the field strength of the last bending dipole at the entrance to the straight sections is significantly reduced compared to the normal arc dipole field. This weak bend lowers the critical energy of SR photons to be well below 100 keV.

However, as shown in Fig. 9.3(a), without a complex system of collimators designed to shield the experimental detectors, there would be simply too many SR photons striking the vacuum chamber in the experiments. Optimization of the collimator system is carried out with the Geant4 based BDSim software package []. It generates and tracks SR photons from the relevant magnetic elements in the region of the experimental detectors. Particular care must be taken for a realistic simulation in the tails of the beam density distributions (up to 10 $\sigma_{x/y}$), as particles form the tails are most effective in producing background particles. Collimators made with high Z materials (e.g. tungsten) are introduced to block scattering photons. Three mask tips, located at $|Z| = 1.4$ m, 2.1 m and 3.93 m with respect to the IP, are introduced to suppress SR photons effectively, as shown in Fig. 9.3(b).

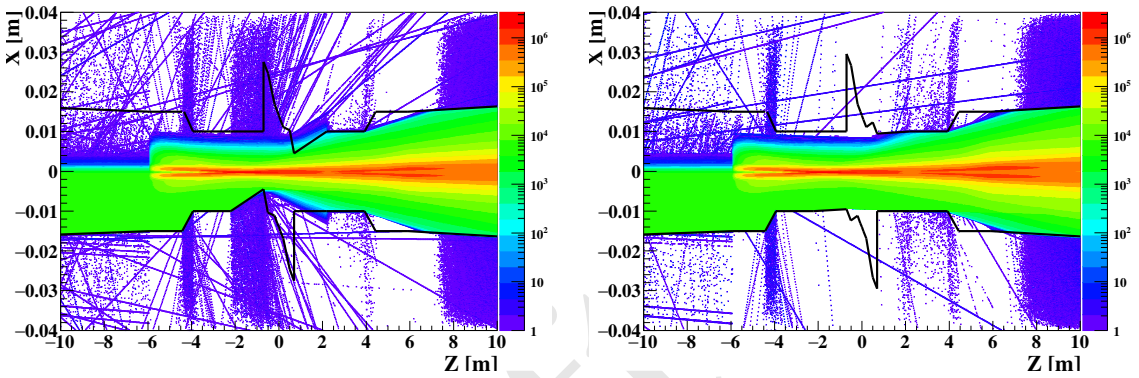

(a) (b)

Figure 9.3: Distribution of the synchrotron photon flux in the experimental detector region before (a) and after (b) introducing collimators.

9.3.2 Beam-beam interactions

Beamstrahlung is considered as another important background at CEPC and requires careful evaluation. Due to the pinch effect in the beam-beam interaction, the trajectories of beam particles in the bunches are bent, causing the emission of beamstrahlung photons. This process has been studied with the Monte Carlo simulation program GUINEA-PIG [6], which takes into account dynamically changing bunch effects, reduced particle energies and their impacts on the fields. Design parameters for machine operation at different energies are listed in Table 9.2, and serve as the input to GUNEA-PIG simulation. It should be noted that compared to other consequent processes, electron-positron pair production generates most significant detector backgrounds and can be categorized as:

- *Coherent Production*: e^+e^- pairs are produced via the interaction of virtual or real photons (e.g. beamstrahlung photons) with the coherent field of the oncoming bunch. Particles can be highly energetic but are dominantly produced with small angle and confined in the beam pipe.
- *Incoherent Production*: e^+e^- pairs are produced through interactions involving two real and/or virtual photons. Most of the particles are confined in the beam pipe by the strong detector solenoid field. However, a small fraction of them are produced with high transverse momentum and large polar angle.

Table 9.2: The input machine parameters to the GUINEA-PIG simulation.

Parameter	Unit	H	W	Z
Beam energy	GeV	120	80	45.5
Particles per bunch	10^{10}	15	0.34	0.036
Transverse size σ_x/σ_y	μm	20.9/0.068	13.9/0.049	5.9/0.078
Bunch length σ_z	μm	3260	3620	6000
Normalized emittance $\varepsilon_x/\varepsilon_y$	mm·mrad	284.1/0.728	126.8/0.376	39.9/0.939

The charged particles originating from the e^+e^- pair production can develop a sharp edge. Detector components and the beam pipe must be placed outside the edge. Fig. 9.4 shows the particle helices projected the $R-Z$ plane, taking into account the beam crossing angle of 33 mrad and the detector solenoid of 3 Tesla. The red dashed line indicates the position of the central beam pipe.

Figure 9.4: Helices of the electrons and positrons from pair production projected in $R-Z$.

Draft-v02

9.3.3 Off-energy beam particles

Circulating beam particles can lose significant amounts of energy in scattering processes. If exceeding 1.5% of the nominal energy (defined as the machine energy acceptance), such scattered particles can be kicked off their orbit and get lost close to or in the interaction region. They can interact with machine and/or detector components and contribute to the detector backgrounds. There are three main scattering processes that are almost entirely responsible for the losses of beam particles:

- Beamstrahlung
- Radiative Bhabha scattering
- Beam-gas interaction

While beamstrahlung events following beam-beam interactions are generated with GUINEA-PIG, radiative Bhabha events with small angles are generated with the BBBREM program [7]. Interactions between the beam particles and the residual gas in the beam pipe are simulated with custom code, assuming the gas pressure to be 10^{-7} mbar. Beam particles after interactions are tracked with SAD [8]. Beam particles lost close to the interaction region after multiple turns are interfaced to Geant4 [9–11] to simulate their interactions with detector components, as well as the beam pipe and the final focusing magnets in the forward region.

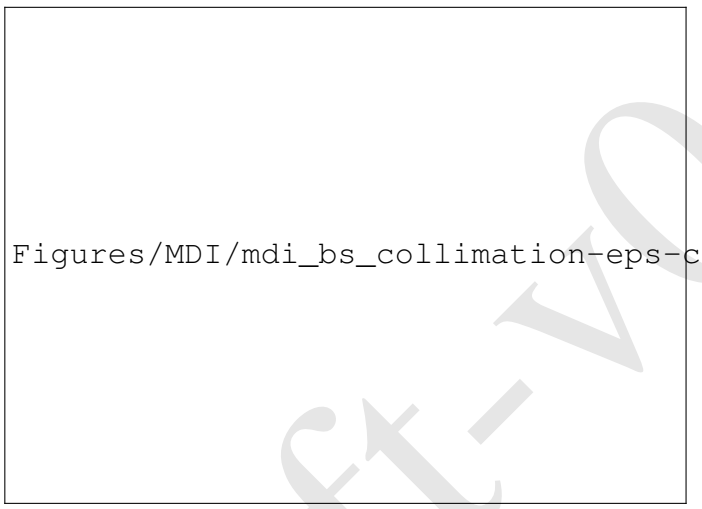

Figure 9.5: Off-energy beam particles are significantly reduced after introducing the collimaotrs.

Backgrounds introduced by off-energy beam particles can be effectively suppressed with proper collimation. The designed collimator aperture needs be small enough to stop as much as possible off-energy beam particles, but must be sufficiently large without disturbing the beam. Two sets of collimator pairs, APTX1/Y1 and APTX2/Y are placed in the arch region, with aperture size of 5 mm and 1 mm, in the horizontal and vertical planes, respectively. They are equivalently 14 σ_x and 39 σ_y, which are sufficiently away from the beam clearance region. Fig. 9.5 shows off-energy beam particles entering the IR are reduced significantly after introducing the collimation system.

9.3.4 Predicted radiation background levels

The deleterious effects of the background radiation can be roughly characterized by hit density, total ionizing dose (TID), and non-ionizing energy loss (NIEL). While TID is an important quantity for understanding surface damage effects in electronics, NIEL, represented in 1 MeV neutron equivalent fluence ($\Phi_{1\ \mathrm{MeV}}$), is important for understanding the bulk damage to silicon sensors and can be used to predict leakage currents. In background estimation, after either generating background particles directly in the IR (e.g. pair production) or propagating them to the region close enough to the IR (e.g. SR photons and off-energy beam particles), further particle interactions with detector components are simulated with Geant4. The calculation of background characterization quantities follows the same methodology as presented in [12].

NUMBERS AND PLOTS, AND THEIR INTERPRETATIONS TO BE ADDED!

Draft-v0.2

Hit density

Total ionizing dose

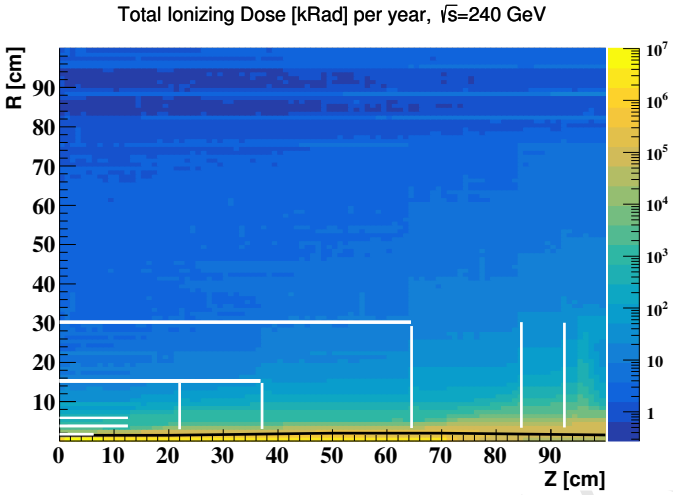

Figure 9.6: TID distribution, contribution form off-energy beam particles to be added.

Non-ionizing energy loss

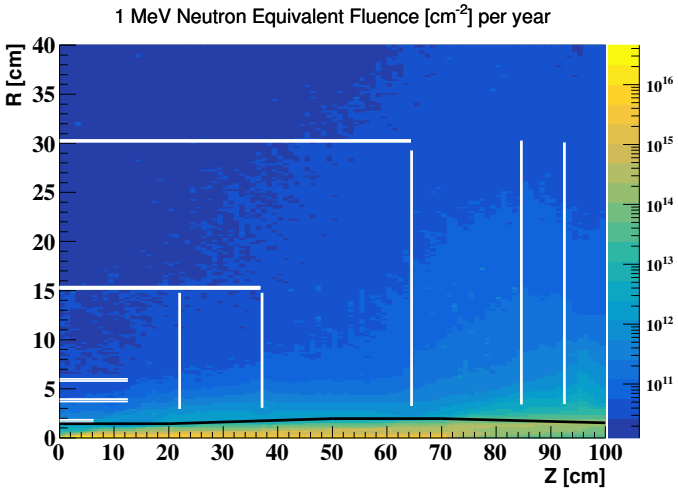

Figure 9.7: NIEL distribution, contribution from off-energy beam particles to be added.

Table 9.3: Summary of radiation background levels at the first vertex detector layer ($r = 1.6$ cm).

	H	W	Z
Hit Density [hits/BX]	XX	XX	XX
TID [MRad/year]	XX	XX	XX
$\Phi_{1\ \mathrm{MeV}}$ [10^{14} cm^{-2}/year]	XX	XX	XX

SUMMARY OF DETECTOR BACKGROUNDS, TO BE UPDATED

9.4 Luminosity instrumentation

Very forward region at CEPC will be instrumented with a luminometer (LumiCal), aiming to measure integral luminosity with a precision of 10^{-3} and 10^{-4} in e^+e^-collisions at the center-of-mass energy of 240 GeV and at the Z pole, respectively. The precision requirements on the integral luminosity measurement are motivated by the CEPC physics program, intended to test the validity scale of the Standard Model through precision measurements in the Higgs and the electroweak sectors with 10^6 Higgs and 10^{10} Z bosons. Many sensitive observables for such measurements critically depend on the uncertainty of the integral luminosity.

Luminosity at an e^+e^- collider is best measured by counting the Bhabha events of elastic e^+e^- scattering. Its theoretical interpretation is better than 0.05% at the Z pole [13]. The scattered electrons are distributed in the forward direction with a $1/\theta^3$ dependence. The cross section of the BHLUMI [14] simulation is illustrated in Fig. 9.8(a).

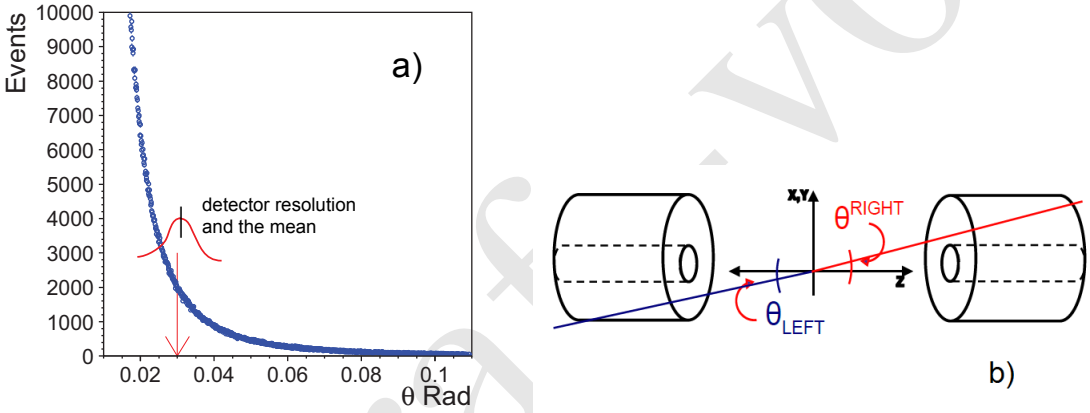

Figure 9.8: a) Distribution of scattered electrons in azimuthal angle of the BHLUMI simulation. The Gaussian curve illustrates the detector resolution to θ measured at a given fiducial edge. The offset of the mean in measurement contributes to the systematic errors. b) Bhabha events is measured preferably in the forward direction of the e^+e^-collision characterized by the back-to-back of elastic scattering and the electromagnetic shower of the electrons.

A Bhabha event is detected with a pair of scattered electrons back-to-back in direction, and the momenta of beam energy. Therefore the luminosity detector is consists of a pair of forward calorimeters with high precision on detecting electron impact positions. The configuration is sketched in Fig. 9.8(b). Bhabha events are detected in the angular coverage ($\theta_{min} < \theta < \theta_{max}$) of the forward calorimeters. The integrated luminosity (L) of the leading order calculation is

$$\sigma^{vis} = \frac{16\pi\alpha^2}{s}\left(\frac{1}{\theta^2_{min}} - \frac{1}{\theta^2_{max}}\right), \quad \mathcal{L} = \frac{1}{\epsilon}\frac{N_{acc}}{\sigma^{vis}}, \quad \frac{\Delta\mathcal{L}}{\mathcal{L}} \sim \frac{2\Delta\theta}{\theta_{min}}, \tag{9.1}$$

where ϵ is the detection efficiency to be evaluated. The systematic uncertainties are contributed mostly by the error on θ_{min}, mainly due to mechanical alignment and the detector resolution. The error propagates to the luminosity is about twice on magnitude.

The dimension of the detector is favorable to have the θ_{min} as low as possible to optimize coverage of the Bhabha cross section. The position of the luminosity detector is planned to be mounted in front of the quadruple magnets at $z = \pm 100$ cm. With the

θ_{min} of ∼30 mrad, corresponding to a radius of 30 mm to the beam pipe at $z = 100$ cm, the cross-section, σ^{vis}, after event selection will reach ~ 50 nb. A large detector coverage of σ^{vis} is necessary for statistics required for the Z line-shape study, where the $Z \to qq$ cross section is 41 nb. The precision required for 10^{-4} makes a strong demand on the detector resolution. At $\theta = 30$ mrad, it corresponds to an offset of $\Delta\theta \sim 1.5$ μrad, which is equivalent to 1.5 μm in radius at $z = 100$ cm.

Several technological options for LumiCal design are under study, as described in Sec. 9.4.1, with emphases on the precision of polar angle and energy reconstruction of Bhabha particles scattered in the t-channel $V(V = \gamma, Z)$ exchange. The dual beam-pipe configuration with the beam-crossing at 33 mrad results to a boost to particles of e^+e^- collisions. The back-to-back characteristics of Bhabha electrons is shifted by approximately a horizontal offset of 33 mm. The impact to LumiCal design is discussed. The LumiCal together with the quadruple magnet are inserted into the tracking volume that extended to $z = \pm 200$ cm. Shower leakage of electrons off the LumiCal to central tracker is studied by simulation, which is also discussed.

Luminometer at CEPC is a precision device with challenging requirements on the mechanics and position control. Precision requirements on integral luminosity measurement set the precision of the opening aperture and positioning control of the LumiCal. Various sources of luminosity uncertainty in this respect are reviewed in Sec. 9.4.2. Encouraging estimations on feasibility of the luminosity precision goals are presented. Detailed studies are ongoing, to include the full simulation of physics and machine induced processes and of the detector itself, for various luminometer positioning and technology choices.

9.4.1 Technological and design options

In the current design of the very forward region at CEPC, luminometer is foreseen to cover the polar angle region between 26 mrad and 105 mrad what translates into the detector aperture of 25 mm for the inner radius and 100 mm for the outer, at $z = \pm 100$ cm of the LumiCal front plane from the IP. The detector options shall be considered for

1. precision of the electron impact position to $r \sim 10$ μ m (1 μ m) for the errors on luminosity, corresponding to the systematic errors on luminosity of $\Delta L \sim 10^{-3}$ (10^{-4}) in the Higgs (Z-pole) operations;

2. monitoring of the detector alignment and calibration of detector position by tracking of Bhabha electrons with upstream detectors;

3. energy resolution and separation of e/γ for measurements of single photons and radiative Bhabha events;

4. maximum coverage and segmentation of the LumiCal to accommodate the dual beam-pipe and the beam crossing of 33 mrad;

5. minimizing shower leakage into the central tracking volume.

The detector option for the 1 μm precision on electron impact position is very much limited silicon detectors segmented in strips or pixels. Silicon strip detectors of 50 μm readout pitch is commonly reaching a resolution of $\sigma \sim 5$ μm. The mean on error

Draft-V0.2

($\bar{\sigma} = \sigma/\sqrt{n}$) would be much smaller. The selection of Bhabha events is set on a fiducial edge of θ_{min}, for example, center in the gap between two silicon strips. The systematic error is therefore the number of events being selected with an error of $\bar{\sigma}$ despite the detector resolution, and would be relatively small, which is indicated by the Gaussian curve in Fig.9.8(a). The alignment of the detector position would be the major systematic requirement for an absolute precision of 1 μm.

A conceptional Luminosity detector is illustrated in Fig. 9.9 for the combination of a silicon detector and a calorimeter around the beam pipe for measurement of the electron impact position energy. The segmentation of the calorimeter is considered for the back-to-back resolution detecting a pair of Bhabha electrons, and for separation of e/γ in case of radiative photon accompanied with the electron or from beam background. The thickness is determined for the energy resolution favorable of $> 20X_0$ for shower containment of a 50 GeV electron. The option on the calorimeter is limited by the space affordable. The traditional crystal or scintillator-based calorimeter will require more than 20 cm in length for $> 20X_0$. The most compact design would be a sandwiched stack of Silicon samplers with Tungsten in $1X_0$ (3.5 mm thick), to a total of about 10 cm that weights about 400 kg.

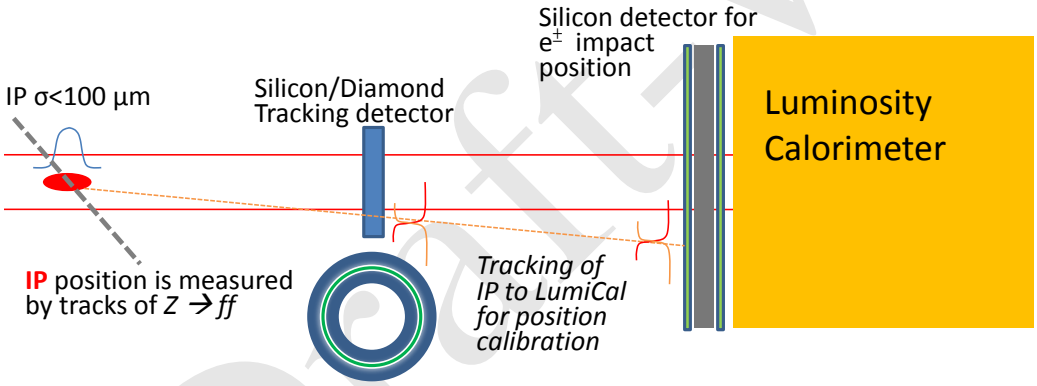

Figure 9.9: A conceptional luminosity detector combination with a upstream silicon/diamond detector for tracking Bhabha electrons to calibrate position of the luminosity detector.

The alignment precision of the front-layer Silicon detector is the most critical issue to reach 1 μm in radius for the luminosity measurement of 10^{-4}. For the precision at the 1 μm level, a monitoring system with laser alignment is required to calibrate the detector position. The θ angle of a detected electron is calculated assuming an IP position measured by the beam steering and the central tracking system. The IP position relative to the luminosity detector could be limited to survey relative to central tracking devices or beam pipe. If feasible, a tracking system on the Bhabha electrons will improve very the measurement precision of the electron theta angle. This is illustrated in Fig. 9.9 for the option that a ring of silicon or diamond detector is mounted in front of the Luminosity detector. Such that a electron track is measure from the IP, the ring detector, and the LumiCal impact position. The ring detector offers a second survey, and by extrapolation, to calibrate the LumiCal silicon strip positions.

The front silicon layer of the luminosity detector will measure electron impact positions to a few micron. If this will be a fine-pitch strip detector, the position is measured by strips collecting the ionization charges generated by a traversing electron. In Fig. 9.10,

Draft v0.2

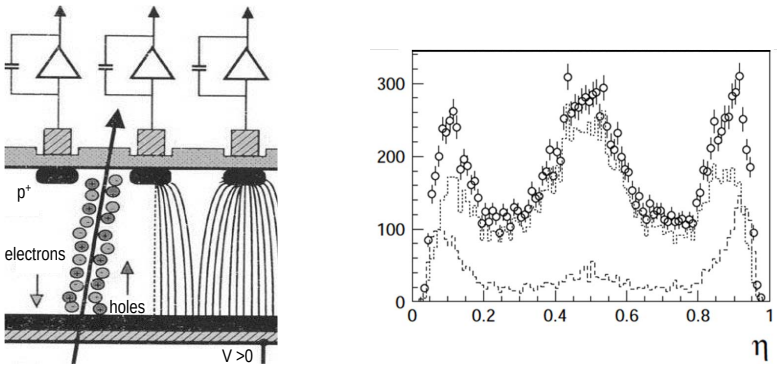

Figure 9.10: Charge collection by silicon strips is illustrated for ionization charges generated by a traversing particle. The $\eta = Q_r/(Q_r + Q_l)$ distributions are made for charge sharing to left and right strips to the impact position, for a test devices with strips implementation in 25 μm pitch and the readout of every other strips in 50 μm pitch. The η distributions are also plotted for contents with charges collected by two-strip (dotted) and three-strip (dashed) cases. The middle bump corresponds to the position of the floating strip between two readout strips.

the charge sharing is illustrated for $\eta = Q_r/(Q_r + Q_l)$ with the ionization charges collected by the strips on the right (left) of the impact position. The distribution is collected for a test device having the strips implanted in 25 μm pitch, and the readout in 50 μm pitch by wire bonding to every other strips. The floating strip between two readout strips attracts charges drifting towards it and results to the bump at $\eta \sim 0.5$, in particular for a wide cluster of charges collected by three strips (dotted line). The impact position of a particle is approximated by center-of-gravity weighted on the charges between two strips. With the η distribution, the non-linear distribution can be corrected to achieve a position resolution of better than ~ 5 μm for the readout pitch of 50 μm. With the strip detectors placed in a magnetic field, the ionization charge in the silicon wafer is drifted toward one side, and therefore the η distribution is tilted un-evenly. Without a proper correction for the η, the true impact position the off-set can be as large as half the readout pitch.

If the luminosity detector will be assembled in a sandwiched silicon-tungsten calorimeter with the type of silicon wafer for the front layer. Wide silicon strips may be chosen in a case like the OPAL LumiCal [15], applying 2.5 mm wide strips in circular span of 11.25°. The resolution on detection of an electron, as well as for e/γ separation is at the 1 mm level. Assuming that the event counting of Bhabha electrons has the fiducial edge, θ_{min}, chosen at the middle between two strips, and the events are evenly divided to left and right strips without charge sharing. The systematic error to luminosity measurement is by the alignment error of the strip position of a few microns, and is not by the resolution.

Charge sharing between the gap of two-strips have been studied with prototype wafers[16] shown in Fig. 9.11. The wafer dimension is 65×65 mm^2 implemented with 2 mm wide strips and the gaps from 50 μm to 160 μm. The beam test was conducted with a set of find-pitch strip detectors as a telescope to provide reference positions of incident electrons scattered across strips and gaps. The charge sharing for electrons in the gaps are compared for η distributions in Fig. 9.11, which are found compatible for the different gap widths. Charge collection shows no loss, and are drifted toward the near strips with the η peaking at the edges. The dispelling charges in the middle of a gap is difficult for deriving

Draft v0.2

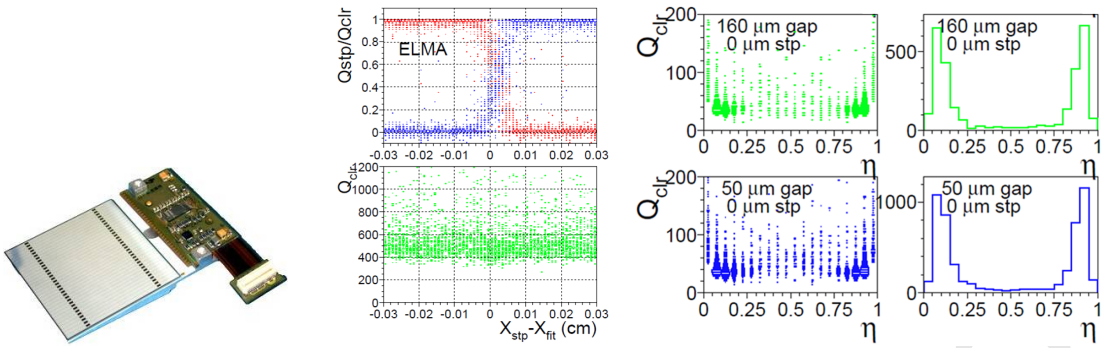

Figure 9.11: Beam tests using prototype silicon wafer of the CMS pre-shower detector (right) were conducted for collection of ionization charges generated by traversing particles across the gap between strips. The charge sharing by adjacent strips are plotted (middle) to the reference impact position (extrapolation of a upstream telescope). The sum strip charges (middle plots) is compatible to the hits on a strip. The charge sharing in $\eta Q_r/(Q_r + Q_l)$ peaks near 0 and 1, indicating non-linear response to the randomly distributed beam particles across the gap.

the position of an incident electron in the gap. But, it does divide the event fraction cleanly to the near side of the strips.

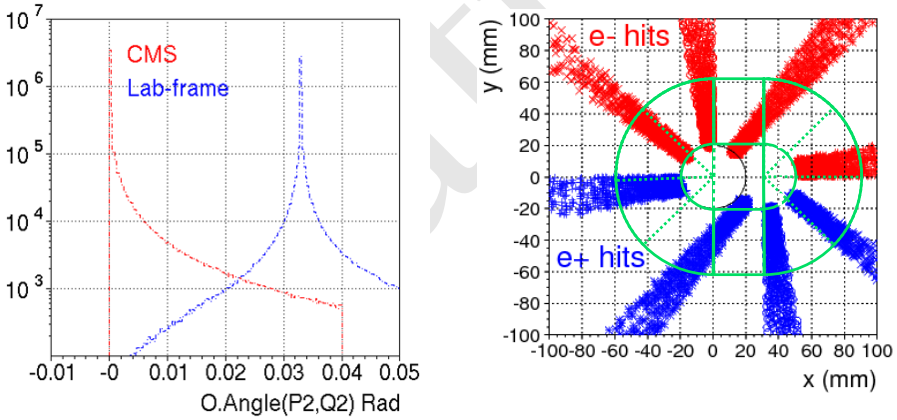

Figure 9.12: Bhabha events of BHLUMI simulation at the Z-pole are plotted for the back-to-back opening angle of scattered electron-position pairs in Center-of-Mass and the laboratory frames (left). The impact positions on the LumiCal front face are plotted in slides of ϕ angles every 45 degrees (right). The detector coverage is illustrated in green lines indicating a beam-pipe of 20 mm, extended from beam center at $x = \pm 16.5$ mm.

The double ring configuration of the CEPC machine design at the interaction point has a beam crossing angle of 33 mrad. The effect to the electrons of Bhabha interaction is a boost off the accelerator ring center, by maximum 16.5 mrad in horizontal direction. The distribution is simulated with the BHLUMI program. The shift on back-to-back angle is plotted in Fig. 9.12. The boost is toward $+x$ direction of the laboratory frame. The electron impact positions on the LumiCal front-layer at $z = 100$ cm are also plotted in Fig. 9.12, in slices of every 45 degrees to indicate the dependence on p_T direction. The beam-pipe centers are at $x = \pm 16.5$ mm. The green lines indicate the beam-pipe area of 20 mm in radius extending horizontally, and the coverage of the LumiCal in segmentation

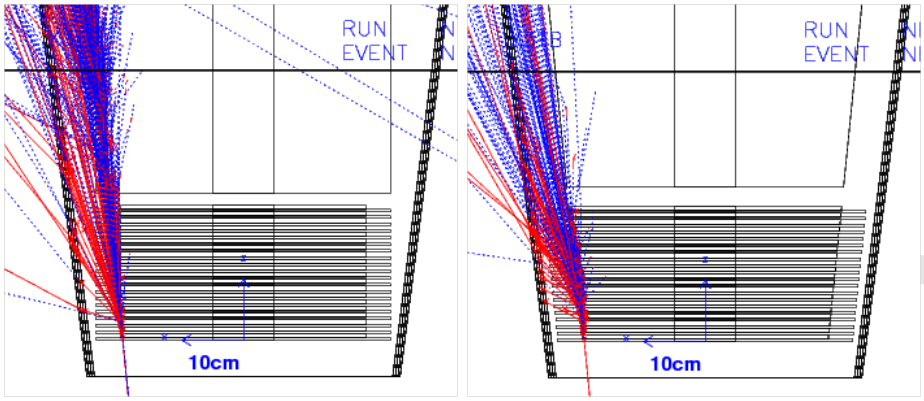

Figure 9.13: Event display of a GEANT simulation for electron shower on the LumiCal configuration stacked with 20 decks of silicon and Tungsten layers in TUBE and CONE shapes.

of circular and rectangular silicon wafers. The electron impact positions are illustrated for >20 mrad to the laboratory frame. Electrons of low scattering angles, in particular for those in $-x$ direction, are lost into beam-pipe. To have both scattered electrons and positrons detected, the corresponding θ_{min} on the horizontal axis is the beam-pipe acceptance plus 16.5 mrad. The loss of vents on vertical direction is much less. With a beam pipe as indicated with $\pm y$ dimension equals radius, the horizontal boost is not losing electrons with a larger y-position. A large detector coverage for Bhabha events is most favorable. The large opening of beam-pipe position is inevitable. We shall pursue the vertical dimension to be low as possible for a total integrated Bhabha cross section of larger than 50 nb.

The LumiCal mounted in front of the quadruple magnet at $z = \pm 100$ cm is half way in the tracking volume of $z = \pm 200$ cm. Shower leakage of electrons at the edge of LumiCal is investigated with a GEANT simulation witn parameters cross-checked with a lateral shower study [17]. The LumiCal is configured assuming a sandwiched Silicon-Tungsten calorimeter stacked in twenty decks of 2 mm air-gap and $1X_0$ tungsten (3.5 mm thick). The air-gap has a layer of silicon wafer of 0.3 mm thick. The front layer of the LumiCal is positioned at $z = 100$ cm. The geometry of the LumiCal is tested in two configurations: a TUBE with uniform inner and outer radii of 25 and 100 mm, respectively; and a CONE shape with the outer edge at a constant angle of $\arctan 0.1$ to the interaction point. The CONE shape is intended for well separated absorption of electron shower in a theta threshold. Illustrated in Fig. 9.13 are the event display of the simulations. Out of the LumiCal, a 5 mm iron cone at $|\cos\theta| = 0.992$ is implemented for absorption of low energy shower secondaries massing into the center tracking volume.

The TUBE configuration leaves a corner of about 5 mrad on the outer edge, where the shower leakage of an incident electron is with energetic shower secondaries. The CONE shape allows the shower fully developed once the electron enters the calorimeter coverage. The shower leakage reaching the Fe-cone is recorded for the particle energies arriving and penetrating through, which are listed in Table 9.4 for 50 GeV and 125 GeV electrons. When the shower is well contained, the leakage is just a few dozens of less than 30 MeV particles. A shower on the edge creates up to 3k secondaries into the tracking

Draft-V0.2

volume mostly of less than 100 MeV. The 5 mm iron layer can filter a large fraction of them, to less than 1k particles traversing through.

9.4.2 Systematic effects

The main measure of luminosity at CEPC is the count of Bhabha events N_{Bh} detected in coincidence in the two halves of the luminosity calorimeter LumiCal. The luminosity figure is then obtained from the equation of $\mathcal{L} = N_{acc}/\sigma^{vis}$. The cross section for the Bhabha process, σ_{vis}, should be integrated over the same phase space as used for the counting of Bhabha events. The limited precision with which the experimental acceptance region is defined gives rise to a number of systematic effects. Further, other processes misidentified as Bhabha and the limited accuracy of the theoretical calculation of σ_{vis} contribute to the overall systematic uncertainty.

A generator-level study was performed to assess the effects related to the precision of the Bhabha acceptance region on Bhabha counting. An underlying assumption of the study is that the LumiCal is centered on the outgoing beam axis. This assumption is essential for data-driven control of the radial offset of Lumical with respect to the IP, as well as for Bhabha event counting based on the mirrored asymmetric polar-angle acceptance regions on the left and right side of the detector [15] (in further text, *OPAL-style selection*). OPAL-style counting cancels out biases due to left-right asymmetries of the experimental angular acceptance. It is further assumed that for the final state particles hitting the radial region between 50 mm and 75 mm, corresponding to the detector fiducial volume (FV), shower leakage has a negligible effect on the reconstruction of the polar angle and the energy.

Bhabha event samples are generated using the BHLUMI generator [14]. Center-of-mass (CM) energy of 240 GeV is assumed, roughly corresponding to the peak of the Higgs production cross section. The particles are generated in the range of polar angles including a ~ 7 mrad margin outside the FV to allow non-collinear final state radiation (FSR) to contribute to the events. After event generation, smearing is applied to the final particle vertices and momenta according to the nominal CEPC parameters. Additional smearing or bias is then applied according to one systematic effect at a time. Four mo-

Table 9.4: Number of particles leaking out of the LumiCal outer radius (N_{enter}) and number of particles passing through the Fe-cone (N_{pass}). Two different detector designs (TUBE and CONE) and two shower energies (50 GeV and 125 GeV) are simulated.

	50 GeV electrons		125 GeV electrons	
	TUBE	CONE	TUBE	CONE
θ (mrad)	$N_{\mathrm{enter}}/N_{\mathrm{pass}}$	$N_{\mathrm{enter}}/N_{\mathrm{pass}}$	$N_{\mathrm{enter}}/N_{\mathrm{pass}}$	$N_{\mathrm{enter}}/N_{\mathrm{pass}}$
40	15.4/5.6	13.6/5.8	38.0/16.0	35.8/14.7
90	392/155	173/76	1028/399	434/19.7
95	501/290	367/152	2389/720	937/382
98	762/216	860/284	1718/473	2176/725
99	553/140	1331/367	1102/273	3306/915

Draft-2018/07/19

menta of close-by particles are summed up to account for cluster merging in LumiCal. The selection criteria to count an event consist of the OPAL-style angular selection and the requirement that the energy of both detected showers is above 50% of the nominal beam energy. The relative acceptance bias is determined as the relative difference between the Bhabha count $N_{\mathrm{Bh},i}$ obtained with the inclusion of the considered effect i and N_{Bh} obtained with the nominal set of parameters.

Table 9.5 lists the requirements on beam delivery, MDI and LumiCal installation, needed to limit individual systematic effects in the luminosity measurement to 1×10^{-3}, such as required for the Higgs program at CEPC. Parameters influencing the integral luminosity precision are given as follows:

- ΔE_{CM}, uncertainty of the available CM energy affecting the Bhabha cross-section,
- $E_{e^+} - E_{e^-}$, asymmetry of the incident beam energies resulting in a net longitudinal boost of the event,
- $\frac{\delta\sigma_{E_{beam}}}{\sigma_{E_{beam}}}$, uncertainty of the beam energy spread,
- Δx_{IP} and Δz_{IP}, radial and axial offsets of the IP w.r.t. the LumiCal,
- Beam synchronization, resulting in axial offset of the IP w.r.t. the LumiCal,
- $\sigma_{x_{\mathrm{IP}}}$ and $\sigma_{z_{\mathrm{IP}}}$, radial and axial fluctuations of the scattering position,
- r_{in}, inner radius of the LumiCal acceptance region,
- $\sigma_{r_{\mathrm{shower}}}$, reconstruction precision of the radial shower coordinate,
- Δd_{IP}, uncertainty of the distance between the luminometer halves.

Most requirements are technically feasible with the present state of the art of accelerator and detector technology. The most important challenge identified is the precision of the inner acceptance radius r_{in} of LumiCal. In order to keep the luminosity precision of 1 permille, r_{in} must be known to within $10\,\mu\mathrm{m}$. The precision requirement of r_{in} scales linearly with the required luminosity precision, implying a correspondingly stricter requirement for the Z-pole run.

9.4.3 Summary on LumiCal

Instrumentation of the very forward region is very important for the realization of the CEPC physics program. Several technology options are under consideration. Some of them have been successfully applied at LEP or are under study at other future projects. We argue that a tracker placed in front of the luminometer can improve polar angle measurement accuracy, facilitate LumiCal alignment and enable electron-photon separation. Luminometer must be centered on the outgoing beam axis to allow control of the systematic effects at the required level. Precision requirements on beam delivery, MDI and LumiCal installation have been addressed by simulation, and proven to be feasible with the present state-of-the-art of accelerator and detector technology.

Draft-v0.2

Table 9.5: Requirements on beam delivery, MDI and LumiCal installation, needed to limit individual systematic effects to 1×10^{-3}.

Parameter	Unit	Limit
ΔE_{CM}	MeV	120
$E_{e^+} - E_{e^-}$	MeV	240
$\frac{\delta\sigma_{E_{beam}}}{\sigma_{E_{beam}}}$		effect canceled
Δx_{IP}	mm	>1
Δz_{IP}	mm	10
Beam synchronization	ps	7
$\sigma_{x_{\text{IP}}}$	mm	1
$\sigma_{z_{\text{IP}}}$	mm	10
r_{in}	mm	10
$\sigma_{r_{\text{shower}}}$	mm	1
Δd_{IP}	μm	500

9.5 Detector integration

Both QD0 and QF1 are located inside the detector, which drastically complicates the support and alignment of the detector and machine components in the interaction region. The two final focus magnets and the LumiCal will possibly be mounted on a dedicated support structure, extended from a pillar outside the detector and suspended from the solenoid cryostat. They might have to been integrated together before being pushed into the interaction region. The shaped beam pipe and surrounded silicon detectors will possibly be supported from a structure of carbon fiber reinforced plastic, which can hang at the flanges of the field cage of the Time Projection Chamber (TPC). Significant effort is required to realize a solid mechanical design and to define a reasonable procedure for detector assembly.

Draft-v0.2

References

[1] CEPC-SPPC Study Group, *CEPC-SPPC Preliminary Conceptual Design Report. 1. Physics and Detector*, . IHEP-CEPC-DR-2015-01, IHEP-TH-2015-01, IHEP-EP-2015-01.

[2] G. von Holtey et al., *Study of beam-induced particle backgrounds at the LEP detectors*, Nucl. Instr. and Meth. **A403** (1998) 205 – 246.

[3] P. M. Lewis et al., *First Measurements of Beam Backgrounds at SuperKEKB*, arXiv:1802.01366 [physics.ins-det].

[4] D. S. Denisov et al., *Machine-Related Backgrounds in the SiD Detector at ILC*, JINST **1** (2006) P12003, arXiv:hep-ex/0608001 [hep-ex].

[5] B. Dalena, J. Esberg, and D. Schulte, *Beam-induced backgrounds in the CLIC 3 TeV CM energy interaction region*, in *International Workshop on Future Linear Colliders (LCWS11) Granada, Spain, September 26-30, 2011*. 2012. arXiv:1202.0563 [physics.acc-ph].

[6] D. Schulte, *Beam-beam simulation with GUINEA-PIG*, In 5th International Computational Accelerator Physics Conference (1998) . CLIC-NOTE 387.

[7] R. Kleiss and H. Burkhardt, *BBBREM – Monte Carlo simulation of radiative Bhabha scattering in the very forward direction*, Comput. Phys. Commun. **81** (1994) 372 – 380.

[8] K. Oide and H. Koiso, *Anomalous equilibrium emittance due to chromaticity in electron storage rings*, Phys. Rev. **E49** (1994) 4474–4479.

[9] GEANT4 Collaboration, S. Agostinelli et al., *GEANT4: A Simulation toolkit*, Nucl. Instrum. Meth. **A506** (2003) 250–303.

[10] J. Allison et al., *Geant4 developments and applications*, IEEE Trans. Nucl. Sci. **53** (2006) 270.

[11] Geant4 Collaboration, M. Asai et al., *Recent developments in Geant4*, Annals Nucl. Energy **82** (2015) 19–28.

[12] S. Baranov et al., *Estimation of Radiation Background, Impact on Detectors, Activation and Shielding Optimization in ATLAS*, . ATL-GEN-2005-001, ATL-COM-GEN-2005-001, CERN-ATL-GEN-2005-001.

[13] S. Jadach, *Theoretical error of luminosity cross-section at LEP*, in *Electroweak precision data and the Higgs mass. Proceedings, Workshop, Zeuthen, Germany, February 28-March 1, 2003*, pp. 85–95. 2003. arXiv:hep-ph/0306083 [hep-ph].

[14] S. Jadach et al., *Upgrade of the Monte Carlo program BHLUMI for Bhabha scattering at low angles to version 4.04*, Comput. Phys. Commun. **102** (1997) 229–251.

[15] OPAL Collaboration, G. Abbiendi et al., *Precision luminosity for Z0 line shape measurements with a silicon tungsten calorimeter*, Eur. Phys. J. **C14** (2000) 373–425, arXiv:hep-ex/9910066 [hep-ex].

[16] P. Bloch et al., *Performance Study of Non-Irradiated Prototype Silicon Preshower Samplers for CMS*, . CMS-NOTE-2000-042.

[17] Y. Chang et al., *Lateral development of electron showers measured by silicon microstrip detectors*, Nucl. Instr. and Meth. **A388** (1997) 135 – 143.

Draft-v0.2

./

Draft-v0.2

CHAPTER 10

PHYSICS PERFORMANCE

Draft-v0.2

10.1 Introduction

The physics performance is determined by the detector geometry and the reconstruction algorithms. A Particle Flow Algorithm Arbor is optimized for the APODIS and a full simulation-reconstruction software chain(cepcsoft) has been developed. Using APODIS detector geometry and the cepcsoft, the physics performance is evaluated at the full simulation level. The cepcsoft and Arbor in briefly introduced in section 10.2, In section 10.3, the physics performance is summarized at physics object level, and with corresponding Higgs signal distributions.

10.2 The CEPC Software and the Arbor

The reconstruction is vital for the high energy physics experiment. Comparing to the conventional reconstruction at the collider experiments, the Particle Flow reconstruction interprets the information from every subsystem coherently and is much complicated. A Particle Flow algorithm, Arbor [**?**], has been developed, and an entire simulation-reconstruction software chain (cepcsoft [**?**]) has been established accordingly.

The cepcsoft developments starts from the ilcsoft [**?**], the software framework & toolkit for the linear collider studies. It uses the same data structure and management (LCIO and Marlin [**?**]), the tracking and flavor tagging modules from the ilcsoft. It also uses several general high energy physics softwares such as the Geant4, the Whizard [**?**], the Madgraph [**?**], the Pythia [**?**], and the Delphes [**?**]. Many dedicated software tools are developed and integrated into the cepcsoft. The information flow and essential modules are introduced in section 10.2.1. The Arbor algorithm is presented in section 10.2.2.

By Copyright © 2018 HEP Community

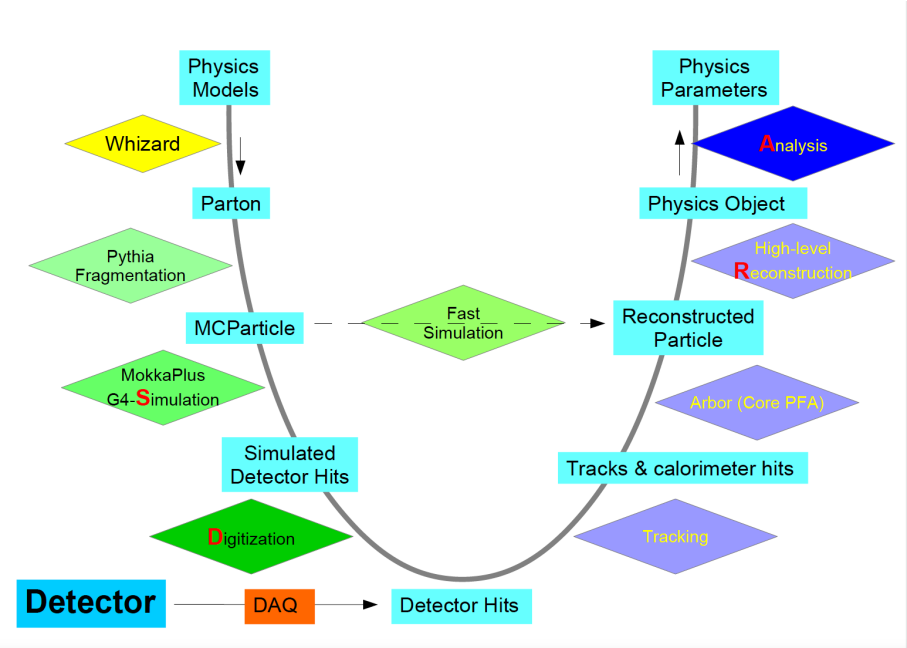

Figure 10.1: Information flow at CEPC simulation studies

10.2.1 The cepcsoft

The information flow at the CEPC simulation-reconstruction is shown in Fig. 10.1. The starting point is the generator softwares. In the full simulation, the generator samples are processed to Geant4 simulation, which generates simulated detector hits that record the energy deposition information in sensitive volumes of the virtual detector. These simulated detector hits are digitized into detector hits, by convoluting the sub-detector responses to the energy deposition information. In the ideal case, the digitized hits should be indistinguishable from the experimental data, and the following reconstruction modules treat them indifferently.

The reconstruction modules include the tracking, the Particle Flow, and the high level reconstruction algorithms. The digitized tracker hits are reconstructed into tracks via the tracking modules. The particle flow algorithm reads the reconstructed tracks and the calorimeter hits, and builds reconstructed particles. The single particle level physics objects, like the leptons, the photons, and the kaons, are identified directly. Subtracting the initial 4-momentum of the system with the accumulated four-momentum of every final state particle leads to the reconstruction of the missing energy and momentum. High level reconstruction algorithms are applied to reconstruct compound physics objects such as the converted photons, the K_ss, the τ leptons, and the jets. Once the jets are identified, the jet flavor tagging algorithm, jet charge measurement algorithm are applied accordingly. The physics observables could then be constructed via the algebraic combinations of the kinematic variables of these physics objects.

From the technical point of view, the cepcsoft is composed of fourteen independent modules:

1, The generator: the Whizard [**?**], the Madgraph [**?**], and the Pythia [**?**]. The Whizard is a widely used generator for the linear collider studies. In cooperating with

the whizard team, dedicated CEPC beam parametrization has been established in its official release. The Whizard generator is used for the SM processes, including both Higgs signal and all the SM backgrounds [**?**]. Meanwhile, Madgraph and Pythia are used to generate New Physics samples.

2, The data format and the data management. CEPC software uses the data format (LCIO) and data management (Marlin) inherited from the ilcsoft.

3, The simulation: the MokkaPlus [**?**]. MokkaPlus is a virtual geometry constructor that compiled with the Geant4 libraries [**?**] and mysql database [**?**]. The MokkaPlus is developed from the Mokka [**?**], the obsoleted simulation framework used in linear collider studies (The linear collider simulation has moved to the recent development of DD4HEP [**?**], however, depends on the software robustness and on the available manpower, we decided to continue developing MokkaPlus). Many new functions have been added to the MokkaPlus and all the CEPC detector models are implemented into MokkaPlus.

4, The digitization algorithms. The digitization algorithm should properly model the amplification procedure and the time-dependent patterns of the sub-detector. These dedicated models need to be established and tuned according to experimental data. The digitization algorithm is sub-detector dependent and technology dependent. We developed a general calorimeter digitization algorithm for both APODIS ECAL and HCAL, which could precisely reproduce the test beam results [**?**]. The tracker digitization modules are inherited from the ilcsoft, whose parameters are adjusted for the optimization studies to the sub-detectors.

5, The tracking algorithm. The CEPC software uses the entire tracking module from the ilcsoft, which is proved to be very efficient. In addition, a dedicated CEPC tracking algorithm is under developing, the preliminary results look promising [**?**].

6, The particle flow algorithm. The particle flow algorithm is the core of the CEPC reconstruction. We developed Arbor algorithm and optimize it for the APODIS detector. More detailed information and typical performance will be given in following sections.

7, The single particle level physics object finding algorithms. Dedicated lepton identification (LICH [**?**]) and photon identification algorithms have been developed. These algorithms have been integrated into Arbor. The performance will be presented in section 10.3.

8, The composed object finder. Coral, a simple algorithm that targets at a general simple composed object finder, is in the early developing and testing phase. Coral target at a high efficiency reconstruction of converted photon, π_0, K_s, *etc*.

9, The tau finding algorithm. A dedicated tau finder has been developed, see [**?**]. Details will be giving in section 10.3.

Draft-V0.2

10, The jet clustering algorithm. Fastjet [**?**] package has been used in CEPC software.

11, The jet flavor tagging algorithm. CEPC software uses the official flavor tagging algorithm, LCFIPlus [**?**], from the ilcsoft.

12, The Event Display. We developed Druid [**?**], one of the official linear collider event display software. Druid has been adjusted to the CEPC studies by including dedicated display setup and geometry files. All the displays demonstrated in this paper is produced by Druid.

13, The general analysis framework. FSClasser [**?**], a general physics analysis framework that automatically calculates the kinematic observables for most of the physics objects, is developed and integrated into CEPC software.

14, The fast simulation. Two fast simulation packages have been developed and validated with the full simulation. The first one is developed using LCIO-Marlin framework, used mainly for the massive processing of SM background for the physics analysis. The second is developed based on the Delphes software, and integrated into its official releases [**?**] [**?**].

To conclude, a fully functional simulation-reconstruction software chain, the cepcsoft has been established for the CEPC detector design studies. The cepcsoft is developed from the ilcsoft [**?**] and integrates many novel developments. Among all fourteen independent modules of the cepcsoft, we developed eight modules (including Arbor) and adjusted two modules (the MokkaPlus and the Digitization) for the CEPC study. Three essential modules, the LCIO-Marlin framework, the tracking and the flavor tagging, are inherited from the ilcsoft. Meanwhile, some of our efforts are also integrated to ilcsoft, such as the LICH [**?**], the Digitization [**?**], and the event display [**?**]. The CEPC software uses other open source softwares such as the generator and the fast simulation, to which we have established collaboration with the developer.

10.2.2 Arbor

The Particle Flow algorithm, Arbor [**?**][**?**], has been optimized for the APODIS detector concept.

Inspired by the simple fact that the tree configuration of particle shower, Arbor creates oriented connectors between calorimeter hits, and iterates (creating/removing connectors and swap their directions) until the connector-hit ensemble follows a tree topology. The branches hence represent the trajectories of charged shower particles. The seeds usually correspond to the impact position of the particle at the calorimeter. Since the separation of the seeds is straightforward, Arbor efficiently separates the particle showers, which is highly appreciated by the Particle Flow principle.

Arbor is composed of a calorimeter clustering module and a matching module. The clustering module reads the calorimeter hits and builds the calorimeter clusters. The matching module identifies the calorimeter clusters induced by charged particles (charged clusters), combines these clusters with tracks, and builds charged reconstructed particles. The remaining clusters are reconstructed into photons, neutral hadrons, and fragments (mainly from charged clusters). The final state particles are therefore reconstructed.

Draft v0.2

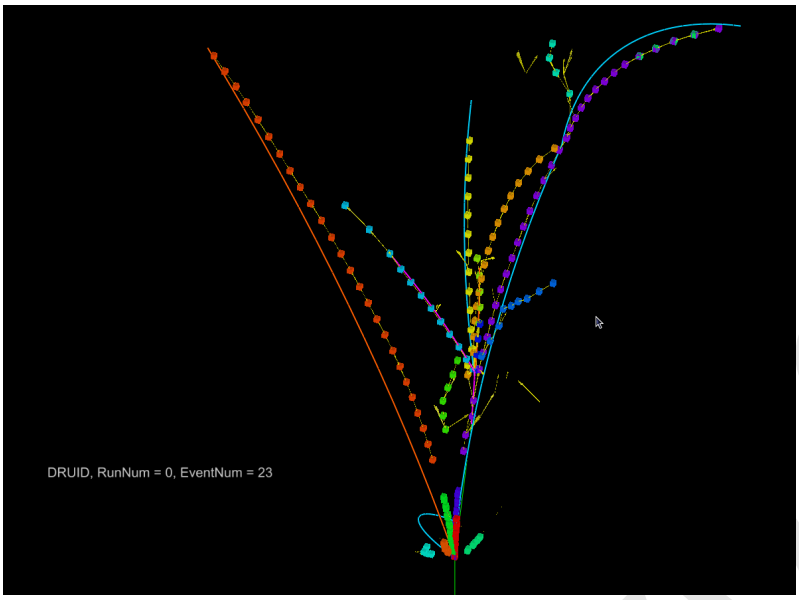

Figure 10.2: K_L shower reconstructed by the Arbor algorithm, the branches – the calorimeter hit clusters – are corresponding to the trajectories of charged particles generated in the shower cascade.

Fig. 10.2 shows a reconstructed calorimeter shower of a 20 GeV K_L^0 particle at the high granularity calorimeter, where the readout density is roughly 1 channel/cm^3. The reconstructed tree branches are demonstrated with different colors. Therefore the trajectory length of charged shower particle can be reconstructed. Fig. 10.3 compares the reconstructed trajectory length with MC truth, the red distribution is the MC truth level trajectory length of charged particles generated inside 40 GeV π showers; the green one is corresponding to the trajectory of the electron and the positron generated in the showers; while the blue is the trajectory length reconstructed by Arbor. Good agreement between the reconstruction and MC truth is found at sufficient trajectory length.

Arbor can also be characterized by the energy collection performance at single neutral particle and the separation performance at bi-particle samples. Typically, Arbor reaches an energy collection efficiency higher than 99% for photons with energy higher than 5 GeV at the APODIS geometry. Higher hit collection efficiency usually leads to a better energy resolution but also increases the chance of confusions, i.e, the wrong clustering of calorimeter hits.

Excellent separation performance is crucial for the jet energy reconstruction, the π^0 reconstruction, and the measurement with τ final states. This performance can be characterized via the reconstruction efficiency of di-photon samples, where two photons with the same energy are shot in parallel at different positions, see Fig. 10.4. According to the distribution of π^0 energy at $Z \to \tau^+\tau^-$ events at CEPC Z pole operation, we set the photon energy to 5 GeV.

The reconstruction efficiency is defined as the probability of successfully reconstructed two photons with anticipated energy (each candidate is required to have an energy within 1/3 to 2/3 of the total induced energy). The efficiency curve naturally exhibits an S-curve dependency on the distance between the photon impact positions, see Fig. 10.5. The distance at which 50% of the events are successfully reconstructed is referred to as the critical distance, which depends on the ECAL transverse cell size. At the cell size

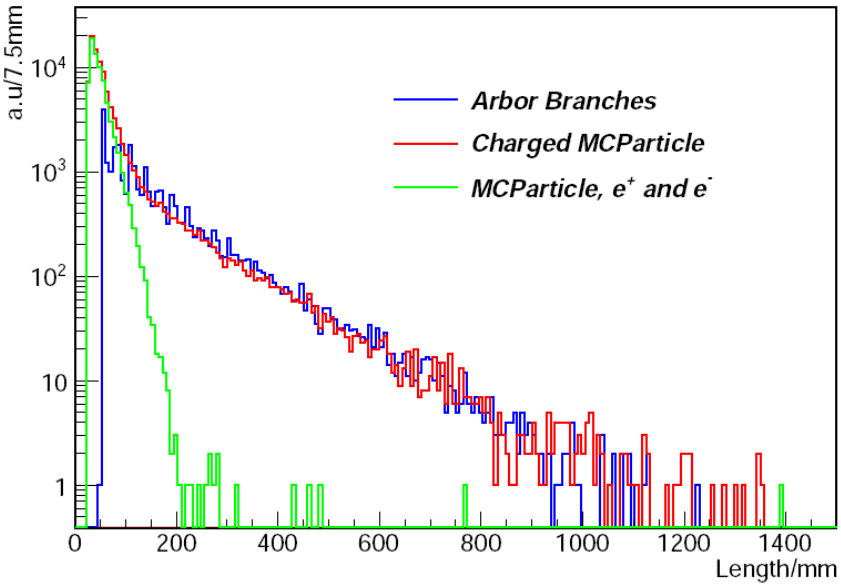

Figure 10.3: Proof of Principle: reconstructed and MC truth particle trajectory length at 40 GeV π showers.

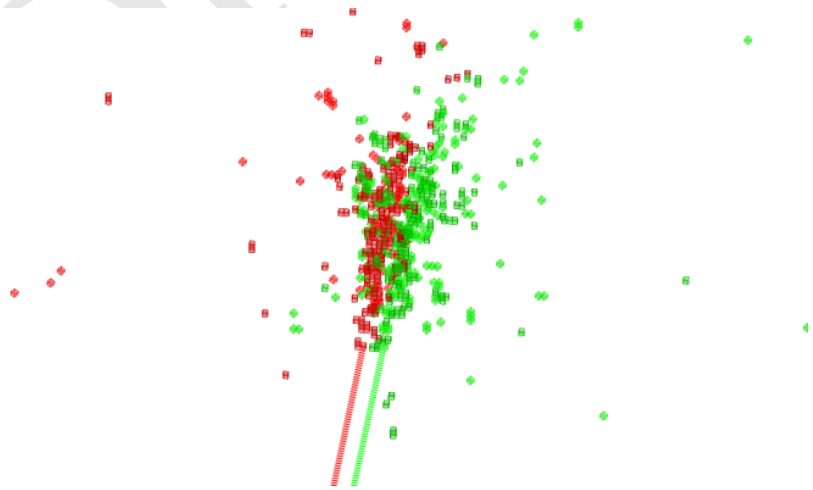

Figure 10.4: A reconstructed di-photon event at Si-W ECAL with 1 mm cell size. Each photon has an energy of 5 GeV, and their impact points are separated by 4 mm.

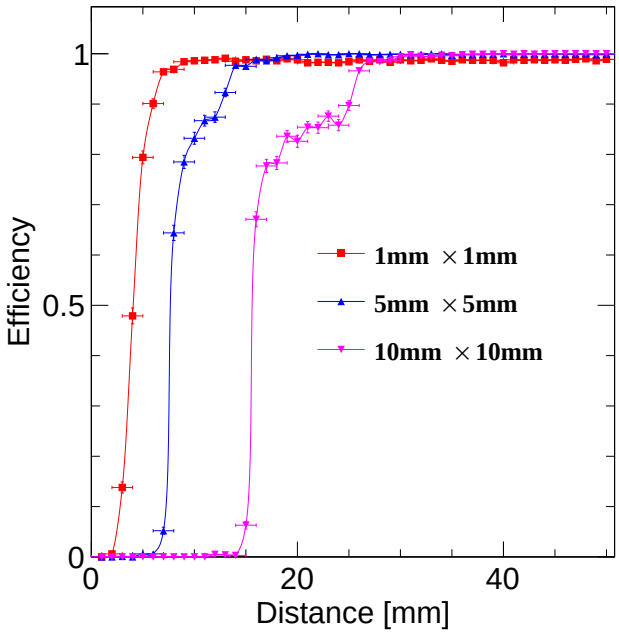

Figure 10.5: Reconstruction efficiency of the di-photon events at different ECAL cell sizes. The X-axis represents the distance between photon impact points.

ECAL cell size	Critical distance for separation
1 mm	4 mm
5 mm	9 mm
10 mm	16 mm

Table 10.1: Arbor critical separation distance at di-photon sample with different ECAL cell size.

smaller than the Moliere radius, the critical distance is roughly 2 times the cell size, see Table. 10.1.

To conclude, Arbor is a geometrical algorithm that reconstructs each shower cluster into a tree topology. At high granularity calorimeter, Arbor efficiently separates nearby particle showers and reconstructs the shower inner structure. It maintains a high efficiency in collecting the shower hits/energy, which is appreciated by the neutral particle energy reconstruction.

To conclude, Arbor, a Particle Flow algorithm that responsible for reconstructing all the final state particles, has been developed for the CEPC studies. A full reconstruction chain has been developed based on Arbor. Arbor could efficiently separate nearby particle showers and reconstructs the shower inner structure. The separation performance is efficiently good that almost all the final state particles could be safely treated as well separated for the CEPC Higgs measurements, which is essential for the Particle Flow reconstruction, and also enables a reliable and straightforward modeling of fast simulation.

Draft-v1.2

The physics performances will be discussed in the following sections. All the samples, unless explicitly stated, are simulated at APODIS and reconstructed with the cepcsoft.

10.3 Performance at the Physics Object level

This section gives a global description of the reconstruction of core physics objects at the CEPC: the leptons, the photons, the kaons, and the jets. The reconstruction of the τ leptons is addressed in the next section **??**, where a full simulation analysis on the $\sigma(XH) * Br(H \rightarrow \tau^+\tau^-)$ is presented. Before we goes into these physics object, a comprehensive diagnosis on the tracking performance is reported.

10.3.1 Tracking performance

The APODIS tracking system is composed of a TPC main tracker and a silicon tracking system. These two subsystems play complementary roles. The TPC has more than 200 radial layers, and has a high efficiency track finding performance. The silicon devices provide high precision spatial point measurements. Comparing to a standalone TPC, this combination improves significantly the tracking momentum resolution, especially for high energy tracks. In addition, the silicon tracking system includes a forward tracker that increases significantly the solid angle coverage of the tracker.

This section presents the tracking performance on two samples: a single muon particle gun sample and a $Z \rightarrow \tau^+\tau^-$ sample corresponding to the CEPC Z pole operation. The particle gun sample describes the tracking efficiency and accuracies for isolated tracks. And the $Z \rightarrow \tau^+\tau^-$, with one of the τ lepton decays into 3 prong final states, provides a critical test for the separation performance of nearby tracks. These samples are reconstructed with Clupatra, the tracking module at the ilcsoft [**?**].

The single muon particle gun sample has a total statistic of 10 million, and covers a momentum range from 0.1 GeV to 100 GeV. Fig. 10.6 shows the extracted differential efficiency and resolution on the polar angle and the particle energy. Clearly, once the energy is larger than 0.5 GeV, and the track is within tracker fiducial region of $|cos(\theta)| < 0.985$, the tracking efficiency converges 100%. While the relative accuracy of transverse momentum resolution reaches per mille level for the energy range of 10 - 100 GeV.

The CEPC Z pole operation provides very clean $Z \rightarrow \tau^+\tau^-$ signal. About 10% of the τ lepton decays into 3-prong final states. A typical event is displayed in Fig. 10.7. Since the τ is highly boosted at the $Z \rightarrow \tau^+\tau^-$ events, the three charged particles decayed from the same τ lepton can be confined in a very narrow cone. Thus, these physics events pose stringent requirement on the nearby track reconstruction performance.

A dedicated $Z \rightarrow \tau^+\tau^-$ sample, with one τ decays into $2\nu\mu$ and the other into three charged pions and one neutrino. Defining the successful reconstruction efficiency as the probability of reconstructing three target tracks in these events with three visible pions in the events. The reconstruction efficiency is close to 100%.

To cross check the performance, two dedicated CEPC tracking algorithms are developed. The comparison shows consistent results is consistent with ilc tracking. A dedicated comparison report could be found in ref. [**?**][**?**].

To conclude, the tracking system at the APODIS provides a high efficiency, and high accuracy reconstruction of the track. In the tracker fiducial angle ($|cos(\theta)| < 0.985$), the

Draft-0.2

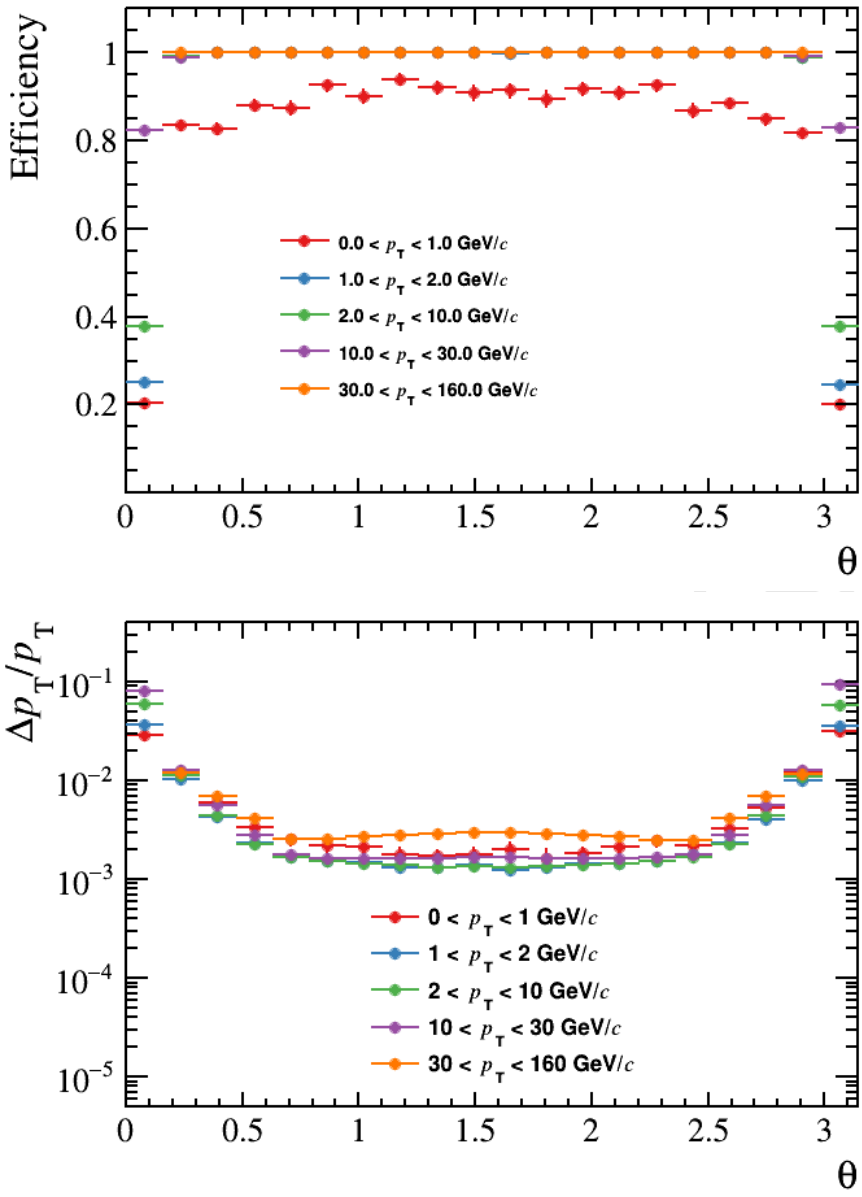

Figure 10.6: Single particle reconstruction efficiency (up plot) and resolution (lower plot) as a function of the track momentum and track polar angle.

reconstruction efficiency reaches 100% for tracks with momentum larger than 0.5 GeV. An overall reconstruction efficiency close to 100% has been achieved for $\tau \rightarrow 3\pi\nu$ sample. A dedicated analysis shows the charge misidentification rate is smaller than 10^{-4}, mostly concentrated at very forward region [**?**]. This tracking performance provides a solid starting point for the Particle Flow reconstruction at the APODIS.

10.3.2 Leptons

The lepton identification is of key importance to the CEPC Higgs program. First of all, about 7% Higgs boson events at the CEPC are generated together with a pair of leptons. Those events are the golden signals for the Higgs recoil analysis, which is the anchor

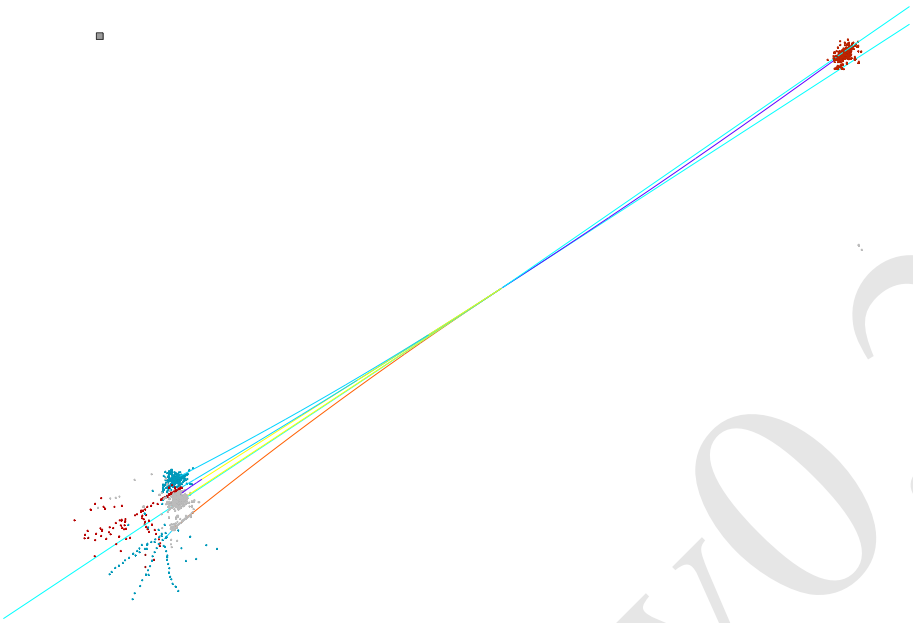

Figure 10.7: A simulated $Z \to \tau^+\tau^-$ event at CEPC Z pole operation. The left hand side τ lepton decays into 3 charged tracks, and 1 FSR photon. Through leptonic decay, the right handed one decays into an electron and two neutrinos.

Draft-v0.2

for the absolute Higgs measurements. A significant fraction of the Higgs boson decays, directly or via cascade, into final states with leptons. 0.02% of SM Higgs decays into muons; the leptons serve as the essentially candles of identification of $H \to WW/ZZ \to$ leptonic/semi-leptonic final states. In addition, a significant fraction of Higgs->bb/cc events generate leptons in their decay cascade.

The PFA oriented detector, especially its calorimeter system, could provide enormous information for the lepton identification. In the CEPC v_4 geometry, a high-energy electron/positron/hadrons is likely to induce thousands of hits in the calorimeter with typical spatial configurations. Using the benchmark calorimeter geometry, the shower fractal dimension could be extracted [1]. In addition, the dE/dx measured by the TPC could efficiently separate electron/positrons from muon and hadrons, at track energy less than 10 GeV.

A dedicated Lepton identification algorithm for the detectors using high granularity calorimeter, LICH [2], has been developed. LICH extract more than 20 distinguish variables from the detector and combine these information into lepton-likelihood via MVA method. The performance of LICH have been scanned over a large range of the granularity for both ECAL and HCAL, while the performance is stable for particles with energy larger than 2 GeV.

At APODIS geometry, applied on isolated charged particle candidate with energy larger than 2 GeV, lepton identification efficiency better than 99.5% could be achieved with a mis-identification rate from hadrons is controlled to be smaller than 1%. This mis-identification is mainly induced by the irreducible background rate from pion decay (to muons) and highly electro-magnetic like pion clusters (via the pion0 generated from the

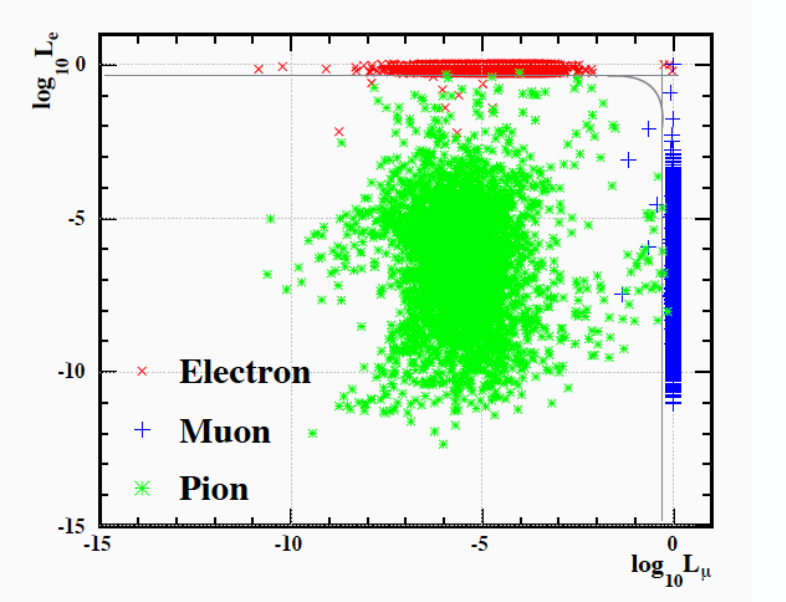

Figure 10.8: The distribution of charged particles in the phase space of calculated lepton likelihoods.

pion-nuclear interactions). Not surprisingly, this performance is significantly better than that at LHC and LEP [**?**][**?**].

In the actual physics event, the lepton identification performance will be limited by the separation power of the detector. Using fully reconstructed llH events, we found the efficiency of successfully identify two leptons with opposite charge reaches 97-98%, In other word, less than 1% of the objective leptons in the llH events will potentially be mis-identified due to the overlapping of their cluster to the nearby showers. This result is consistent with the separation power of APODIS.

In terms of the Higgs signal at the CEPC, the tracking and the lepton identification performance can be characterized by the recoil mass distribution of l^+l^-H events and the invariant mass distribution of the $H \to \mu^+\mu^-$ events. These distributions are presented below.

10.3.2.1 Higgs recoil mass distribution at $\mu^+\mu^-H$ events

The Higgs recoil mass distributions at the l^+l^-H events are the most characteristic distributions of the electron positron Higgs factories. Since the initial 4-momentum is precisely known at the electron positron collider, and the pair of leptons (mostly generated from Z decay but also a few from the Z fusion events) could be precisely reconstructed, the recoil mass of Higgs boson could be calculated. Therefore, without any direct measurement on the Higgs boson decay final states, the Higgs signal could be identified by the characteristic recoil mass peak, whose position indicates the mass of Higgs boson and the total number of signal events is proportional to g^2_{HZZ}.

This distribution leads to a precise determination of the both Higgs boson mass and g_{HZZ}. The measurement of the Higgs boson mass is of strong physics interest itself. More importantly, the measurement of g_{HZZ} is unique at the electron positron Higgs factory. It anchors all the absolute Higgs boson measurements at the electron positron collider, and is highly complementary to the Higgs measurements operated at LHC and HL-LHC.

Draft-v0.2

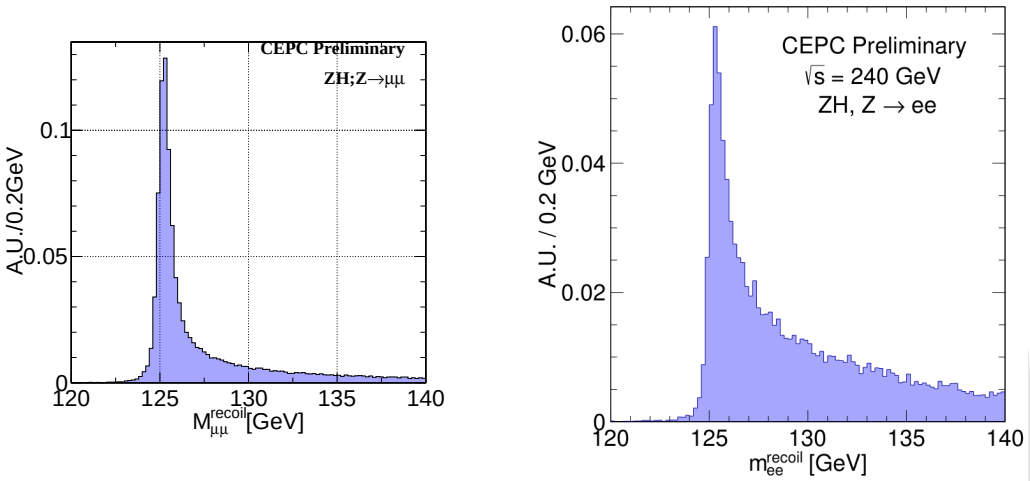

Figure 10.9: Recoil mass distribution of the $\mu^+\mu^- H$ and $e^+e^- H$ events. Normalized to unit area.

The di-muon recoil mass distribution is shown in Fig. 10.9. This distribution has a long high mass tail, induced by many radiation effects (the beamstrahlung, the bremsstrahlung, the final state radiation, and most importantly, the initial state radiation). The width of the peak distribution is determined by the intrinsic track momentum resolution and the beam energy uncertainty, both of which are at per mille level at the CEPC.

In terms of the detector response, the recoil mass measurements require a high efficiency, high precision tracking system, good lepton identification performance.

10.3.2.2 The di lepton invariant mass distribution of $\nu\nu H, H \rightarrow \mu^+\mu^-$ events

CEPC could generate roughly 200 $H \rightarrow \mu^+\mu^-$ events. Thanks to the high precision tracking performance, the signal strength could be measured to a relative accuracy of 15% at the CEPC. The reconstructed di muon invariant mass distribution is shown in Fig. 10.10.

Fig. 10.10 exhibits a low mass tail, induced mainly by the bremsstrahlung and FSR effects of the charged muon. In addition, the Higgs mass peak has a bias of 100 MeV, mainly induced from a tiny bias in the dEdx estimation in current simulation module.

10.3.3 Kaon Identification

Successful identification of the charged kaons is crucial for the flavor physics, and is highly appreciated in the determination of jet flavor and jet charge. According to the Bethe-Bloch equation, in the realistic energy range and at the same track momenta, the dEdx of pions is larger than that of kaons by roughly 10%. In other word, if the dEdx resolution could be measured to a relative accuracy better than 5%, the dEdx could leads to an efficient π-K separation.

The APODIS is equipped with a large TPC main tracker. Depending on the readout hardware performance, the dE/dx resolution leads to 2-4 σ π-K separation for 2-20 GeV charged tracks. See the left plot of Fig. 10.11. The upper boundary is the ideal separation predicted by the Geant4 simulation; while the lower boundary includes a 50% degrading with respect to the MCTruth, and is regarded as the conservative scenario. (A survey of

Draft-v0.1

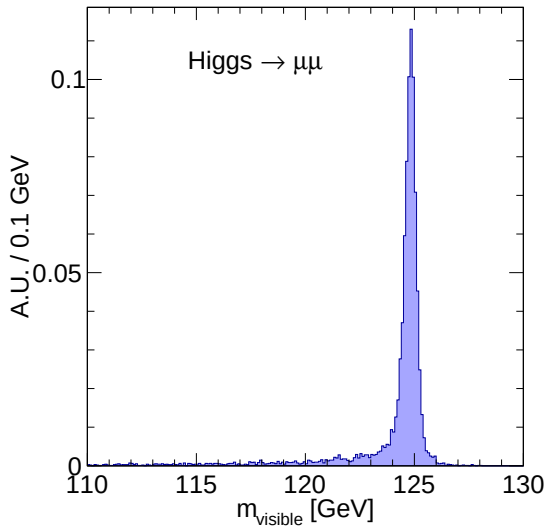

Figure 10.10: The reconstructed Higgs invariant mass of $H \to \mu^+\mu^-$ events at the CEPC v_1 detector geometry. 8k events, normalized to unit area.

the performance at previous experiments shows the degrading varies from 15% to 50%). The dE/dx separation between other charged particles is also demonstrated.

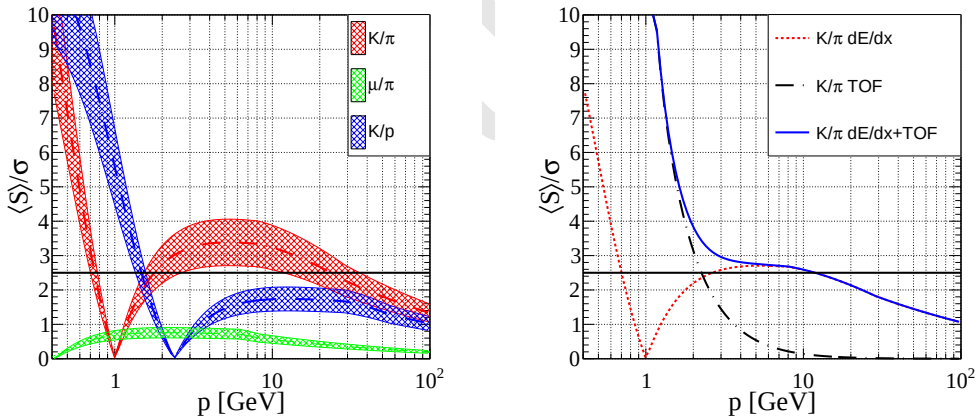

Figure 10.11: π-K separation performance at PICADOR detector. Left plot, dE/dx separation between different charged particles at $0.4 \sim 100$ GeV track momentum. Right plot, the separation power using both dE/dx and ToF information.

The difference between the dE/dx of pions and kaons vanishes at 1 GeV track momentum. Meanwhile, a significant portion of charged particle has energy smaller than 2 GeV at the CEPC. To separation these low energy charged particles, a Time of Flight (ToF) measurement with 50 ps time resolution is proposed. The ToF information could be measured by the ECAL, with a few layers equipped with the Time sensitive ASICs. Using both ToF and dE/dx information, a separation better than 2 σ could be achieved for tracks with momenta smaller than 20 GeV in the conservative scenario.

Considering the CEPC inclusive $Z \to q\bar{q}$ sample and integrate over the full polar angle and the momenta range of $2 \sim 20$ GeV, an over all charged kaon identification

reaches an efficiency and purity of 91%/94% at the APODIS in the conservative scenario. If the dE/dx measurements could be improved to 3.6% (20% degrading comparing to the MCTruth), the efficiency and purity of charged Kaon identification could be improved to better than 95% **??**.

10.3.4 Photons

Successful photon reconstruction is crucial for the jet energy reconstruction, the $Br(H \rightarrow \gamma\gamma)$ measurement, and the physics measurements with τ leptons. Since the separation performance has been demonstrated in the section 10.2.2, this section is devoted to the reconstruction efficiency and the energy measurement of single photon.

The photon reconstruction is sensitive to the tracker material and the calorimeter geometry defects. To quantify their impact, a simplified, defect-free silicon tungsten ECAL geometry is implemented. This simplified geometry uses cylindrical barrel layer and its endcaps are directly attached to the barrel, forming a closed cylinder. The simplified geometry takes its inner radius and length of 1800 mm and 4700 mm (similar to the APODIS parameters). Along the longitudinal direction, the simplified ECAL is divided into 30 identical layers, each consist of one 2.8 mm tungsten absorber layer, one 0.5 mm silicon sensor layer and a 2 mm thick PCB layer. The thickness of the tungsten absorber and silicon sensor is adjustable, with which a dedicated optimization study has been performed and the ECAL geometry of APODIS is determined [**?**].

The reconstruction performance of a single photon is characterized by the finding efficiency and the energy collection efficiency. The finding efficiency is the chance that at least one ECAL cluster is reconstructed for one event with one photon incident into the detector fiducial region. The energy collection efficiency is defined as the accumulated hit energy in the photon cluster divided by that in all the hits.

At the simplified ECAL geometry, the finding efficiency reaches 100% for photons with energy larger than 500 MeV. The finding efficiency decreases to 85% once the photon energy is reduced to 100 MeV. The energy collection efficiency is better than 99% when the photon energy ranges from 1 GeV to 175 GeV. When the photon energy is less than 1 GeV, the energy collection efficiency degrades, i.e., the average energy collection efficiency decreases to 75% for 100 MeV photons. Since the simplified ECAL has no material before the calorimeter, it maintains high efficiencies even for low energy photons.

The single photon energy resolution of the simplified 30-layer ECAL is displayed as the black curve in Figure **??**, which is consistent with the test beam result of ILD ECAL prototype [**?**]. Reducing the number of layers (by enlarging the tungsten absorber thickness at each layer, but keep the) means fewer read-out channels, which leads to lower construction cost and power consumption. Keeping the total absorber thickness at the optimized value of 84 mm, reducing the readout layer numbers and maintaining the local sensor thickness, the ECAL energy resolution degrades as the sensor-absorber ratio decreases. Compared with 30 layers option, the energy resolution degrades by 11% at 25 layers and 26% at 20 layers.

The degradation of photon energy resolution by reducing the number of channels could be compensated by using thicker silicon sensor. We found that the energy resolution of ECAL at 20 layers with 1.5 mm thick silicon wafer, 25 layers with 1 mm thick wafer and the baseline geometry (30 layers with 0.5 mm thick wafer) has the same energy resolution.

Draft-v0.2

This conclusion is confirmed by the analyses at the Higgs physics benchmarks of $H \to \gamma\gamma$ and $H \to gg$ [**?**].

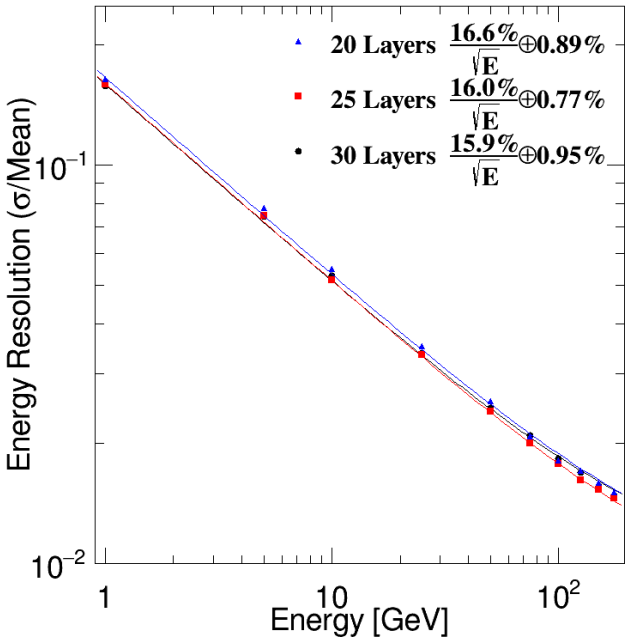

Figure 10.12: Energy resolution with fewer layers and thicker silicon wafers (20 layers with 1.5 mm silicon wafer and 25 layers with 1 mm silicon wafer), compared to 30 layers and 0.5 mm thick silicon wafer.

To conclude, the simplified geometry has an ideal efficiency of photon reconstruction and a consistent energy resolution w.r.t the CALICE ECAL prototype. We found that using thicker silicon wafer, the ECAL number of layers thus its construction cost and power consumption could be significantly reduced. Therefore, we strongly encourage the feasibility study of the thicker silicon sensor wafers.

At the APODIS detector, the total amount of material before the calorimeter is roughly 5-10% of one radiation length. This material will reduce the reconstruction efficiency for the low energy photons, and caused 5-10% of high energy photons to convert into electron-positron pairs. A preliminary converted photon finding algorithm is developed, with which 70% of the converted photon in $H \to \gamma\gamma$ events could be identified [**?**]. In addition, the geometry defects, such as the cracks between the ECAL modules, staves, and the dead zone between the ECAL barrel and endcaps, induces geometry based bias for the photon energy measurements and need to be corrected. The overall photon reconstruction could be benchmarked with the Higgs mass resolution at $H \to \gamma\gamma$ event at both simplified and the APODIS geometry, which will be discussed in section 10.3.4.1.

10.3.4.1 The di photon invariant mass distribution of $\nu\nu H$, $H \to \gamma\gamma$ events

The SM Higgs boson has 0.2% chance to decay into a pair of photons. Since photons could be easily identified, this channel becomes one of the Higgs discovery channels at the LHC. At the CEPC, this channel serves as a benchmark to characterize the ECAL performance.

Using the reconstructed $\nu\nu H, H \rightarrow \gamma\gamma$ sample and calculate the invariant mass of two most energetic photon candidates, we acquire the objective distributions at both simplified ECAL geometry and at APODIS, see Fig. 10.13 and **??**.

At the simplified ECAL geometry, a clean Gaussian distribution is identified with a tiny low mass tail. The low mass tail is induced by the artificial splitting of the photon cluster. A relative mass resolution of 1.7% is achieved, which agrees with the intrinsic electromagnetic energy resolution measured at the CALICE Si-W ECAL prototype test beam experiments [**?**].

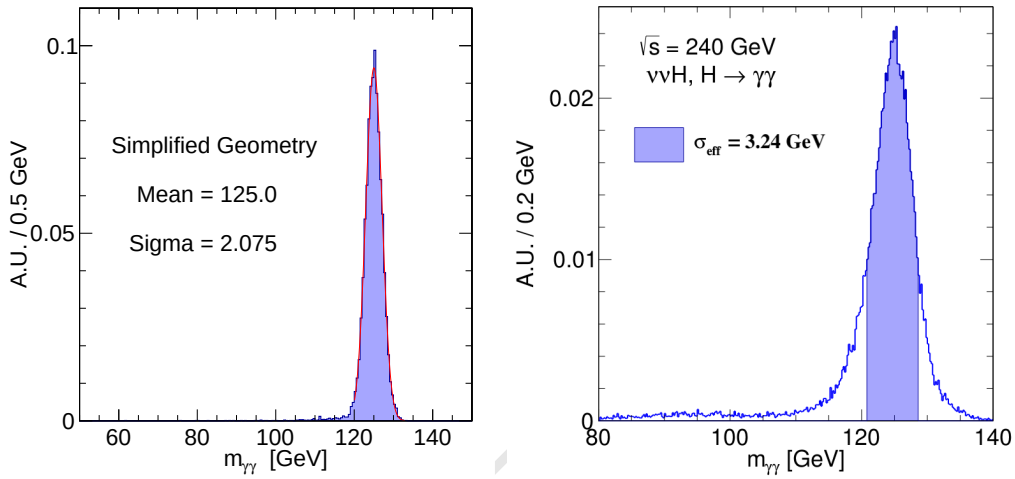

Figure 10.13: The reconstructed Higgs invariant mass of $H \rightarrow \gamma\gamma$ events at the simplified detector geometry (Left) and at APODIS (Right). 10k and 6k events are reconstructed correspondingly. Each distribution is normalized to unit area.

Comparing to the simplified geometry, the relative resolution of the Higgs mass at APODIS degrades significantly. A preliminary geometry based correction algorithm has been developed, which scales the energy of EM clusters located at the geometry cracks. This distribution could be fit to a core Gaussian center and a wider Gaussian with a lower mean value. The core gaussian exhibits a mass resolution of 1.9%, while the low-mass wider gaussian is caused by the fact that the correction algorithm is only optimized. The average mass resolution (taking a weighted average of both Gaussian) is then 2.3%. The latter can be improved with much dedicated correction algorithm.

To summarize, our simulation predicts the Higgs mass resolution at two-photon final state reaches 1.6-2.3% level at the CEPC. This result is consistent with the CALICE prototype test beam result. The reconstruction of converted photons and the correction of the geometry defects at any realistic detector geometry is crucial for the photon reconstruction.

10.3.5 Jet

The jet is fundamental for the CEPC physics program. About 90% of the SM Higgs boson decays into final states with jets (70% directly to di-jet final states; and roughly 20% via decay cascade from the ZZ^*, WW^*), while 70% of W and Z bosons decay into di-jet final states. Roughly 60% of the jet energy is carried by the charged particles, and the Particle

Flow could improve significantly the precision of jet energy measurement with respect to the calorimeter based reconstruction.

In the Particle Flow reconstruction, the jet candidates are constructed from the reconstructed final state particles via the jet clustering algorithms. The ambiguity from the jet clustering is significant and usually dominants the uncertainty, especially for these events with more than two final state jets such as the measurement of $g(H\bar{b}\bar{b})$, $g(Hc\bar{c})$, and $g(Hgg)$ via $ZH \rightarrow 4jet$ events.

To characterize the jet reconstruction performance, a two-stage evaluation has been applied at the CEPC studies. The first stage is the Boson Mass Resolution (BMR) analysis designed to avoid the complexity induced by the jet clustering. The second is the individual jet response analysis, which requests the jet clustering.

The Boson Mass Resolution analysis is applied to physics events with two final state jets decayed mostly from one intermediate gauge boson, including

1, $\nu\tilde{\nu}q\bar{q}$ events via the ZZ intermediate state;

2, $l\nu q\bar{q}$ events via mostly WW intermediate state;

3, $\nu\tilde{\nu}H$ events with $H \rightarrow b\bar{b}, c\bar{c},$ or gg.

In these processes, besides the jet final state particles, the other particles are either invisible or could be easily identified. The invariant mass of all the final state particles decayed from a massive boson can therefore be reconstructed. Therefore, disentangled from the jet clustering algorithm, the BMR evaluates the jet reconstruction. Meanwhile, the BMR shows immediately how these massive gauge bosons can be separated at jet final state.

Using the jet clustering and matching algorithms, the jet response is also analyzed at each individual jet. The overall response includes the detector resolution, the ambiguous induced by the jet clustering and the mismatching. These effects are physics process dependent and a complete analysis is beyond the scope of this manuscript. In this paper, this analysis is limited to individual jet reconstruction performance at $\nu\tilde{\nu}q\bar{q}$ process.

Corresponding to 5 ab^{-1} integrated luminosity at the CEPC, we simulate 1.8 millions $\nu\tilde{\nu}q\bar{q}$, 11 millions $l\nu q\bar{q}$ and 170 thousands $\nu\tilde{\nu}H, H \rightarrow jj$ events at $\sqrt{s} = 250\ GeV$ with the CEPC v_1 geometry. All these samples are reconstructed with Arbor. Fig. 10.14 shows the inclusive reconstructed boson mass distributions normalized to unit area. These distributions are well separated, each exhibits a peak at the expected boson mass. These mass distributions are all asymmetric for different reasons. At the low mass side, the green distribution, corresponding to $\nu\tilde{\nu}H, H \rightarrow jj$ events, has a long tail. This tail is mainly stemmed from the neutrinos generated in the heavy jets fragments (most of the $H \rightarrow jj$ events are $H \rightarrow b\bar{b}$ events). The heavy jet components are also responsible for the low mass tail in the other two distributions. Because W boson hardly decays into b-jets, the low mass tail of $l\nu q\bar{q}$ sample is much less significant. The Breit-Wigner width of massive gauge bosons and the phase space effects also contribute to the long tails at the $l\nu q\bar{q}$ and the $\nu\tilde{\nu}q\bar{q}$ samples. The high mass tail induced by ISR photon(s) is observed in each distribution.

To decouple the detector response from these physics effects, a standard cleaning procedure is designed:

Draft-v0.2

1, The jets are generated from light flavor quarks (u, d) or gluons.

2, Acceptance: the partons should have a significant angle to the beam pipe: $|cos(\theta)| < 0.85$.

3, ISR veto: there is no energetic visible final state ISR photon: the accumulated scalar transverse momentum of the ISR photons should be smaller than 1 GeV.

4, Neutrino veto: there is no energetic neutrino generated from the jet fragmentation cascade: the accumulated scalar transverse momentum of the jet neutrinos should be smaller than 1 GeV.

This event selection clearly leads to narrow boson mass distribution and better separation, see Fig. **??**.

After this event selection, the mass distributions are much symmetric. The Higgs boson mass could be simply fit to a Gaussian, while the other two distributions include the non-negligible intrinsic widths. The efficiency of this event selection depends on the decay branching ratio (condition 1), differential cross section (condition 2), the radiation behavior (condition 3) and jet fragmentation (condition 4). As in the $\nu\tilde{\nu}H, H \to gg$ sample, this event selection has an overall efficiency of 65% (75%/94%/94% for the 2nd/3rd/4th condition, respectively). The relative mass resolution of the Higgs mass is then 3.8%, providing a quantitative reference for the BMR.

It should be remarked that both lepton identification and jet flavor tagging information are available in current reconstruction. Combing these information enhances the distinguishing power on different physics processes.

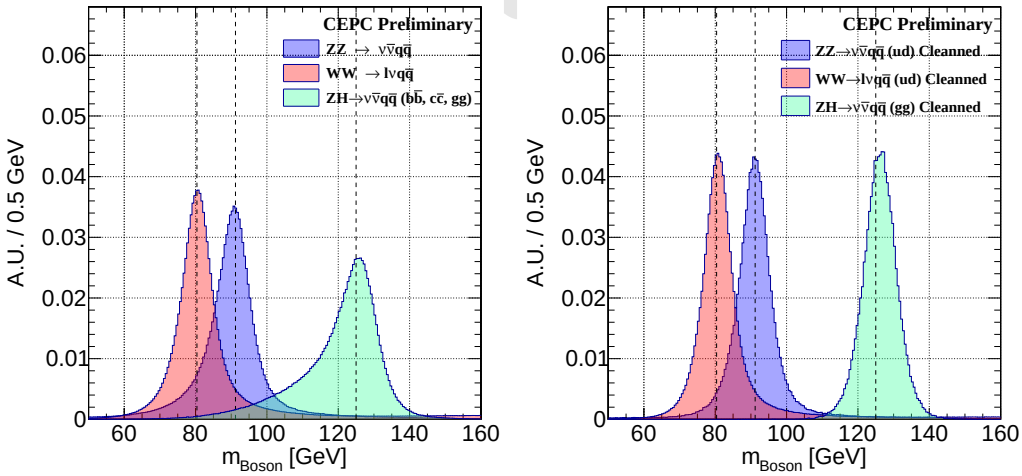

Figure 10.14: Reconstructed boson masses of the inclusive (Left) and cleaned (Right) $l\nu q\bar{q}$ (red), $\nu\tilde{\nu}q\bar{q}$ (blue) and $\nu\tilde{\nu}H, H \to jj$ samples (green).

The calibration process plays an important role in measuring the jet energy. Technically, Arbor was calibrated via two steps, the single particle level calibration, and the data-driven calibration. The single particle calibration is to figure out the global ECAL/HCAL calibration constants according to the comparison between the reconstructed neutral particle energy and the truth. The ECAL calibration constant is derived from photon samples

while the HCAL calibration constant at K_L^0 samples. Due to the Particle Flow double counting, i.e. the fragments of charged particle showers are misidentified as neutral particles, the single particle calibration leads to typically 1% overestimation on the boson mass. The data-driven calibration is to scale all the reconstructed boson masses according to the W mass peak exhibited in the $l\nu q\bar{q}$ events, the leading physics processes of the above three. This simple calibration simultaneously scales the three boson mass peak positions to the expected positions. To fully appreciate the enormous productivity of massive bosons at the CEPC, sophisticated calibration methods must be developed and validated for the real experiments, i.e. control and corrections of differential dependences, in-situ calibrations, detector homogeneity monitoring and control, *etc*.

The reconstruction performance of individual jet is explored via the same $\nu\tilde{\nu}q\bar{q}$ sample. Using ee-anti-kt algorithm (a.k.a Durham algorithm [**?**]), all the reconstructed particles are forced into two jets (recojets). The same jet-clustering algorithm is applied to the visible final state particles at the MC truth level, forming the generator level jets (genjets). Using a matching algorithm that minimizes the angular difference, the jet reconstruction performance is characterized by the difference between the 4-momentum of the initial quarks, the genjets, and the recojets. The difference between the quarks and the genjets is mainly coming from the fragmentation and the jet clustering processes, while the difference between the genjets and the recojets is induced by the jet clustering, matching, and the detector response. A dedicated analysis shows that, even at this simple di-jet process, the uncertainty induced by the jet clustering and matching can be as significant as those from the detector response [**?**].

These two reconstructed jets are classified into leading/sub-leading jets according to their energy. The relative energy difference between genjet and recojet is then fit with a double-sided crystal ball function. The exponential tails are mainly induced by the jet clustering algorithm, the matching performance, and the detector acceptance. The Gaussian core then describes the detector resolution, therefore we define its mean value as the Jet Energy Scale (JES) and its relative width as the Jet Energy Resolution (JER).

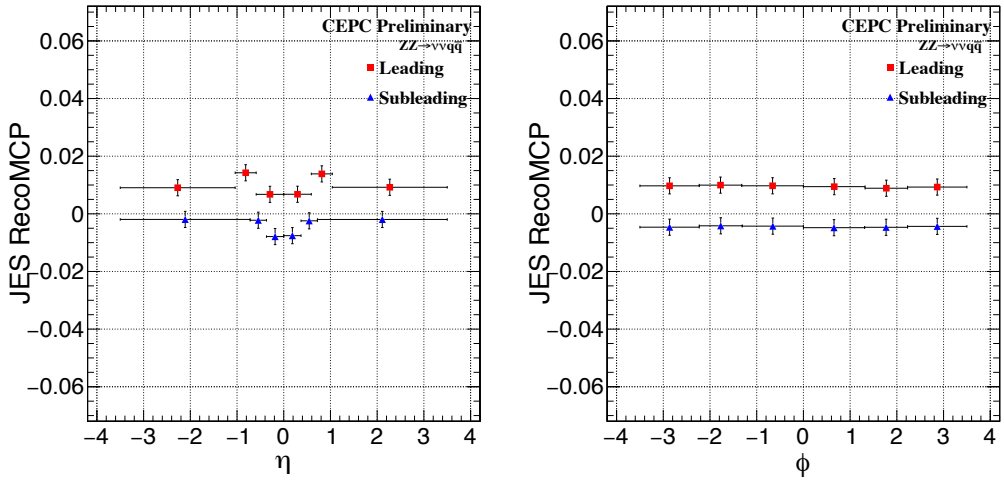

Figure 10.15: Jet energy scale at different jet directions.

Fig. 10.15 shows the JES at different jet directions. The JES is flat along the azimuth angle. Along the polar angle, the JES increases significantly for the leading jets in the

overlap part between the endcap and the barrel. The JES is also larger in the endcap than in the barrel. These patterns are correlated with the Particle Flow confusions, especially the artificial splitting of the charged clusters. Not surprisingly, the leading jets have a systematically higher JES comparing to the sub-leading one. Without any corrections, the entire amplitude of the JES is controlled to 1% level, which is significantly better than that of LHC even after the correction [**?**].

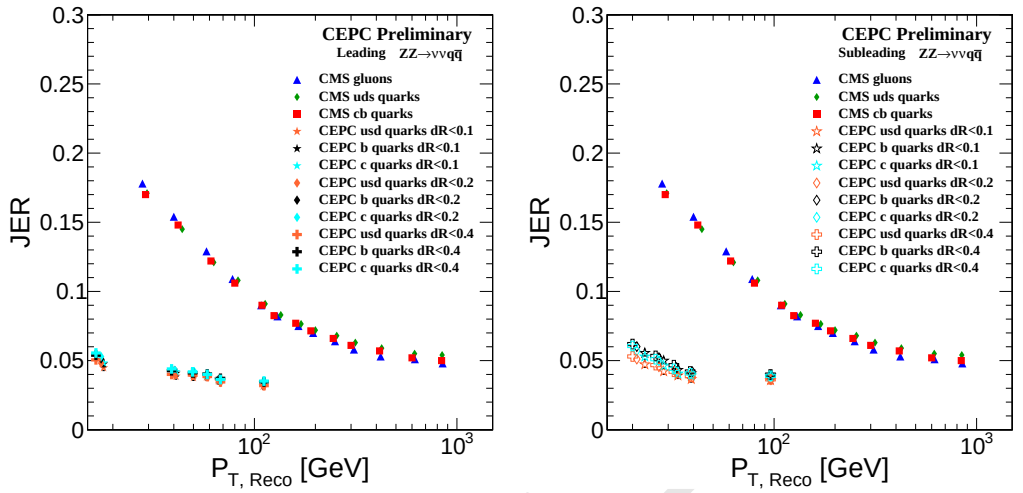

Figure 10.16: The jet energy resolution for leading (upper) and sub-leading jets (lower), as a function of the jet transverse momenta. The performance at the CMS [**?**] has been overlapped for comparison.

The jet energy resolution (JER) at different jet transverse momenta is displayed in Fig. 10.16. The overall JER takes a value between 6% (at $P_t < 20$ GeV) to 3% (at $P_t > 100$ GeV). The leading jets usually has a slightly better JER comparing to the sub-leading ones. Taking the performance of the CMS detector as a reference, the JER at the CEPC reference detector is 2-4 times better at the same P_t range [**?**].

To conclude, the jet energy response has been analyzed at the BMR level and at the individual jet level. For physics events with only two jets, the boson mass could be measured to a relative accuracy better than 4% at CEPC v_1 using a standard event selection. This resolution ensures significant separation between the W boson, the Z boson, and the Higgs boson. At individual jets, the JES is controlled to 1% level and the JER of 3% to 6%, both are significantly better than the LHC detector performances. This superior performance is based on the clean electron-positron collision environment, the PFA oriented detector design and reconstruction. It is highly appreciated for the CEPC physics program, i.e. the measurements of W boson mass at the CEPC Higgs operation. It should also be emphasized that the jet-clustering algorithm has a strong and even dominant impact on the physics measurements with multiple jets in the final states. Tested at the $\nu\bar{\nu}H, H \to jj$ events, the APODIS detector model gives the same jet energy resolution.

10.3.5.1 Total visible mass distribution of $H \to bb, cc, gg$ events

The majority of the SM Higgs boson decay into di-jet final states: 58%/3% into a pair of b/c quarks via the direct Yukawa coupling, and 8% into a pair of gluon mainly via top quark loop. These di-jet events could be easily identified using its invariant masses. The jet performance has been intensively discussed in section **??**, where the inclusive invariant mass distribution of $\nu\nu H, H \to di-jets$ and a cleaned distribution of $\nu\nu H, H \to gg$

-	$H \to bb$	$H \to cc$	$H \to gg$
Sample statistic	10k	10k	9.6k
$\epsilon_{ISRveto}$	94%	94%	94%
$\epsilon_{neutrinoveto}$	41%	69%	94%
$\epsilon_{acceptance}$	74%	74%	74%
Relative mass resolution	$3.60 \pm 0.07\%$	$3.76 \pm 0.05\%$	$3.69 \pm 0.04\%$

Table 10.2: Statistics, cut efficiencies on the $vvH, H \to dijet$ samples and the relative mass resolution after the cleaning.

are both presented. In this section, we are going to show all these 6 distributions of $vvH, H \to bb, cc, gg$ wi/wo cleaning.

These inclusive distributions (Fig. 10.17) clearly exhibit nongaussian, asymmetric patterns. As discussed in section **??**, these patterns are induced from visible ISR photons, neutrinos generated in Higgs decay cascade, and the detector acceptance. Applying the corresponding cuts in the standard cleaning procedure (defined in section **??**), these patterns disappear, see Fig. **??**.

The corresponding efficiencies and statistics are summarized in Table 10.2. For three different decay modes, the neutrino veto condition has different efficiencies, and vetoed more than half of the $H \to bb$ events. The other two condition have essentially identical efficiencies. After the cleaning, the relative mass resolution for three different decay modes converge to a similar level.

10.3.5.2 Total visible mass distribution of $H \to WW^*$ and ZZ^* events

The Higgs boson have large couplings to the massive gauge mediator. It has a branching ratio of 21%/3% to decays into a pair of W/Z boson, respectively. Limited by the Higgs mass, only one of the massive gauge boson is on shell. The total visible mass for the $vvH, H \to WW^*/ZZ^*$ events are shown in Fig. 10.18.

The cascade decay of $H \to ZZ^* \to 4l$ is the other Higgs discovery channel at the LHC, as multiple leptons is a clean signature. At the CEPC, combining the $Br(H \to ZZ^*)$ measurements and the g_{HZZ} measurements via the recoil mass methods leads to a direct, model independent determination of Higgs total width, therefore this measurement is of strong physics interests. The $Br(H \to WW^*)$ also a gateway measurement to the absolute Higgs width measurement. In addition, the large statistic of $H \to WW^*$ events makes it a sensitive probe to the new physics.

Both W and Z bosons decays into SM fermions except the top quarks. Therefore, a successful reconstruction of the $Br(H \to WW^*/ZZ^*)$ signal requires a proper reconstruction of leptons, taus, missing energy and jets.

The $H \to WW^*$ events could cascade decay into hadronic, semi-leptonic, and full-leptonic final states. The mass distributions corresponding to different decay modes are separated in the left hand plot of Fig. 10.18. A full mass peak, corresponding to the full-hadronic final states, could be clearly identified.

Draft-v0.2

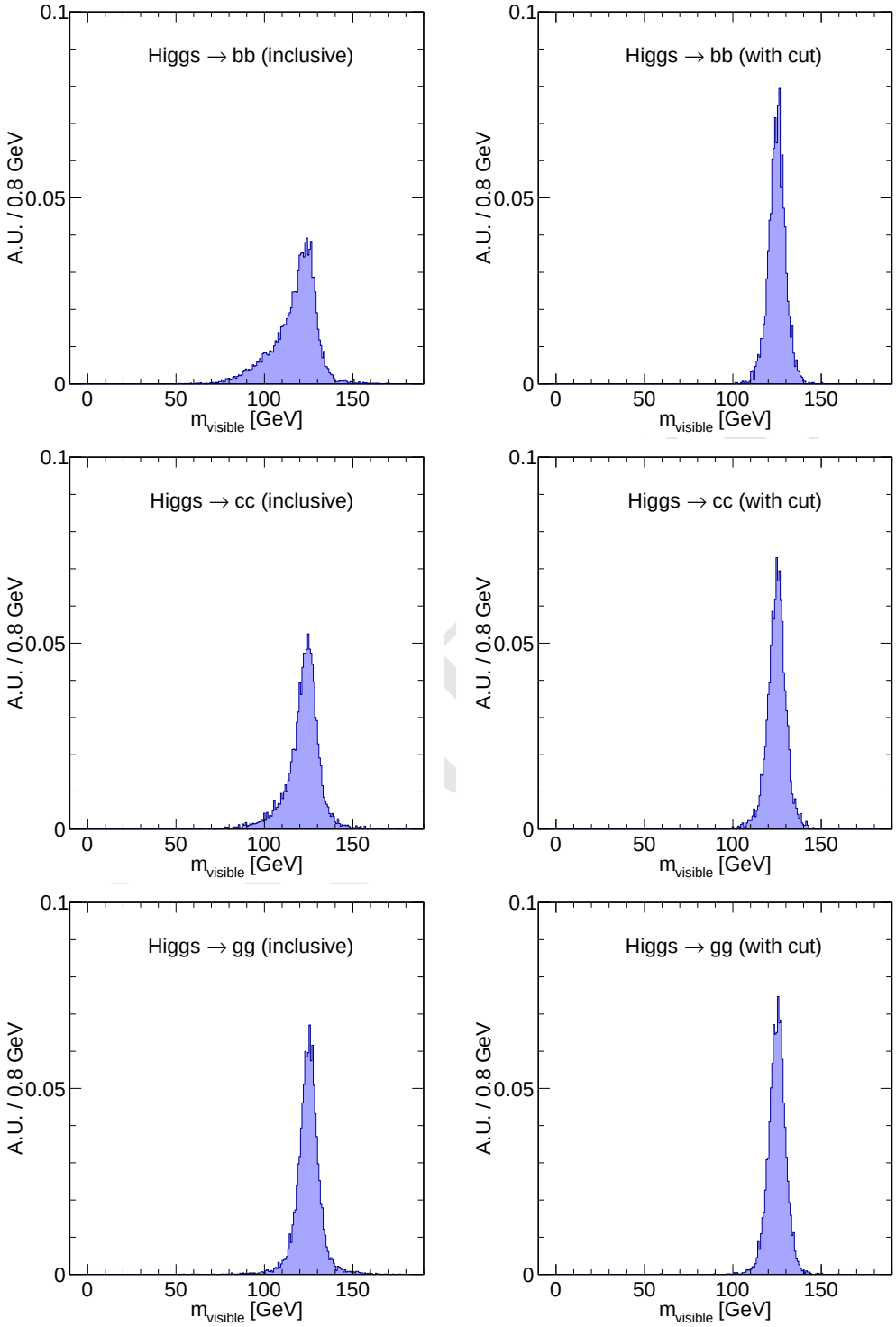

Figure 10.17: Total visible mass distribution of $vvH, H \rightarrow di-jet$ events, with/without cleaning

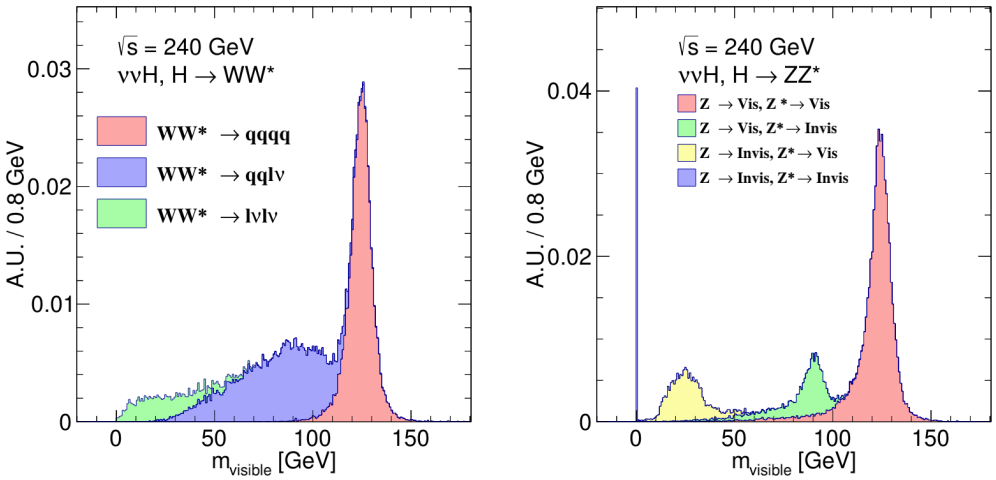

Figure 10.18: Total visible mass distribution of $H \to WW^*$ (Left) and $H \to ZZ^*$ events (right).

Four peaks could be identified at the distribution of $Br(H \to ZZ^*)$. The peak at zero corresponding to the total invisible decay mode where both Z and Z* decays into neutrinos and has a branching ratio of roughly 4%. The peak at the Higgs boson mass (125 GeV) is corresponding to the total visible mode. The other two peaks are corresponding to the conjugation case where $Z \to visible, Z^* \to invisible$ and $Z^* \to visible, Z \to visible$. Because of the heavy flavor and τ component of the Z boson decay, the peak at 125 GeV and at the Z boson mass exhibit a tail at the low mass side. For both $H \to WW^*$ and $H \to ZZ^*$ final states, a relative mass resolution of 3.8% is achieved with the full visible peak, which is consistent with the results at $H \to 2jets$ final states.

Fig. **??** exhibits beautiful separations of different components of $H \to ZZ^*$ events, those clear signature is highly appreciated in the physics measurements. In fact, using only the conjugating events where the $H \to ZZ^*$ signal decays into $llvvqq$ final states, a relative accuracy of 5% on the $Br(H \to ZZ^*)$ measurement could be achieved [**?**]. The statistic uncertainty of $Br(H \to WW^*)$ measurement should be controlled well below 1%.

10.3.6 Jet flavor tagging

Identification of the jet flavor is essentially for the measurement of the Higgs couplings ($g(Hb\bar{b}), g(Hc\bar{c}), g(Hgg)$) and the EW observables at the CEPC. During the jet fragmentation cascade, the heavy flavor quarks (b and c) are mostly fragmented into heavy hadrons (i.e. B^0, $B^{\pm}$, B_s, D^0, $D^{\pm}$, *etc*). Those heavy hadrons have a typical $c\tau$ of a few hundred micrometers. Therefore, the reconstruction of the secondary vertex is crucial for the flavor tagging. The information of jet mass, vertex mass, number of leptons, *etc*, are also frequently used in flavor tagging.

Technically, the flavor tagging is operated using the LCFIPlus package [**?**], the default flavor tagging algorithm for the linear collider studies. At CEPC studies, the LCFIPlus takes the reconstructed final state particles from Arbor, reconstructs the second vertexes and performs the flavor tagging. For each jet, LCFIPlus extracts more than 60 distinguish observables and calculates the corresponding b-likeness and c-likeness using the Boost Decision Tree method [**?**]. Since the b-mesons have longer lifetime compared

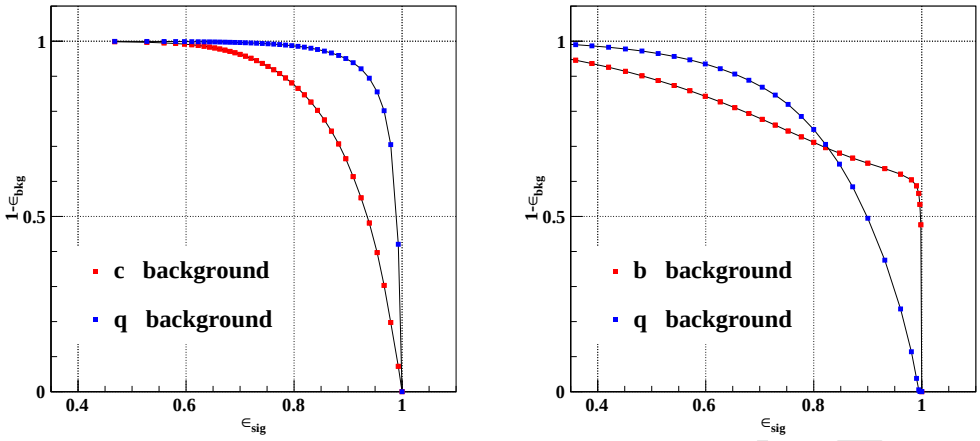

Figure 10.19: The jet flavor tagging performance using Arbor and LCFIPlus reconstruction at APODIS.

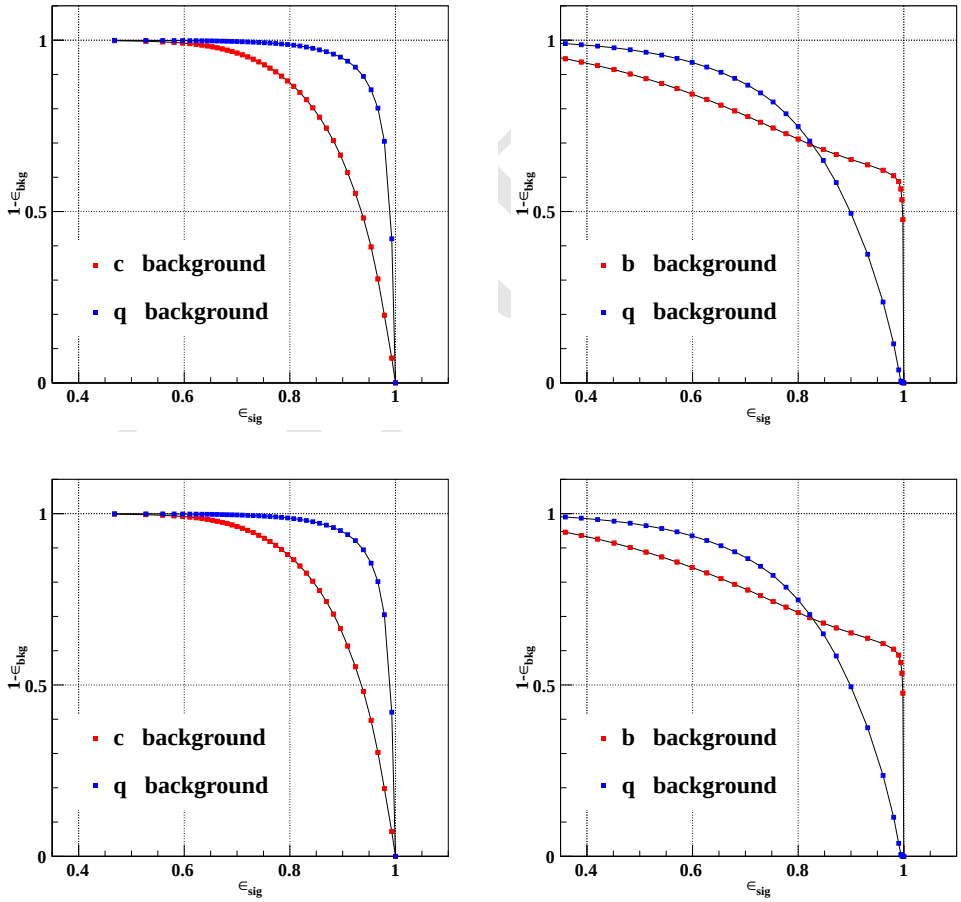

Figure 10.20: The heavy flavor jet likelihood for Higgs samples: a, $H \to bb$; b $H \to cc$; c, $H \to gg$, and d, $H \to 2jets$

to the c-mesons, the c-tagging is much more challenging than the b-tagging. Thanks to the high precision vertex system, the c-jet could be distinguished from other jets at the ILD detector and the CEPC v_1 detector. Fig. 10.19 shows the reference ROC curve trained on $Z \rightarrow q\bar{q}$ sample at 91.2 GeV center of mass energy. The X-axis indicates the b/c-jet efficiency, while the Y-axis represents the surviving rate for the backgrounds.

Applying to the inclusive $Z \rightarrow q\bar{q}$ sample, the typical performance of the b-tagging reaches an efficiency/purity of 80%/90%, changing the working point to a reduced efficiency of 60%, the purity could be enhanced close to 100%. While for c-tagging, a typical working point has the efficiency/purity of 60%/60%.

The distribution on the phase space for $H \rightarrow 2jets$ samples are displayed in Fig. 10.20. Depending on the Higgs decay final states, those distributions clearly exhibits different patterns. It should be emphasized that, with the current detector geometry design and reconstruction algorithm, the c-tagging is still very difficult. As a result, the accuracy of $g(Hc\bar{c})$ measurement is largely limited by the contamination from the $H \rightarrow b\bar{b}$ events.

10.4 conclusion

Targeting at precise measurements of the Higgs boson properties and the EW observables, the CEPC detector is required to reconstruct all the corresponding physics objects at high efficiency and high accuracy. The performance of the baseline detector design, the APODIS, has been intensively analyzed at full simulation level. The following object level performances have been achieved.

1, Lepton identification: $\epsilon_{e\rightarrow e} > 99.5\%$, $\epsilon_{\mu\rightarrow\mu} > 99.5\%$, $P_{h\rightarrow lepton} < 1\%$ for isolated tracks with energy larger than 2 GeV;

2, Charged Kaon identification: efficiency/purity of 95%/95% at inclusive Z pole sample with the energy range of 2 - 20 GeV;

3, Photon reconstruction: a relative accuracy of 1.7%/2.6% is achieved for the Higgs mass reconstruction at $H \rightarrow \gamma\gamma$ event using simplified/APODIS detector geometry;

5, Jet energy resolution: A relative accuracy of 3.8% of Boson mass reconstruction is achieved at a cleaned $H \rightarrow gg$ event sample. The Higgs boson, the Z boson, and the W boson can be efficiently separated from each other in their hadronic decay modes. The jet energy scale is controlled to 1% level. At individual jet, the relative jet energy varies from 3% to 6%, depending on the jet transverse momentum.

6, Jet Flavor Tagging: at the inclusive $Z \rightarrow q\bar{q}$ samples at 91.2 GeV, the b-jets could be identified with an efficiency/purity of 80%/90%; while the c-jets could be identified with efficiency/purity of 60%/60%.

Essentially, all the physics objects are successfully reconstructed by the CEPC baseline. The performances at the single particle level, such as the leptons, the kaons, and the photons at simplified geometry, are close to the physics and/or hardware limits. The separation and high-efficiency reconstruction of charged particles/photons ensure good τ

Draft V0.2

	Higgs→ $\mu\mu$	Higgs→ $\gamma\gamma$	Higgs→bb
CEPC (APODIS)	0.20%	2.59%	3.63%
LHC (CMS, ATLAS)	∼2% [**?** **?**]	∼1.5% [**?** **?**]	∼10% [**?** **?**]

Table 10.3: Higgs boson mass resolution ($\sigma/Mean$) at different decay modes with jets as final state particles, after the event cleaning

lepton reconstruction. The jet energy resolution leads to a clear separation between massive bosons at di-jet events. The LCFIPlus algorithm could then distinguish b-jet, c-jet, and light-jet from each other.

A comprehensive analysis of the Higgs signal distributions shows that the SM Higgs signals are well established and have clean signatures. Based on the APODIS detector design, we characterize the Higgs signatures at the $e^+e^- \rightarrow \nu\nu Higgs$ events. The detector resolution could then be directly characterized by the mass resolution with Higgs $\rightarrow \mu\mu, \gamma\gamma$, and jet final states. Comparing to the LHC, the reconstruction accuracy at Higgs $\rightarrow \mu\mu$ events is improved by about one magnitude, and that at Higgs $\rightarrow$ di-jets events is improved by about 3 times. The resolution at Higgs $\rightarrow \gamma\gamma$ events degrades by roughly 30-60%, limited by the absence of geometry based correction and fine-tuned calibration, and the sampling fraction of ECAL, see Table 10.3.

To conclude, the baseline design fulfills the physics requirements discussed in Chapter 3.

References

[1] M. Ruan, *Shower fractal dimension analysis in a highly-granular calorimeter*, Journal of Physics: Conference Series **490** (2014) no. 1, 012227. http://stacks.iop.org/1742-6596/490/i=1/a=012227.

[2] D. Yu, M. Ruan, V. Boudry, and H. Videau, *Lepton identification at particle flow oriented detector for the future e^+e^- Higgs factories*, Eur. Phys. J. **C77** (2017) no. 9, 591, arXiv:1701.07542 [physics.ins-det].

Draft-v0.2

CHAPTER 11

BENCHMARK PHYSICS

Draft-v0.2

The historic discovery of a Higgs boson in 2012 by the ATLAS and CMS collaborations [1, 2] and the subsequent studies of the properties of the particle [3–9] indicate the compatibility with the Standard Model (SM) predictions. Although all of the particles in the SM have been discovered, some fundamental questions, e.g. vast difference between the Planck scale and the weak scale, the nature of electroweak phase transition have not been fully understood. The attempt to further address those questions will involve the new physics beyond the SM which could lead a deviation from SM expectations for the precision measurement of the SM. A circular electron positron collider will provide an unique opportunity to have precise measurements of the Higgs, W and Z properties.

The CEPC produces huge statistics of massive SM Bosons. Its physics potential is explored on two different classes of physics benchmarks, the Higgs physics, the precision EW physics. Using the software tools introduced in section 10.2, the physics potential on Higgs physics is analyzed at full simulation level, see section 11.1. The accuracies on the EW precision measurements are mainly limited by systematic errors and are estimated in section 11.2. The synergies of these different physics measurements, the complimentary and comparison to the HL-LHC and other high energy physics programs are discussed in Chapter 12.

References

[1] ATLAS Collaboration Collaboration, *Observation of a new particle in the search for the Standard Model Higgs boson with the ATLAS detector at the LHC*, Phys. Lett. B **716** (2012) 1, arXiv:1207.7214 [hep-ex].

[2] CMS Collaboration Collaboration, *Observation of a new boson at a mass of 125 GeV*

By Copyright © 2018 HEP Community

with the CMS experiment at the LHC, Phys. Lett. **B716** (2012) 30, arXiv:1207.7235 [hep-ex].

[3] ATLAS Collaboration, G. Aad et al., *Measurements of Higgs boson production and couplings in diboson final states with the ATLAS detector at the LHC*, Phys. Lett. **B726** (2013) 88–119, arXiv:1307.1427 [hep-ex]. [Erratum: Phys. Lett.B734,406(2014)].

[4] ATLAS Collaboration, G. Aad et al., *Evidence for the spin-0 nature of the Higgs boson using ATLAS data*, Phys. Lett. **B726** (2013) 120–144, arXiv:1307.1432 [hep-ex].

[5] CMS Collaboration Collaboration, S. Chatrchyan et al., *Observation of a new boson with mass near 125 GeV in pp collisions at* $\sqrt{s}$ *= 7 and 8 TeV*, JHEP **1306** (2013) 081, arXiv:1303.4571 [hep-ex].

[6] CMS Collaboration Collaboration, *Evidence for the direct decay of the 125 GeV Higgs boson to fermions*, Nature Phys. **10** (2014) , arXiv:1401.6527 [hep-ex].

[7] CMS Collaboration, V. Khachatryan et al., *Constraints on the spin-parity and anomalous HVV couplings of the Higgs boson in proton collisions at 7 and 8 TeV*, Phys. Rev. **D92** (2015) no. 1, 012004, arXiv:1411.3441 [hep-ex].

[8] ATLAS, CMS Collaboration, G. Aad et al., *Combined Measurement of the Higgs Boson Mass in* pp *Collisions at* $\sqrt{s} = 7$ *and 8 TeV with the ATLAS and CMS Experiments*, Phys. Rev. Lett. **114** (2015) 191803, arXiv:1503.07589 [hep-ex].

[9] ATLAS, CMS Collaboration, G. Aad et al., *Measurements of the Higgs boson production and decay rates and constraints on its couplings from a combined ATLAS and CMS analysis of the LHC pp collision data at* $\sqrt{s} = 7$ *and 8 TeV*, JHEP **08** (2016) 045, arXiv:1606.02266 [hep-ex].

Draft-v0.2

11.1 Higgs Boson Physics

At the CEPC, in contrast to the LHC, Higgs boson candidate events can be identified through a technique known as the recoil mass method without tagging its decays. Therefore, Higgs boson production can be disentangled from its decay in a model independent way. Moreover, the cleaner environment at a lepton collider allows much better exclusive measurement of Higgs boson decay channels. All of these give the CEPC impressive reach in probing Higgs boson properties. With a sample of over one million Higgs bosons produced in 5 ab^{-1} . the CEPC will be able to measure the Higgs boson coupling to the Z boson with an accuracy of 0.25% [update], more than a factor of 10 better than the High Luminosity (HL)-LHC. Such a precise measurement gives the CEPC unprecedented reach into interesting new physics scenarios which are very difficult to probe at the LHC. The CEPC also has strong capability in detecting Higgs boson invisible decay. For example, with 5 ab^{-1}, it can improve the accuracy of the measurement of invisible decay branching ratio to 0.14%. In addition, it is expected to have good sensitivities to exotic decay channels which are swamped by backgrounds at the LHC. It is also important to stress that an e^+e^- Higgs factory can perform *model independent* measurement of the Higgs boson width. This unique feature in turn allows for model independent determination of the Higgs boson couplings.

11.1.1 Higgs boson production and decay

Production processes for a 125 GeV SM Higgs boson at the CEPC are $e^+e^- \to ZH$ (ZH associate production or Higgsstrahlung), $e^+e^- \to \nu\bar{\nu}H$ (W fusion) and $e^+e^- \to e^+e^-H$ (Z fusion) as illustrated in Fig. 11.1. The W and Z fusion processes are collectively referred to as vector-boson fusion (VBF) production.

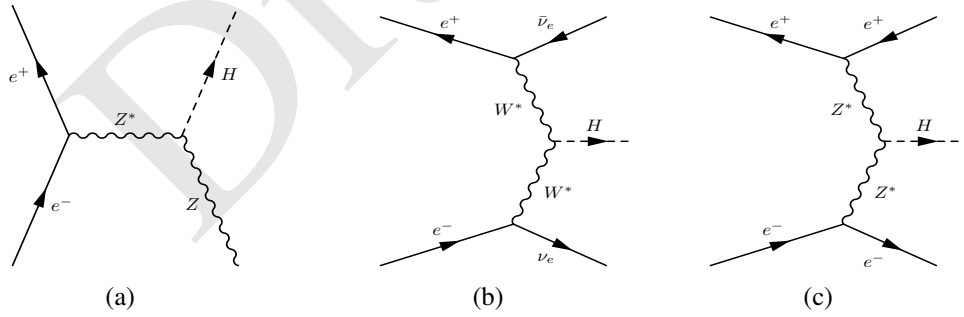

Figure 11.1: Feynman diagrams of the Higgs boson production processes at the CEPC: (a) $e^+e^- \to ZH$, (b) $e^+e^- \to \nu\bar{\nu}H$ and (c) $e^+e^- \to e^+e^-H$.

The total and individual cross sections for the production of a SM Higgs boson with a mass of 125 GeV as functions of center-of-mass energy are plotted in Fig. 11.2 while its decay branching ratios and total width are shown in Table **??**. As an s-channel process, the cross section of the $e^+e^- \to ZH$ process reaches its maximum at $\sqrt{s} \sim 250$ GeV, and then decreases asymptotically as $1/s$. The VBF production processes are through $t-$channel exchanges of vector bosons. Their cross sections increase logarithmically as $\ln^2(s/M_V^2)$. Because of the accidental small neutral-current Zee coupling, the VBF cross

section is dominated by the W fusion process. Numerical values of these cross sections at $\sqrt{s} = 240$ GeV are listed in Table 11.1.

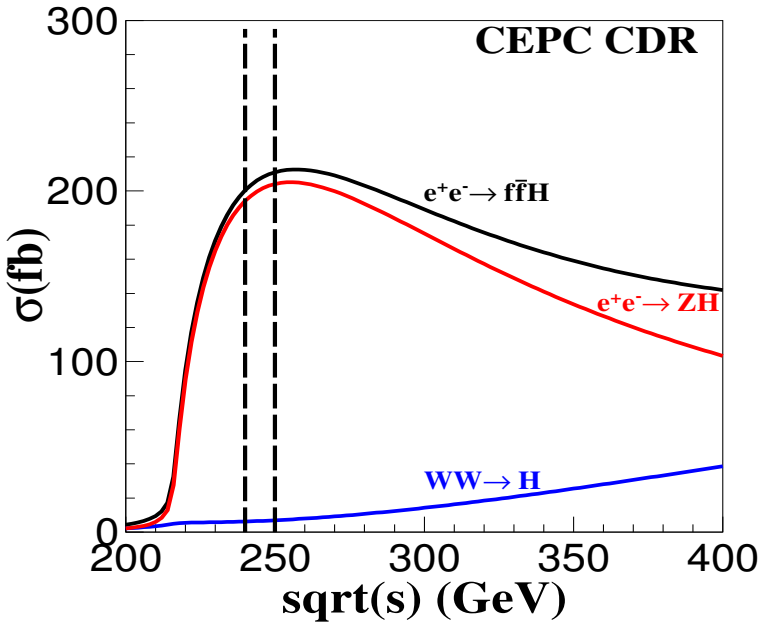

Figure 11.2: Production cross sections of $e^+e^- \to ZH$ and $e^+e^- \to (e^+e^-/\nu\bar{\nu})H$ as functions of $\sqrt{s}$ for a 125 GeV SM Higgs boson. Need polishing: the x-axis title should be "$\sqrt{s}$ [GeV]", adjust the y-axis title location etc., legends...

The CEPC as a Higgs boson factory is designed to deliver a total of 5 ab^{-1} integrated luminosity to two detectors in 7 years. Over 10^6 Higgs boson events will be produced during this period. The large statistics, well-defined event kinematics and clean collision environment will enable the CEPC to measure Higgs boson production cross sections as well as its properties (mass, decay width and branching ratios, etc.) with precision far beyond those achievable at the LHC. Compared with hadron collisions, e^+e^- collisions are unaffected by underlying event and pile-up effects. Theoretical calculations are less dependent on higher order QCD radiative corrections. Therefore, more precise tests of theoretical predictions can be performed at the CEPC. The tagging of $e^+e^- \to ZH$ events using the invariant mass of the system recoiling against the Z boson, independent of the Higgs boson decay, is unique to lepton colliders. It provides a powerful tool for the model-independent measurements of the inclusive $e^+e^- \to ZH$ production cross section, $\sigma(ZH)$, and of Higgs boson decay branching ratios. Combinations of these measurements will enable to determine the total Higgs boson decay width and to extract the Higgs boson couplings to fermions and vector bosons, providing sensitive probes to potential new physics beyond the SM.

SM background processes include $e^+e^- \to e^+e^-$ (Bhabha scattering), $e^+e^- \to Z\gamma$ (ISR return), $e^+e^- \to WW/ZZ$ (diboson) as well as the single boson production of $e^+e^- \to e^+e^-Z$ and $e^+e^- \to e^+\nu W^-/e^-\bar{\nu}W^+$. Their cross sections and expected numbers of events for an integrated luminosity of 5 ab^{-1} at $\sqrt{s} = 240$ GeV are shown in Table 11.1 as well. The energy dependence of the cross sections for these and the Higgs boson production processes are shown Fig. **??**. Note that many of these processes can lead to

Table 11.1: Cross sections of Higgs boson production and other SM processes at $\sqrt{s} = 250$ GeV and numbers of events expected in 5 ab^{-1}. The cross sections are calculated using the Whizard program [1]. Note that cross sections do not include potential interference effects between the same final states from different processes after W and Z boson decays (see text).

Process	Cross section	Events in 5 ab^{-1}
Higgs boson production, cross section in fb		
$e^+e^- \to ZH$	204.7	1.02×10^6
$e^+e^- \to \nu\bar{\nu}H$	6.85	3.43×10^4
$e^+e^- \to e^+e^-H$	0.63	3.15×10^3
Total	212.1	1.06×10^6
Background processes, cross section in pb		
$e^+e^- \to e^+e^-$ (Bhabha)	25.1	1.3×10^8
$e^+e^- \to q\bar{q}\,(\gamma)$	50.2	2.5×10^8
$e^+e^- \to \mu^+\mu^-\,(\gamma)$ [or $\tau^+\tau^-\,(\gamma)$]	4.40	2.2×10^7
$e^+e^- \to WW$	15.4	7.7×10^7
$e^+e^- \to ZZ$	1.03	5.2×10^6
$e^+e^- \to e^+e^-Z$	4.73	2.4×10^7
$e^+e^- \to e^+\nu W^-/e^-\bar{\nu}W^+$	5.14	2.6×10^7

identical final states and thus can interfere. For example, $e^+e^- \to e^+\nu_e W^- \to e^+\nu_e e^-\bar{\nu}_e$ and $e^+e^- \to e^+e^-Z \to e^+e^-\nu_e\bar{\nu}_e$ have the same final state. Unless otherwise noted, these processes are simulated together to take into account interference effects for the studies presented in this paper.

11.1.2 Higgs boson tagging

Unlike in hadron collisions, the energy of e^+e^- collisions is known. For a Higgsstrahlung event where the Z boson decays to a pair of visible fermions (ff), the mass of the system recoiling against the Z boson, commonly known as the recoil mass, can be calculated assuming the event has a total energy $\sqrt{s}$ and zero total momentum:

$$M^2_{\text{recoil}} = (\sqrt{s} - E_{ff})^2 - p^2_{ff} = s - 2E_{ff}\sqrt{s} + m^2_{ff}. \tag{11.1}$$

Here E_{ff}, p_{ff} and m_{ff} are, respectively, the total energy, momentum and invariant mass of the fermion pair. The M_{recoil} distribution should show a peak at the Higgs boson mass m_H for $e^+e^- \to ZH$ and $e^+e^- \to eeH$ processes, and is expected to be smooth without a resonance structure for background processes in the mass region around 125 GeV. Two important measurements of the Higgs boson can be performed from the M_{recoil} mass spectrum. The Higgs boson mass can be determined from the position of the resonance in the spectrum. The width of the resonance structure is dominated by the beam energy spread (including ISR effects) and energy/momentum resolution of the detector as the natural Higgs boson width is only 4.07 MeV. The best precision of the mass measurement can

Draft-v0.2

be achieved from the leptonic $Z \to \ell\ell\,(\ell = e, \mu)$ decays. The height of the resonance is a measure of the Higgs boson production cross section $\sigma(ZH)$[1]. By fitting the M_{recoil} spectrum, the $e^+e^- \to ZH$ event yield, and therefore $\sigma(ZH)$, can be extracted, independent of Higgs boson decays. Higgs boson decay branching ratios can then be determined by measuring the ZH cross sections for individual Higgs boson decay modes. The recoil mass spectrum has been investigated for both leptonic and hadronic Z boson decays as presented below.

Leptonic Z decay is ideal for studying the recoil mass spectrum of the $e^+e^- \to ZX$ events. The decay is easily identifiable and the lepton momenta can be precisely measured. Figure 11.3 shows the reconstructed recoil mass spectra of $e^+e^- \to ZX$ candidates for the $Z \to \mu\mu$ and $Z \to ee$ decay modes. The analyses are based on the full detector simulation for the signal events and on the fast detector simulation for background events. They are performed with event selections entirely based on the information of the two leptons, independent of the final states of Higgs boson decays. This approach is essential for the measurement of the inclusive $e^+e^- \to ZH$ production cross section and the model-independent determination of the Higgs boson branching ratios. SM processes with at least 2 leptons in their final states are considered as backgrounds. Leading background contributions after the selection are from ZZ, WW and $Z\gamma$ events. As shown in Fig. 11.3(a), the analysis has a good signal-to-background ratio. The long high-mass tail is largely due to the initial-state radiation. Compared to the analysis of the $Z \to \mu\mu$ decay, the analysis of the $Z \to ee$ decay suffers from additional and large background contributions from Bhabha and single boson production. The recoil mass distribution of the selected events is shown in Fig. 11.3 (b).

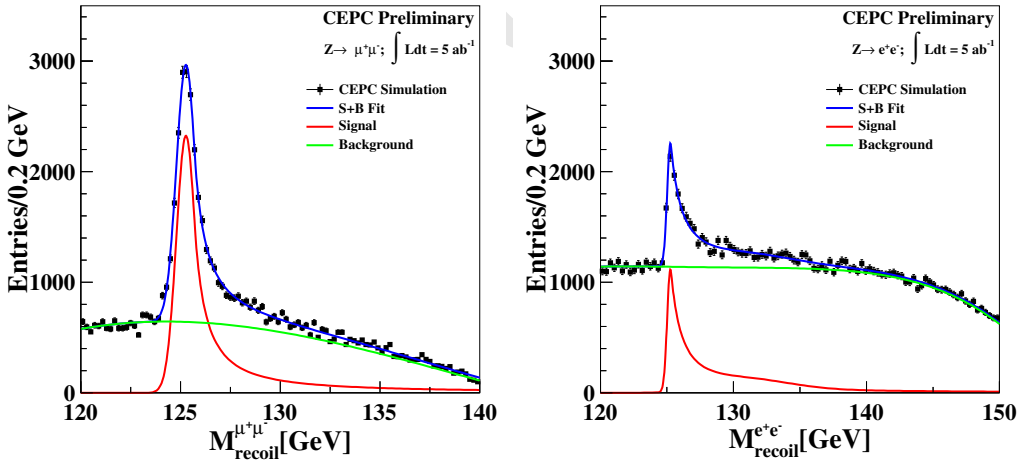

(a) (b)

Figure 11.3: The recoil mass spectra of $e^+e^- \to ZX$ candidates for (a) $Z \to \mu\mu$ and (b) $Z \to ee$ with an integrated luminosity of 5 ab^{-1}. Need update!

The recoil mass technique can also be applied to the hadronic Z boson decays ($Z \to q\bar{q}$) of the $e^+e^- \to ZX$ candidates. This analysis benefits from a larger $Z \to q\bar{q}$ decay

[1]For the $Z \to e^+e^-$ decay, there will be a small contribution from $e^+e^- \to e^+e^-H$ production.

branching ratio, but suffers from the fact that jet energy resolution is worse than the track momentum and electromagnetic energy resolutions. In addition, ambiguity in selecting jets from the $Z \to q\bar{q}$ decay, particularly in events with hadronic decays of the Higgs boson, can degrade the analysis performance and also introduce model-dependence to the analysis. Therefore, the measurement is highly dependent on the performance of the PFA and the jet clustering algorithm. Following the same approach as the ILC study [2], an analysis based on the fast simulation has been performed. After the event selection, main backgrounds arise from $Z\gamma$'s and WW production. Figure 11.4 shows the reconstructed recoil mass distribution. Compared with the leptonic decays, the signal-to-background ratio is considerably worse and the recoil mass resolution is significantly poorer.

Event selections independent of Higgs boson decays are essential for the model-independent measurement of $\sigma(ZH)$. Additional selections using the Higgs boson decay information can, however, be applied to improve the Higgs boson mass measurement. This will be particularly effective in suppressing the large backgrounds from Bhabha scattering and single W or Z boson production for the analysis of the $Z \to ee$ decay. This improvement is not implemented in the current study.

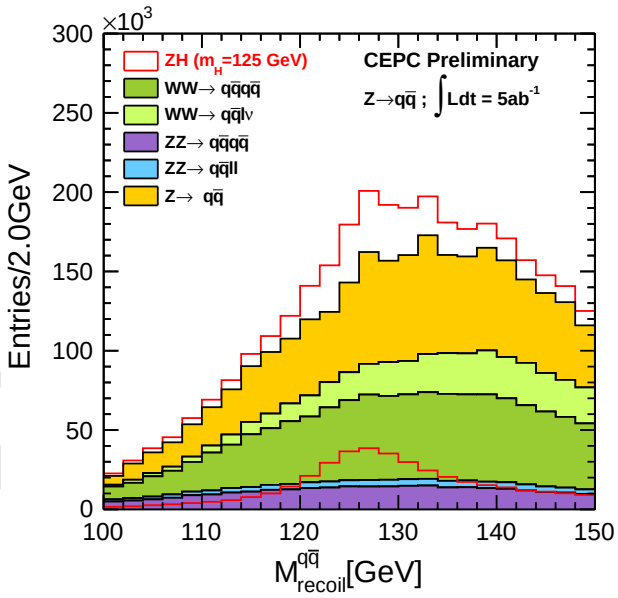

Figure 11.4: The recoil mass spectrum of the $e^+e^- \to ZX$ candidates in the $Z \to q\bar{q}$ decay channel for 5 ab^{-1} integrated luminosity.

11.1.3 Measurements of $\sigma(ZH)$ and m_H

The inclusive $e^+e^- \to ZH$ production cross section $\sigma(ZH)$ and Higgs boson mass m_H can be extracted from fits to the recoil mass distributions of the $e^+e^- \to Z + X \to \ell^+\ell^-/q\bar{q} + X$ candidates (Figs. 11.3, 11.4). For the leptonic $Z \to \ell\ell$ decays, the recoil mass distribution of the signal process $e^+e^- \to ZH$ (and $e^+e^- \to e^+e^-H$ in case of the $Z \to e^+e^-$ decay) is modeled with a Crystal Ball function [**?**] whereas the total background is modeled with a polynomial function in the fit. As noted above, the recoil

mass distribution is insensitive to the intrinsic Higgs boson width if it were as small as predicted by the SM. The Higgs boson mass can be determined with precision of 6.5 MeV and 14 MeV from the $Z \to \mu\mu$ and $Z \to ee$ decay modes, respectively. In combination, an uncertainty of 5.9 MeV can be achieved. $e^+e^- \to Z + X \to q\bar{q} + X$ events contribute little to the precision of the m_H measurement due to the poor $Z \to q\bar{q}$ mass resolution, but dominates the precision of the $e^+e^- \to ZH$ cross section measurement benefiting from its large statistics. A relative precision of 0.65% of $\sigma(ZH)$ is predicted from a simple event counting analysis. In comparison, the corresponding precision from the $Z \to ee$ and $Z \to \mu\mu$ decays is estimated to be 2.1% and 0.9%, respectively. The combined precision of the three measurements is 0.5%.

11.1.4 Analyses of individual Higgs boson decay modes

Different decay modes of the Higgs boson can be identified through their unique signatures, leading to the measurements of production rates for these decays. For the $e^+e^- \to ZH$ production process in particular, the candidate events can be tagged from the visible decays of the Z bosons, the Higgs boson decays can then be probed by studying the rest of the events. These measurements combined with the inclusive $\sigma(ZH)$ measurement discussed above will permit the extraction of the Higgs boson decay branching ratios in a model-independent way. With the reliable performances of the physics objects described in Section 10.3, the analyses for individual channels are implemented and the precision measurements of $\sigma(ZH) \times \mathrm{BR}$ are extracted with an integrated luminosity of 5 ab^{-1}.

Discuss more final states that are difficult at LHC, for example, $H \to c\bar{c}$ and $H \to \gamma\gamma$... For Higgs decaying into two jets, four Z decay modes $Z \to ee, \mu^+\mu^-, qq, \nu\nu$ are taken into account for the analyses. Multivariate variables based on the secondary decay vertex are implemented to separate b, c and light jets. Combining all Z boson decay channels, a relative statistical precision for $\sigma(ZH) \times \mathrm{BR}$ of 0.3%, 3.5% and 1.4% can be achieved for the $H \to b\bar{b}$, $c\bar{c}$ and gg decays, respectively.

For $H \to WW^*$ decay, the statistical dominant subchannels $Z \to \nu\bar{\nu}H \to WW^* \to \ell\nu q\bar{q}, q\bar{q}q\bar{q}$ and $Z \to q\bar{q}H \to WW^* \to q\bar{q}q\bar{q}$ provide the highest precision which are 1.8% and 1.9% respectively. The other two subleading channels taking into account are $Z \to eeH \to WW^* \to \ell\nu\ell'\nu$, $\ell\nu q\bar{q}$ and $Z \to \mu\mu H \to WW^* \to \ell\nu\ell'\nu$, $\ell\nu q\bar{q}$ and the corresponding precisions are 3.0% and 2.7%. Finally, the combined precision for $H \to WW^*$ can reach 1.0% after combining all of the four subchannels.

For $H \to ZZ^*$, studies are performed for a few selected ZH final states: $Z \to ee$ and $H \to ZZ^* \to \ell^+\ell^- q\bar{q}$, $Z \to \mu\mu$ and $H \to ZZ^* \to \nu\bar{\nu}q\bar{q}$, $Z \to \nu\bar{\nu}$ and $H \to ZZ^* \to \ell^+\ell^- q\bar{q}$. The W and Z boson fusion processes, $e^+e^- \to e^+e^-H$ and $e^+e^- \to \nu\bar{\nu}H$, are included in the $Z(e^+e^-)H$ and $Z(\nu\bar{\nu})H$ studies assuming their SM values for the rates. For all the final states, the SM ZZ production is the main background which is also small for all of the final states. The combination of different final states, mainly from $H \to ZZ^*H \to ZZ^* \to \nu\bar{\nu}q\bar{q}$ and $Z \to \nu\bar{\nu}H \to ZZ^* \to \ell^+\ell^- q\bar{q}$ leads to a sensitivity of 5.2% for the expected precision on $\sigma(ZH) \times \mathrm{BR}(H \to ZZ^*)$.

Four different Z boson decay modes: $Z \to \mu\mu$, $\tau^+\tau^-$, $\nu\bar{\nu}$ and $q\bar{q}$, except $Z \to ee$ decay due to large background from Bhabha process, are considered for $H \to \gamma\gamma$ studies. Selections on the kinematic variables and angular variables for photons and photon lepton system are implement to suppress backgrounds. With an energy resolution of $16\%/\sqrt{E} \oplus 1\%$ for the electromagnetic calorimeter, a relative precision of 7.4% on $\sigma(ZH) \times \mathrm{BR}(H \to$

Draft-v0.2

$\gamma\gamma$) can be achieved using a two dimensional fit on the mass (Fig. 11.5 (a) shows the invariant mass distribution for di-photon for the decay mode of $Z \to \nu\bar{\nu}$) and the recoil mass of the di-photon.

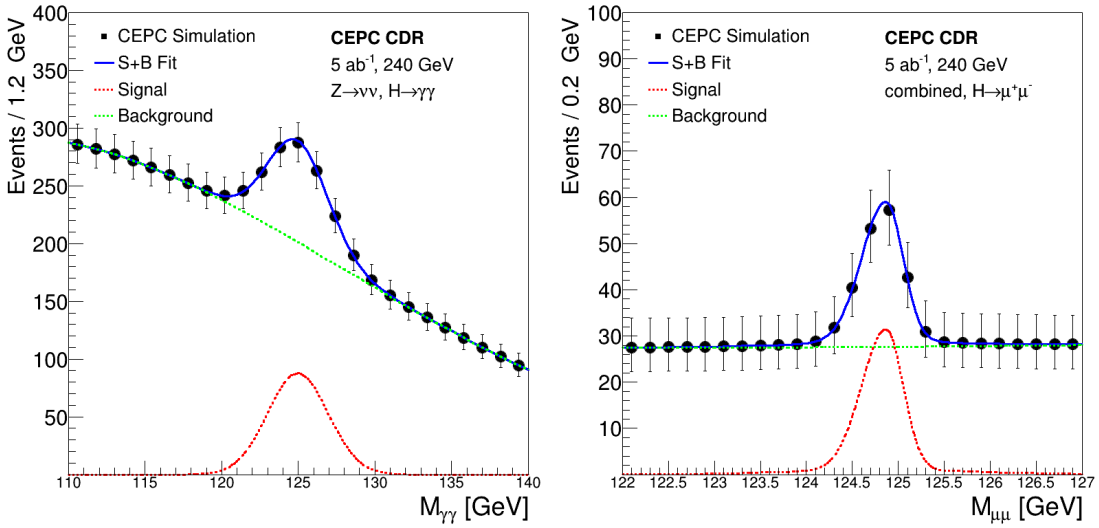

(a) (b)

Figure 11.5: (a) ZH production with $H \to \gamma\gamma$: the diphoton invariant mass distribution for the $Z \to \nu\bar{\nu}$ decay. (b)ZH production with the $H \to \mu^+\mu^-$ decay: dimuon invariant mass distribution of the selected $H \to \mu^+\mu^-$ candidates. The distribution combines contributions from $Z \to \ell\ell$, $Z \to \nu\bar{\nu}$, and $Z \to q\bar{q}$ decays. For both plots, the solid curve is the fit results and the dashed curves are the signal and background components. In addition, the markers and their uncertainties in (a) and (b) represent expectations from a CEPC dataset of 5 ab^{-1}.

The $H \to Z\gamma$ analysis targets the signal process of $ZH \to ZZ\gamma \to \nu\bar{\nu}q\bar{q}\gamma$, in which one of the Z bosons decays into a pair of quarks and the other decays into a pair of neutrinos. The mass differences $\mathrm{dMass} = M_{q\bar{q}\gamma} - M_{q\bar{q}}$ and $\mathrm{dMass} = M_{\nu\bar{\nu}\gamma} - M_{\nu\bar{\nu}}$, are calculated are computed as a discriminating variable to extract the signal yield with the implementation of a likelihood fit. A relative precision of 19% on $\sigma(ZH) \times \mathrm{BR}(H \to Z\gamma)$, equivalently a statistical significance of 4σ can be reached.

Simulation studies are performed for the $e^+e^- \to ZH$ production with $H \to \tau^+\tau^-$ and $Z \to \mu^+\mu^-, \nu\bar{\nu}$ and $q\bar{q}$ decays. For $Z \to \mu\mu$ and $Z \to \nu\bar{\nu}$, a BDT selection based on the information of numbers of tracks and photons and the angles between them etc.., are applied to identify di-tau candidates. The signal yields are finally extracted from fits to the distributions of variables based on the impact parameters of the leading tracks of the two tau candidates as shown in Fig. 11.6. The estimated precision on $\sigma(ZH) \times \mathrm{BR}(H \to \tau^+\tau^-)$ expected for $Z \to \mu^+\mu^-, \nu\bar{\nu}$ and $q\bar{q}$ decay modes studied are 2.8%, 2.8% and 1.0% respectively. The extrapolated precision for $Z \to e^+e^-$ from $Z \to ee$ decay mode is 2.9%. The combination of these 4 decay modes results in the expected relative precision 0.87% for the $\sigma(ZH) \times \mathrm{BR}(H \to \tau^+\tau^-)$.

Studies are performed for the $ZH \to \mu\mu$ production with the Z decay modes: $Z \to \ell\ell$, $Z \to \nu\bar{\nu}$, and $Z \to q\bar{q}$. For the statistical dominant subchannel $Z \to q\bar{q}H \to \mu\mu$, a BDT is used to optimize the analysis. Because $m_{\mu\mu}$ has a very descent resolution, a maximum likelihood fit on the $m_{\mu\mu}$ mass spectrum (Fig. 11.5 (b)) is applied to extract the

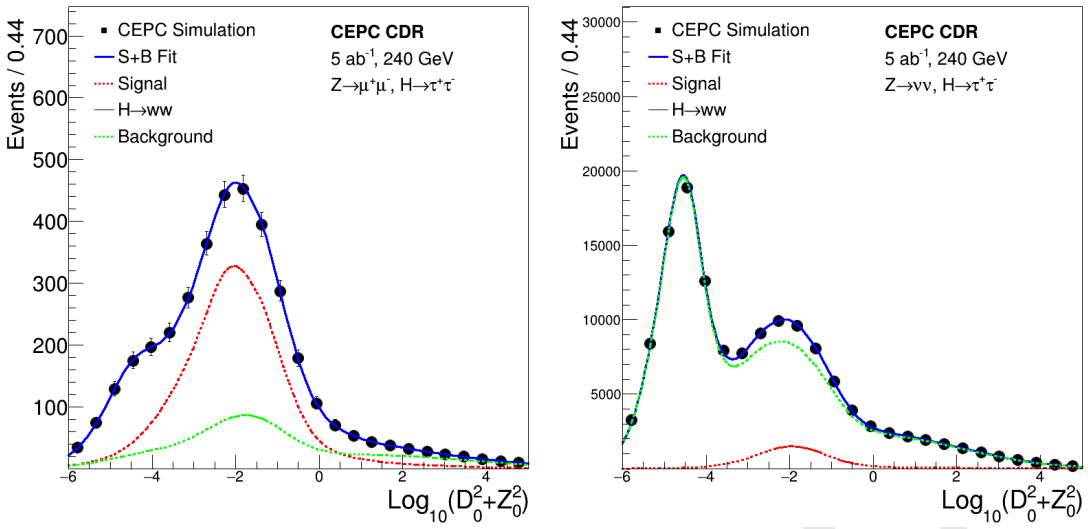

(a) (b)

Figure 11.6: Distributions of the impact parameter variable of the leading tracks from the two tau candidates in the Z decay mode: (a) $Z \to \mu\mu$ and (b) $Z \to \nu\bar{\nu}$.

signal strength for all channel, leading to the estimated combined relative precision on the $\sigma(ZH) \times \mathrm{BR}(H \to \mu^+\mu^-)$ measurement about 16.8%.

The $H \to ZZ^* \to \nu\bar{\nu}\nu\bar{\nu}$ decay is used to as a benchmark to model the $H \to$ inv decay in both the SM and its extensions. After the pre-selections, a BDT selection on the kinematics is implemented to further separate the signal from background. The expected precision for the the $\mathrm{BR}(H \to \mathrm{inv})$ is $(0.11 \pm 0.18)\%$ with the contributions of $(0.11 \pm 0.38)\%$,$(0.11 \pm 0.28)\%$ and $(0.11 \pm 0.26)\%$ from the $Z \to ee\mu^+\mu^-, and q\bar{q}$ modes respectively.

The production of the cross section of W-fusion process and the branching ratio $\mathrm{BR}(H \to b\bar{b})$ is crucial for the model independent determination of the Higgs width. Same multivariate variables as $ZH(H \to b\bar{b})$ analysis are used to identify b quark. In order to separate $\nu\bar{\nu}H$ and $Z(\nu\bar{\nu})H$ contributions, a 2-dimensional fit in the plane of the recoil mass and polar angle of the $b\bar{b}$ system is performed, which leads to relative precision of 3.2% for $\sigma(\nu\bar{\nu}H) \times \mathrm{BR}(H \to b\bar{b})$ and 0.32% for $\sigma(ZH) \times \mathrm{BR}(H \to b\bar{b})$.

More description of the analysis strategies, selections and results of the current CEPC simulation studies of different Higgs boson decay modes are documented in detail in [3], where the baseline detector geometry CEPC v_1 is used. The impacts of the migration of detector geometry from CEPC v_1 to CEPC v_4 are discussed in [3] and Chapter 10. The change of the magnetic field from 3.5T to 3T mainly causes a 17% degradation of the resolution of the Higgs mass for the channel of di-muon decay. These effects together with the variation of the cross section from 250 GeV to 240 GeV on the precision measuremnts for individual channels are small, mostly at the level of a few percent.

For the study of a specific Higgs boson decay mode, the other decay modes of the Higgs boson often contribute as well. These contributions are fixed to their SM expectations unless otherwise noted. However for the combination of all decay modes studied, they are allowed to vary within the constraints of the measurements of those decays. In addition to the invariant and recoil mass, two other mass observables, visible mass and

missing mass, are often used in analyses described below. They are defined, respectively, as the invariant mass and recoil mass of all visible particles such as charged leptons, photons and jets, *i.e.* practically all particles other than neutrinos.

Though the current study covers a large number of final states of the ZH production, there are many remain to be studied. The sensitivities of some important missing final states are obtained by extrapolating from the ILC and FCC-ee studies [4, 5] whenever possible. The extrapolation assumes the same signal and background selection efficiencies, but takes into account differences such as beam polarization conditions. The expected yields for the signal and background processes are scaled to an integrated luminosity of 5 ab^{-1}.

11.1.5 Combination of individual analyses

Suggest to combine with the above section into one on the Higgs boson branching ratio measurements With the measurements of inclusive cross section $\sigma(ZH)$ and the cross sections of individual Higgs boson decay mode $\sigma(ZH) \times \mathrm{BR}$, the Higgs boson decay branching ratio, BR, can be extracted. Most of the systematic uncertainties associated with the measurement of $\sigma(ZH)$ cancels in this procedure. A maximum likelihood fit is used to estimate the precision on BRs. For a given Higgs boson decay mode, the likelihood has the form:

$$L(\mathrm{BR}, \theta) = \mathrm{Poisson}\left[N^{\mathrm{obs}} \middle| N^{\mathrm{exp}}(\mathrm{BR}, \theta)\right] \cdot G(\theta), \tag{11.2}$$

where BR is the parameter of interest and θ represent nuisance parameters associated with systematic uncertainties. N^{obs} is the number of the observed events, $N^{\mathrm{exp}}(\mathrm{BR}, \theta)$ is the expected number of events, and $G(\theta)$ is a set of constraints on the nuisance parameters within their estimated uncertainties. The number of expected events is the sum of signal and background events. The number of signal events is calculated from the integrated luminosity, the $e^+e^- \to ZH$ cross section $\sigma(ZH)$ measured from the recoil method, Higgs boson branching ratio BR, the event selection efficiency ϵ. The number of the expected background events, N^b, is estimated from Monte Carlo samples. Thus

$$N^{\mathrm{exp}}(\mathrm{BR}, \theta) = \mathrm{Lumi}(\theta^{\mathrm{lumi}}) \times \sigma_{ZH}(\theta^{\sigma}) \times \mathrm{BR} \times \epsilon(\theta^{\epsilon}) + N^b(\theta^b), \tag{11.3}$$

where θ^X ($X = \mathrm{lumi}, \sigma$, ϵ and b) are the nuisance parameters of their corresponding parameters or measurements. Even with 10^6 Higgs boson events, statistical uncertainties are expected to be dominant and thus systematic uncertainties are not taken into account for the current studies. Thus the nuisance parameters are fixed to their nominal values.

For the individual analyses discussed in Section 11.1.4, contaminations from Higgs boson production or decays other than the one under study are fixed to their SM values for simplicity. In the combination, however, these constraints are removed and the contaminations are constrained only by the analyses targeted for their measurements. For example, the $H \to b\bar{b}$, $c\bar{c}$, gg analysis suffers from contaminations from the $H \to WW^*, ZZ^* \to q\bar{q}q\bar{q}$ decays. For the analysis discussed in Section **??**, these contaminations are estimated from SM. In the combination fit, they are constrained by the $H \to WW^*$ and $H \to ZZ^*$ analyses described in Sections **??** and **??**, respectively. Taking into account these across-channel contaminations properly generally leads to small improvements in precision. For

Draft-v0.2

example, the precision on $\sigma(ZH) \times \mathrm{BR}(H \to ZZ^*)$ is improved from 5.4% of the standalone analysis to 5.1% from the combination.

Table 11.2: Estimated precision of Higgs boson property measurements for the CEPC-v1 detector concept operating at $\sqrt{s} = 250$ GeV. All precision are relative except for m_H and $\mathrm{BR_BSM}(H \to \mathrm{inv})$ for which Δm_H and 95% CL upper limit are quoted respectively. The extrapolated precision for the CEPC-v4 concept operating at $\sqrt{s} = 240$ GeV are included for comparisons, see Section **??**.

Property	Estimated Precision	
	CEPC-v1	CEPC-v4
m_H	5.9 MeV	
Γ_H	3.2%	3.3%
$\sigma(ZH)$	0.50%	0.50%
$\sigma(\nu\bar{\nu}H)$	3.05%	3.20%
Decay mode	$\sigma(ZH) \times \mathrm{BR}$	
$H \to b\bar{b}$	0.28%	0.29%
$H \to c\bar{c}$	3.27%	3.45%
$H \to \gamma\gamma$	1.28%	1.37%
$H \to \tau^+\tau^-$	0.83%	0.87%
$H \to \mu^+\mu^-$	15.9%	16.8%
$H \to WW^*$	1.00%	1.04%
$H \to ZZ^*$	5.12%	5.21%
$H \to \gamma\gamma$	6.66%	7.38%
$H \to Z\gamma$	21%	21%
$\mathrm{BR_{BSM}}(H \to \mathrm{inv})$	$< 0.31\%$	$< 0.33\%$

Table 11.2 summarizes the estimated precision of Higgs boson property measurements, combining all studies described in this paper. For the leading Higgs boson decay modes, namely $b\bar{b}$, $c\bar{c}$, gg, WW^*, ZZ^* and $\tau^+\tau^-$, percent level precision are expected. The best achievable statistical uncertainties for 5 ab^{-1} are 0.28% for $\sigma(e^+e^- \to ZH) \times \mathrm{BR}(H \to b\bar{b})$ and 0.5% for $\sigma(e^+e^- \to ZH)$. Even for these measurements, statistics is likely the dominant source of uncertainties. Systematic uncertainties from the efficiency/acceptance of the detector, the luminosity and the beam energy determination are expected to be small. The integrated luminosity can be measured with a 0.1% precision, a benchmark already achieved at the LEP [6], and can be potentially improved in the future. The center-of-mass energy will be known better than 1 MeV, resulting negligible uncertainties on the theoretical cross section predictions and experimental recoil mass measurements.

Draft-v0.2

11.1.6 Higgs boson width

The Higgs boson width (Γ_H) is of special interest as it is sensitive to BSM physics in Higgs boson decays that are not directly detectable or searched for. However, the 4.07 MeV width predicted by the SM is too small to be measured with a reasonable precision from the distributions of either the invariant mass of the Higgs boson decay products or the recoil mass of the system produced in association with the Higgs boson. Unique to lepton colliders, the width can be determined from the measurements of Higgs boson production cross sections and its decay branching ratios. This is because the inclusive $e^+e^- \to ZH$ cross section $\sigma(ZH)$ can be measured from the recoil mass distribution, independent of Higgs boson decays.

Measurements of $\sigma(ZH)$ and BR's have been discussed in Sections 11.1.2 and 11.1.4. Combining these measurements, the Higgs boson width can be calculated in a model-independent way:

$$\Gamma_H = \frac{\Gamma(H \to ZZ^*)}{\mathrm{BR}(H \to ZZ^*)} \propto \frac{\sigma(ZH)}{\mathrm{BR}(H \to ZZ^*)} \tag{11.4}$$

Here $\Gamma(H \to ZZ^*)$ is the partial width of the $H \to ZZ^*$ decay. Because of the small expected $\mathrm{BR}(H \to ZZ^*)$ value for a 125 GeV Higgs boson (2.64% in the SM), the precision of Γ_H is limited by the $H \to ZZ^*$ statistics. It can be improved using the decay final states with the expected large BR values, for example the $H \to b\bar{b}$ decay:

$$\Gamma_H = \frac{\Gamma(H \to b\bar{b})}{\mathrm{BR}(H \to b\bar{b})} \tag{11.5}$$

$\Gamma(H \to b\bar{b})$ can be independently extracted from the cross section of the W fusion process $e^+e^- \to \nu\bar{\nu}H \to \nu\bar{\nu}\,b\bar{b}$:

$$\sigma(\nu\bar{\nu}H \to \nu\bar{\nu}\,b\bar{b}) \propto \Gamma(H \to WW^*) \cdot \mathrm{BR}(H \to b\bar{b}) = \Gamma(H \to b\bar{b}) \cdot \mathrm{BR}(H \to WW^*) \tag{11.6}$$

Thus the Higgs boson total width

$$\Gamma_H = \frac{\Gamma(H \to b\bar{b})}{\mathrm{BR}(H \to b\bar{b})} \propto \frac{\sigma(\nu\bar{\nu}H \to \nu\bar{\nu}\,b\bar{b})}{\mathrm{BR}(H \to b\bar{b}) \cdot \mathrm{BR}(H \to WW^*)} = \frac{\sigma(e^+e^- \to \nu\bar{\nu}H)}{\mathrm{BR}(H \to WW^*)} \tag{11.7}$$

Here $\mathrm{BR}(H \to b\bar{b})$ and $\mathrm{BR}(H \to WW^*)$ are measured from the $e^+e^- \to ZH$ process. The limitation of this method is the precision of the $\sigma(e^+e^- \to \nu\bar{\nu}H \to \nu\bar{\nu}\,b\bar{b})$ measurement.

The expected precision on Γ_H is 5.1% from the measurements of $\sigma(ZH)$ and $\mathrm{BR}(H \to ZZ^*)$ and is 3.4% from the measurements of $\sigma(\nu\bar{\nu}H \to \nu\bar{\nu}b\bar{b})$, $\mathrm{BR}(H \to b\bar{b})$ and $\mathrm{BR}(H \to WW^*)$. The former is dominated by the precision of the $\mathrm{BR}(H \to ZZ^*)$ measurement while the latter by the $\sigma(\nu\bar{\nu}H \to \nu\bar{\nu}b\bar{b})$ measurement. The combined Γ_H precision of the two measurements is 3.2%, taking into account correlations between the two measurements.

11.1.7 Higgs Boson Coupling Measurements

To understand the implications of the predicted measurement precision shown in Table 11.2 on possible new physics models, one would need to translate them into constraints

Draft-v0.2

on the parameters in the Lagrangian. This is frequently referred to as Higgs boson coupling measurement, even though this way of phrasing it can be misleading as discussed in the following.

There are different ways of presenting the constraints. Before going into CEPC results, we briefly comment on the reasons behind choices of schemes in this section. First, the goal of theory interpretation is different from analyzing actual data, where a lot of detailed work will be done to derive the extended sets of observables. Instead, obtaining a broad brushed big picture of the basic capability of the Higgs boson coupling measurement at the CEPC is the goal. Ideally, the presentation would be simple with a intuitive connection with the observables. The presentation would ideally also be free of underlying model assumptions. In addition, it would be convenient if the result presentation can be interfaced directly with higher order computations, RGE evolutions, and so on. However, achieving all of these goals simultaneously is not possible. Two of the most popular and balanced approaches are the so-called κ-framework and the Effective Field Theory (EFT) analysis. As discussed in more detail later, none of these is perfect. At the same time, neither of these is wrong as long as one is careful not to over interpreting the result. Another important aspect of making projections on the physics potential of a future experiment is that they will be compared with other possible future experiments. Hence, CEPC follows the most commonly used approaches to facilitate such comparisons.

Motivated by these arguments, in the following, CEPC presents the projections using both the κ-framework and EFT approach. In the later part of this section, Higgs physics potential beyond coupling determination will be discussed.

11.1.7.1 Coupling fits in the κ-framework

The Standard Model makes specific predictions for the Higgs boson couplings to the SM fermions, $g(Hff;\mathrm{SM})$, and to the SM gauge bosons $g(HVV;\mathrm{SM})$. [2] In the κ-framework, the potential deviations are parameterized by

$$\kappa_f = \frac{g(Hff)}{g(Hff;\mathrm{SM})}, \quad \kappa_V = \frac{g(HVV)}{g(HVV;\mathrm{SM})}, \tag{11.8}$$

with $\kappa_i = 1$ indicating agreement with the SM prediction.

In addition to couplings which are present at tree level, the Standard Model also predicts effective couplings $H\gamma\gamma$ and Hgg, in terms of other SM parameters. Changes in the gluon and photon couplings can be induced by the possible shifts in the Higgs boson couplings described above. In addition, these couplings can also be altered by loop contributions from new physics states. Hence, these couplings will be introduced as two independent couplings, with their ratios to the SM predictions denoted as κ_γ and κ_g.

Furthermore, it is possible that the Higgs boson can decay directly into new physics particles. In this case, two type of new decay channels will be distinguished:

1. Invisible decay. This is a specific channel in which Higgs boson decay into invisible particles. This can be searched for and, if detected, measured.

2. Exotic decay. This includes all the other new physics channels. Whether they can be observed, and, if so, to what precision, depends sensitively on the particular final states. In one extreme, they can be very distinct and can be measured very well. In

[2] For the discussion of coupling fits and their implications, "H" is used to denoted the 125 GeV Higgs boson.

another extreme, they can be in a form which is completely swamped by the background. Whether postulating a precision for the measurement of the exotic decay or treating it as an independent parameter (essentially assuming it can not be measured directly) is an assumption one has to make. In the latter case, it is common to use the total width Γ_H as an equivalent free parameter.[3]

In general, possible deviations of all Standard Model Higgs boson couplings should be considered. However, in the absence of obvious light new physics states with large couplings to the Higgs boson and other SM particles, a very large deviation ($> \mathcal{O}(1)$) is unlikely. In the case of smaller deviations, the Higgs boson phenomenology will not be sensitive to the deviations [**?**]κ_e, κ_u, κ_d and κ_s. Therefore, they will not be considered here and set to be their SM values.

The CEPC will not be able to directly measure the Higgs boson coupling to top quarks. A deviation of this coupling from its SM value does enter $H\gamma\gamma$ and Hgg amplitudes. However, this can be viewed as parametrized by κ_γ and κ_g already. Therefore, we will not include κ_t as an independent parameter. Hence, the following set of 10 independent parameters is considered:

$$\kappa_b,\ \kappa_c,\ \kappa_\tau,\ \kappa_\mu,\ \kappa_Z,\ \kappa_W,\ \kappa_\gamma,\ \kappa_g,\ \mathrm{BR}_{\mathrm{inv}},\ \Gamma_H. \tag{11.9}$$

Several assumptions can be made that can lead to a reduced number of parameters (see also [7, 8]). It can be reduced to a 7-parameter set, by assuming lepton universality, and the absence of exotic and invisible decays (excluding $H \to ZZ^* \to \nu\bar{\nu}\nu\bar{\nu}$) [7, 9]:

$$\kappa_b,\ \kappa_c,\ \kappa_\tau = \kappa_\mu,\ \kappa_Z,\ \kappa_W,\ \kappa_\gamma,\ \kappa_g. \tag{11.10}$$

This is useful for hadron collider studies since it can not measure the Higgs boson total width with precision; it is more useful for models in which this assumption is satisfied.

There are some pros and cons of the κ-framework. κ_is give a simple and intuitive parameterization of potential deviations. It has a direct connection with the observables shown in Table 11.2. It does cover a lot of possible modifications of the coupling. At the same time, κ-framework has its limitations. Strictly speaking, it should not be understood as modifying the SM renormalizable Lagrangian by a multiplicative factor. For instance, individual κ modifications violates gauge invariance. The higher order corrections in the κ framework is not easily defined. κ_is do not summarize all possible effects of new physics neither. For example, in addition to the overall size, potential new physics can also introduce form factors which can change the kinematics of particles connected to a vertex. Manifestations of this effect will be seen in the discussion of the EFT approach. It is useful to pause here and compare with the EFT scheme introduced in detail in the next subsection. The EFT scheme relates κ_Z and κ_W, and further expanse them into three different Lorentz structures. In addition, some of these higher dimensional HVV coupling are also in connection with κ_γ and anomalous trilinear gauge couplings. The current EFT scheme does not include important new degree of freedom $\mathrm{BR}_{\mathrm{inv}}$ and Γ_H as independent parameters. Overall, κ-framework does capture the big picture of the capability of precision Higgs boson measurement at CEPC. It is useful as long as we understand its limitation.

The LHC and especially the HL-LHC will provide valuable and complementary information about the Higgs boson properties. For example, the LHC is capable of directly

[3]Total width is a very useful parameter in understanding and deriving parameter precisions in the κ-scheme.

Draft-v0.2

measure the ttH process [10, 11]. In addition, the LHC could use differential cross sections to differentiate top-loop contributions and other heavy particle-loop contributions to the Higgs boson to gluon coupling [12–15], and similarly to separate contributions from different operators to the Higgs boson to vector boson couplings [16]. For the purpose of the coupling fit in the κ-framework, the LHC with its large statistics, helps improving precision on rare processes such as Higgs to diphoton couplings. Note that a large portion of the systematics intrinsic to a hadron collider would be canceled by taking ratios of measured cross sections. For example, combining the ratio of the rates $pp \to H \to \gamma\gamma$ and $pp \to H \to ZZ^*$ and the measurement of HZZ coupling at the CEPC can significantly improve the measurement of κ_γ. These are the most useful inputs from the LHC to combine with the CEPC. Similar studies of combination with the LHC for the ILC can be found in Refs. [17–21].

Table 11.3: Coupling measurement precision in percentage from the 7-parameter fit and 10-parameter fit described in the text for the CEPC, and corresponding results after combination with the HL-LHC. All the numbers refer to are relative precision except for $\mathrm{BR}_{\mathrm{inv}}^{\mathrm{bsm}}$ of beyond standard model for which 95% CL upper limit are quoted respectively. Some entries are left vacant for the 7-parameter fit to stress them being dependent parameter under the fitting assumptions of the 7-parameter fit scheme.

	10-parameter fit		7-parameter fit	
	CEPC	+HL-LHC	CEPC	+HL-LHC
Γ_H	3.4	2.6	–	–
κ_b	1.7	1.3	1.6	1.2
κ_c	2.4	2.0	2.3	2.0
κ_g	1.7	1.3	1.7	1.3
κ_W	1.5	1.1	1.5	1.1
κ_τ	1.6	1.2	1.6	1.2
κ_Z	0.25	0.25	0.16	0.16
κ_γ	4.3	1.7	4.2	1.7
κ_μ	8.6	5.0	–	–
$\mathrm{BR}_{\mathrm{inv}}^{\mathrm{bsm}}$	0.31	0.31	–	–

The 10-parameter fit and the 7-parameter fit for CEPC with integrate luminosity of $5\ \mathrm{ab}^{-1}$ are shown in Table 11.3. In addition, the combinations with expectations (optimistically assuming no theoretical uncertainties) from the HL-LHC from Ref. [22] are shown in the same tables as well.[4] We assume the HL-LHC will operate at 14 TeV center-of-mass energy and accumulate an integrated luminosity of 3000 fb^{-1}.

The CEPC Higgs boson properties measurements mark a giant step beyond the HL-LHC. First of all, in contrast to the LHC, a lepton collider Higgs factory is capable of measuring the absolute width and coupling strengths of the Higgs boson. A comparison with the HL-LHC is only possible with model dependent assumptions. One of such com-

[4]We note here that the LHC and the CEPC have different sources of theoretical uncertainties, for detailed discussion, see Refs. [8, 9, 23–25].

Draft-v0.2

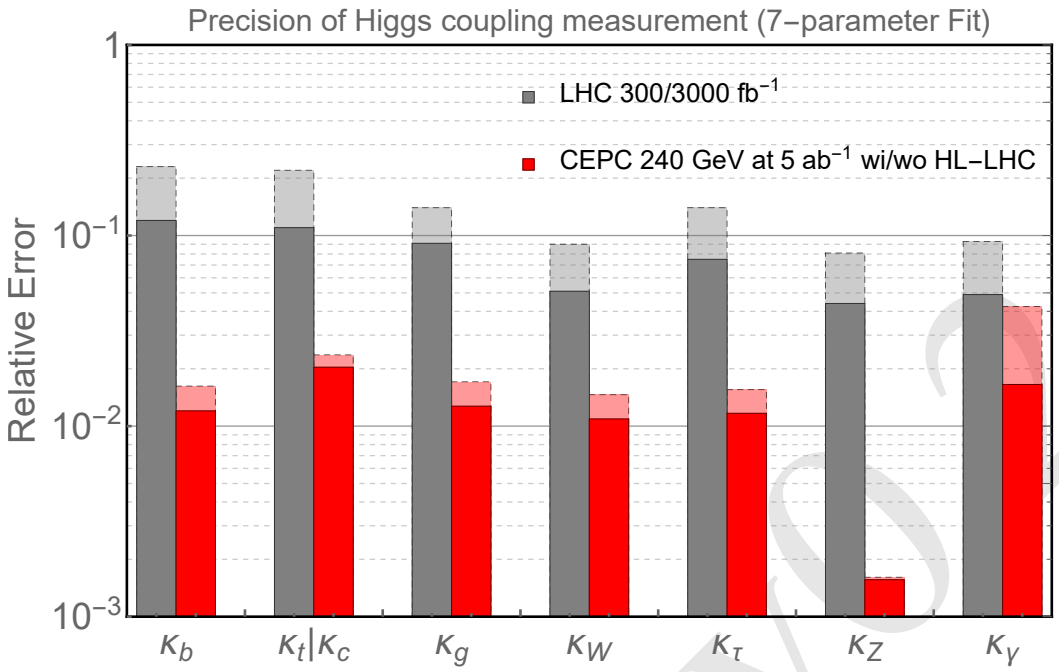

Figure 11.7: The 7 parameter fit result, and comparison with the HL-LHC [22]. The projections for the CEPC at 240 GeV with 5 ab^{-1} integrated luminosity are shown. The CEPC results without combination with the HL-LHC input are shown with dashed edges. The LHC projections for an integrated luminosity of 300 fb^{-1} are shown in dashed edges.

parison is within the framework of a 7-parameter fit, shown in Fig. 11.7. Even with this set of restrictive assumptions, the advantage of the CEPC is still significant. The measurement of κ_Z is more than a factor of 10 better. The CEPC can also improve significantly on a set of channels which suffers from large background at the LHC, such as κ_b, κ_c, and κ_g. Note that this is in comparison with the HL-LHC projection with aggressive assumptions about systematics. Such uncertainties are typically under much better control at lepton colliders. Within this 7-parameter set, the only coupling which the HL-LHC can give a competitive measurement is κ_γ, for which the CEPC's accuracy is limited by statistics. This is also the most valuable input that the HL-LHC can give to the Higgs boson coupling measurement at the CEPC, which underlines the importance of combining the results of these two facilities.

The direct search limit for BSM Higgs decay into invisibles $\mathrm{BR}_{\mathrm{inv}}^{\mathrm{bsm}}$ is well motivated, in close connection to dark sectors. The CEPC with 5 ab^{-1} can measure this to a high accuracy as 95% upper limit 0.31%, as shown in Table 11.3. At the same time, the HL-LHC can only manage a much lower accuracy 6-17% [9] and some improved analysis may reach 2-3.5% [**?**].

As discussed above, one of the greatest advantages of lepton collider Higgs boson factory is the capability of determining the Higgs boson coupling *model independently*. The projection of such a determination at the CEPC is shown in Fig. 11.8. The advantage of the higher integrated luminosity at a circular lepton collider is apparent. The CEPC has a clear advantage in the measure of κ_Z. It is also much stronger in κ_μ and $\mathrm{BR}_{\mathrm{inv}}$ measurements.

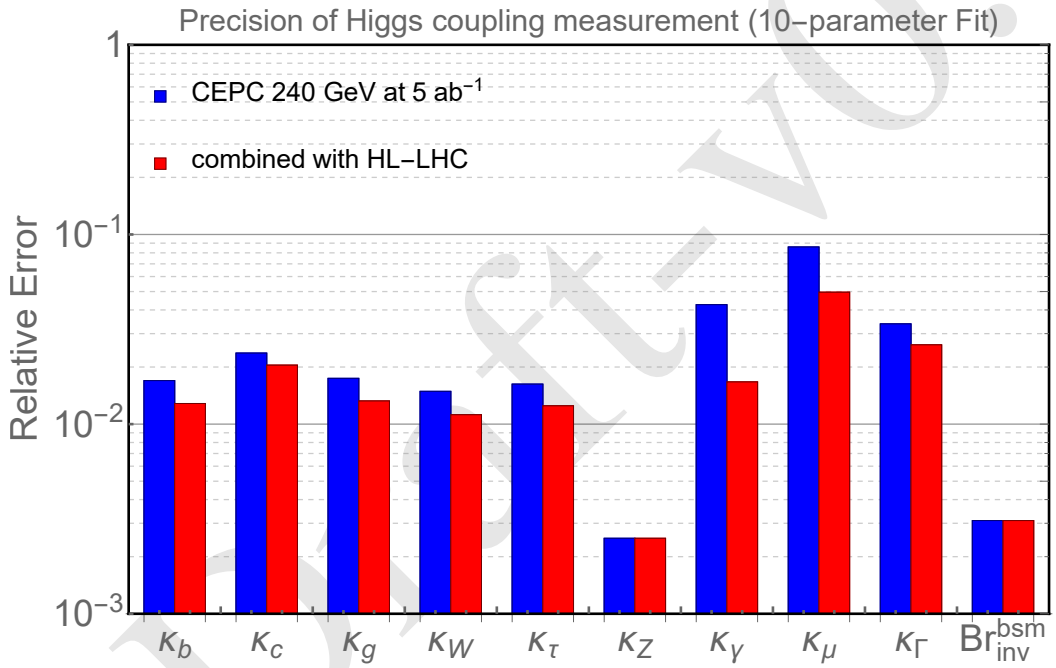

Figure 11.8: The 10 parameter fit result for CEPC at 240 GeV with 5 ab^{-1} integrated luminosity (blue) and in combination with HL-LHC inputs (red). All the numbers refer to are relative precision except for $\mathrm{BR}^{\mathrm{bsm}}_{\mathrm{inv}}$ for which 95% CL upper limit are quoted respectively.

Draft v0.2

11.1.7.2 Effective-field-theory analysis

With the assumption that the new physics particles are heavier than the relevant energy of the Higgs factory, their effect can be characterized in the effective-field-theory (EFT) framework, in which higher dimensional operators supplement the Standard Model Lagrangian. Imposing baryon and lepton numbers conservations, all higher dimensional operators are of even dimension:

$$\mathcal{L}_{\rm EFT} = \mathcal{L}_{\rm SM} + \sum_i \frac{c_i^{(6)}}{\Lambda^2}\mathcal{O}_i^{(6)} + \sum_j \frac{c_j^{(8)}}{\Lambda^4}\mathcal{O}_j^{(8)} + \cdots \tag{11.11}$$

The leading effects of new physics at the electroweak scale would be the dimension-six operators. To obtain robust constraints on the Wilson coefficients c_i, a global analysis is required which includes the contributions from all possible dimension-six operators. While a large number of dimension-six operators can be written down, only a subset of them contribute to the Higgs boson processes at leading order. Among these operators, some are much better constrained by other measurements. It is thus reasonable to focus on the operators that primarily contribute to the Higgs boson processes and reduce the parameter space by making appropriate assumptions, as done in many recent studies of EFT global analysis at future lepton colliders [21, 26–31]. Following these studies, the CP-violating operators as well as the ones that induce fermion dipole interactions are discarded in this analysis. At leading order, CP-violating operators do not have linear contributions to the rates of Higgs processes. While they do contribute to the angular observables at the leading order [32, 33], these operators are usually much better constrained by EDM experiments [34–36], though some rooms are still possible for the CP-violating couplings of Higgs boson to the heavy flavor quarks and leptons [37, 38]. The interference between the fermion dipole interactions with SM terms are suppressed by the fermion masses. The corresponding operators also generate dipole moments, which are stringently constrained especially for light fermions. For the operators that modify the Yukawa matrices, only the five diagonal ones that correspond to the top, charm, bottom, tau, and muon Yukawa couplings are considered, which are relevant for the Higgs boson measurements at CEPC.

Before presenting the projections, some brief comments on the EFT framework are in order. In comparison with the κ-framework, a significant advantage of the EFT framework is that it gives physical parameterizations of the new physics effect. EFT operators can be used directly in computations. It also allows natural inclusions of new observables, with possible correlations automatically taken into account. At the same time, the connections with experimental observables are less direct and intuitive. Sometimes, the EFT approach is referred to as model-independent. This is only accurate to a certain extent. At least, it assumes that there are no new light degrees of freedom. In practice, assumptions are often made to simplify the set of EFT operators, as also done here.

The electroweak precision observables are already tightly constrained by the LEP Z-pole and W mass measurements. The CEPC Z-pole run can further improve the constraints set by LEP, thanks to the enormous amount ($\sim 10^{11}$) of Z bosons that can be collected. The W mass can also be constrained within a few MeVs at CEPC even without a dedicated WW threshold run. Given that the expected precisions of the Z-pole observables and the W mass are much higher than the ones of Higgs boson observables, in the Higgs boson analysis, it is assumed that the former ones are perfectly constrained, which significantly simplifies the analysis. In particular, in a convenient basis all the contact

Draft-v0.2

CEPC 240 GeV ($5\,\mathrm{ab}^{-1}$)				
	uncertainty	correlation matrix		
		$\delta g_{1,Z}$	$\delta\kappa_\gamma$	λ_Z
$\delta g_{1,Z}$	1.3×10^{-3}	1	0.08	-0.90
$\delta\kappa_\gamma$	1.0×10^{-3}		1	-0.42
λ_Z	1.4×10^{-3}			1

Table 11.4: The estimated constraints on aTGCs from the measurements of the diboson process ($e^+e^- \to WW$) in the semi-leptonic channel at CEPC 240 GeV with $5\,\mathrm{ab}^{-1}$ data and unpolarized beams. All angular distributions are used in the fit. Only the statistical uncertainties of the signal events are considered, assuming a selection efficiency of 80%.

interaction terms of the form $hVf\bar{f}$ can be discarded since they also modify the fermion gauge couplings. Realistic Z-pole constraints have also been considered in recent studies [21, 29, 31], but certain assumptions (such as flavor-universality) and simplifications are made. Future studies with more general frameworks are desired to fully determine the impact of the Z-pole measurements on the Higgs boson analysis.

The measurements of the triple gauge couplings (TGCs) from the diboson process ($e^+e^- \to WW$) play an important role in the Higgs boson coupling analysis under the EFT framework. Focusing on CP-even dimension-six operators, the modifications to the triple gauge vertices from new physics can be parameterized by three anomalous TGC parameters (aTGCs), conventionally denoted as $\delta g_{1,Z}$, $\delta\kappa_\gamma$ and λ_Z [39, 40]. Among them, $\delta g_{1,Z}$ and $\delta\kappa_\gamma$ are generated by operators that also contribute to the Higgs boson processes. At 240 GeV, the cross section of $e^+e^- \to WW$ is almost two orders of magnitude larger than the one of the Higgsstrahlung process. The measurements of the diboson process thus provide strong constraints on the operators that generate the aTGCs. A dedicated study on the TGC measurements at CEPC is not available at the current moment. A simplified analysis is thus performed to estimate the precision reaches on the aTGCs. The results are shown in Table 11.4. The analysis roughly follows the methods in Refs. [28, 41]. Only the WW events in the semi-leptonic (electron or muon) channel are used, which have good event reconstructions and also a sizable branching fraction ($\approx 29\%$). In particular, the production polar angle, as well as the two decay angles of the leptonic W, can be fully reconstructed, which contain important information on the aTGCs. The two decay angles of the hadronic W can only be reconstructed with a two-fold ambiguity. A χ^2 fit of the three aTGC parameters to the binned distribution of all five angles is performed, from which the one-sigma precisions of the three aTGCs as well as the correlations among them are extracted. A signal selection efficiency of 80% is assumed. The effects of systematics and backgrounds are not considered, assuming they are under control after the selection cuts.

Under the assumptions specified above, the contributions to the Higgs boson and diboson processes from dimension-six operators consist of a total number of twelve degrees of freedom. While all non-redundant basis are equivalent, it is particularly convenient to choose a basis in which the twelve degrees of freedom can be mapped to exactly twelve operators, while the rest are removed by the assumptions. Two such bases are considered in our analysis, one is defined by the set of dimension-six operators in Table 11.5, the other is the so-called "Higgs basis," proposed in Ref. [42]. In the Higgs basis, the param-

Draft-2018/07/19

$\mathcal{O}_H = \frac{1}{2}(\partial_\mu \lvert H^2 \rvert)^2$	$\mathcal{O}_{GG} = g_s^2 \lvert H \rvert^2 G^A_{\mu\nu} G^{A,\mu\nu}$
$\mathcal{O}_{WW} = g^2 \lvert H \rvert^2 W^a_{\mu\nu} W^{a,\mu\nu}$	$\mathcal{O}_{y_u} = y_u \lvert H \rvert^2 \bar{Q}_L \tilde{H} u_R \quad (u \to t, c)$
$\mathcal{O}_{BB} = g'^2 \lvert H \rvert^2 B_{\mu\nu} B^{\mu\nu}$	$\mathcal{O}_{y_d} = y_d \lvert H \rvert^2 \bar{Q}_L H d_R \quad (d \to b)$
$\mathcal{O}_{HW} = ig(D^\mu H)^\dagger \sigma^a (D^\nu H) W^a_{\mu\nu}$	$\mathcal{O}_{y_e} = y_e \lvert H \rvert^2 \bar{L}_L H e_R \quad (e \to \tau, \mu)$
$\mathcal{O}_{HB} = ig'(D^\mu H)^\dagger (D^\nu H) B_{\mu\nu}$	$\mathcal{O}_{3W} = \frac{1}{3!} g \epsilon_{abc} W^{a\,\nu}_{\mu} W^b_{\nu\rho} W^{c\,\rho\mu}$

Table 11.5: A complete set of CP-even dimension-six operators that contribute to the Higgs and TGC measurements, assuming there is no correction to the Z-pole observables and the W mass, and also no fermion dipole interaction. For $\mathcal{O}_{y_u}$, $\mathcal{O}_{y_d}$ and $\mathcal{O}_{y_e}$, only the contributions to the diagonal elements of the Yukawa matrices that corresponds to the top, charm, bottom, tau, and muon Yukawa couplings are considered.

eters are defined in the broken electroweak phase, and can be directly interpreted as the size of the Higgs couplings. Different from the original Higgs basis, this analysis follows Ref. [28], with the parameters associated with the Hgg, $H\gamma\gamma$ and $HZ\gamma$ vertices normalized to the SM one-loop contributions, and denoted as $\bar{c}_{gg}$, $\bar{c}_{\gamma\gamma}$ and $\bar{c}_{Z\gamma}$. The parameter $\bar{c}_{gg}^{\text{eff}}$ is further defined to absorb all contributions to the Hgg vertex, as shown in Eq. **??**. These redefined parameters can be more conveniently interpreted as the precisions of the Higgs couplings analogous to those in the κ framework. The exact definitions of the Higgs basis and the translation to the basis in Table 11.5 can be found in the end of the section.

The estimated precisions of all the Higgs rate measurements in Section **??** (Table 11.2), along with the correlations among them, are included as inputs for the EFT global analysis. In addition, the angular observables of the channel $e^+e^- \to HZ$, $Z \to \ell^+\ell^-$, $H \to b\bar{b}$ are included, following the studies in Refs. [32, 33]. This channel is almost background-free after the selection cuts, with a signal selection efficiency of about 40%. For the TGC measurements, the results in Table 11.4 are used as inputs. The global χ^2 is obtained by summing over the χ^2 of all the measurements. Due to the high precision of the measurements, it is shown that for all observables, keeping only the linear terms of all EFT parameters gives a very good approximation [28]. This greatly simplifies the fitting procedure, as the total χ^2 can be written as

$$\chi^2 = \sum_{ij} (c - c_0)_i \, \sigma_{ij}^{-2} \, (c - c_0)_j \,, \qquad \text{where} \quad \sigma_{ij}^{-2} \equiv (\delta c_i \, \rho_{ij} \, \delta c_j)^{-1} \,, \tag{11.12}$$

where c_i's are the EFT parameters, c_0's are the corresponding central values which are zero by construction, as the measurements are assumed to be SM-like. The one-sigma uncertainties δc_i and the correlation matrix ρ can be obtained from $\sigma_{ij}^{-2} = \partial^2 \chi^2 / \partial c_i \partial c_j$.

For comparison, the reaches of the LHC 14 TeV are also considered, with a total luminosities of $300\,\text{fb}^{-1}$ or $3000\,\text{fb}^{-1}$, which are combined with the diboson ($e^+e^- \to WW$) measurements at LEP as well as the LHC 8 TeV Higgs measurements. For the LHC 14 TeV Higgs measurements, the projections by the ATLAS collaboration [22] are used, while the composition of each channel is obtained from Refs. [43–47]. The constraints from the LHC 8 TeV Higgs measurements and the diboson measurements at LEP are obtained directly from Ref. [48]. While the LHC diboson measurements could potentially improve the constraints on aTGCs set by LEP [49], they are not included in this analysis due to the potential issues related to the validity of the EFT [50, 51] and the TGC dominance assumption [52].

Draft-2018/07/19

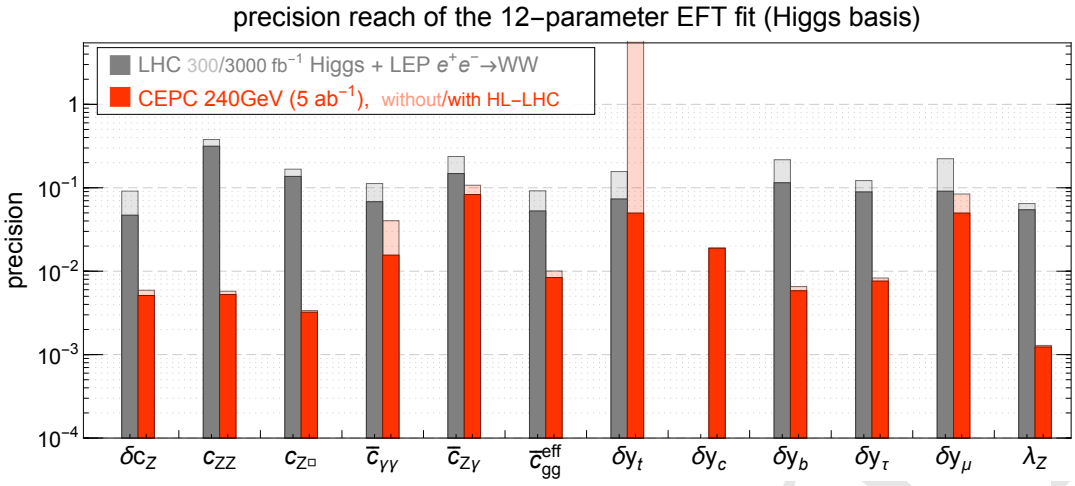

Figure 11.9: One-sigma precision reach of the twelve parameters in the Higgs basis. The first column shows the results from the LHC Higgs measurements with $300\,\mathrm{fb}^{-1}$ (light shade) and $3000\,\mathrm{fb}^{-1}$ (solid shade) combined with LEP diboson ($e^+e^- \to WW$) measurement. The second column shows the results from CEPC with $5\,\mathrm{ab}^{-1}$ data collected at 240 GeV with unpolarized beam. The results from CEPC alone are shown in light shades, and the ones from a combination of CEPC and HL-LHC are shown in solid shades. δy_c is fixed to zero for the LHC fits.

The results of the 12-parameter fit at CEPC are shown in Fig. 11.9 for the Higgs basis and Fig. 11.10 for the basis in Table 11.5. The results from LHC Higgs measurements (both $300\,\mathrm{fb}^{-1}$ and $3000\,\mathrm{fb}^{-1}$) combined with LEP diboson measurements are shown in comparison. The results of the combination of CEPC with HL-LHC ($3000\,\mathrm{fb}^{-1}$) are also shown in addition to the ones of CEPC alone. In Fig. 11.9, the results are shown in terms of the one-sigma precision of each parameter. The LHC results are shown with gray columns with $300\,\mathrm{fb}^{-1}$ ($3000\,\mathrm{fb}^{-1}$) in light (solid) shades, while the CEPC ones are shown with the red columns, with the CEPC-alone (combination with HL-LHC) results shown in light (solid) shades. In Fig. 11.10, the results are presented in terms of the reaches of $\Lambda/\sqrt{|c_i|}$ at 95% confidence level (CL), where Λ is the scale of new physics and c_i is the corresponding Wilson coefficient for each operator, defined in Eq. 11.11. Four columns are shown separately for LHC $300\,\mathrm{fb}^{-1}$, LHC $3000\,\mathrm{fb}^{-1}$, CEPC alone and CEPC combined with HL-LHC. The results of the global fits are shown with solid shades. The results from individual fits are shown with light shades, which are obtained by switching on one operator at a time with the rest fixed to zero.

It is transparent from Fig. 11.9 that CEPC provides very good reaches on the precisions of Higgs couplings, which are of one order of magnitude better than the ones at the LHC. For the parameters $\bar{c}_{\gamma\gamma}$, $\bar{c}_{Z\gamma}$ and δy_μ, the clean signal and small branching ratios of the corresponding channels ($H \to \gamma\gamma/Z\gamma/\mu\mu$) makes the HL-LHC precisions comparable with the CEPC ones. The combination with additional LHC measurements thus provides non-negligible improvements, especially for those parameters. It should be noted that, while δy_t modifies the Hgg vertex via the top loop contribution, CEPC alone could not discriminate it from the Hgg contact interaction ($\bar{c}_{gg}$ in Eq. **??**) obtained from integrating out a heavy new particle in the loop. The parameter $\bar{c}_{gg}^{\mathrm{eff}}$ absorbs both contributions and reflects the overall precision of the Hgg coupling. The combination with the LHC $t\bar{t}H$ measurements could resolve this flat direction. The CEPC measurements, in turn, could improve the constraint on δy_t set by the LHC by providing much better con-

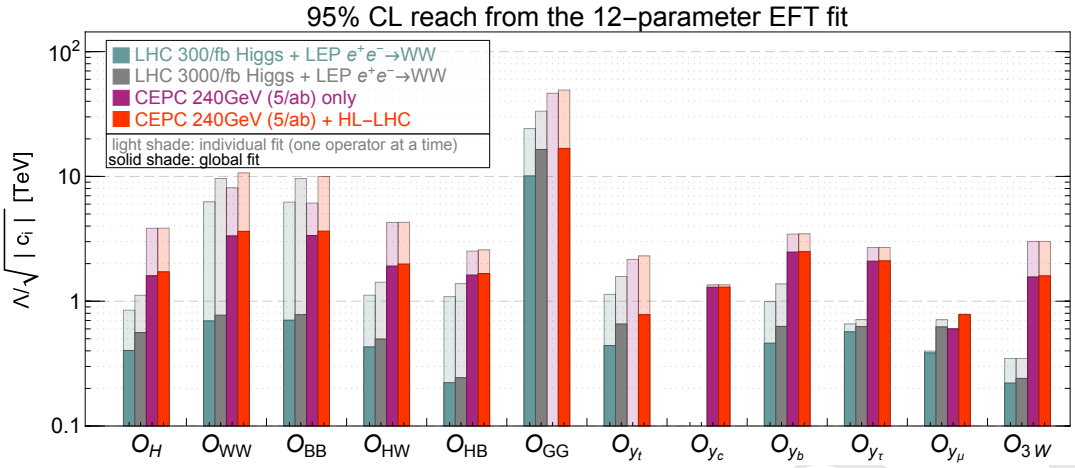

Figure 11.10: The 95% CL reach on $\Lambda/\sqrt{|c_i|}$ for the operators in the basis defined in Table 11.5. The first two columns show the results from LHC Higgs measurements with $300\,\text{fb}^{-1}$ and $3000\,\text{fb}^{-1}$ combined with LEP diboson ($e^+e^- \to WW$) measurement. The last two columns show the results from CEPC alone and the combination of CEPC and HL-LHC ($3000\,\text{fb}^{-1}$). The results of the global fits are shown with solid shades. The results from individual fits (by switching on one operator at a time) are shown with light shades. δy_c is fixed to zero for the LHC fits.

straints on the other parameters that contribute to the $t\bar{t}H$ process. It should also be noted that the measurement of the charm Yukawa coupling is not reported in Ref. [22], while the projection of its constraint has a large variation among different studies and can be much larger than one [53–58]. Therefore, δy_c is fixed to be zero for the LHC-only fits, as treating δy_c as an unconstrained free parameter generates a flat direction in the fit which makes the overall reach much worse. The CEPC, on the other hand, provides excellent measurements of the charm Yukawa and can constrain δy_c to a precision of $\sim 2\%$.

Regarding the reaches of $\Lambda/\sqrt{|c_i|}$ in Fig. 11.10, it is also clear that CEPC has a significantly better performance than the LHC. If the couplings are naïvely assumed to be of order one ($c_i \sim 1$), the Higgs measurements at CEPC would be sensitive to new physics scales at multiple TeVs. While the individual reach for some of the operators at the LHC can be comparable to the ones at CEPC (*e.g.*, O_{WW} and O_{BB} from the measurement of $H \to \gamma\gamma$), the reaches of CEPC are much more robust under a global framework thanks to its comprehensive measurements of both the inclusive HZ cross section and the exclusive rates of many Higgs decay channels. Operators O_{GG} and O_{y_t} both contribute to the Hgg vertex. While the CEPC could provide strong constraints on either of them if the other is set to zero, they can only be constrained in a global fit if the $t\bar{t}h$ measurements at the LHC are also included. It is also important to note that the validity of EFT could be a potential issue for the LHC measurements [50]. Depending on the size of the couplings, the inferred bounds on the new physics scale Λ could be comparable with or even smaller than the energy scale probed by the LHC. The CEPC has a smaller center of mass energy and much better precisions, which ensures the validity of EFT for most new physics scenarios.

In Table 11.6 and Fig. **??**, the numerical results of the global fit are presented for CEPC in terms of the one-sigma precisions of the 12 parameters and the correlations among them. The results assume an integrated luminosity of $5\,\text{ab}^{-1}$ at 240 GeV with unpolarized beams, both without and with the combination of HL-LHC ($3000\,\text{fb}^{-1}$) Higgs measurements. With both the one-sigma bounds and the correlation matrix, the corre-

sponding *chi-squared* can be reconstructed, which can be used to derive the constraints in any other EFT basis or any particular model that can be matched to the EFT. This offers a convenient way to study the reaches on new physics models, as detailed knowledge of the experimental measurements are not required.

Higgs basis											
δc_Z	c_{ZZ}	$c_{Z\Box}$	$\bar{c}_{\gamma\gamma}$	$\bar{c}_{Z\gamma}$	$\bar{c}_{gg}^{\rm eff}$	δy_t	δy_c	δy_b	δy_τ	δy_μ	λ_Z
0.0059	0.0058	0.0034	0.040	0.11	0.010	–	0.019	0.0065	0.0083	0.084	0.0013
0.0051	0.0053	0.0032	0.016	0.083	0.0084	0.050	0.019	0.0058	0.0076	0.050	0.0012
c_i/Λ^2 [TeV^{-2}] of dimension-six operators											
c_H	c_{WW}	c_{BB}	c_{HW}	c_{HB}	c_{GG}	c_{y_t}	c_{y_c}	c_{y_b}	c_{y_τ}	c_{y_μ}	c_{3W}
0.20	0.045	0.044	0.14	0.19	–	–	0.30	0.082	0.11	1.4	0.20
0.17	0.038	0.038	0.13	0.18	0.0018	0.82	0.30	0.080	0.11	0.82	0.20

Table 11.6: The one-sigma uncertainties for the 12 parameters from CEPC (240 GeV, $5\,\mathrm{ab}^{-1}$) in the Higgs basis and the basis of dimension-six operators. For both cases, the upper (lower) row correspond to results without (with) the combination of the HL-LHC Higgs measurements.. Note that, without the $t\bar{t}h$ measurements, δy_t can not be constrained in a global fit, thus c_{GG} and c_{y_t} can not be resolved.

In the EFT framework, it is explicitly assumed that the Higgs total width is the sum of all the widths of its SM decay channels. This is because the EFT expansion in Eq. 11.11 relies on the assumption that the new physics scale is sufficiently large, while any potential Higgs exotic decay necessarily introduces light BSM particles, thus in direct conflict with this assumption. One could nevertheless treat the Higgs total width as a free parameter in the EFT global fit and obtain an indirect constraint of it, as done in Ref. [21]. With this treatment, the CEPC could constrain the Higgs total width to a precision of 1.8% (1.7% if combined with HL-LHC). This result is significantly better than the one from the 10-parameter coupling fit in Table 11.3 ($3.4\%/2.6\%$). The improvement is mainly because the HWW and HZZ couplings are treated as being independent in the 10-parameter coupling fit, while in the EFT framework they are related to each other under gauge invariance and custodial symmetry. It should also be noted that the Higgs width determined using Eq. (11.4) and (11.7) explicitly assumes that the HWW and HZZ couplings are independent of the energy scale. Such an assumption is not valid in the EFT framework with the inclusion of the anomalous couplings.

11.1.7.3 The Higgs self-coupling

The Higgs boson self-coupling is a critical parameter governing the dynamics of the electroweak symmetry breaking. In the Standard Model, the Higgs trilinear and quadrilinear couplings are fixed once the values of the electroweak VEV and the Higgs mass are known. Any deviation from the SM prediction is thus clear evidence of new physics beyond the SM. The Higgs trilinear coupling is probed at the LHC with the measurement of the double-Higgs process, $pp \to HH$. Current bounds on the Higgs trilinear coupling is at the $\mathcal{O}(10)$ level, while the HL-LHC is expected to improve the precision to the level of $\mathcal{O}(1)$ [**?**]. The prospects for extracting the Higgs quadrilinear coupling are much less promising, even for a 100 TeV hadron collider [**?**].

To measure the double-Higgs processes at a lepton collider, a sufficiently large center of mass energy ($\gtrsim 400\,\mathrm{GeV}$) is required, which is likely to be achieved only at a linear collider. The CEPC, instead, can probe the Higgs trilinear coupling via its loop contributions to the single Higgs processes. This indirect approach nevertheless provides competitive reaches since the loop suppression is compensated by the high precision of

the Higgs measurements at CEPC [59]. With a precision of 0.5% on the inclusive HZ cross section at 240 GeV, the Higgs trilinear coupling can be constrained to a precision of 35%, assuming all other Higgs couplings that contributes to $e^+e^- \to HZ$ are SM-like. [5] While this indirect bound is comparable to the direct ones at linear colliders, it relies on strong assumptions which are only applicable to some specific models. A more robust approach is to include all possible deviations on the Higgs couplings simultaneously and constrain the Higgs trilinear coupling in a global fit. The EFT framework presented in Section 11.1.7.2 is ideal for such an analysis. Under this framework, the one-loop contributions of the trilinear Higgs coupling to all the relevant Higgs production and decay processes are included, following Ref. [30]. The new physics effect is parameterized by the quantity $\delta\kappa_\lambda \equiv \kappa_\lambda - 1$, where κ_λ is the ratio of the Higgs trilinear coupling to its SM value,

$$\kappa_\lambda \equiv \frac{\lambda_3}{\lambda_3^{\rm sm}}\,, \qquad \lambda_3^{\rm sm} = \frac{m_H^2}{2v^2}\,. \tag{11.13}$$

The global fit is performed simultaneously with $\delta\kappa_\lambda$ and the 12 EFT parameters in Section 11.1.7.2. The results are presented in Table 11.7. The results for HL-LHC are also shown, which were obtained in Ref. [60] under the same global framework. For CEPC 240 GeV, the one-sigma bound on $\delta\kappa_\lambda$ is around ± 3, significantly worse than the 35% in the $\delta\kappa_\lambda$-only fit. This is a clear indication that it is difficult to resolve the effects of $\delta\kappa_\lambda$ from those of other Higgs couplings. For HL-LHC, the reach on $\delta\kappa_\lambda$ is still dominated by the double-Higgs process. However, as a result of the destructive interferences among diagrams, the double-Higgs process at LHC could not constrain $\delta\kappa_\lambda$ very well on its positive side, even with the use of differential observables [**?**]. The combination of HL-LHC and CEPC 240 GeV thus provides a non-trivial improvement to the HL-LHC result alone, in particular for the two-sigma bound on the positive side, which is improved from $+6.1$ to $+2.8$. This is illustrated in Fig. 11.11, which plots the profiled χ^2 as a function of $\delta\kappa_\lambda$ for the two colliders.

bounds on $\delta\kappa_\lambda$	$\Delta\chi^2 = 1$	$\Delta\chi^2 = 4$
CEPC 240 GeV $(5\,\text{ab}^{-1})$	$[-3.2, +3.3]$	$[-6.3, +6.7]$
HL-LHC	$[-0.9, +1.3]$	$[-1.7, +6.1]$
HL-LHC + CEPC 240 GeV	$[-0.8, +1.0]$	$[-1.5, +2.8]$
240 GeV $(5\,\text{ab}^{-1})$ + 350 GeV $(1.5\,\text{ab}^{-1})$	$[-0.48, +0.48]$	$[-0.96, +0.96]$

Table 11.7: The $\Delta\chi^2 = 1$ (one-sigma) and $\Delta\chi^2 = 4$ (two-sigma) bounds of $\delta\kappa_\lambda$ for various scenarios, obtained in a global fit by profiling over all other EFT parameters. The results for HL-LHC are obtained from Ref. [60].

It is also important to note that the reach on $\delta\kappa_\lambda$ in the global framework is significantly improved if an additional run at a higher energy, such as 350 GeV, is available. The global constraint on $\delta\kappa_\lambda$ is improved by almost one order of magnitude with $1.5\,\text{ab}^{-1}$ data collected at the 350 GeV on top of the $5\,\text{ab}^{-1}$ at 240 GeV. The usefulness of the 350 GeV run in discriminating different EFT parameters is thoroughly discussed in Ref. [28]. In

[5] A better precision can be obtained by also using the exclusive channels, such as $\sigma(HZ) \times \text{BR}(H \to b\bar{b})$, but would require an even stronger assumption that all Higgs couplings contributing to the branching ratios are also SM-like except the Higgs trilinear coupling.

Draft-v0.2

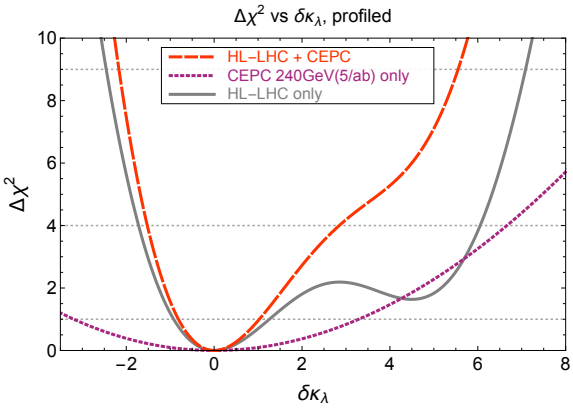

Figure 11.11: Chi-square as a function of $\delta\kappa_\lambda$ after profiling over all other EFT parameters for HL-LHC, CEPC and their combination.

addition, it was pointed out in Refs. [30, 59] that the sensitivity of $\sigma(HZ)$ to $\delta\kappa_\lambda$ is maximized near the HZ threshold and decreases as the center of mass energy increases – a feature not exhibited by the other EFT parameters. Measuring $e^+e^- \to HZ$ at two different energies is thus particularly helpful in discriminating $\delta\kappa_\lambda$ with other EFT parameters.

11.1.7.4 Higgs and top couplings

Interactions of the Higgs boson with the top quark are widely viewed as a window to new physics beyond the Standard Model. Parameterizing effects of new physics in terms of dimension-six gauge-invariant operators modifying the Higgs-top interactions [**?** **?**], the Higgs top couplings physics potential at CEPC can be evaluated [**?** **?** **?** **?**]. This EFT basis enlarges the Higgs EFT considered above. Moreover, the CP violation effects in the third generation Yukawas can be reflected as the complexity of the Wilson coefficients of operator $\mathcal{O}_{y_t}$ and $\mathcal{O}_{y_b}$,

$$\Delta y_t = y_t^{\rm SM}\left(\Re[C_{y_t}]\frac{v^3}{2m_t\Lambda^2} + i\Im[C_{y_t}]\frac{v^3}{2m_t\Lambda^2}\right) \tag{11.14}$$

$$\Delta y_b = y_t^{\rm SM}\left(\Re[C_{y_b}]\frac{v^3}{2m_b\Lambda^2} + i\Im[C_{y_b}]\frac{v^3}{2m_b\Lambda^2}\right). \tag{11.15}$$

In this section, the effect of introducing CP phases in the Yukawa operators in Higgs physics are discussed. For more detailed discussion on a complete set of Higgs and Top operators, see Ref. [**?**]. The dominant sources of constraints are from $H \to \gamma\gamma$ and $H \to gg$ for $\mathcal{O}_{y_t}$, and $H \to gg$ and $H \to b\bar{b}$ for $\mathcal{O}_{y_b}$. Given that $H \to gg$ measurements are sensitive to both operators, a joint analysis of $\mathcal{O}_{y_t}$ and $\mathcal{O}_{y_b}$ will yield a significantly different result comparing to individual operator analysis. A joint analysis for these two operators in terms of Yukawa coupling strengths and the associated CP phases is performed at CEPC. The important physics cases for such considerations are highlighted.

In Fig. 11.12 constraints on the top and bottom Yukawa coupling strengths and their CP phases are presented in the left panel and right panel, respectively. The 68% and 95% exclusion bands are shown in solid and dashed lines. The limits for CEPC are shown in *bright* black and magenta lines for individual operator analysis and the *bright* green and yellow shaded regions representing the 68% and 95% allowed parameter space, respectively. The *dimmed* thick black curves represent the results after turning on both operators

Draft-v0.2

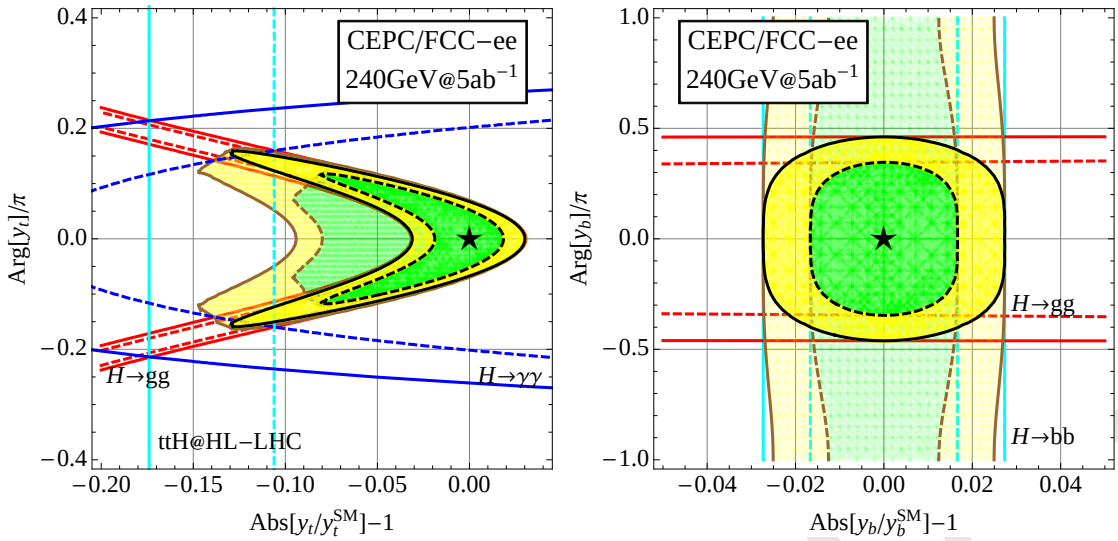

Figure 11.12: Results for analysis on C_{y_t} and C_{y_b} in the projected allowed regions for modification to top and bottom Yukawa couplings in magnitude and CP phase at 68% and 95% confidence level. The combined results for CEPC are shown in black curves. The source of individual constraints for the single operator analysis are labeled correspondingly. For a joint analysis of simultaneous appearance of both $\mathcal{O}_{y_t}$ and $\mathcal{O}_{y_b}$ operators, the results for CEPC are shown in the enlarged yellow (95%) and green regions (68%) with thick brown boundary lines.

$\mathcal{O}_{tH}$ and $\mathcal{O}_{bH}$ at the same time, using a profile-likelihood method profiling over other parameters. Furthermore, in the left panel the cyan band represents constraints from HL-LHC $t\bar{t}H$ measurements, red bands are constraints from CEPC $H \to gg$ measurements and blue bands are constraints from CEPC $H \to \gamma\gamma$ measurements. Similarly in the right panel, the cyan bands are constraints from $H \to b\bar{b}$ and the red bands are constraints from $H \to gg$ at CEPC.

The left panel of Fig. 11.12 shows that the expected sensitivity on the modification in the magnitude of top Yukawa is at around $\pm 3\%$ for the single operator analysis, which is relaxed to $[-9.5\%, +3\%]$ for the joint analysis allowing the bottom Yukawa and the associated CP phase to vary freely, in the case of zero CP phase in the top Yukawa. The phase of the top Yukawa could be constrained to be $\pm 0.16\pi$. The constraints on the phase of the top Yukawa is driven by the $H \to \gamma\gamma$ measurements, where a sizable phase shift will enlarge the Higgs to diphoton rate via reducing the interference with SM W-loop. The constraints on the magnitude of the top Yukawa modification is driven by the $H \to gg$ measurements due to the dominant contribution to $H \to gg$ being from top-loop. Note that constraints from $H \to gg$ measurement is not entirely vertical, this is a result of the different sizes of the top-loop contribution to Hgg through scalar and pseudoscalar couplings. Similarly, as shown in the right panel of Fig. 11.12 for the bottom Yukawa magnitude modification, the constraint is $\pm 2.5\%$ and, for the bottom Yukawa CP phase, the constraints changes from $\pm 0.47\pi$ to no constraint for simultaneous modification to top Yukawa.

11.1.8 Searches for exotic decays

11.1.9 Tests of Higgs boson spin/CP

The CP parity of a Higgs boson, and more generally its anomalous couplings to gauge bosons in the presence of BSM physics, can be measured at the CEPC based on the $e^+e^-(\rightarrow Z^*) \rightarrow ZH \rightarrow \mu^+\mu^- b\bar{b}$ process. It is convenient to express the anomalous coupling measurements in terms of physical quantities of effective fractions of events of the anomalous contribution relative to the SM predictions as detailed in Refs. [61–63], which are invariant under independent re-scalings of all couplings.

Two of the anomalous HZZ coupling measurements are of particular interest at the CEPC: the fraction of the high-order CP-even contribution due to either SM contribution or new physics, f_{a2}, and the fraction of a CP-odd contribution due to new physics, f_{a3}. The following two types of observables can be used to measure these anomalous couplings of the Higgs bosons.

1. The dependence of the $e^+e^- \rightarrow Z^* \rightarrow ZH$ cross section on $\sqrt{s}$ is different for different CP property of the Higgs boson [63]. Therefore, measurements of the cross section at several different energies will yield useful information about anomalous HZZ couplings. However this has non-trivial implications to the accelerator design and is not included in this study as a single value of $\sqrt{s}$ assumed for the CEPC operating as a Higgs boson factory.

2. Angular distributions, $\cos\theta_1$ or $\cos\theta_2$ and Φ as defined in Ref. [63]. These angles are also sensitive to interference between CP-even and CP-odd couplings. In particular forward-backward asymmetry with respect to $\cos\theta_1$ or $\cos\theta_2$ and non-trivial phase in the Φ distributions can lead to an unambiguous interpretation of CP violation.

To estimate the sensitivities on the anomalous couplings, a maximum likelihood fit [63] is performed to match observed three-dimensional angular distributions to theory predictions including signal and background processes. In this likelihood fit, the signal probability density functions are from analytical predictions that are validated using a dedicated MC program, the JHU generator [61, 62], which incorporates all the anomalous couplings, spin correlations, interference of all contributing amplitudes. The background probability density function is modeled from simulation based on $e^+e^- \rightarrow ZZ \rightarrow \ell^+\ell^- b\bar{b}$ process in Madgraph. The total integrated luminosity is assumed to be 5 ab^{-1}.

Several thousand statistically-independent experiments are generated and fitted to estimate the sensitivity to f_{a2} and f_{a3}, defined as the smallest values that can be measured with 3σ away from 0. All other parameters in the fit, including the number of expected signal and background events, are fixed. Figure 11.13 shows precision on f_{a2} and f_{a3} obtained with generated experiments. The expected sensitivity on f_{a2} and f_{a3} are 0.018 and 0.007 respectively.

The sensitivities of f_{a2} and f_{a3} are then converted to the equivalent parameters defined for the on-shell $H \rightarrow ZZ^*$ decays, $f_{a2}^{\rm dec}$ and $f_{a3}^{\rm dec}$, in order to compare with the sensitivities from other experiments as described in Ref. [63]. The corresponding sensitivities of $f_{a2}^{\rm dec}$ and $f_{a3}^{\rm dec}$ are 2×10^{-4} and 1.3×10^{-4} respectively. The much smaller values in the $f_{a2,a3}^{\rm dec}$ are due to the much larger $m^2_{Z^*}$ in the $Z^* \rightarrow ZH$ production compared to the value in the $H \rightarrow ZZ^*$ decays. A simultaneous fit of f_{a2} and f_{a3} can also performed with the 68% and 95% confidence level contours shown in Figure 11.13.

Draft-v0.2

Compared to the ultimate sensitivity from HL-LHC experiments as shown in Ref. [63], the sensitivities in the f_{a2} and f_{a3} at the CEPC are a factor of 300 and 3 better. Further improvements can be achieved by exploring kinematics in the $H \to b\bar{b}$ decays, including other Z decay final states, and combining with the overall cross-section dependence of the signal with a threshold scan in $\sqrt{s}$.

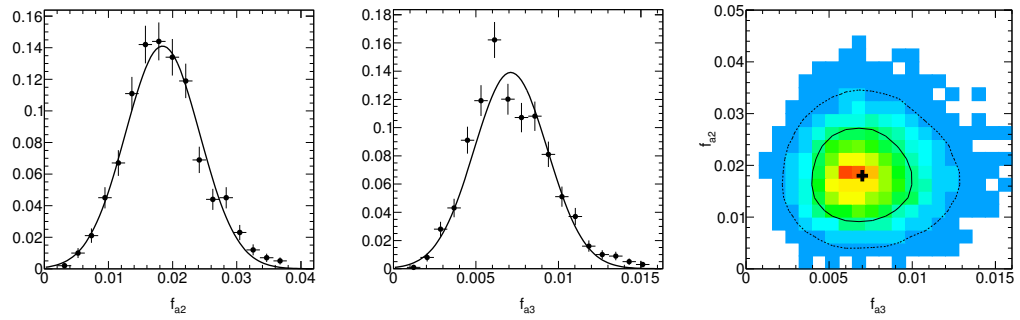

Figure 11.13: Distribution of fitted values of f_{a2} and f_{a3} in a large number of generated experiments. In the left and middle plots, only the parameter shown is floated. Other parameters are fixed to SM expectations. Right plot: simultaneous fit of non-zero f_{a2} and f_{a3}, with 68% and 95% confidence level contours shown.

References

[1] W. Kilian, T. Ohl, and J. Reuter, *WHIZARD: Simulating Multi-Particle Processes at LHC and ILC*, Eur. Phys. J. **C71** (2011) 1742, arXiv:0708.4233 [hep-ph].

[2] Y. Haddad, *Feasibility of a minimum bias analysis of $e^+e^- \to ZH \to q\bar{q} + X$ at a 250 GeV ILC*, arXiv:1404.3164 [hep-ph].

[3] CEPC Collaboration, A. A. et al., *Higgs Physics at CEPC*, arXiv:1307.1347 [hep-ph].

[4] D. Asner, T. Barklow, C. Calancha, K. Fujii, N. Graf, et al., *ILC Higgs White Paper*, arXiv:1310.0763 [hep-ph].

[5] TLEP Design Study Working Group Collaboration, M. Bicer et al., *First Look at the Physics Case of TLEP*, JHEP **1401** (2014) 164, arXiv:1308.6176 [hep-ex].

[6] ALEPH, DELPHI, L3, OPAL, LEP Electroweak Collaboration, S. Schael et al., *Electroweak Measurements in Electron-Positron Collisions at W-Boson-Pair Energies at LEP*, Phys. Rept. **532** (2013) 119, arXiv:1302.3415 [hep-ex].

[7] LHC Higgs Cross Section Working Group Collaboration, A. David et al., *LHC HXSWG interim recommendations to explore the coupling structure of a Higgs-like particle*, arXiv:1209.0040 [hep-ph].

[8] LHC Higgs Cross Section Working Group Collaboration, S. Heinemeyer et al., *Handbook of LHC Higgs Cross Sections: 3. Higgs Properties*, arXiv:1307.1347 [hep-ph].

Draft-V1

[9] S. Dawson, A. Gritsan, H. Logan, J. Qian, C. Tully, et al., *Working Group Report: Higgs Boson*, arXiv:1310.8361 [hep-ex].

[10] CMS Collaboration Collaboration, *Search for the associated production of the Higgs boson with a top-quark pair*, JHEP **1409** (2014) 087, arXiv:1408.1682 [hep-ex].

[11] ATLAS Collaboration Collaboration, *Search for $H \to \gamma\gamma$ produced in association with top quarks and constraints on the Yukawa coupling between the top quark and the Higgs boson using data taken at 7 TeV and 8 TeV with the ATLAS detector*, Phys. Lett. **B740** (2015) 222, arXiv:1409.3122 [hep-ex].

[12] A. Banfi, A. Martin, and V. Sanz, *Probing top-partners in Higgs+jets*, JHEP **1408** (2014) 053, arXiv:1308.4771 [hep-ph].

[13] A. Azatov and A. Paul, *Probing Higgs couplings with high p_T Higgs production*, JHEP **1401** (2014) 014, arXiv:1309.5273 [hep-ph].

[14] C. Grojean, E. Salvioni, M. Schlaffer, and A. Weiler, *Very boosted Higgs in gluon fusion*, JHEP **1405** (2014) 022, arXiv:1312.3317 [hep-ph].

[15] M. Buschmann, C. Englert, D. Goncalves, T. Plehn, and M. Spannowsky, *Resolving the Higgs-Gluon Coupling with Jets*, Phys. Rev. **D90** (2014) 013010, arXiv:1405.7651 [hep-ph].

[16] J. Ellis, V. Sanz, and T. You, *Complete Higgs Sector Constraints on Dimension-6 Operators*, JHEP **1407** (2014) 036, arXiv:1404.3667 [hep-ph].

[17] T. Han, Z. Liu, and J. Sayre, *Potential Precision on Higgs Couplings and Total Width at the ILC*, Phys. Rev. **D89** (2014) 113006, arXiv:1311.7155 [hep-ph].

[18] M. Klute, R. Lafaye, T. Plehn, M. Rauch, and D. Zerwas, *Measuring Higgs Couplings at a Linear Collider*, Europhys. Lett. **101** (2013) 51001, arXiv:1301.1322 [hep-ph].

[19] M. E. Peskin, *Estimation of LHC and ILC Capabilities for Precision Higgs Boson Coupling Measurements*, arXiv:1312.4974 [hep-ph].

[20] K. Fujii et al., *Physics Case for the 250 GeV Stage of the International Linear Collider*, arXiv:1710.07621 [hep-ex].

[21] T. Barklow, K. Fujii, S. Jung, R. Karl, J. List, T. Ogawa, M. E. Peskin, and J. Tian, *Improved Formalism for Precision Higgs Coupling Fits*, arXiv:1708.08912 [hep-ph].

[22] ATLAS Collaboration, *Projections for measurements of Higgs boson signal strengths and coupling parameters with the ATLAS detector at a HL-LHC*, ATL-PHYS-PUB-2014-016 (2014) . http://cds.cern.ch/record/1956710.

[23] A. Denner, S. Heinemeyer, I. Puljak, D. Rebuzzi, and M. Spira, *Standard Model Higgs-Boson Branching Ratios with Uncertainties*, Eur. Phys. J. **C71** (2011) 1753, arXiv:1107.5909 [hep-ph].

Draft-v0.2

[24] L. G. Almeida, S. J. Lee, S. Pokorski, and J. D. Wells, *Study of the standard model Higgs boson partial widths and branching fractions*, Phys. Rev. **D89** (2014) 033006, arXiv:1311.6721 [hep-ph].

[25] G. P. Lepage, P. B. Mackenzie, and M. E. Peskin, *Expected Precision of Higgs Boson Partial Widths within the Standard Model*, arXiv:1404.0319 [hep-ph].

[26] J. Ellis and T. You, *Sensitivities of Prospective Future e+e- Colliders to Decoupled New Physics*, JHEP **03** (2016) 089, arXiv:1510.04561 [hep-ph].

[27] J. Ellis, P. Roloff, V. Sanz, and T. You, *Dimension-6 Operator Analysis of the CLIC Sensitivity to New Physics*, arXiv:1701.04804 [hep-ph].

[28] G. Durieux, C. Grojean, J. Gu, and K. Wang, *The leptonic future of the Higgs*, JHEP **09** (2017) 014, arXiv:1704.02333 [hep-ph].

[29] T. Barklow, K. Fujii, S. Jung, M. E. Peskin, and J. Tian, *Model-Independent Determination of the Triple Higgs Coupling at e+e- Colliders*, arXiv:1708.09079 [hep-ph].

[30] S. Di Vita, G. Durieux, C. Grojean, J. Gu, Z. Liu, G. Panico, M. Riembau, and T. Vantalon, *A global view on the Higgs self-coupling at lepton colliders*, arXiv:1711.03978 [hep-ph].

[31] W. H. Chiu, S. C. Leung, T. Liu, K.-F. Lyu, and L.-T. Wang, *Probing 6D Operators at Future e^-e^+ Colliders*, arXiv:1711.04046 [hep-ph].

[32] M. Beneke, D. Boito, and Y.-M. Wang, *Anomalous Higgs couplings in angular asymmetries of $H \to Z\ell^+\ell^-$ and $e^+ e^- \to HZ$*, JHEP **11** (2014) 028, arXiv:1406.1361 [hep-ph].

[33] N. Craig, J. Gu, Z. Liu, and K. Wang, *Beyond Higgs Couplings: Probing the Higgs with Angular Observables at Future $e^+ e^-$ Colliders*, JHEP **03** (2016) 050, arXiv:1512.06877 [hep-ph].

[34] S. M. Barr and A. Zee, *Electric Dipole Moment of the Electron and of the Neutron*, Phys. Rev. Lett. **65** (1990) 21–24. [Erratum: Phys. Rev. Lett.65,2920(1990)].

[35] J. Fan and M. Reece, *Probing Charged Matter Through Higgs Diphoton Decay, Gamma Ray Lines, and EDMs*, JHEP **06** (2013) 004, arXiv:1301.2597 [hep-ph].

[36] ACME Collaboration, J. Baron et al., *Order of Magnitude Smaller Limit on the Electric Dipole Moment of the Electron*, Science **343** (2014) 269–272, arXiv:1310.7534 [physics.atom-ph].

[37] Y. T. Chien, V. Cirigliano, W. Dekens, J. de Vries, and E. Mereghetti, *Direct and indirect constraints on CP-violating Higgs-quark and Higgs-gluon interactions*, JHEP **02** (2016) 011, arXiv:1510.00725 [hep-ph]. [JHEP02,011(2016)].

[38] R. Harnik, A. Martin, T. Okui, R. Primulando, and F. Yu, *Measuring CP violation in $h \to \tau^+\tau^-$ at colliders*, Phys. Rev. **D88** (2013) no. 7, 076009, arXiv:1308.1094 [hep-ph].

Draft-v0.2

[39] K. Hagiwara, S. Ishihara, R. Szalapski, and D. Zeppenfeld, *Low-energy effects of new interactions in the electroweak boson sector*, Phys. Rev. **D48** (1993) 2182–2203.

[40] G. Gounaris et al., *Triple gauge boson couplings*, in *AGS / RHIC Users Annual Meeting Upton, New York, June 15-16, 1995*, pp. 525–576. 1996. arXiv:hep-ph/9601233 [hep-ph]. http://alice.cern.ch/format/showfull?sysnb=0215385. [,525(1996)].

[41] L. Bian, J. Shu, and Y. Zhang, *Prospects for Triple Gauge Coupling Measurements at Future Lepton Colliders and the 14 TeV LHC*, JHEP **09** (2015) 206, arXiv:1507.02238 [hep-ph].

[42] A. Falkowski, *Higgs Basis: Proposal for an EFT basis choice for LHC HXSWG*, LHCHXSWG-INT-2015-001 (2015) . https://cds.cern.ch/record/2001958.

[43] *Projections for measurements of Higgs boson cross sections, branching ratios and coupling parameters with the ATLAS detector at a HL-LHC*, ATL-PHYS-PUB-2013-014 (2013) . https://cds.cern.ch/record/1611186.

[44] *HL-LHC projections for signal and background yield measurements of the $H \to \gamma\gamma$ when the Higgs boson is produced in association with t quarks, W or Z bosons*, ATL-PHYS-PUB-2014-012 (2014) . https://cds.cern.ch/record/1741011.

[45] *Update of the prospects for the $H \to Z\gamma$ search at the High-Luminosity LHC*, ATL-PHYS-PUB-2014-006 (2014) . https://cds.cern.ch/record/1703276.

[46] *Prospects for the study of the Higgs boson in the VH(bb) channel at HL-LHC*, ATL-PHYS-PUB-2014-011 (2014) . https://cds.cern.ch/record/1740962.

[47] *Studies of the VBF $H \to \tau_l\tau_{had}$ analysis at High Luminosity LHC conditions*, ATL-PHYS-PUB-2014-018 (2014) . https://cds.cern.ch/record/1956732.

[48] A. Falkowski, M. Gonzalez-Alonso, A. Greljo, and D. Marzocca, *Global constraints on anomalous triple gauge couplings in effective field theory approach*, Phys. Rev. Lett. **116** (2016) no. 1, 011801, arXiv:1508.00581 [hep-ph].

[49] A. Butter, O. J. P. Éboli, J. Gonzalez-Fraile, M. C. Gonzalez-Garcia, T. Plehn, and M. Rauch, *The Gauge-Higgs Legacy of the LHC Run I*, JHEP **07** (2016) 152, arXiv:1604.03105 [hep-ph].

[50] R. Contino, A. Falkowski, F. Goertz, C. Grojean, and F. Riva, *On the Validity of the Effective Field Theory Approach to SM Precision Tests*, JHEP **07** (2016) 144, arXiv:1604.06444 [hep-ph].

Draft-v0.2

[51] A. Falkowski, M. Gonzalez-Alonso, A. Greljo, D. Marzocca, and M. Son, *Anomalous Triple Gauge Couplings in the Effective Field Theory Approach at the LHC*, JHEP **02** (2017) 115, arXiv:1609.06312 [hep-ph].

[52] Z. Zhang, *Time to Go Beyond Triple-Gauge-Boson-Coupling Interpretation of W Pair Production*, Phys. Rev. Lett. **118** (2017) no. 1, 011803, arXiv:1610.01618 [hep-ph].

[53] ATLAS Collaboration, *Search for the Standard Model Higgs and Z Boson decays to $J/\psi\,\gamma$: HL-LHC projections*, ATL-PHYS-PUB-2015-043 (2015) . http://cds.cern.ch/record/2054550.

[54] G. T. Bodwin, F. Petriello, S. Stoynev, and M. Velasco, *Higgs boson decays to quarkonia and the $H\bar{c}c$ coupling*, Phys. Rev. **D88** (2013) no. 5, 053003, arXiv:1306.5770 [hep-ph].

[55] G. Perez, Y. Soreq, E. Stamou, and K. Tobioka, *Constraining the charm Yukawa and Higgs-quark coupling universality*, Phys. Rev. **D92** (2015) no. 3, 033016, arXiv:1503.00290 [hep-ph].

[56] I. Brivio, F. Goertz, and G. Isidori, *Probing the Charm Quark Yukawa Coupling in Higgs+Charm Production*, Phys. Rev. Lett. **115** (2015) no. 21, 211801, arXiv:1507.02916 [hep-ph].

[57] F. Bishara, U. Haisch, P. F. Monni, and E. Re, *Constraining Light-Quark Yukawa Couplings from Higgs Distributions*, arXiv:1606.09253 [hep-ph].

[58] L. M. Carpenter, T. Han, K. Hendricks, Z. Qian, and N. Zhou, *Higgs Boson Decay to Light Jets at the LHC*, Phys. Rev. **D95** (2017) no. 5, 053003, arXiv:1611.05463 [hep-ph].

[59] M. McCullough, *An Indirect Model-Dependent Probe of the Higgs Self-Coupling*, Phys. Rev. **D90** (2014) 015001, arXiv:1312.3322 [hep-ph].

[60] S. Di Vita, C. Grojean, G. Panico, M. Riembau, and T. Vantalon, *A global view on the Higgs self-coupling*, arXiv:1704.01953 [hep-ph].

[61] Y. Gao, A. V. Gritsan, Z. Guo, K. Melnikov, M. Schulze, and N. V. Tran, *Spin determination of single-produced resonances at hadron colliders*, Phys. Rev. **D81** (2010) 075022, arXiv:1001.3396 [hep-ph].

[62] S. Bolognesi, Y. Gao, A. V. Gritsan, K. Melnikov, M. Schulze, N. V. Tran, and A. Whitbeck, *On the spin and parity of a single-produced resonance at the LHC*, Phys. Rev. **D86** (2012) 095031, arXiv:1208.4018 [hep-ph].

[63] I. Anderson et al., *Constraining anomalous HVV interactions at proton and lepton colliders*, Phys. Rev. **D89** (2014) no. 3, 035007, arXiv:1309.4819 [hep-ph].

Draft-v0.2

11.2 W, Z measurements at the CEPC

With high production cross sections and large integrated luminosity, the CEPC will reach a new level of precision for measurements of the properties of the W and Z bosons. Precise measurements of the W and Z boson masses, widths, and couplings are critical to test the consistency of the SM [1]. In addition, many BSM models predict new couplings of the W and Z bosons to other elementary particles. Precise electroweak measurements performed at the CEPC could discover deviations from the SM predictions and reveal the existence of new particles that are beyond the reach of current experiments.

Significant improvements are expected from the CEPC measurements. Table 11.8 lists the expected precision from CEPC compared to achieved precisions from the LEP experiments for various measurements. Details about the estimation of these uncertainties are described in this section.

Table 11.8: The expected precision in a selected set of EW precision measurements in CEPC and the comparison with the precision from LEP experiments. The CEPC accelerator running mode and total integrated luminosity expected for each measurement are also listed. Depending on detector solenoid field during Z pole operation, the integrated luminosity varied from $8ab^{-1}$ to $16ab^{-1}$.

Observable	LEP precision	CEPC precision	CEPC runs	$\int \mathcal{L}$ needed in CEPC
m_Z	2 MeV	0.5 MeV	Z threshold scan	$8ab^{-1} - 16\text{ab}^{-1}$
$A_{FB}^{0,b}$	1.7%	0.1%	Z threshold scan	$8ab^{-1} - 16\text{ab}^{-1}$
$A_{FB}^{0,\mu}$	7.7%	0.3%	Z threshold scan	$8ab^{-1} - 16\text{ab}^{-1}$
$A_{FB}^{0,e}$	17%	0.5%	Z threshold scan	$8ab^{-1} - 16\text{ab}^{-1}$
$\sin^2\theta_W^{\text{eff}}$	0.07%	0.001%	Z threshold scan	$8ab^{-1} - 16\text{ab}^{-1}$
R_b	0.3%	0.02%	Z pole	$8ab^{-1} - 16\text{ab}^{-1}$
R_μ	0.2%	0.01%	Z pole	$8ab^{-1} - 16\text{ab}^{-1}$
N_ν	1.7%	0.05%	ZH runs	5.6ab^{-1}
m_W	33 MeV	2-3 MeV	ZH runs	5.6ab^{-1}
m_W	33 MeV	1 MeV	WWthreshold	2.6ab^{-1}

11.2.1 Z pole measurements

The CEPC offers the possibility of dedicated low-energy runs at the Z pole for at least two years with a high instant luminosity ($1.6 - 3.2 \times 10^{35} cm^{-2} s{-}1$). The expected integrated luminosity for CEPC Z pole runs is more than 8 ab^{-1}, and it is expected to produce about 10^{12} Z bosons (Tera-Z).

These runs allow high precision electroweak measurements of the Z boson decay partial widths, e.g. the parameters $R_b = \Gamma_{Z\to b\bar{b}}/\Gamma_{\text{had}}$ and $R_\ell = \Gamma_{\text{had}}/\Gamma_{Z\to \ell\bar{\ell}}$. (Notice that R_ℓ is defined as the ratio to any *one* charged lepton flavor, assuming lepton universality, not the ratio to the sum of all lepton flavors.) It would also perform high precision measurements of the forward-backward charge asymmetry (A_{FB}), the effective weak mix-

Draft-v0.2

ing angle ($\sin^2\theta_W^{\rm eff}$), number of light neutrino species (N_ν), and the mass of the Z boson (M_Z). It is also possible to perform some measurements with the Z boson without these dedicated low-energy runs near or at the Z pole. For example, the direct measurement of the number of light neutrino species can be performed in ZH runs at 240 GeV.

11.2.1.1 R_b

The width of the Z boson to each of its decay channels is proportional to the square of the fundamental Z-fermion couplings. The partial width R_b is sensitive to electroweak radiative corrections from new physics particles. For example, the existence of the scalar tops or charginos in supersymmetry could lead to a visible change of R_b from the SM prediction.

Precise measurements of R_b have been made by LEP collaborations [2–6] and by the SLD collaboration [7] at SLAC using hadronic Z events.

Decays of b-hadrons were tagged using tracks with large impact parameters and/or reconstructed secondary vertices, complemented by event shape variables. The combination of LEP and SLD measurements yields a value of 0.21629 ± 0.00066 for R_b. The relative statistical uncertainty of R_b is above 0.2%, and systematic uncertainty is about 0.2%.

A precision of 0.05% can be achieved for the measurement of R_b at CEPC, and it will improve the current precision in experimental measurement by one order of magnitude. The statistical uncertainty improves by two order of magnitude and the systematic uncertainties will also reduce. The main systematic uncertainty is the uncertainty due to hemisphere tag correlations in $Z \to b\bar{b}$ events (0.05%).The uncertainty due to hemisphere tag correlations will be reduced to a level of 0.05% due to the expected improvement in the b-tagging performance of the CEPC detector. The improvement of b-tagging efficiency is important to reduce this corrections, and this correlation becomes irrelevant in the limit of 100% b-tagging efficiency. Due to that fact that a next-generation vertex detector will be used in the CEPC detector, the b-tag efficiency is expected to be around 70% with a b-jet purity of 95% as shown in Fig. **??**, which is about 15%-20% higher than the efficiency in than previous measurements. The uncertainty due to hemisphere tag correlations can be reduce to 0.05% level, which is a factor of four lower than previous measurements.

11.2.1.2 The partial decay width of $Z \to \mu^+\mu^-$

The $\mu^+\mu^-$ channel provides the cleanest leptonic final state. Combining the measurements from all four LEP experiments [8–11], the overall uncertainty of R_μ is 0.2%. The statistical uncertainty of R_μ is 0.15%.

A precision of 0.01% can be achieved at the CEPC. The main systematic is the uncertainty of photon energy scale in the $Z \to \mu^+\mu^-\gamma$ process. About 2% of the $Z \to \mu^+\mu^-$ sample are classified as $Z \to \mu^+\mu^-\gamma$ events with a photon detected in ECAL. For this class of events, the most critical cut is that on the difference between the expected and measured photon energy ($|E_\gamma^{expected} - E_\gamma^{expected}| < 5\sigma_\gamma$), which is very efficient in removing the $Z \to \tau\tau$ background. The

The energy resolution in the EM calorimeter of the CEPC detector is expected to be 16%/sqrt(E), which is significantly better than the resolution in previous measurements. Therefore, the uncertainty due to photon energy scale and resolution in $Z \to \mu^+\mu^-\gamma$ process can be reduced to 0.01%. The main challenge in this measurement is to reduce the systematics due to QED ISR events. More detailed studies of radiative events in Z

Draft-V0.2

threshold scan runs are expected. Benefitting from high statistics in Z threshold scan runs, the source of uncertainty can be reduced to a level of 0.03%.

11.2.1.3 The forward-backward asymmetry A_{FB}^{b} at the Z pole

The measurement of the forward-backward asymmetry in $e^+e^- \rightarrow b\bar{b}$ events at the Z pole, $A_{FB}^{b,0}$, gives an important test of the Standard Model. $A_{FB}^{b,0}$ offers the most precise determination of the weak mixing angle. The measurements have been made at SLD and LEP experiments [12–16].

$Z \rightarrow b\bar{b}$ events were identified by tagging two b jets. Each event was divided into forward and backward categories by the plane perpendicular to the thrust axis which contains the interaction point. The combination of the LEP and SLD measurements gives a measured value of $A_{FB}^{b,0} = 0.1000 \pm 0.0017$. The statistical uncertainty is 1.2% and the main systematic uncertainties come from hemisphere tag correlations for b events (1.2%), tracking resolution and vertex detector alignment (0.8%), charm physics modeling (0.5%), and QCD and thrust axis correction (0.7%).

A precision of 10^{-4} can be achieved for the measurement of $A_{FB}^{b,0}$ at the CEPC, improving the current precision by more than a factor of 10. The expected statistical uncertainty is at a level of 0.05%. The uncertainty due to hemisphere tag correlations for b events can be reduced to 0.1% due to high b-tagging efficiency. The uncertainty due to charm physics modeling can be reduced to 0.05% by choosing a tighter b-tagging working point. The uncertainty due to tracking resolution and vertex detector alignment can be reduced to 0.05%. The expected tracking momentum resolution in the CEPC detector is $\sigma/p_T = 2 \times 10^{-4} \times p_T + 0.005$, which is 10 times better than the resolutions of the LEP detectors. The uncertainty due to QCD and thrust axis correction can be reduced to 0.1% due to at least 10 times better granularity in the CEPC calorimeters. Overall, the expected systematics at CEPC measurement can be reduced to a level of 0.15%.

11.2.1.4 The prospects for the effective weak mixing angle measurement

The weak mixing angle $\sin^2\theta_W^{\rm eff}$ is a very important parameter in the electroweak theory of the SM. It is the only free parameter that fixes the relative couplings of all fermions to the Z. It describes the rotation of the original W^0 and B^0 vector boson states into the observed γ and Z bosons as a result of spontaneous symmetry breaking. The weak mixing angle is very sensitive to electroweak radiative corrections, and it can be used perform a precise test of the SM theory. Furthermore, if there is any new heavy gauge boson Z', the weak mixing angle is expected to deviate from the SM prediction due to the contribution from physics in loop corrections. Therefore $\sin^2\theta_W^{\rm eff}$ is very sensitive to new physics as well.

The centre-of-mass energy dependence of the forward-backward asymmetry arises from the interference of the Z boson with the virtual photon and thus depends on $\sin^2\theta_W^{\rm eff}$. In other words, the effective weak mixing angle can be extracted by studying the $\sqrt{s}$ dependence of the forward-backward asymmetry.

The effective weak mixing angle measurement has been performed in LEP using $Z \rightarrow b\bar{b}$ events and $Z \rightarrow \ell^+\ell^-$ events. The forward-backward asymmetry A_{FB} in one Z-pole dataset and two off Z-pole datasets ($\sqrt{s}$ = 89.4 GeV , $\sqrt{s}$ = 93.0 GeV) are used to extract $\sin^2\theta_W^{\rm eff}$. The current experimental result is $\sin^2\theta_W^{\rm eff} = 0.23153 \pm 0.00016$. $Z \rightarrow b\bar{b}$ events were identified by tagging two b jets. The main uncertainty includes uncertainty on

Draft-v0.2

the A_{FB}^{b} measurement as described in Sec. 11.2.1.3. and the statistical uncertainty in off Z-pole datasets.

Both Z-pole and off Z-pole runs are needed to perform the effective weak mixing angle measurement at the CEPC. The Z off-peak runs are expensive, therefore we need to optimize the integrated luminosity for off-peak runs. In order to improve the precision of $\sin^2\theta_W^{\text{eff}}$ by a factor of 3, the required CEPC integrated luminosity for Z-pole runs are $8-16$ ab^{-1} and at least $2-4$ ab^{-1} integrated luminosity is needed for off Z-pole runs.The expected precision of effective weak mixing angle measurement in CEPC using $Z \to b\bar{b}$ events is expected to be 0.02%.

11.2.1.5 Z mass measurement

The mass m_Z is a fundamental parameter in the SM and was determined with an overall uncertainty of 2 MeV by four LEP experiments. The mass scan around the Z peak was performed from 88 GeV to 94 GeV. The Z mass was measured by a combined fit to the hadronic and leptonic cross sections in the on-peak and off-peak datasets. Most of the m_Z information is extracted from the off-peak runs. Taking the OPAL measurement as one example, six off-peak datasets were used to complete the m_Z scan. The main uncertainty of m_Z includes the statistical uncertainty (1 MeV$/c^2$), and the LEP beam energy (about 1 MeV$/c^2$).

A precision of 0.5 MeV can be achieved in CEPC measurement. The mass scan around the Z peak is the key for improving m_Z measurements.

The LEP measurement was limited by the statistics in their off-peak runs, therefore the luminosity in Z off-peak runs plays an important role in the m_Z measurement. We propose six off-peak runs and one on-peak run in CEPC Z mass scan, as listed in Table **??**. The expected m_Z uncertainty in CEPC due to statistics is about 0.1 MeV.

Another important systematic is beam momentum scale uncertainty. The beam momentum uncertainty in the CEPC accelerator is expected to be accurate to the 10 ppm level, which is about five times better than LEP. The uncertainty on m_Z due to the uncertainty on the beam energy can be reduced to less than 0.5 MeV.

Hadronic decay channels of the Z events are also expected to be used to measure m_Z since the leptonic decay channels suffer from low statistics. The uncertainty due to jet energy scale and resolution results in about 0.1 MeV in the m_Z measurement.

11.2.1.6 Neutrino species counting

Two different methods have been used to determine the number of neutrino species (N_ν) at LEP.

The first method is an indirect method using the analysis of the Z lineshape, and it uses the data collected by the Z threshold scan runs. The second method is a direct measurement, which is based on the measurement of the cross section for the radiative process $e^+e^- \to \nu\nu\gamma$. The second method at CEPC is supposed to use the ZH runs.

These two methods use different theoretical inputs from the Standard Model and also use completely different datasets, therefore they are independent and complementary. The sensitivity to new physics will be different for these two methods. In the direct method, one can measure N_ν as a function of $sqrts$. This is very sensitive to new physics at high energy scales. Possible contributions include WIMP dark matter particles, and other weakly coupled particles such as exotic neutrinos, gravitinos, or KK gravitons in theories

Draft-v0.2

with large extra dimensions. Thus, when we refer to the number of neutrino species, we actually include any number of possible invisible particles other than neutrinos.

Indirect method from Z line shape The indirect method assumed all contributions from invisible channels are coming from the $Z \to \nu\bar{\nu}$. This method used the analysis of Z line-shape, subtracting the visible partial widths of the hadrons ($\Gamma_{\rm had}$), and the partial widths of the leptons (Γ_ℓ) from the total width Γ_Z. The invisible width $\Gamma_{\rm inv}$ can be written as:

$$\Gamma_{\rm inv} = N_\nu \Gamma_\nu = \Gamma_Z - \Gamma_{\rm had} - 3\Gamma_\ell. \tag{11.16}$$

We take as our definition of the number of neutrinos $N_\nu = \Gamma_{\rm inv}/\Gamma_\nu$, i.e. the ratio of the invisible width to the Standard Model expectation for the partial width to a single neutrino species.

Using the input from SM model, we can rewrite equation 11.16 as the following:

$$N_\nu = \frac{\Gamma_\ell}{\Gamma_\nu}\left(\sqrt{\frac{12\pi R_\ell}{M_Z^2 \sigma^0_{\rm had}}} - R_\ell - 3\right). \tag{11.17}$$

As shown in equation 11.17, the precision of N_ν depends on the the lepton partial width R_ℓ measurement, the Z mass measurement, and the hadronic cross section of the Z boson on its mass peak ($\sigma^0_{\rm had}$). The precision of $\sigma^0_{\rm had}$ gives the largest impact to N_ν measurement, and it is very sensitive to the precision of the luminosity. Therefore the precise luminosity measurement is the key to determine N_ν.

Precise measurements of N_ν have been made by LEP collaborations, and they obtained a precision of 0.27% using this indirect method. The main systematics of the N_ν measurement is coming from the uncertainty of luminosity (0.14%) and the theory uncertainty in the predicted cross section of the small angle Bhabha process (0.11%).

The precision of 0.1% in N_ν measurement with the indirect method can be achieved in CEPC measurement, which improves the current precision by a factor of three. Benefitting from the recent development of luminosity detector technology, the uncertainty due to luminosity can be reduced to 0.05%. The uncertainty from the small angle Bhabha process can be reduced to 0.05% due to recent progress in studying this process.

Direct method using $e^+e^- \to \nu\bar{\nu}\gamma$ events The most precise direct N_ν measurements at LEP were carried out by the L3 collaboration and Delphi collaboration. By combining the direct measurements at LEP, the current experimental result is $N_\nu = 2.92 \pm 0.05$. The statistical uncertainty of N_ν in the previous measurement is 1.7%. The main systematic uncertainty from the L3 measurement includes the uncertainty in single photon trigger efficiency (0.6%), and photon identification efficiency (0.3%), and the uncertainty in identifying the converted photons (0.5%).

A precision of 0.2% can be achieved for the direct measurement of N_ν at CEPC, and it will improve the current precision by a factor of 10. Due to the excellent performance of the CEPC inner tracker, the uncertainty due to converted photons' selection efficiency is expected to be negligible. The granularity of the CEPC EM calorimeter is expected to be 10 to 100 times better than the detectors at LEP. Therefore photons can be identified with high purity with loose EM shower shape based selection. The uncertainty of photon efficiency can be reduced to less than 0.05%.

Draft-v0.2

11.2.2 W mass measurement

In e^+e^- collisions, W bosons are produced mainly through $e^+e^- \rightarrow W^+W^-$ process. The cross section of this process at the WW production threshold is very sensitive to m_W. m_W can be measured from polarized threshold scan runs.

At centre-of-mass energies above W^+W^- production threshold, the mass of the W bosons can be determined by measuring the momentum of its decay products. This is called the direct measurement approach in this section.

The measurements have been made at LEP using both the polarized threshold scan method and a direct measurement approach. The threshold scan method suffered from large statistical uncertainty (about 200 MeV). The direct measurement approach using $\ell\nu qq$ and $qqqq$ channels at LEP provides a better measurement. The uncertainty due to limited data statistics in the direct measurement was found to be about 30 MeV. The main systematic uncertainties from the measurement include the modeling of hadronization (13 MeV) and radiative corrections (8 MeV), and the energy scale of lepton and missing energy (10 MeV).

Using the threshold scan method, a precision of 1.0 MeV can be achieved for the measurement at the CEPC. We assume that the CEPC can provide a 4-point threshold scan with 2.6 ab^{-1} integrated luminosity. The $\sqrt{s}$ values of threshold scan runs are assumed to be 157.5, 161.5, 162.5, and 172.0 GeV. The proposed run plan is shown in Table 11.9. The list of systematic uncertainties is summarized in Table 11.10.

Table 11.9: Using threshold scan measurement method in dedicated WW threshold scan runs, The proposed 4 $e^+e^- \rightarrow W^+W^-$ threshold scan runs and their integrated luminosity.

Beam Energy (GeV)	Lumiosity (ab^{-1})	Cross section(pb)	Number of WW pairs (million)
157.5	0.5	1.3	0.6
161.5	0.2	3.9	0.8
162.5	1.3	5.0	6.5
172.0	0.5	12.2	6.1

Using the direct measurement method, a precision of 3 MeV can be achieved for the measurement at CEPC. The main advantage of the direct measurement method is that no dedicated run is needed: all the measurements can be performed in ZH runs with $\sqrt{s} = 240$ GeV. Another advantage is that this method has a lower requirement for accelerator performance. The main challenge of this method is to handle the uncertainty due to QED radiation. The energy spread from beamstrahlung is proportional to the square of the beam energy. To reduce the dependence of the m_W precision on the absolute beam polarization and momentum determination, a dedicated study using radiative return ($e^+e^- \rightarrow Z\gamma$) events is necessary. The uncertainty due to the beamstrahlung effect can be reduced to the 1 MeV level using 5.6 ab^{-1} data. Other systematic uncertainties include the lepton momentum scale and the modeling of hadronization. The list of systematic uncertainties are summarized in Table 11.11.

Draft-v02

Table 11.10: Using threshold scan measurement method in dedicated WW threshold scan runs, the expected precision in m_W measurement in CEPC detectors and the comparison with LEP experiments.

ΔM_W(MeV)	LEP	CEPC
$\sqrt{s}$(GeV)	161	240
$\int \mathcal{L}$(fb^{-1})	3	2600
beam energy scale	13	0.4
luminosity,background,signal acceptance	10	0.5
statistics	20	0.8
total	36	1.0

Table 11.11: Using direct measurement method in ZH runs, the expected precision in m_W measurement in CEPC detectors and the comparison with the LEP experiments.

ΔM_W(MeV)	LEP	CEPC
$\sqrt{s}$(GeV)	$180-203$	240
$\int \mathcal{L}$(fb^{-1}	3	5600
channel	$l\nu qq, qqqq$	$l\upsilon qq$
beam energy	9	1.0
hadronization	13	1.5
radiative corrections	8	1.0
lepton and missing energy scale	10	1.5
bias in mass reconstuction	3	0.5
statistics	30	0.5
total	36	3.0

Draft-v0.2

References

[1] J. Erler, S. Heinemeyer, W. Hollik, G. Weiglein, and P. Zerwas, *Physics impact of GigaZ*, Phys.Lett. **B486** (2000) 125–133, arXiv:hep-ph/0005024 [hep-ph].

[2] ALEPH Collaboration, DELPHI Collaboration, L3 Collaboration, OPAL Collaboration, LEP Electroweak Working Group Collaboration, J. Alcaraz et al., *A Combination of preliminary electroweak measurements and constraints on the standard model*, arXiv:hep-ex/0612034 [hep-ex].

[3] L3 Collaboration, M. Acciarri et al., *Measurement of R(b) and Br($b \to$ lepton neutrino X) at LEP using double tag methods*, Eur. Phys. J. **C13** (2000) 47–61, arXiv:hep-ex/9909045 [hep-ex].

[4] OPAL Collaboration, G. Abbiendi et al., *A Measurement of R(b) using a double tagging method*, Eur. Phys. J. **C8** (1999) 217–239, arXiv:hep-ex/9810002 [hep-ex].

[5] DELPHI Collaboration Collaboration, P. Abreu et al., *A Precise measurement of the partial decay width ratio* $R_b^0 = \Gamma(b\bar{b})/\Gamma(\mathrm{had})$, Eur.Phys.J. **C10** (1999) 415–442.

[6] ALEPH Collaboration, R. Barate et al., *A Measurement of R(b) using mutually exclusive tags*, Phys. Lett. **B401** (1997) 163–175.

[7] SLD Collaboration Collaboration, K. Abe et al., *Measurement of the branching ratio of the Z0 into heavy quarks*, Phys.Rev. **D71** (2005) 112004, arXiv:hep-ex/0503005 [hep-ex].

[8] OPAL Collaboration, G. Abbiendi et al., *Precise determination of the Z resonance parameters at LEP: 'Zedometry'*, Eur. Phys. J. **C19** (2001) 587–651, arXiv:hep-ex/0012018 [hep-ex].

[9] DELPHI Collaboration, P. Abreu et al., *Cross-sections and leptonic forward backward asymmetries from the Z0 running of LEP*, Eur. Phys. J. **C16** (2000) 371–405.

[10] L3 Collaboration, M. Acciarri et al., *Measurements of cross-sections and forward backward asymmetries at the Z resonance and determination of electroweak parameters*, Eur. Phys. J. **C16** (2000) 1–40, arXiv:hep-ex/0002046 [hep-ex].

[11] ALEPH Collaboration, R. Barate et al., *Measurement of the Z resonance parameters at LEP*, Eur. Phys. J. **C14** (2000) 1–50.

[12] SLD Collaboration, K. Abe et al., *Direct measurements of A(b) and A(c) using vertex/kaon charge tags at SLD*, Phys. Rev. Lett. **94** (2005) 091801, arXiv:hep-ex/0410042 [hep-ex].

[13] ALEPH Collaboration Collaboration, A. Heister et al., *Measurement of A^b(FB) using inclusive b hadron decays*, Eur.Phys.J. **C22** (2001) 201–215, arXiv:hep-ex/0107033 [hep-ex].

Draft-v0.2

[14] OPAL Collaboration Collaboration, G. Abbiendi et al., *Measurement of the b quark forward backward asymmetry around the Z0 peak using an inclusive tag*, Phys.Lett. **B546** (2002) 29–47, arXiv:hep-ex/0209076 [hep-ex].

[15] DELPHI Collaboration Collaboration, J. Abdallah et al., *Determination of A^b(FB) at the Z pole using inclusive charge reconstruction and lifetime tagging*, Eur.Phys.J. **C40** (2005) 1–25, arXiv:hep-ex/0412004 [hep-ex].

[16] L3 Collaboration Collaboration, M. Acciarri et al., *Measurement of the $e^+e^- \to Z \to b\bar{b}$ forward–backward asymmetry and the B0 anti-B0 mixing parameter using prompt leptons*, Phys.Lett. **B448** (1999) 152–162.

Draft-v0.2

CHAPTER 12

FUTRUE PLANS AND R&D PROSPECTS

This [1] is an example with plots, please edit ...

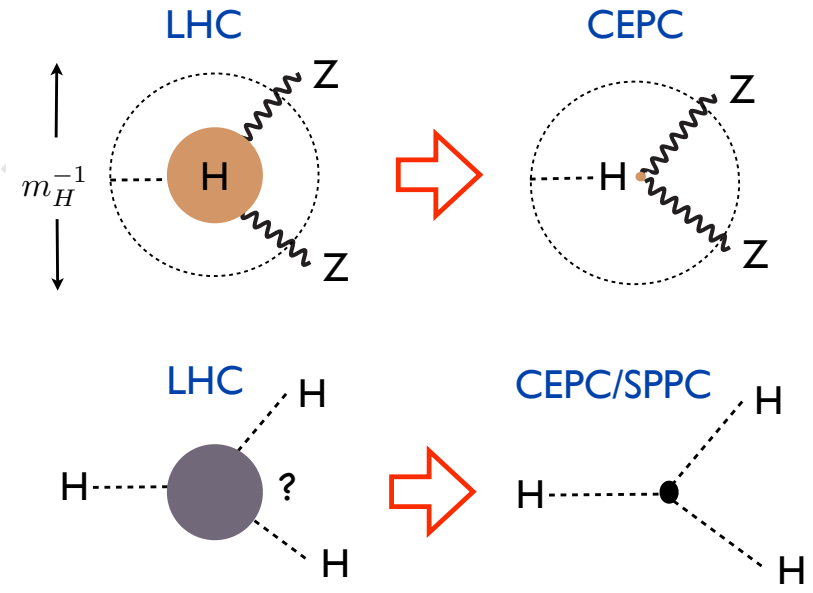

Figure 12.1: A sketch of two of the central goals of the CEPC and SPPC. The CEPC will probe whether the Higgs is truly “elementary", with a resolution up to a hundred times more powerful than the LHC. The SPPC will see, for the first time, a fundamentally new dynamical process — the self-interaction of an elementary particle — uniquely associated with the Higgs.

By Copyright © 2018 HEP Community

12.1 New Colliders for a New Frontier

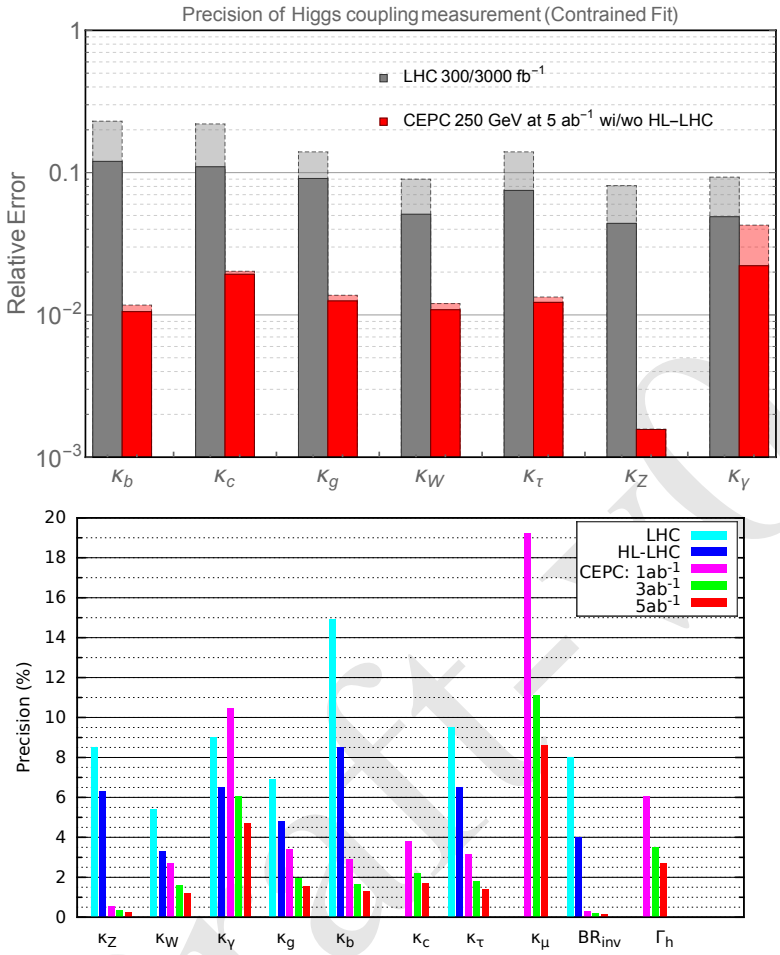

Figure 12.2: Top: The 7 parameter fit, and comparison with the HL-LHC, discussed in detail in Chapter 10. The projections for CEPC at 250 GeV with 5 ab^{-1} integrated luminosity are shown. The CEPC results without combination with HL-LHC input are shown with dashed edges. The LHC projections for an integrated luminosity of 300 fb^{-1} are shown in dashed edges. Bottom: Comparison between the LHC and several benchmark luminosities of the CEPC.

References

[1] CEPC project website. http://cepc.ihep.ac.cn.

Draft-2018.7